

# ***Ph.D. THESIS IN CHEMICAL ENGINEERING***

***XXV Cycle***



## ***Water condensation for submicronic particles abatement***

***Scientific committee***

***Prof. Antonio Cavaliere***

***Eng. Maria Rosaria de Joannon***

***Dott. Michela Alfè***

***Candidate***

***Gennaro Cozzolino***



***Water condensation for submicronic particles abatement***

***Table of contents***

<b><i>Introduction: motivation and aim</i></b>	<b><i>1</i></b>
<b><i>Chapter 1</i></b>	
<b><i>The formation and growth of droplets. State of art.</i></b>	<b><i>9</i></b>
<b><i>1.1 General aspects</i></b>	<b><i>10</i></b>
<b><i>1.2 Thermodynamic of phase transitions</i></b>	<b><i>11</i></b>
<b><i>1.3 Homogeneous nucleation</i></b>	<b><i>12</i></b>
<b><i>1.3.1 Kelvin's formula</i></b>	<b><i>13</i></b>
<b><i>1.3.2 Homogeneous nucleation rate</i></b>	<b><i>18</i></b>
<b><i>1.4 Heterogeneous nucleation</i></b>	<b><i>22</i></b>
<b><i>1.4.1 Nucleation enhanced by insoluble particles</i></b>	<b><i>22</i></b>
<b><i>1.4.1.1 Analysis of the wettability transition for liquid-solid system.</i></b>	<b><i>27</i></b>
<b><i>1.4.1.2 Effect of surface roughness on wettability</i></b>	<b><i>40</i></b>
<b><i>1.4.2 Heterogeneous nucleation rate</i></b>	<b><i>46</i></b>
<b><i>1.4.2.1 Activation probability</i></b>	<b><i>49</i></b>
<b><i>1.4.3 Nucleation enabled by soluble particles</i></b>	<b><i>51</i></b>
<b><i>1.4.4 Nucleation activated by ions</i></b>	<b><i>54</i></b>
<b><i>1.4.5 Nucleation activated insoluble solid charged particles</i></b>	<b><i>55</i></b>
<b><i>1.4.6 Physics of capillary condensation</i></b>	<b><i>58</i></b>
<b><i>1.4.7 Wetting and hydration of insoluble soot particles</i></b>	<b><i>71</i></b>
<b><i>1.5 Diffusional Growth</i></b>	<b><i>75</i></b>
<b><i>1.6 Coagulation</i></b>	<b><i>75</i></b>
<b><i>1.7 Particles growth rate</i></b>	<b><i>77</i></b>

*Table of contents*

**Chapter 2**

<b><i>Experimental facility for condensational growth studies</i></b>	<b>91</b>
<b>2.1 <i>Experimental configurations for the study of nucleation process</i></b>	<b>91</b>
<b>2.2 <i>Experimental lay-out</i></b>	<b>100</b>

**Chapter 3**

<b><i>Diagnostics and diagnostic set-up</i></b>	<b>109</b>
<b>3.1 <i>Laser Light Scattering</i></b>	<b>110</b>
<b>3.1.1 <i>Rayleigh Theory</i></b>	<b>116</b>
<b>3.1.2 <i>Mie Theory</i></b>	<b>117</b>
<b>3.1.3 <i>Polarization ratio</i></b>	<b>119</b>
<b>3.2 <i>Scattering by a composite sphere with an absorbing inclusion</i></b>	<b>121</b>
<b>3.3 <i>Description of the optical diagnostic system</i></b>	<b>131</b>
<b>3.4 <i>Dynamic Light Scattering</i></b>	<b>133</b>
<b>3.5 <i>TEM and HRTEM</i></b>	<b>141</b>
<b>3.6 <i>Absorption (UV-Vis)</i></b>	<b>144</b>
<b>3.7 <i>Electrical Low Pressure Impactor - E.L.P.I</i></b>	<b>147</b>
<b>3.8 <i>B.E.T.</i></b>	<b>148</b>
<b>3.9 <i>FT-IR</i></b>	<b>149</b>
<b>3.10 <i>Thermogravimetry</i></b>	<b>150</b>

**Chapter 4**

<b><i>Experimental Results</i></b>	<b>151</b>
<b>4.1 <i>Characterization of the solid particulate</i></b>	<b>151</b>

*Table of contents*

<i>4.2</i>	<i>Effect of inlet Temperature</i>	<i>168</i>
<i>4.3</i>	<i>Effect of particles number concentration</i>	<i>180</i>
<i>4.4</i>	<i>Effect of particle dimension</i>	<i>183</i>
<i>4.5</i>	<i>Effect of vapour concentration</i>	<i>184</i>
<i>4.6</i>	<i>Effect of local conditions</i>	<i>190</i>

*Chapter 5*

<i>Discussion</i>	<i>195</i>	
<i>5.1</i>	<i>Polarization ratio and evolution of condensation process: a scheme of interpretation</i>	<i>196</i>
	<i>5.1.1 Comparison of polarization of particles with a liquid layer</i>	<i>197</i>
	<i>5.1.2 Qualitative spatial/temporal evolution of condensation process</i>	<i>203</i>
<i>5.2</i>	<i>Effect of local conditions: activation processes and saturation conditions</i>	<i>205</i>
<i>5.3</i>	<i>Effect of particles chemical nature</i>	<i>218</i>
<i>5.4</i>	<i>Effect of particles number concentration</i>	<i>219</i>
<i>5.5</i>	<i>Effect of initial particles dimension</i>	<i>220</i>
<i>5.6</i>	<i>Characteristic times of the condensation process</i>	<i>221</i>
<i>5.7</i>	<i>Evaluation of particles dimension and growth factor</i>	<i>224</i>

*Chapter 6*

<i>Conclusion</i>	<i>233</i>
<i>Appendix</i>	<i>240</i>
<i>References</i>	<i>248</i>

## ***Introduction***

The phenomenon of air pollution is largely connected to human model of economic and social development; it is particularly related to the urban background since its main anthropogenic sources are vehicular traffic, productive processes in the civil sector and industrial activity.

Air pollutants can be divided into two main categories: the particulate matter and gaseous contaminants (SO<sub>x</sub> , NO<sub>x</sub>, CO, CO<sub>2</sub>). The first, comprises the group of substances suspended either in solid or liquid form in the atmosphere as, carbonaceous or metals particles, fibers and acids droplet, with a diameter ranging from a few nanometers up to 500 microns. The Particulate Matter is better known by the acronym PM followed by the size in microns, (one-thousandth of a millimeter) it is usually classified into groups based on the aerodynamic diameter of the particles.

Atmospheric (natural) aerosol consists of particles and corpuscles suspended in the atmosphere. Their chemical composition is variable and it depends on the origin of the aerosol which can be introduced in the atmosphere by the action of winds on deserts and the consequent transportation of ultrafine sands, or by the action of winds on oceans and the consequent transportation of sea foam. Furthermore large quantities of aerosol could be produced by volcanoes or are caused by industrial emissions.

The sources of particulate emissions are mainly related to industrial activities, even if the higher risk of exposure was located in densely populated areas, affected by an intense urban traffic. Aerosols act as aggregation nuclei for the water vapour molecules and thus contribute to the formation of clouds. They also play an important role in the process of scattering of solar radiation, in fact they represent the diffusion centers of solar radiation which, is deflected from particles surface in a different direction from that of incidence; therefore they contribute in a considerably way to the redistribution of solar energy - radiation while only in

small amount they contribute to the absorption of such radiation. The increase of atmospheric aerosols due to pollution has led in recent years to the emergence of a phenomenon known as global dimming, which partly compensates for the global warming. For this reason, various national and international agencies have defined over the years specific environmental regulations for emissions of particulate matter in the atmosphere and air quality criteria for internal and urban areas. Some directives regarding the emissions of particulates in the air set the limit to  $PM_{10}$ , but this parameter is proving to be relatively slightly restrictive. In the matter of industrial plants (factories, power plants, incinerators) this restriction is even more inadequate, because it refers only to the total weight of the particulates and not to their size. Since 2010, the  $PM_{10}$  annual limit value in ambient air has been fixed at  $20 \mu\text{gm}^{-3}$  and the daily limit value at  $50 \mu\text{gm}^{-3}$ , which cannot be exceeded more than 7 times over a year; for  $PM_{5}$  and  $PM_{2.5}$ , these limits correspond to  $25 \mu\text{gm}^{-3}$  and  $10 \mu\text{gm}^{-3}$  respectively. Similarly, stricter rules were applied to emissions produced by internal combustion engines of vehicles (Euro 4, Euro 5 and Euro 6 starting from 2014).

Among the diseases ascribed to fine and ultrafine particles, mainly  $PM_{2.5}$  and  $PM_{1}$ , there are acute and chronic pathologies of the breathing apparatus.

Particulate matter emissions are mainly due to combustion sources. Under ideal conditions, the complete combustion of the carbon based fuel should give rise only to the generation of carbon dioxide and water. Other combustion products, including the particulate matter, are often commonly defined as products of incomplete combustion process.

Most of the combustion processes is man-made and the related particulate matter produced, in terms of particles number, is largely attributable to the ultrafine category. Their chemical composition is complex, containing many elements present in trace, originally present in the fuel.

In several cases the combustion of a specific fuel such as coal, releases into the atmosphere not only the typical products of the incomplete combustion but an entire class of elements, including: Mg, Ca, Al, K, Sc, Fe and Mn. (Oberdöster G., 2001) (Table 1 in Appendix A)

Since most of the "intruders" elements present in the fuel, does not undergo chemical and physical transformations, they tend to be passively transported into the atmosphere after that they were released from the carbonaceous matrix.

The concentration values of the elements above mentioned, can be extremely variable, as can be seen from Table 2 in Appendix A, which shows the concentrations of aerosols, of different chemical nature, produced by different industrial processes. (Simonenkov DVET al., 2004).

The concentration of these components can vary by several orders of magnitude, this due to the properties of the fuel used in a specific industrial process.

However, despite of this scenario, the traditional abatement devices are not optimized to operate in the range of submicron particles dimensions.

Improvements in the operation at optimal working conditions might be facilitated by increasing the dimension of the particles to be eliminated upstream of the standard cleaning processes.

For particle diameters ranging from 0.1  $\mu\text{m}$  to 1  $\mu\text{m}$  (Greenfield gap), the removal efficiency of traditional abatement systems decreases to approximately 25%, thereby making the application of these systems impractical also because they do not reach the required specifications imposed by environmental regulations.

This is due to the size and physical properties of such particles. The existing technologies such as filters, cyclones, separators, whose operating principle is based on inertial forces acting on the particles, are ineffective for the removal of ultrafine particles from gas streams.

This is because the motion of these particles is determined mainly by molecular and inertial forces, the latter having less influence with decreasing particle size.

Usually, complex systems consisting of abatement equipment placed in series, are used. Fibrous filters may be useful in the removal of finer particles, but operate with high pressure drops. The wet-scrubber require a liquid spray at high speed, but also in this case the pressure drops are high in such devices. The sleeve filters have a good collection efficiency for coarse particles and for fine dust, but cannot operate with humid charge and they also are subject to explosion problems. It is therefore necessary to develop new techniques and better methods for the treatment and for the abatement of submicronic particles.

A promising technique for both industrial and domestic applications relies on increasing the diameter of fine and ultra-fine particles by condensing water vapor onto the particles themselves thus to improve the performances of traditional particle collection devices. The easy availability of vapor at relatively low temperatures makes this technique interesting for a wide range of industries, including chemical, glass, cement and metallurgy production systems and combustion facilities, all of which are interested in the removal of fine particles from waste gases. It might be even more relevant to combustion systems containing significant amounts of vapour, such as MILD or coal oxy-fuel combustion processes.

In comparison to traditional condensation systems, providing for condensation of water present in exhaust gas primarily oriented to energy recovery, the use of a suitable quantity of vapour in this process and its consecutive condensation, could enable a drastic reduction of particulate emission with the abatement efficiency possibly reaching more than 90%.

Condensation scrubbers are a rather new development of wet scrubbers technology and they are usually employed for fine and ultrafine particulates abatement with an efficiency of more than 90% whereas traditional technologies have a very low efficiency.

In this case, particles act as condensation nuclei for the formation of water drops. Generally the gas-vapour mixture is lead to saturation condition and then is subsequently injected into the device, then heterogeneous condensation occurs.

Water drops of suitable size which incorporate the particulate are thereafter removed by traditional mist eliminators.

Scrubbers are employed to remove particulates and/or pollutant from industrial waste gas. These systems were traditionally designed to remove pollutants from gas streams by means the interaction of liquid jets or flows with the gas stream.

“Wet” scrubbers are so defined because they use liquids (mainly water) to remove pollutants from gas streams through multiple interaction mechanisms. The gas stream interacts with the liquid in several ways; the liquid can be atomized into the gas stream or the gas can bubble through the liquid. The fluid dynamic configuration used (i.e. the design of the adduction system for the liquid flow and the interaction mechanism employed) heavily depends on the nature of the pollutant that has be removed. Such devices remove the particles from the gas stream incorporating them in liquid droplets or sheets and thereafter separate the liquid phase from the gas. The principal parameters influencing the process of the particles capturing are:

- size of particulate;
- size of droplets;
- relative speed between particulates and droplets;

In general bigger particulates are easier to capture. The particles collection efficiency by droplet cloud spray, increases as the droplets size reduces and their number density grows.

The greater energy needed to cause the dispersion of very thin and dense droplets justifies the previous statement that higher efficiency amounts to higher energy consumption. Furthermore a higher relative velocity between the gas stream (and particulate present in it) and the liquid droplets facilitates the particles collection.

Capture of gaseous pollutants occurs through a mechanism of dissolution in the liquid. It is essential that the gas which has to be eliminated is soluble in the liquid, if needed it is possible to add some additives to increase gas to liquid solubility. In this case the fluid dynamic configuration should be such to guarantee a high degree of mixing of the two phases for an adequately long residence time assuring a suitable dissolution of the gas in the liquid.

The smaller the particles are, the more they tend to follow the gas streamlines. The impact frequency between the droplets and particles depends on their relative size and velocity.

The probability of impact between droplets and particles increases with the increase of their relative velocity and particles size because of their reduced availability to follow the streamlines of the gas flow, as seen in Fig. 1a. Moreover, smaller droplets improve frequency impact. Impact is the predominant collection mechanism for gas speed higher than 0.3 m/s and for particles of micronic size. Very small particles (less than  $0.1 \mu\text{m}$  in diameter) generally tend to follow gas streamlines around the droplets. For this reason, their chance to inertially impact on the droplets is extremely low and the previously described mechanism is substantially inactive. However these particles are susceptible to significant random motion (Brownian motion) due to their interaction with gas molecules, as shown in Figure 1b.

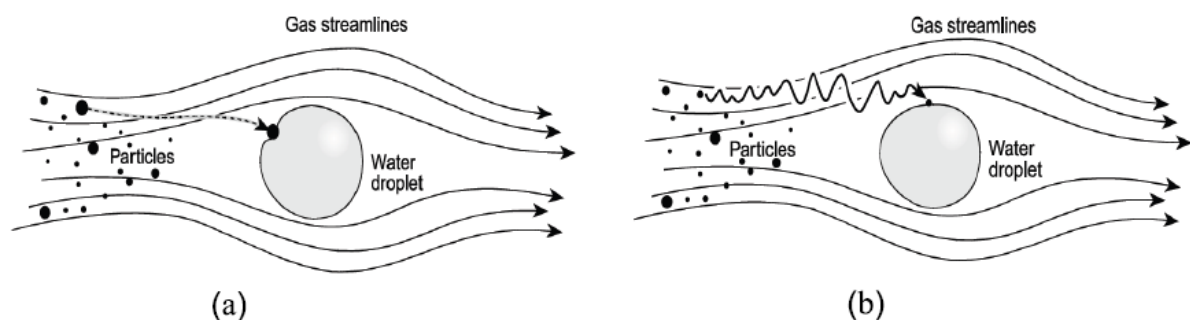


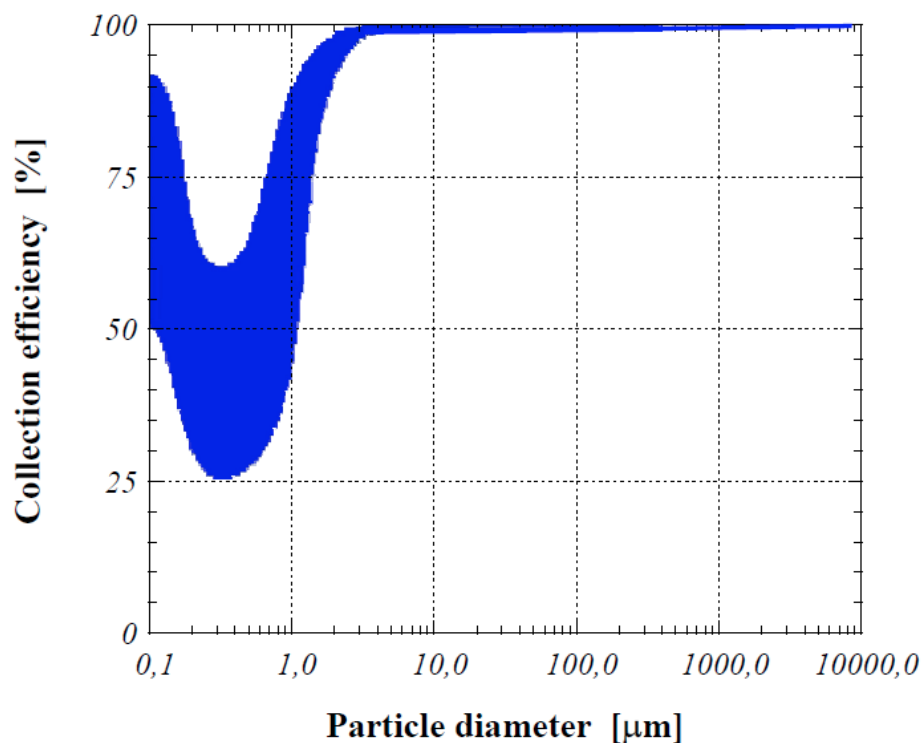
Figure 1: (a) Inertial impact and (b) Brownian motion

Such casual motion lets the particles to diffuse through the gas independently from the streamlines of the gas motion field. This allows them to impact with liquid droplets. In

practice, as regards very small particles (and suitable conditions) such collection mechanism is the most notable.

Figure 2 reports the trend of collection efficiency as a function of particles size (<http://www.epa.gov/apti/bces/module3/collect/collect.htm>).

For particles diameter ranging between 0.1 and 1  $\mu\text{m}$ , none of the previously described mechanisms guarantees an high removal efficiency.



The primary aim of this PhD thesis is to analyze the flue gases cleaning process by means of activation heterogeneous water nucleation mechanism on particles surface as a function working condition (inlet temperature and vapor concentration) with particular regard to the effect of their dimension, number concentration, morphology and chemical nature on nucleation activation process.

The study has been conducted carrying out a very deep bibliographic research, illustrated in Chapter 1, concerning the process of vapor nucleation and formation of droplets to identify

the dependencies of the process from environmental parameters and the characteristics of the particle functioning as condensation nucleus. In Chapter 2 a review of experimental systems potentially useful to study the process of particulate abatement has been presented. Then the chosen system to study the particles activation process via heterogeneous nucleation, has been described.

The experimental tests has been realized through optical diagnostics techniques described in Chapter 3. In conclusion, Chapter 4 reports a complete experimental evaluation of droplet formation and growth process on particles surface that can be assimilated to that potentially present in the exhaust gas of an industrial or combustion process.

## **CHAPTER 1**

### ***The formation and growth of droplets. State of art.***

The formation and growth of droplets activated via heterogeneous nucleation, is a very complex process that depends on a great number of parameters, both of environment and condensing substance coupled with solid substrate properties that acts as condensation nuclei, including dimensions, number concentration and history. This chapter summarizes the state of the art and the pertinent literature on the formation and growth process of droplets. The fundamental steps of evolution of this process are described. It must be stressed that temperature, pressure, vapor concentration, fluid-dynamic field, as well as particle characteristics, influence each single sub-process, that evolve in series and/or parallel, with the advancement of condensation process, thus making it difficult to directly relate an overall trend to a specific effect. Furthermore it is worth emphasizing that the factors influencing the particles wetting show a tremendous dependence on the surface chemical composition and microstructure. Hence a deep knowledge of these sub-processes, is very important for a full comprehension of the mechanisms involved in the particles wetting and subsequent formation and growth of droplets on their surface. Finally a clear overview of the processes involved in the mechanisms of growth and formation of droplets is necessary for a good interpretation of the experimental results.

## 1.1 General aspects

The process of formation and growth of the droplets and or crystals during the condensation process is described qualitatively in Fig. 1.1.

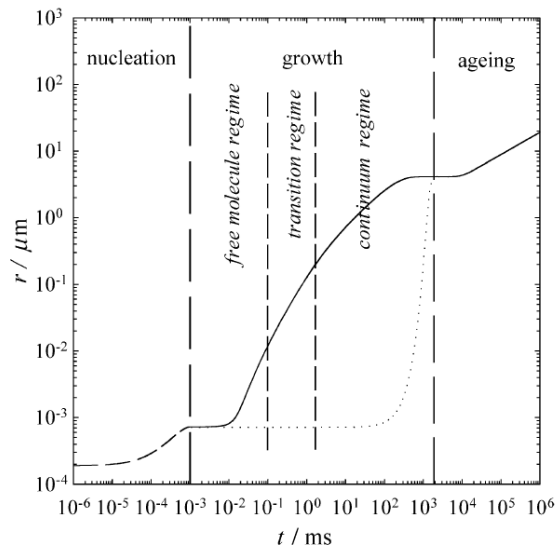


Figure 1.1: Evolution of an aerosols from molecular dimensions up to micrometer droplets (Fladerer et al., 2003)

If  $S=p/p_0$  is the saturation, it takes place in supersaturation conditions ( $S>1$ ), through a first step, where nucleation leads to the formation of a stable embryo with characteristic times lower than the microsecond. The nucleation is the process by which, through the agglomeration of vapor molecules, embryos of a new phase are formed.

Thus the new phase is formed from embryos, or molecular aggregates which can be unstable due to thermal agitation. The steam then remains in a metastable situation and there is not an effective condensation. By increasing supersaturation embryos become more stable and their survival probability increases for supersaturation higher than critical value ( $S>S_c$ ). When this process takes place within of a pure substance, it is identified as homogeneous nucleation and

is characterized by a high value of supersaturation. When small foreign particles are present in the steam, these can act as condensation nuclei. In this case the heterogeneous nucleation occurs and the supersaturation required is much lower.

The nucleation plays a very important role in different fields. For example, it is involved in the formation of submicronic embryos, metallic and or ceramic, many of which are characterized by new chemical and physical properties related to the small size of such structures. Furthermore, the control of nucleation in equipment such as turbines, missiles, jet engines and combustion processes is the key to efficient and eco-compatible operations.

The growth is controlled by the kinetic, for particles of size smaller than 10 nm. For particles larger than 200 nm the growth phase is controlled by the diffusion of molecules of vapor towards the droplet surface until reaching larger dimensions. In the range of sizes between 10 nm and 200 nm there is a transition zone where the dimensional growth of the droplets is controlled by the two mechanisms just mentioned.

The process of nucleation and growth by condensation causes a decrease in vapor concentration in the gas phase and that make the increase droplets diameter terminate. A further increase in droplet size is due to the coagulation among the just formed droplets (Fladerer et al. , 2003).

## ***1.2 Thermodynamic of phase transitions***

Let us consider a monophasic homogeneous system with enthalpy equal to  $H = U + pV$ . It is possible to define these quantities:

$$A = -TS \tag{1.1}$$

$$G = H - TS = U - TS + pV \tag{1.2}$$

which are respectively Helmholtz and Gibbs free energy,. Taking into account the first law of thermodynamics ( $dU = Tds - pdV$ ), the equations (1.1) and (1.2) can be written in differential forms as follow:

$$dA = -SdT + pdV \quad (1.3)$$

$$dG = -SdT + Vdp \quad (1.4)$$

If a system is in equilibrium at constant temperature and pressure ( $dT = dp = 0$ )  $G$  is constant ( $dG = 0$ ) and it is possible to show that it has a minimum. In any spontaneous process since the final state must be closer to equilibrium than the initial state,  $A$  and  $G$  must decrease. In a system at constant pressure, such as an atmospheric system, one can refer to the free energy of Gibbs that will simply call free energy.

In a system contains  $n_1$  molecules in the phase 1, and  $n_2$  molecules in the phase 2  $G$  is the free energy of the system and the partial molar quantities:

$$\left(\frac{\partial G}{\partial n_i}\right)_{T,p,n_j} = \left(\frac{\partial U}{\partial n_i}\right)_{S,V,n_{j \neq i}} \rightarrow \mu_i = \mu_j \quad (1.5)$$

are the chemical potentials of the phase  $i$ . The two phases  $i$  and  $j$  are in equilibrium when  $dG = 0$ .

### ***1.3 Homogeneous nucleation***

Homogeneous nucleation refers to the spontaneous creation of a new phase from a metastable phase. The phase change can be from the vapor to a condensed phase (condensation), from a condensed phase to the vapor, or from a solution phase to solid phase.

### 1.3.1 Kelvin's formula

If  $\mu_v$  is the chemical potential of water molecule in the vapor phase, and  $\mu_l$  is the chemical potential of a water molecule in the liquid state and, the molecules are aggregated in the vapor phase to form a liquid droplet of radius  $r$ , volume  $V$ , and surface  $A$ , the system free energy variation is:

$$\Delta G = (\mu_l - \mu_v)n_l V + \sigma_{lv}A \quad (1.6)$$

Where  $n_l$  is the number of molecules per unit volume in the liquid phase and  $\sigma_{lv}$  is the interface free energy per unit area between liquid and vapor. In a liquid  $\sigma_{lv}$  is, equivalent to the surface tension. If the two phases are in equilibrium, the chemical potential is the same in the two phases, ( $\mu_v(p_s) = \mu_l$ ). In this case the liquid is in equilibrium at a pressure  $p$  with saturated steam at  $p_s$  above a liquid flat surface:

$$\mu_l - \mu_v = \mu_v(p_s) - \mu_v(p) \quad (1.7)$$

If the pressure varies by an infinitesimal quantity  $dp$  at constant temperature ( $dT=0$ )

$$dG = -SdT + Vdp = Vdp \quad (1.8)$$

the chemical potential variation is

$$d\mu_v = V_v dp = \frac{k_B T}{p} dp \quad (1.9)$$

where  $V_v$  is the volume occupied by a single molecule in the vapor phase, at  $(T, p)$ .

Similarly for the liquid phase the variation of the chemical potential for a pressure change  $dp$  at constant  $T$  is:

$$d\mu_l = V_l dp \quad (1.10)$$

where  $V_l$  is the volume occupied by a single molecule in the liquid phase at (T, p). Since  $V_v \gg V_l$  then:

$$d(\mu_v - \mu_l) \cong V_v dp = \frac{k_B T}{p} dp \quad (1.11)$$

Integrating it is obtained

$$\int_0^{\mu_v - \mu_l} d(\mu_v - \mu_l) = \int_{p_s}^p \frac{k_B T}{p} dp \quad (1.12)$$

$$\mu_v - \mu_l = -k_B T \log \frac{p}{p_s} \quad (1.13)$$

where  $k_B$  is the Boltzmann constant and  $p/p_s = S$  is the saturation ratio. The equation (1.8) shows that variation  $(\mu_v - \mu_l)$  is positive when the vapor is not saturated and negative when the vapor is supersaturated. Assuming the formation of a spherical embryo the equation (1.6) becomes:

$$\Delta G = -\frac{4}{3}\pi r^3 n_l k_B T \log \frac{p}{p_s} + 4\pi r^2 \sigma_{lv} \quad (1.14)$$

$n_l$  being the number of water molecules that constitute the embryo.

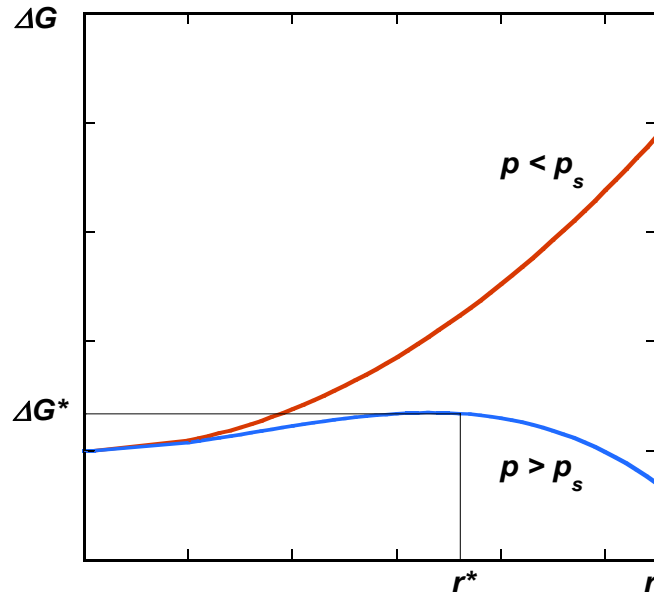


Figure 1.2: Trend of  $\Delta G$  for a supersaturated ( $p > p_s$ ) and for an unsaturated system ( $p < p_s$ )

The variation of Gibbs energy as a function of  $r$  is shown in Figure 1.2, both for unsaturated and for supersaturated cases. It is clear that the free energy required to form embryos sharply increases with their size for the unsaturated case  $p < p_s$ .

Because of thermal fluctuations, it is expected that the number of embryos of a fixed size is given by a Boltzmann distribution. If it is assumed that the total number of embryos is negligible in comparison with the number of dissociated molecules then the distribution is:

$$N(r) \approx N(I) \exp\left(-\frac{\Delta G(r)}{k_B T}\right) \quad (1.15)$$

Where  $N(r)$  is the number of molecular embryos per unit of volume with radius  $r$ , and  $N(I)$  is the number of molecules per unit volume.

For  $p < p_s$  a large number of embryos is present because of the hetero-phase fluctuation, i.e. the distribution is in dynamic equilibrium and there is no tendency to condensation, because the large drops are unstable.

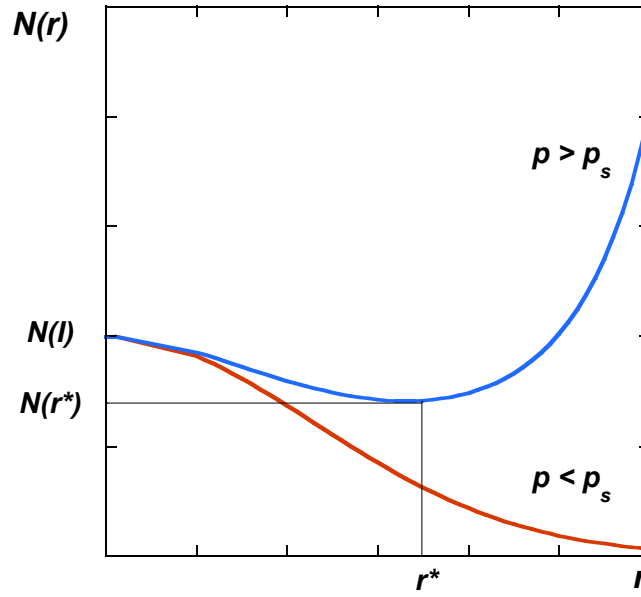


Figure 1.3: Trend of total embryo numbers as function of  $r$  for a supersaturated ( $p > p_s$ ) and for an unsaturated system ( $p < p_s$ )

For  $p > p_s$  free energy necessary to the formation of a stable embryo has a maximum equal to  $\Delta G^*$  for a value of  $r = r^*$ . Embryos with radius  $r < r^*$  are unstable and tend to disappear under the effect of thermal agitation. Embryos with radius  $r > r^*$  tend to grow without limit and embryos become larger.  $r^*$  can be obtained from  $\partial \Delta G / \partial r = 0$  that leads to:

$$r^* = \frac{2\sigma_{lv}}{n_L k_B T \log \frac{p}{p_s}} \quad (1.16)$$

where  $n_L$  is the molecules number in the vapor phase. Since embryos of radius  $r^*$  are in equilibrium with vapor at pressure  $p$ , the equation (1.16) can be written in the form:

$$\log \left( \frac{p}{p_s} \right) = \frac{2\sigma_{lv}}{n_L k_B T r^*} \quad (1.17)$$

known as Kelvin's formula. By substituting (1.17) into (1.14) the maximum value of the variation of free energy for the formation of an embryo is obtained:

$$\Delta G_{hom}^* = \frac{4}{3}\pi r^{*2}\sigma_{lv} \quad (1.18)$$

Figure 1.4 shows the trend of the critical embryo dimension by varying vapor concentration for different temperatures. As working plane, for a fixed concentration and temperature of the vapor in the system, it indicates the value of the critical radius of stable nuclei and therefore the optimal working conditions for the activation of the nucleation process. It shows that for a fixed temperature a decrease in the vapor concentration make the critical dimension of the embryos increase. For example, for  $T = 320$  K and an  $x_v = 1$  embryos become stable for a dimension equal to 0.5 nm, while for a vapor concentration of  $x_v = 0.25$  a stable embryos must have a critical radius of at least 1 nm.

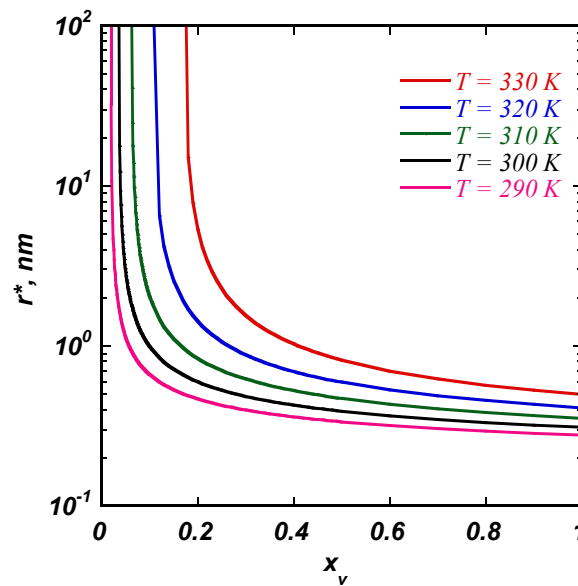


Figure 1.4: Trend of Kelvin radius as function of vapor concentration for some fixed values of temperature

### 1.3.2 Homogeneous nucleation rate

A key parameter in the study of nucleation is the rate of production of molecular critical size embryos formed by vapor phase which can then evolve towards larger drops, identified as nucleation rate. From a general point of view the rate of formation of critical size embryos, is given by an expression of the following form:

$$J = K \exp\left(-\frac{\Delta G^*}{k_B T}\right) \quad (1.19)$$

where  $K(T, P)$  is a collisional frequency factor, and  $\Delta G^*$  is the energy of formation of an embryo of critical dimensions (Oxtoby DW et al., 1992). The value of  $K$  is sometimes uncertain and is affected by the particular type of nucleation process and by system.  $J$  is influenced largely by  $\Delta G^*$  and not by  $K$ . Taking into account the equation (1.19), the homogeneous nucleation rate, can be expressed as follows:

$$J_{hom} = K_{hom} \exp\left(-\frac{\Delta G_{hom}^*}{k_B T}\right) \quad (1.20)$$

where the pre-exponential kinetic factor has the following form (Giechaskiel B. et al., 2011):

$$K_{hom} = R_{growth} F Z_{nucl} \quad (1.21)$$

$K_{hom}$  is equal to the product of three terms: the embryos growth rate  $R_{growth}$ , the Zeldovich non-equilibrium factor  $Z_{nucl}$ , and the term  $F$  is the total number of molecules that are

nucleating and can be obtained by the product of the numerical concentration of the vapor molecules and the volume of the system (Drossinos and Kevrekidis, 2003).

The growth rate of the critical embryo  $R_{growth}$  is obtained by considering the growth by collisions with the individual molecules of steam, neglecting surface growth by diffusion, and assuming that the exposed surface of the critical embryo is approximately the surface of liquid-vapor interface. Thus

$$R_{growth} = 4\pi r^{*2} \beta_v \quad (1.22)$$

where

$$\beta_v = \frac{P_v}{(2\pi k_B T m_{v,mol})^{1/2}} \quad (1.23)$$

$\beta_v$  is the molecular flow toward the embryo of critical size  $r^*$  and it can be calculated from the kinetic theory of gases. In equation (1.23)  $m_{v,mol} = M_v/N_a$  is the molecular mass of vapor species,  $N_a$  is Avogadro's number,  $P_v$  the partial pressure,  $k_B$  is the Boltzmann constant and  $T$  the absolute temperature. The Zeldovich non-equilibrium factor of  $Z_{nucl}$ , is derived from the number of fluctuations in the critical embryo that may cause it to shrink. It is a dimensionless factor expressed as:

$$Z_{nucl} = Z_{hom} = \frac{\sigma_{lv}^{1/2} \tilde{v}_v}{2\pi r^{*2} (k_B T)^{1/2}} \quad (1.24)$$

At equilibrium, the number of nucleated embryos of radius  $r^*$  does not change. The homogeneous nucleation theory asserts that the system is not always in equilibrium thus while some embryos reach the critical size, others decay into smaller one due to evaporation or

thermal agitation. This leads to a variation of the number of nucleated embryos with time.  $Z_{nucl}$  takes into account the remaining differences between equilibrium and non-equilibrium concentration of embryos. In equation (1.24)  $\tilde{v}_v = v_v/N_a$  is the molecular volume of the liquid phase, and  $\sigma_{lv}$  the surface tension of the liquid phase.

Summarizing, the expression of homogeneous nucleation is the following:

$$J_{hom} = 4\pi r^{*2} \beta_v Z_{nucl} \exp\left(-\frac{\Delta G_{hom}^*}{k_B T}\right) \quad (1.25)$$

The equation (1.25) is one of the several expressions present in literature for the nucleation rate and is the one that has been taken into account in the different evaluation reported in this thesis. However, it is of interest to give an indication on other available expressions of  $J_{hom}$ . Thus in table 1.1 different expressions of the nucleation rate found in the literature have been summarized.

Table 1.1. Expressions of nucleation rate.

<b>Classical theory (Fladerer, 2003)</b>	$J = \sqrt{\frac{8\sigma_{lv}M}{\pi k_B R^3}} \cdot \left(\frac{p_s}{T}\right)^2 \cdot \frac{N_A}{2\rho_l} \cdot S^2 \exp\left\{-\frac{16\pi}{3k_B} \cdot \left(\frac{\sigma_{lv}}{T}\right)^3 \cdot \left(\frac{v_l M}{R \cdot \ln S}\right)^2\right\}$
<b>(Hering, 2005)</b>	$J = \frac{2}{\rho_l} \sqrt{\frac{m_l \sigma_{lv}}{2\pi}} \left(\frac{p_v}{k_B T}\right)^2 \exp\left[-\frac{\pi \sigma_{lv}}{3k_B T} d^{*2}\right]$
<b>(Chukanov, 2007)</b>	$J = \frac{1}{s} \sqrt{\frac{2\sigma_{lv}}{\pi m}} \left(\frac{P_V}{k_B T}\right)^2 \frac{m}{\rho} \exp\left[-\frac{16}{3} \pi \left(\frac{\sigma_{lv}}{k_B T}\right)^3 \left(\frac{m}{\rho \cdot \ln S}\right)^2\right]$
<b>(Kotzick, 1996)</b>	$J \cong 4\pi r^{*2} 10^{25} \exp\left(-\frac{16\pi \sigma^3 M^2}{3k_B T (\rho RT \cdot \ln S)^2}\right)$
<b>(Kumala et al., 1992)</b>	$J = n_s^2 s v_l \sqrt{\frac{2\sigma_{lv}}{\pi m}} \exp\left(\theta' - \frac{4\theta'^3}{27 \log^2(S)}\right)$ $\theta' = s \sigma_{lv} / k_B T$
<b>(Kashichiev, 2006)</b>	$J = \frac{A}{16B^4} \exp\left(\frac{3B^{1/3}}{4^{1/3}}\right) (\ln S)^{12m} S \exp\left[-\frac{B}{(\ln S)^{2m}}\right]$ $A = \frac{M}{\rho_l N_A} \sqrt{\frac{2\sigma_{lv}}{\pi m}} \left(\frac{P_V}{k_B T}\right)^2 \quad B = \frac{16\pi v_l^2 \sigma_{lv}^3}{3(k_B T)^3}$

Despite the numerous expressions of  $J_{\text{hom}}$  found in the literature, it is not possible to identify a general one, able to reproduce the available experimental data in different temperature and saturation ranges. These expressions, given the high degree of empiricism, may differ up to several orders of magnitude. On the other hand it is necessary to underline that such expressions reported in literature have been generally validated for atmospheric conditions, so that their effectiveness in the operating conditions adopted in this study has to be proven and makes the choose of the proper model difficult. The complexity increases even more when heterogeneous nucleation is considered. In fact, in such a case other terms have to be taken into account. In Figure 1.5 a comparison of different expressions of the nucleation rate of Table 1.1 has been reported as function of supersaturation for three different temperatures.

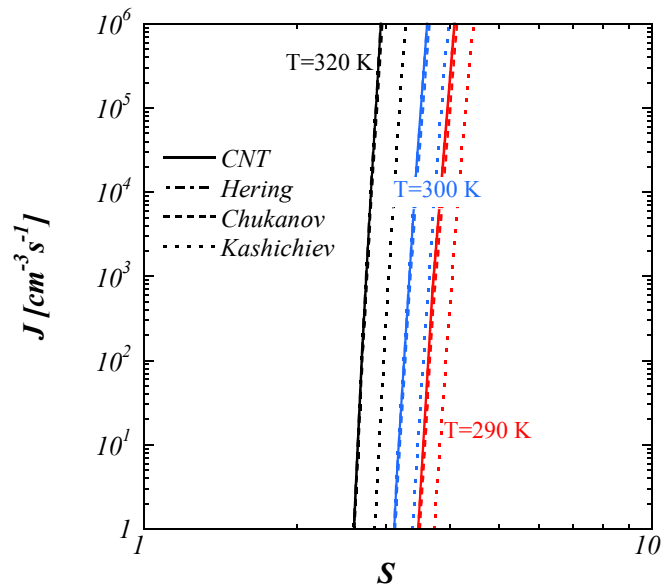


Figure 1.5: Comparison of different nucleation rate, evaluated at different temperatures, by varying the degree of supersaturation,  $S$ .

The trends of  $J$  in Figure 1.5 for three temperatures show that the expression of  $J$  derived from the classical theory are nearly equivalent to one reported by Hering and Chukanov. On the contrary the expression reported by Kashichiev shows a significant difference that increases with increasing temperature.

## ***1.4 Heterogeneous nucleation***

In the previous paragraph the process of homogeneous nucleation has been described by means of the thermodynamic and kinetic equations that lead to the identification of the controlling parameters of the process and to several semi-empirical expression of the nucleation rate. However, it is worth to note that the homogeneous nucleation is a rare process in nature. Indeed, it is generally overcome by heterogeneous nucleation to which competes a more favorable energetic condition with respect to the homogeneous nucleation process. In the following paragraph the main issues related to the heterogeneous condensation process have been discussed in details with particular regard to aspects of interest in this thesis.

### ***1.4.1 Nucleation enhanced by insoluble particles***

The nucleation in the atmosphere occurs on foreign particles (heterogeneous nucleation). Thus it is crucial to understand how microscopic powder particles, hygroscopic crystals or other natural contaminants act as condensation nuclei. The heterogeneous nucleation on particles is of great interest in many engineering fields, and it is of great importance to understand the dependence of efficiency of nucleation on the controlling parameters, such as the size, nature and surface characteristics of the particles and the temperature and the saturation of the environment. The most popular theory of heterogeneous condensation is the one reported by Fletcher (1958). It assume that the particle which acts as a nucleus of condensation is an homogeneous sphere.

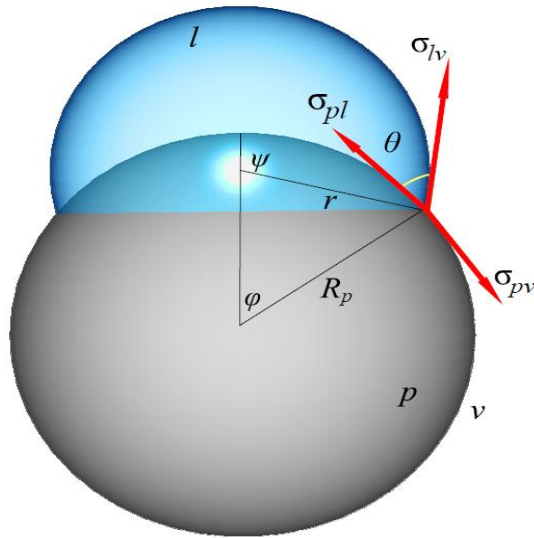


Figure 1.6: Schematic representation of the nucleated embryo on solid particle.

This assumption is necessary for simplicity of mathematical treatment, and is a physically reasonable assumption in several cases. In addition, it represents the simplest configuration to consider. (N.H Fletcher, 1958).

Similar assumptions are made for embryos formed on the particles surface, which are similar to a spherical cap. In this condition the interfacial free energy associated to the edges becomes appreciable.

The system to which the Fletcher theory refers is schematized in Figure 1.6. In such a figure v represents the vapor phase, l the molecular embryo, i.e. liquid phase, and p the solid particle. If V is the volume and S the surface, then the free energy of formation of an embryo of radius r on an insoluble solid core of radius  $R_p$  is given by:

$$\Delta G = -\frac{4}{3}\pi r^3 n_l k_B T \log \frac{p}{p_s} + 4\pi r^2 \sigma_{lv} + (\sigma_{lp} - \sigma_{vp}) S_{lp} \quad (1.26)$$

Considering the contact angle  $\theta$  of the liquid drop on a solid perfectly smooth surface, as shown in the Figure 1.6, the balance of the free interfacial energies at the surface leads to the expression:

$$\sigma_{pv} = \sigma_{pl} + \sigma_{lv}\cos\theta \quad (1.27)$$

known as *Young's equation*. From the equation (1.27)

$$m = \cos\theta = \frac{\sigma_{vp} - \sigma_{lp}}{\sigma_{lv}} \quad (1.28)$$

where  $\sigma_{pv}, \sigma_{pl}, \sigma_{lv}$  are respectively the free interface energies between vapor-solid, liquid-solid, and liquid-vapor phases.: The equation (1.23) represents the standard definition of the contact angle. As a consequence,  $-1 \leq m \leq 1$ .

From the Figure 1.6 it is possible to obtain the following relations:

$$\left\{ \begin{array}{l} S_{vl} = 2\pi r^2(1 - \cos\psi) \\ S_{lp} = 2\pi R_p^2(1 - \cos\phi) \\ V_l = \frac{1}{3}\pi r^3(2 - 3\cos\psi + \cos^3\psi) - \frac{1}{3}\pi R_p^3(2 - 3\cos\phi + \cos^3\phi) \end{array} \right. \quad (1.29)$$

and

$$\left\{ \begin{array}{l} \cos\phi = (R_p - r\cos\theta)/d = (R_p - rm)/d \\ \cos\psi = (r - R_p\cos\theta)/d = (r - R_p m)/d \end{array} \right. \quad (1.30)$$

where

$$d = (R_p^2 + r^2 - 2rR_p m)^{\frac{1}{2}} \quad (1.31)$$

To evaluate the critical free energy  $\Delta G^*$  corresponding to the formation of a stable embryo on the particle surface the expression of  $S_{ip}$  from (1.29) must be replaced in (1.26) and to impose:

$$(\partial \Delta G / \partial r)^* = 0 \quad (1.32)$$

The free energy of formation of an embryo critical on a solid particle is as follows:

$$\Delta G_{het}^* = \Delta G_{hom}^* f(m, x) \quad (1.33)$$

In the case of heterogeneous nucleation, it contains a form factor  $f(m, x)$ , that is function of the size, the shape and characteristics of the solid particles. It determines a reduction of the energy barrier of nucleation due to the presence of solid particles in vapor phase. In particular, it is always that  $\Delta G_{het}^* \leq \Delta G_{hom}^*$  and then the heterogeneous nucleation is always thermodynamically favored with respect to homogeneous nucleation. The factor form is expressed as follows:

$$f(m, x) = \frac{1}{2} \left[ 1 + \left( \frac{1 - mx}{g} \right)^3 + x^3 \left[ 2 - 3 \left( \frac{x - m}{g} \right) + \left( \frac{x - m}{g} \right)^3 \right] + 3mx^2 \left( \frac{x - m}{g} - 1 \right) \right] \quad (1.34)$$

where

$$x = \frac{R_p}{r^*} \quad e \quad g = (1 + x^2 - 2mx)^{1/2} \quad (1.35)$$

Figure 1.7 shows the typical trend of the factor  $f(m, x)$  as a function of the relative size of the foreign particle  $x$ , for fixed values of  $m$ .

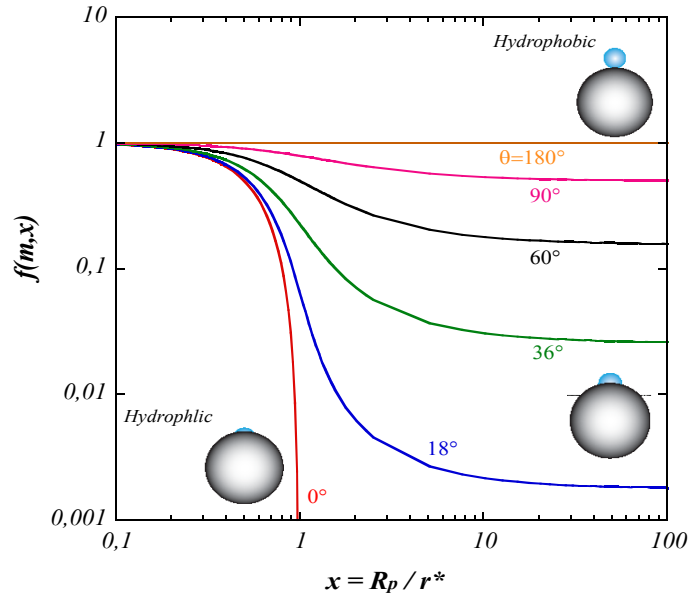


Figure 1.7: Trend of  $f(m, x)$  as function of the relative size,  $x$ , between the solid particle and the critical radius drop, for fixed values of contact angle (adapted from Fletcher, 1958) .

The expression (1.28) for  $m = 1$  ( $\theta = 180$ ) i.e. total absence of wettability, coincides to the case of homogeneous nucleation. For  $x = \infty$ , that correspond to a solid surface with infinite radius of curvature, the expression of the form factor will no longer depend on the size of the solid core but only by its chemical-physical and morphological properties. Such a case can be identified as wall nucleation. In these conditions, the form factor will have the following expression:

$$f(m) = \frac{(2 + m)(1 - m)^2}{4} \quad (1.36)$$

Furthermore, since  $-1 \leq m \leq 1$ , then  $0 \leq f(m) \leq 1$ , as shown in Figure 1.8.

Summarizing, the factor  $f(m)$  makes the difference between homogeneous and heterogeneous nucleation. The foreign surfaces reduce the free energy required to form an embryo of critical size.

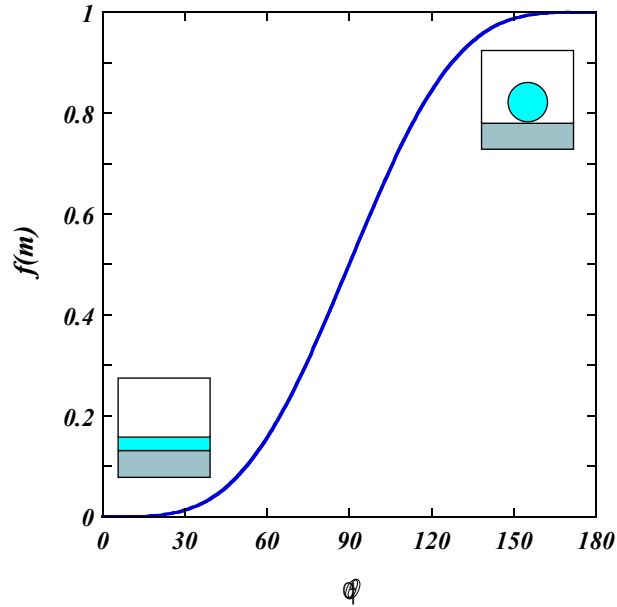


Figure 1.8: Trend of  $f(m)$  over a flat homogeneous surface as function of contact angle  $\theta$ .

#### 1.4.1.1 Analysis of the wettability transition for liquid-solid system.

A condition of complete wettability, or wettability transition, is realized when the contact angle of a liquid drop on a surface, varies from a finite value to zero. It is possible to research temperature,  $T_w$ , at which a (perfect  $\theta=0$ , or partial  $0<\theta<90$ ) wettability condition is reached between the water and the graphite. Some models present in the literature predict that the value of  $T_w$ , for non-polar liquids is a function of the parameter  $D$ , known as well-depth potential, of the absorption potential (Gatica SM et al., 2004).

A liquid drop formed on a surface takes the form that minimizes the surface energy of the system. In particular the drop forms a contact angle with the surface whose value depends on the chemical nature of the substrate, of the liquid and on the morphology of the surfaces. For

droplet smaller than 10 nm the contact angle varies because of line tension effect, so macroscopic contact angle differs from microscopic contact angle.

In this regard, considering a liquid drop on a substrate represented by the surface of the solid particle of radius  $R_p$  (Figure 1.6). With reference to the Young 's equation (1.22), the contact angle  $\theta$  becomes equal to zero is satisfied when a particular condition of equality:

$$\sigma_{pv} = \sigma_{pl} + \sigma_{lv} \quad (1.37)$$

A transition to complete wetting is achieved, when the contact angle  $\theta$  varies from a finite value to a value equal to zero (Ragil et al., 1996). In particular, correlating the surface wettability of a liquid with the measurement of the angle  $\theta$ , it is possible to distinguish four cases represented respectively in Figure 1.10 that shows the variation of contact angle subjecting the solid substrate at different treatments surface.

The value  $\theta = 0^\circ$  ( $\cos\theta = 1$ ) corresponds to a situation of "complete wetting";

- the case of  $0^\circ \leq \theta \leq 90^\circ$  ( $\cos\theta < 1$ ) corresponds to a situation of "partial wetting", and it increases with the decrease of  $\theta$ , becoming maximum for  $\theta = 0^\circ$ ;
- the case where  $\theta > 90^\circ$  ( $\cos\theta < -1$ ) that corresponds to a "poor wetting"; the limiting case in which the value of the contact angle is equal or tends to  $\theta = 180^\circ$  ( $\cos\theta = -1$ ) corresponds to a state of "complete hydrophobicity". In this case the sum of the free energies of solid-vapor and the liquid-vapor interface is equal to that at the solid-liquid interface. In such a condition the liquid does not wet the solid, and the drop of liquid remains separate from the particle surface.

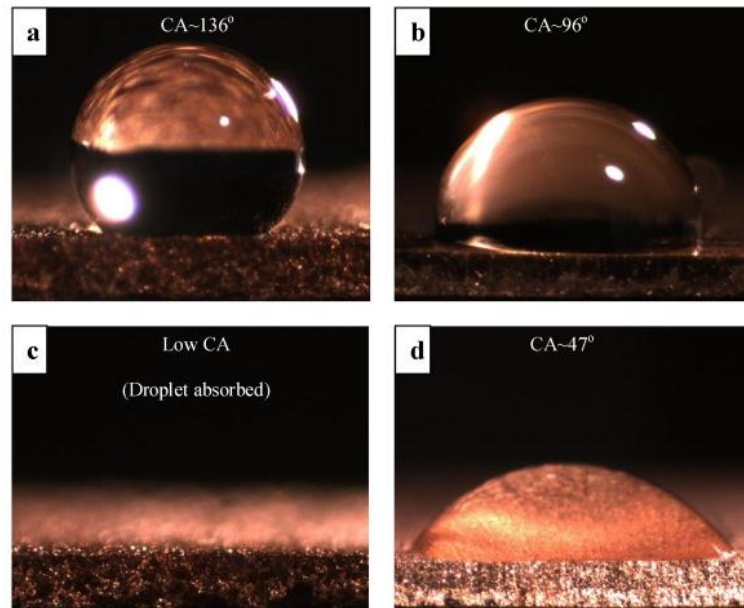


*Figure 1.9: Wettability of a liquid droplet on a solid surface: (a, b) state of hydrophobicity and poor wetting, (c) state of partial wetting, (d) state of complete wetting (Mahmood et al.,2012)*

It is shown that if a fluid does not wet a particular surface at low temperature, it is expected that a transition to wettability occurs at higher temperatures,  $T_w$ . This temperature is always less than the critical temperature  $T_{cr}$  of the vapor phase present in the system.  $T_w$  therefore separates a condition of complete wettability by a partial wettability of (Ebner et al., 1987) . The values of  $T_{cr}$  and  $T_{pt}$  were reported in Figure 1.10 where was showed the phase diagram of water.

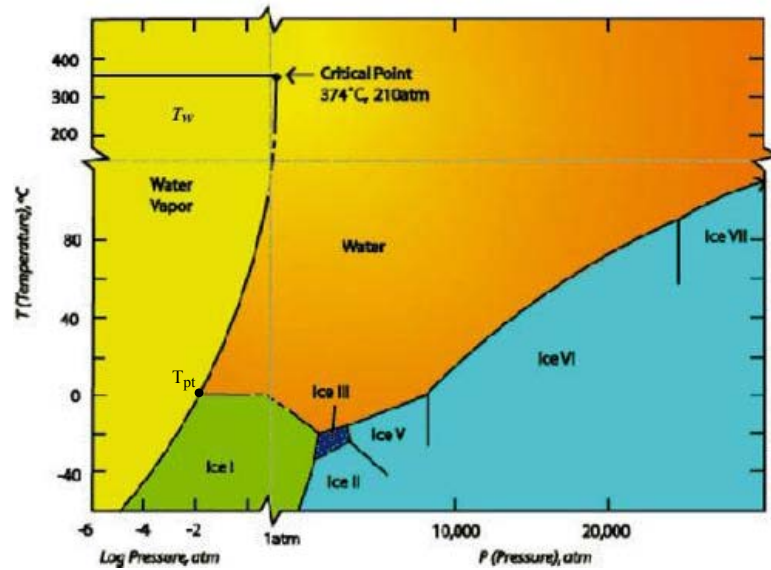


Figure 1.10: Phase diagram of water.

The common origin of this phenomenon is that the vapor-surface interaction  $V(z)$  is only weakly attractive, promoting a condition of non-wettability to temperatures close to the temperature of the triple point  $T_{pt}$ . The dividing line between a condition of wettability or non-wettability at  $T_{pt}$ , approximately corresponds to the situation in which the absorption potential hole  $D = 3.5\varepsilon$  (Curtarolo et al., 2000) where  $\varepsilon$  is the adsorbate intermolecular interaction potential well-depth. The physics of this phenomenon is qualitatively simple: at pressures close to saturation pressure, the gas is on the condensing limit to form a liquid phase bulk. If the surface provides a strongly attractive interaction, the condensed vapor, nucleating on the solid surface, will form a liquid film on it, which will grow with continuity on the surface, until the pressure  $p$  reaches the value  $p_s$  to the saturation pressure. Instead, if the interaction is weakly attractive, the nucleation does not occur for a pressure value less than the saturation value. In these conditions, the liquid on the surface, under saturation condition, will tend to form a sphere rather than spread on the surface. The difference between the two types of behavior is therefore associated with the relative forces of cohesion and adhesion between the solid substrate and the condensing vapor specie.

In any case it must be taken into account that the working conditions of a hypothetical apparatus for the particulate abatement are subject to particular restrictions due to both the principle of operation and at same time their operating conditions. In particular the typical temperature and pressure range should be between  $T = 300 - 375$  K and  $P = 1$  atm. In these ranges it is necessary to find the optimal conditions to maximize the efficiency of the process, by varying chemical and physical characteristics of the particulate.

From this point of view it would be very interesting to analyze the effect of operating pressure on the abatement efficiency by condensation process activated via heterogeneous nucleation. In fact, an increase in operating pressure would allow obtaining high degrees of supersaturation even with low concentrations of vapor. Furthermore it is possible to work at higher temperatures maximizing the particles wettability, directly improving the interaction between solid substrate and the condensing vapor specie.

- ***Transition model description***

The contact angle can be estimated by the equation (1.22) knowing the values of the three free interface energies. Unfortunately, in some cases, only  $\sigma_{lv}$  is known. Thus, a simple model can be used (Cheng et al., 1993; Chizmeshya et al., 1998; Curtarolo et al., 2000; Gatica et al., 2004), in which the solid-liquid ( $\sigma_{pl}$ ) interfacial tension is approximated in the following way:

$$\sigma_{pl} \approx \sigma_{pv} + \sigma_{lv} + \rho_l \int V(z) dz \quad (1.38)$$

where,  $V(z)$  is the absorption potential which is only a function of the distance normal to the surface  $z$ . The integral between the minimum of the potential of interaction  $z = z_{\min}$  and  $z =$

$\infty$ , approximates the energy of gas-surface interaction in terms of the density of the liquid phase  $\rho_l$ . The physical content of the equation (1.38) is that the total work of the free energy of the solid-liquid interface is equal to the work of the solid-vapor interface energy plus the liquid-vapor interface energy plus a correction factor, represented by last term of equation (1.38). It takes into account the interaction energy between solid and liquid. Combining the equations (1.22) and (1.38) it is possible to obtain:

$$\cos(\theta) = \frac{(\sigma_{pv} - \sigma_{pl})}{\sigma_{lv}} = -1 - \left(\frac{\rho_l}{\sigma_{lv}}\right) \int V(z) dz \quad (1.39)$$

The equation (1.39) must be interpreted considering that the potential  $V(z)$  is negative for the whole range of integration. Therefore, in case of a weak potential  $V(z)$  is approximately equal to zero, and the contact angle is  $\theta = 180^\circ$ . Leaving unchanged the temperature  $T$ , and increasing the energy intensity of the substrate, the last term of (1.39) increases in magnitude (but remains negative). Then the contact angle decreases slowly. When the interaction reaches a critical value, such that it carries out the condition  $\cos(\theta) = 1$  and  $\theta = 0^\circ$ , the drop is completely dispersed on the surface, spreading over it forming a liquid layer. When the intensity of the interaction is increased further, the equation (1.39) becomes invalid, and the contact angle is always zero. A similar process can be obtained, even when increasing the ratio  $\rho_l/\sigma_{lv}$  for example altering the composition of the liquid, or by increasing the temperature. Thus contact angles of water on substrates of different nature can be calculated. This situation can be realized by means of a substrate consisting of layers of different materials. Changing the composition and thickness of the layers, the intensity of the potential varies. A model of solid-atom potential used for the study of adsorption or wetting properties is the "potential 3-9" given by the following expression:

$$V(z) = \frac{4C^3}{27D^2z^9} - \frac{C}{z^3} \quad (1.40)$$

This potential is similar to the interatomic potential of "Lennard-Jones 6-12" and is adopted for similar purposes. It combines a form strictly correct for the attraction asymptotic ( $V \approx -C/z^3$ ) and a power law for the repulsion, in order to obtain a functional form qualitatively plausible and mathematically convenient.

- **Potential well-depth**

The constant  $D$  represents the potential well-depth, which has a minimum value for  $z_{min} = [2C/(3D)]^{1/3}$ . Adding layers of different materials on the surface of the solid, or by varying the distribution and or the charge density on the surface of the solid for example by applying an external electric field, the parameter  $D$  is varied, while  $C$  is not changed, because it is determined by the composition of the solid and by the nature of the condensing species.

- **Van der Waals's dispersion coefficient**

In literature there are sufficient data for the gas-surface interactions, while, for the liquid-surface interactions such as water-graphite there are few data available. In the case of interaction of a water molecule on a graphite layer there are two independent contributions of this coefficient (Gatica et al., 2004):

$$C = C_{perm} + C_{vdw} \quad (1.41)$$

The first contribution is due to the interaction of the dipole moment  $p$ , and its "image" on the dielectric substrate, while the second term is related to dipolar coupled charge fluctuations due to the electrons present on the molecule and those present in the substrate.

For the case of a molecule having a permanent dipole moment  $p$  oriented by an angle  $\phi$  relative to the normal of surface, so that  $p_z = p \cos\phi$ ,  $C_{perm}$  assumes the form:

$$C_{perm}(\phi) = gp^2(1 + \cos^2\phi)/16 \quad (1.42)$$

In the case of random angle orientation, or for a molecule that can rotate freely, because the mean value of  $\cos^2\phi$  for a randomly oriented dipole is equal to 1/3, the equation (1.42) becomes:

$$C_{perm} = \langle C_{perm}(\phi) \rangle = gp^2/12 \quad (1.43)$$

In the case of water and graphite, with  $g = 0619$  (Brunch et al, 1997) and  $p = 1.85$  Debye  $C_{perm}=104 \text{ meV } \text{\AA}^3$  (See Appendix B).

The second contribution is due to Van der Waals interaction. A model for water dynamic polarizability (with characteristic energy  $E_{water}$ ) produces an expression of the following type:

$$C_{vdW} = \frac{g \alpha E_s}{8 \left(1 + \frac{E_s}{E_{water}}\right)} \quad (1.44)$$

where  $E_{water} = 18,1 \text{ eV}$  and  $\alpha = 1,4 \text{ \AA}^3$ , is obtained  $C_{vdW} = 971 \text{ meV } \text{\AA}^3$ . (see Appendix B)

Note that the contribution of the permanent moment of this coefficient is about 10%.

- **Contact angle calculation**

Using equation (1.40), the integral term of equation (1.39) can be written in the following way (Gatica et al., 2004):

$$I = - \int_{z_{min}}^{\infty} V(z) dz = \frac{11}{24} \left( \frac{3}{2} \right)^{\frac{2}{3}} (CD^2)^{1/3} \quad (1.45)$$

Thus it is possible to obtaining the contact angle at the water-substrate interface as a function of temperature from equation (1.45) by setting the parameters C and D:

$$\cos(\theta) = -1 + \left( \frac{\rho_l}{\sigma_{lv}} \right) I \quad (1.46)$$

In this simple model, the parameter I contains the information about the substrate, while the multiplication factor  $(\rho_l/\sigma_{lv})$  depends both on the composition of both the liquid and the vapor and on temperature. Figure 1.11 shows the results for the water-graphite interaction, whose parameters are  $C=1075 \text{ meV}\text{\AA}^3$  e  $D=100$  (Gatica et al., 2004). The graph shows the evolution of  $\theta$  for  $D = 50, 75, 150, 200 \text{ meV}$ , with the same C value.

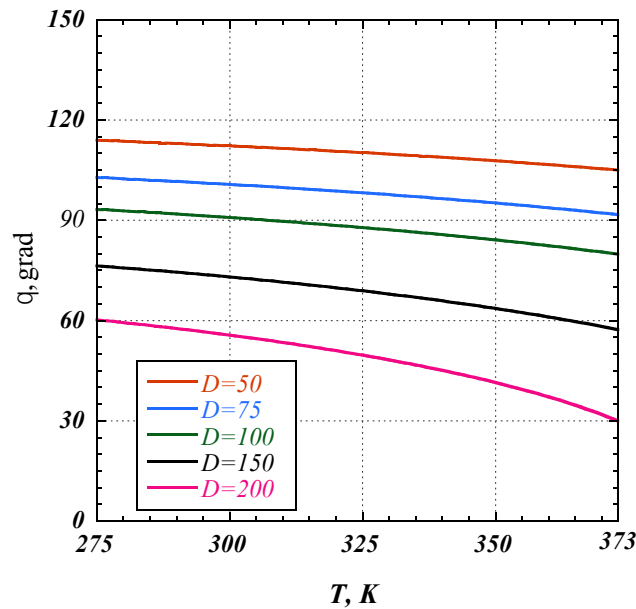


Figure 1.11: Trend of the contact angle as a function of temperature for different values of the parameter D, and for a fixed value of  $C = 1075 \text{ meV}\text{\AA}^3$ .

The curves of the potential  $V(z)$ , shown in Figure 1.12 have been obtained using the equation (1.40). The same curves have been used to calculate the contact angles shown in the Figure 1.11.

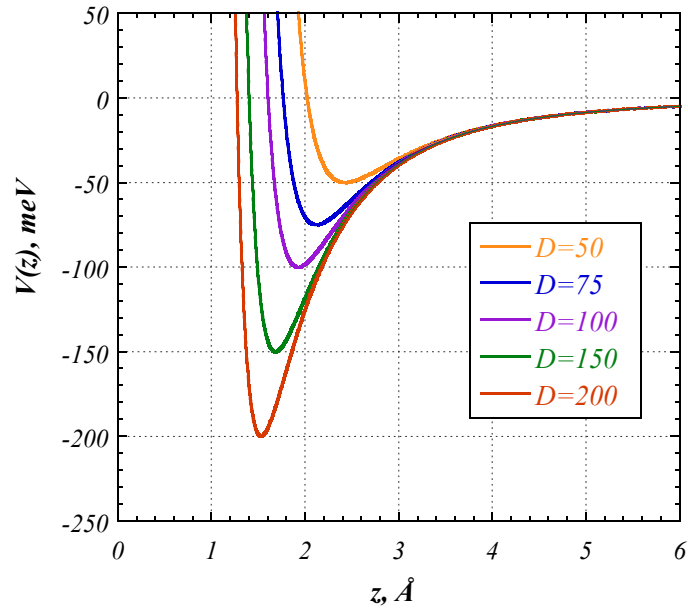


Figure 1.12: Interaction potential

- **Transition wettability temperature calculation**

Combining (1.45) with (1.46), it is possible to calculate the wettability transition temperature obtaining the value of the temperature for which the following relationship is satisfied:

$$(CD^2)^{1/3} = \left[ (\cos(\theta) + 1) / \left( \frac{11}{24} \left( \frac{3}{2} \right)^{2/3} \right) \right] \left( \frac{\sigma_{lv}}{\rho_l} \right)_T \quad (1.47)$$

In fact it is possible to calculate the temperature of complete wettability by imposing  $\theta = 0^\circ$  ( $\cos\theta = 1$ ) and obtaining the value of  $T$  for which the condition  $(CD^2)^{1/3} = 3.33(\sigma_{lv}/\rho_l)_T$  is satisfied.

Furthermore, as shown in Figure 1.13a it is possible to predict the temperature  $T_w$  of  $\theta = 0^\circ$  (complete wetting condition), as a function of the potential well  $D$ , fixed the value of  $C$  obtained by the equation (1.46). Figure 1.13b shows instead  $T_w$  for  $\theta = 90^\circ$  (temperature of partial wetting condition)

In the figures are also represented the  $T_w$  for surfaces of different chemical nature.  $T_w$  is obtained by solving equation (1.47) as function of temperature.

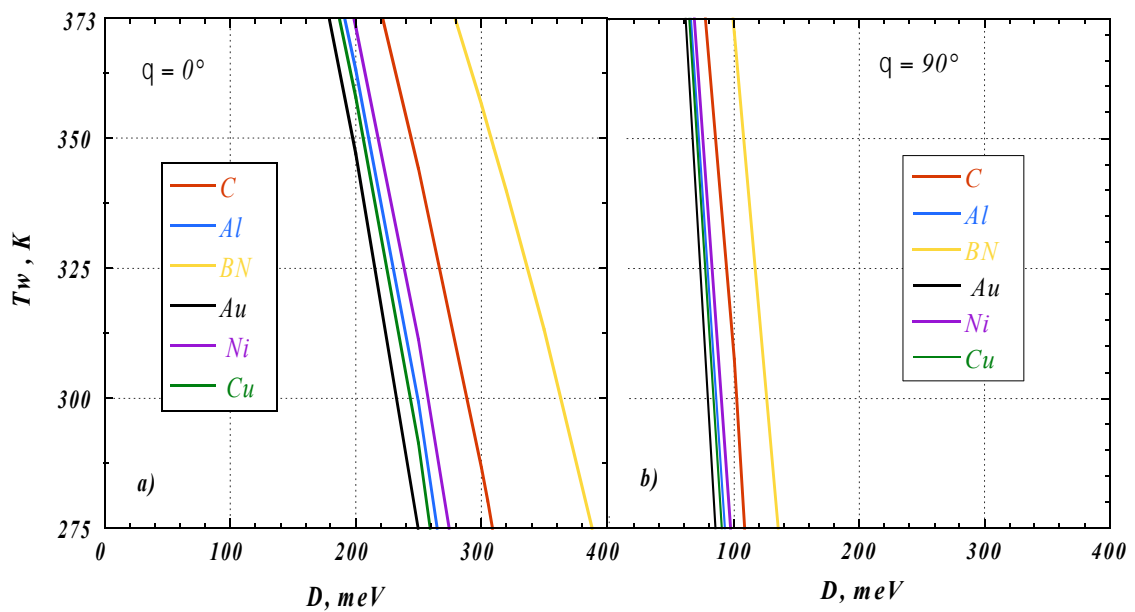


Figure 1.13: (a) Complete wettability Temperature; (b) Transition wettability temperature; As function of potential well-depth  $D$ ,. Setting the respective values of  $C$  for each material

- **Wettability on other surfaces**

Similar calculations of  $C$  were made for the water on other surfaces. For a surface  $x$ , it is possible to calculate the dependence  $\underline{D_x(T_w)}$  of the potential well-depth from  $T_w$  by Eq.

(1.47) by means of the functional dependency  $D_g(T_w)$  related to the graphite (Gatica et al., 2004):

$$D_x(T_w) = \left(\frac{C_g}{C_x}\right)^{1/2} D_g(T_w) \quad (1.48)$$

In this case,  $C_g/C_x$  is the ratio of the van der Waals coefficients for the surface of interest and for graphite. Only the physical - adsorption of water is considered and the assumption that the solid retains its structure and its chemical integrity in every case was made.

Figure 1.14 shows the trend of the contact angle as a function of temperature for different materials, known the respective values of C and D (Appendix B)

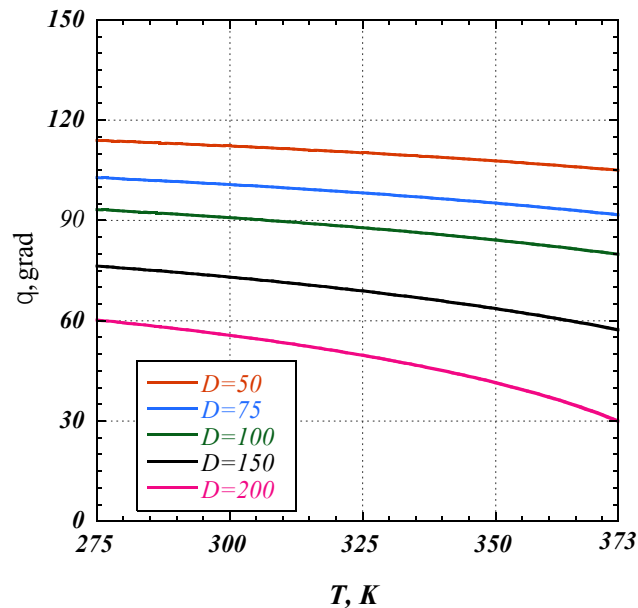


Figure 1.14: Trend of the contact angle as the temperature varies for different materials.

It is very interesting to assess the contact angle as a function of the parameters C and D at ambient temperature, as shown in Figure 1.15a. The red symbol in the figure shows the C and D values of the potential interaction of water - graphite at ambient temperature, in particular

$D = 100 \text{ meV}$  and  $C = 1075 \text{ meV}\text{\AA}^3$ . This graph provides a suggestion of how a material can be designed giving a condition either of complete wettability or complete hydrophobicity acting directly on the value of the contact angle. As mentioned above, the parameter  $D$  is dependent on the surface layers and the charge density on the surface of the substrate while the parameter  $C$  depends both on the nature and the characteristics of the solid substrate and by its interaction with the condensing species. For example, the  $C$  values for water on graphite, BN, Al, Au are 1075, 678, 1444, 1644  $\text{meV}\text{\AA}^3$  respectively (Gatica et al., 2004)

Figure 1.15b shows values of the contact angle influenced by changes in the density and / or surface tension of the condensed vapor species (liquid) ,\_obtained by varying the temperature from 300 up to 350 K

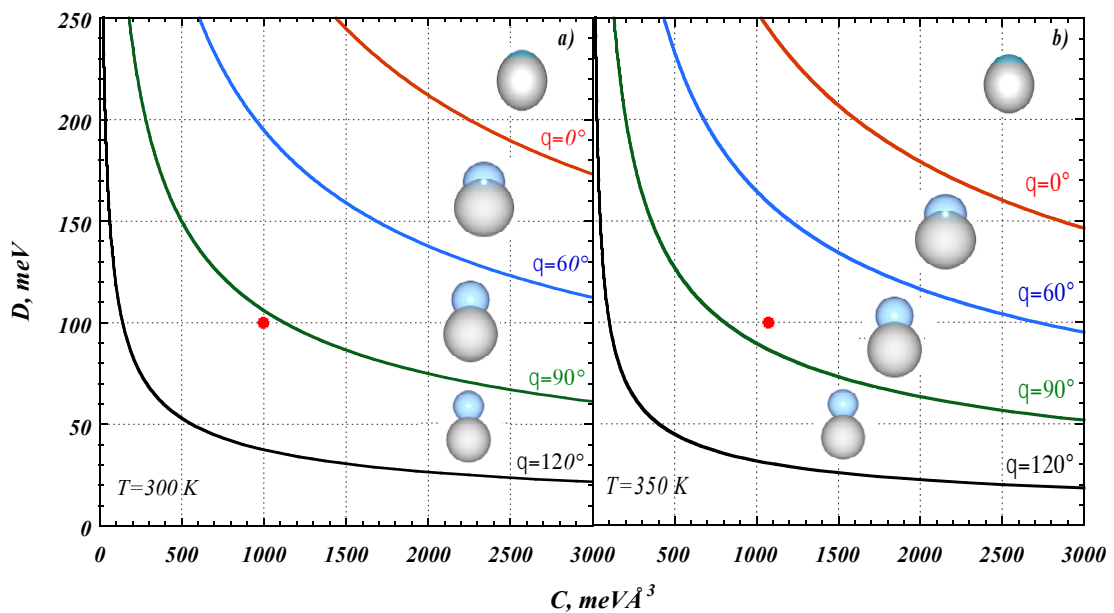


Figure 1.15: Trends of the contact angle as a function of the parameters  $C$  and  $D$  for  $T = 300\text{K}$  (a) and for  $T = 350\text{K}$  (b). The red dot indicates the  $C$  and  $D$  values for the water-graphite interaction.

The Figure 1.15 clearly shows that, for an increase of temperature, the ratio  $\rho_l/\sigma_{lv}$  varies, so that the point on the graph that indicates the water - graphite interaction moves from values of  $\theta$  greater than  $90^\circ$  to smaller values showing clearly a wetting transition.

#### ***1.4.1.2 Effect of surface roughness on wettability***

The experimental values of the contact angle depend on several factors such as the method of preparation, the cleaning and surface roughness (Adamson, 1990; Israelachvili, 1992). Experimentally it has been shown that the roughness affects the value of the contact angle. For example, Yost et al. (1995) demonstrated that the roughness improves the wettability of a surface of copper with a welding eutectic Sn - Pb. In particular, In addition, the contact angle decreases with the increase of the roughness for wettable surfaces, while it increases with the roughness for not wettable surfaces. In fact Erbil et al. (2003) showed that the contact angle of polypropylene ( $\theta = 104^\circ$ ) increases by increasing the surface roughness. In general, it can be affirmed that few solid surfaces are very flat, thus it is necessary to consider a "roughness factor" in the evaluation of the wettability of a surface.

Wenzel (Wenzel, 1936) found that the contact angle of a liquid with a rough surface is different from the contact angle of a liquid with a smooth surface due to the change of the contact area of solid-liquid and the corresponding interface energy. He studied the case in which there is full contact between solid and liquid, i.e. the liquid penetrates the roughness of the solid surface, as shown in Figure 1.16a (Barbieri, 2006). It was also demonstrated that, for very rough surfaces, a composite interface solid - liquid - gas with gas pockets trapped in the roughness of the solid may be formed described by the Cassie's model (Cassie A., Baxter S, 1944), such as shown in Figure 1.16b.

- **Wenzel's model**

Considering a liquid drop in contact with a surface the contact angle is determined by the following relation (Wenzel, 1936):

$$\cos\theta_w = \frac{dA_{LG}}{dA_F} = \frac{A_{SL}}{A_F} \frac{dA_{LG}}{dA_{SL}} = R_w \cos\theta \quad (1.49)$$

Where the term  $\theta_w$  is the apparent contact angle and  $\theta$  is the contact angle for a smooth surface (as assessed by the relation of Young, eq. (1.22)),  $A_{SL}$  and  $A_{LG}$  are the contact areas between solid - liquid and liquid - gas surface, while the term  $A_F$  is the flat area of solid - liquid contact. Thus, in the Wenzel's model a linear relation between the apparent contact angle and the roughness factor  $R_w$  is established  $R_w$  is defined as the ratio between real area of the contact surface and the projected area, that is:

$$R_w = \frac{A_{SL}}{A_F} \quad (1.50)$$

If  $R_w = 1$  (smooth surface), we obtain the Young equation, while the Wenzel equation is obtained for a rough surface  $1 < R_w < 2$ .

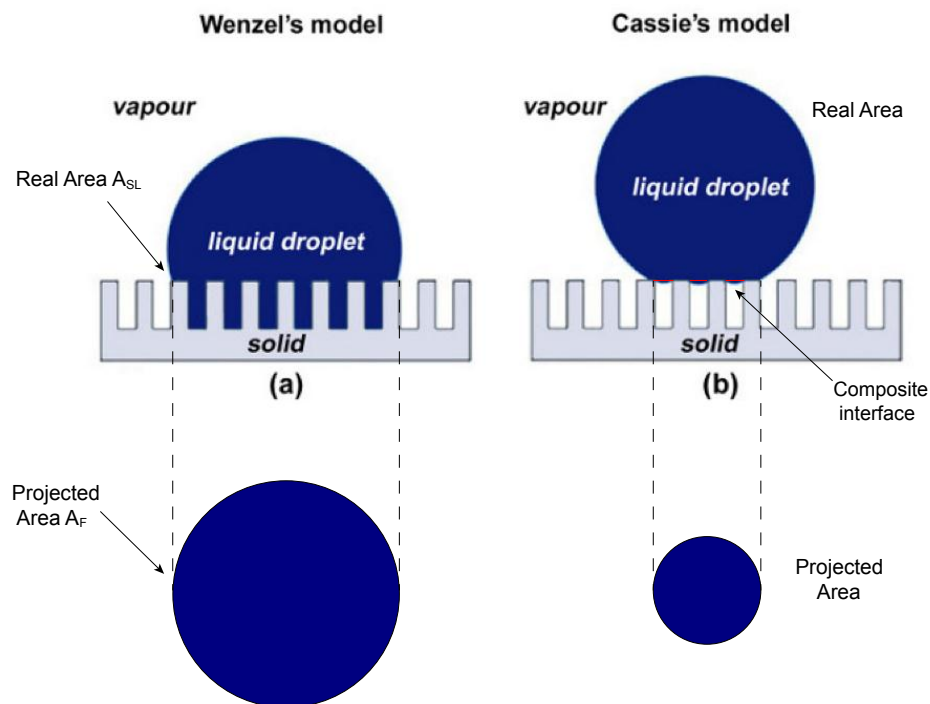


Figure 1.16: Schematic representation of the contact liquid-solid for the two models considered. (a) Wenzel model, (b) Cassie-Baxter model.

The dependence of the contact angle on the roughness factor is represented in Figure 1.17 for different values of the contact angle  $\theta$  of the smooth surface as obtained by the equation (1.49).

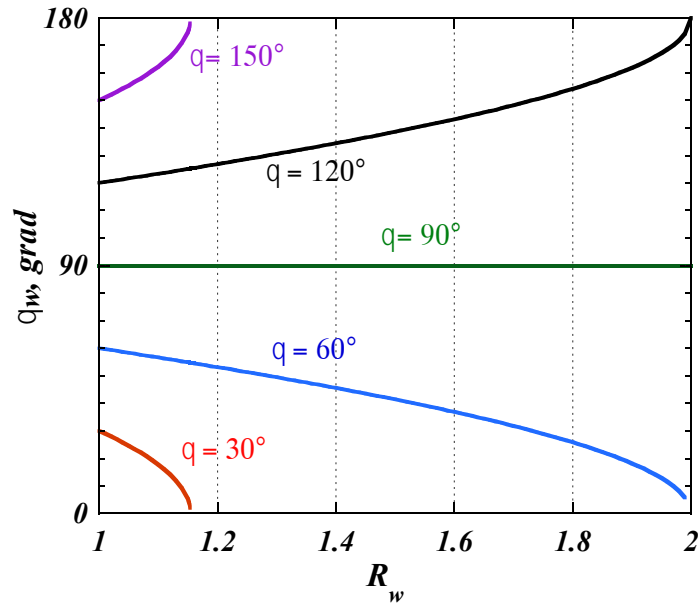


Figure 1.17: Trend of the contact angle for a rough surface as a function of the roughness factor  $R_w$  for fixed values of the contact angle  $\theta$ .

It has been observed, that if a liquid wets a flat surface ( $\cos\theta > 0$ ), it will be also wet the rough surface formed by the same material with a contact angle  $\theta_w < \theta$ , since  $A_{SL}/A_F > 1$ . In addition, for not wettable surfaces ( $\cos\theta < 0$ ), the contact angle related to a rough surface is greater than the contact angle obtained for a flat surface,  $\theta_w > \theta$ .

In conclusion it can be affirmed that the surface roughness improves both the hydrophobicity and the hydrophilicity of a material, depending on the nature of the corresponding flat surface. (D. Quere, 2002)

- **Cassie and Baxter model for composite regime**

If a surface presents a very marked roughness, the Cassie and Baxter model predicts that, in the case of partial or complete wetting, the liquid is fully absorbed by the cavities of the rough surface. In the case of poor wettability, the liquid cannot penetrate into the cavities of

the surface with local large gradients, with consequent formation of gas pockets, thereby leading to the formation of a composite solid - liquid - gas interface. Note that the contact areas of solid - liquid are located on the tops of the bumps, while the gas cavity and the contact areas of solid - gas are located in the concavity of the surface.

The equation (1.54), which was originally developed for solid - liquid homogeneous interfaces, has also been extended to composite interfaces (Cassie and Baxter, 1944), as shown in Figure 1.16

In this case the contact angle is given by:

$$\cos\theta_{CB} = R_f f_{SL} \cos\theta_0 - (1 - f_{SL}) \quad (1.51)$$

where  $f_{SL}$  is the fraction of solid-liquid interface in contact with the base of the droplet surface, and  $R_f$  is the roughness ratio of the wetted surface, and  $(1 - f_{SL})$  represents the fraction solid-gas interface at the same contact point with the base of the droplet. For  $f_{SL} = 1$ ,  $R_f = R_w$ , the equation (1.51) is similar to the equation of Wenzel.

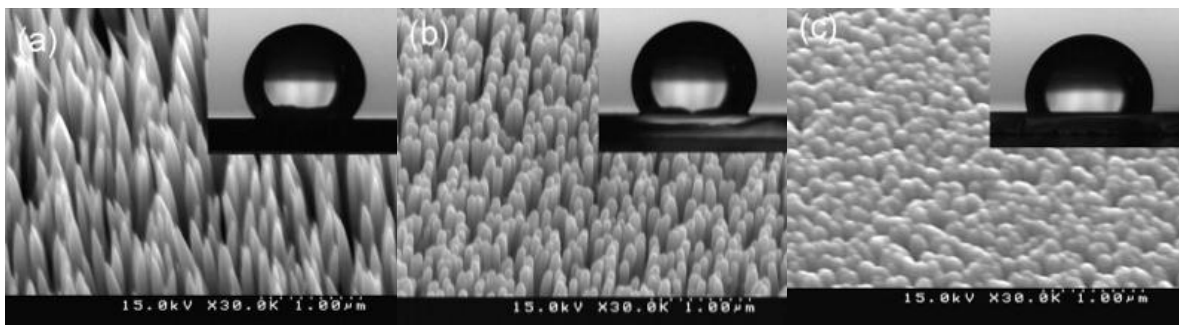


Figure 1.18: Effect of surface roughness on the contact angle (Das et al., 2009)

Fig. 1.18(a–c) is typical FESEM images of ZnO NR arrays prepared with different growth conditions. The samples constitute uniform and densely packed NR arrays with different surface morphologies, namely nanoneedles (Fig. 1.18(a)), nanonails (Fig. 1.18(b)) and NRs with rounded tip (Fig. 1.18(c)). Photograph of water droplet on three representatives ZnO NR

arrays with different surface morphologies are shown in the insets of Fig. 1.18(a–c). It is clear that the droplets are nearly spherical in shape. The contact angle of water, measured at room temperature, was varied between  $135^\circ$  and  $104^\circ$ .

### 1.4.1.3 Line tension effect on wetting transition

Consider a simple three-phase system, such as a droplet resting on a *perfect* homogeneous, horizontal, isotropic solid surface. If this droplet is sufficiently large so that the effects of the three-phase contact line can be neglected, the change of the free energy due to the change in droplet size can be written as:

$$dF = \sigma_{sl}dA_{sl} + \sigma_{sv}dA_{sv} + \sigma_{lv}dA_{lv} = (\sigma_{sl} - \sigma_{sv} + \sigma_{lv}\cos\theta)dA_{sl} \quad (1.52)$$

At mechanical equilibrium the free interface energy  $F$  is minimum ( $dF=0$ ) and the Young's equation (1.22) can be obtained which describes the mechanical equilibrium of the forces per unit length on the three-phase contact line in the plane of the solid surface. Young's equation is strictly valid only for macroscopic droplets at mechanical equilibrium with any adsorbed prewetting film of thickness  $l_1$ , (see Fig.1.19) on a molecularly smooth horizontal solid surface as shown in Figure 1.19.

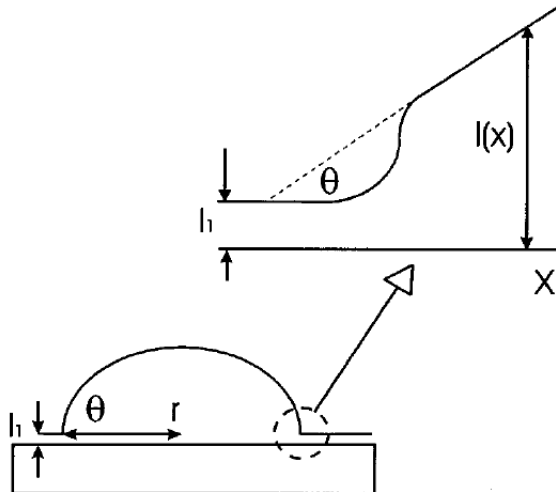


*Figure 1.19: Schematic diagram of a microscopic droplet situated on a solid substrate. The droplet has a contact angle  $\theta$  and base radius  $r$  and is in mechanical equilibrium with an adsorbed layer of thickness  $l_1$ . The interface displacement profile  $l(x)$  is also shown in the vicinity of the solid and/or liquid and/or vapor contact line.*

For microscopic droplets, the contact angle is influenced both by surface interactions and by the nature of the three-phase solid-liquid-vapor contact line of length  $L_{slv}$ , which contributes with an additional free energy per unit length or line tension  $\tau$  to the excess free energy of the droplet. This effect adds an excess energy term  $\tau L_{slv}$  to equation (1.52). Hence for a spherical droplet of contact angle  $\theta$  and lateral radius  $r$  (Figure 1.20) the modified Young's equation can be obtained:

$$\cos\theta = \cos\theta_\infty - \frac{\tau}{r\sigma_{lv}} \quad (1.53)$$

where  $\theta_\infty$  is the contact angle in the limit of very large droplets ( $r \rightarrow \infty$ ). Hence from Eq. 1.53 the quantities  $\tau$  and  $\cos\theta$  can be determined from a study of  $\cos\theta$  as a function of  $1/r$ . The contact angle  $\theta_\infty$  provides important information about the wettability of a surface. A liquid partially wets a surface if a large droplet possesses a finite contact angle,  $\theta_\infty > 0$ . If, however, this liquid has a contact angle  $\theta_\infty = 0$  the liquid completely wets the surface and the surface is covered by a thick liquid film. For an appropriate solid-liquid combination it is sometimes possible to find a wetting transition as a function of increasing temperature. In this case below the wetting temperature  $T_w$  a droplet possesses a finite, nonzero contact angle  $\theta_\infty$  whereas above  $T_w$  the contact angle  $\theta_\infty = 0$ . The contact angle decreases and vanishes on raising the temperature to the wetting transition temperature  $T_w$ . The line tension is therefore only defined for  $T < T_w$ . Above  $T_w$  the three-phase contact line disappears. A number of different theoretical approaches have been used to study the singular behaviour of the line tension at  $T_w$ . These approaches have produced very different results for  $\tau$ , where this

quantity was observed to be zero, finite, or to diverge to infinity at  $T_w$ . Thus for a while, there was great confusion concerning the theoretically predicted behavior of the line tension at  $T_w$ . A consensus has recently been reached which asserts that the singular behavior of the line tension, upon approaching  $T_w$ , depends sensitively on both the order of the wetting transition and the range of the intermolecular forces. It is possible to affirm that  $\tau$  has a value of about  $\pm k \cdot 10^{-10}$  N where  $k \in [1 \div 5]$  (J. Y. Wang et al., 2001). From this point of view, it is reported that the line tension effect is negligible for droplets greater than 10-50 nm. If all the parameter that affect the contact angle are considered, such as temperature, surface morphology, droplet radius, the following expression is obtained:

$$\cos\theta(T, r, R_f, f_{SL}) = R_f f_{SL} \cos\theta_0(T) - (1 - f_{SL}) - \frac{\tau}{r\sigma_{lv}} \quad (1.54)$$

#### 1.4.2 Heterogeneous nucleation rate

In the case of heterogeneous nucleation, the rate of embryo formation  $J$  strongly depends on the characteristics of the particles acting as condensation nuclei, such as their chemical nature, morphology, size and charge.

This leads to a decrease of the critical supersaturation at which the nucleation occurs. Similarly, the supersaturation required decreases with the increase of the diameter of the particle or when there is a greater wettability between the condensed vapor species and the solid substrate.

The expression of the heterogeneous nucleation rate  $J_{het}^*$  is given by:

$$J_{het}^* = K_{het} \exp\left(-\frac{\Delta G_{het}^*}{k_B T}\right) \quad (1.55)$$

Also in this case, the nucleation rate can be expressed as the product of a collisional factor  $K$  multiplied by a Arrhenius kinetic type term. The  $K$ -factor (Giechaskiel et al., 2011) can be put in the form:

$$K_{het} = R_{growth} F Z_{nucl} \quad (1.56)$$

and is equal as in the case of homogeneous nucleation to the product of three terms. It differs from  $K_{hom}$  expressed in (1.21) only for the quantity  $F$ , while  $R_{growth}$  and  $Z_{nucl}$  are similar and respectively equal to (1.22) and (1.24).

The evaluation of  $F$  is not as simple as in the case of homogeneous nucleation. A frequently used approximation considers  $F = N_{ads} A_{ads}$ , where  $N_{ads}$  is the total number of molecules adsorbed per unit area of the particle (Hamill et al., 1982; Lazaridis et al., 1991) and  $A_{ads}$  is the surface area available for adsorption,  $A_{ads} = 4\pi R_p^2$ , making the  $F$  the number of adsorbed molecules per particle. The surface concentration of adsorbed molecules is  $N_{ads} = \beta_{ads} \tau$ , where  $\beta_{ads}$  is the collision rate of vapor molecules per unit area of the particle and  $\tau$  is the average time of a molecule of water remaining adsorbed on particle surface (Lazaridis et al., 1991; Wagner et al., 2003; Winkler et al., 2008b).

In this case we use  $\beta_{ads} = \beta_v$  (eq 1.18) (Hamill et al., 1982). The time which a molecule spends on the surface of the solid particle is (Lazaridis et al., 1991):

$$\tau = \tau_0 \exp(E_v/R_g T) \quad (1.57)$$

In this expression, the term  $E_v$  is the enthalpy of adsorption of the vapor species, which depends on the surface type of the properties of the condensing gas.  $\tau_0$  is the characteristic time of adsorption, which is the inverse of the characteristic frequency of vibration of the molecules, and depends on the nature of the surface and the condensing gas. It has been found

that for the nucleation of the water on solid carbon particles  $\tau_0 \approx 2.4 \times 10^{-16}$  s and  $E_v \approx 45188$  Jmol<sup>-1</sup> (Hamill et al., 1982).

The term  $\tau_0$  corresponds to  $1/\nu_0$ , where  $\nu_0$  is the characteristic frequency of vibration. The vibration between two molecules can be calculated using the approximation of the harmonic oscillator between two adjacent particles. The angular frequency ( $\omega$ ) of the oscillator is

$$\omega = 2\pi\nu = \sqrt{\frac{d^2V(z)}{dz^2} \frac{1}{m_\mu}} \quad (1.58)$$

and

$$\tau_0 = 2\pi m_\mu^{1/2} \left( \frac{d^2V(z)}{dz^2} \right)^{-\frac{1}{2}} \quad (1.59)$$

where  $m_\mu$  is the reduced mass of the two molecules, and  $V(z)$  is the intermolecular interaction potential. So the pre exponential factor becomes:

$$K_{het} = R_{growth}^F Z_{nucl} = 4\pi r^{*2} \beta_v^2 Z_{hom} 4\pi R_p^2 \tau \quad (1.60)$$

The heterogeneous nucleation rate (1.32) becomes:

$$J_{het}^* = 4\pi r^{*2} \beta_v^2 Z_{hom} 4\pi R_p^2 \tau \exp\left(-\frac{\Delta G_{het}^*}{k_B T}\right) \quad (1.61)$$

If using a coefficient of  $10^{25}$  cm<sup>-2</sup> s<sup>-1</sup> probably will not make a big mistake for the evaluation of the nucleation rate in the case just considered (Fletcher, 1958). If the particle which acts as a condensation nucleus has a radius  $R_p$ , the nucleation rate can be written as follows:

$$J_{het}^* = 4\pi R_p^2 10^{25} \exp\left(-\frac{\Delta G_{het}^*}{k_B T}\right) \quad (1.62)$$

According to the heterogeneous nucleation theory (Fletcher, 1958, Fan et al., 2009 Lee et al., 2003), the critical supersaturation required to activate an insoluble and spherical particle is given by the following expression for  $J_{het}^* = 1 \text{ s}^{-1}$ :

$$S_{het}^* = \frac{p}{p_s} = \exp \left[ \frac{1}{R_v T \rho} \sqrt{\frac{8\pi M_w^2 \sigma_{lv}^3}{3k_B T \ln(4\pi R_p^2 K)}} f(m, x) \right] \quad (1.63)$$

known  $m$ ,  $x$  and  $R_p$  it is possible to calculate  $p/p_s$ .  $S_{het}^*$  is strongly affected by the particle size and decreases with the increase with particle size and gas temperature.

#### 1.4.2.1 Activation probability

Once the heterogeneous nucleation rate is estimated it is possible to calculate the activation probability of the particles. The probability that a particle is activated, involves its rapid growth from submicron to micron size. The activation probability  $P_a(t)$  is the ratio of the concentration of activated particles  $N$  with respect to their initial concentration  $N_0$  (Giechaskiel et al., 2011) and, as it is defined, the activation probability results to be the scavenging efficiency of the process. An activated particle can be easily removed from a gas stream by means abatement techniques currently used in the industrial field.

$$P_a(t) = \frac{N}{N_0} 1 - \exp(-kt) \quad (1.64)$$

where  $t$  is time,  $k$  represents the rate constant of activation. In this case it can be matched to the heterogeneous nucleation rate  $J_{het}^* = k, (s^{-1})$  per unit area of the particle, which, as described above, depends on the chemical composition and the characteristics of the preexisting particles and from properties of the condensing phase. The activation probability

can therefore be calculated from the theory of heterogeneous nucleation. The time  $t$  is approximately the time associated with the heterogeneous nucleation of the supersaturated vapor. This value varies from about 0.001s up to 1000 s. Thus, the activation of the particles depends on parameters such as temperature and pressure, also by the size of the particles themselves and by the nature of the condensing vapor. The latter dependence is formalized through the dependence on the contact angle  $\theta$ , which is linked to the interaction substrate/condensing phase and to the roughness of the substrate surface. Its value is very sensitive to the latter parameter, so that substrates constituted by the same material but obtained with different techniques or systems may be characterized by significantly different contact angles. For the soot particles  $\theta$  values reported in the literature range from  $28^\circ$  to  $85^\circ$  (Popovicheva O. et al., 2008; T.Werder et al., 2003). It is, therefore, possible to evaluate the dependence of the activation probability of the particles to vary the size of the particles themselves, as can be seen from the diagram of Figure 1.9.

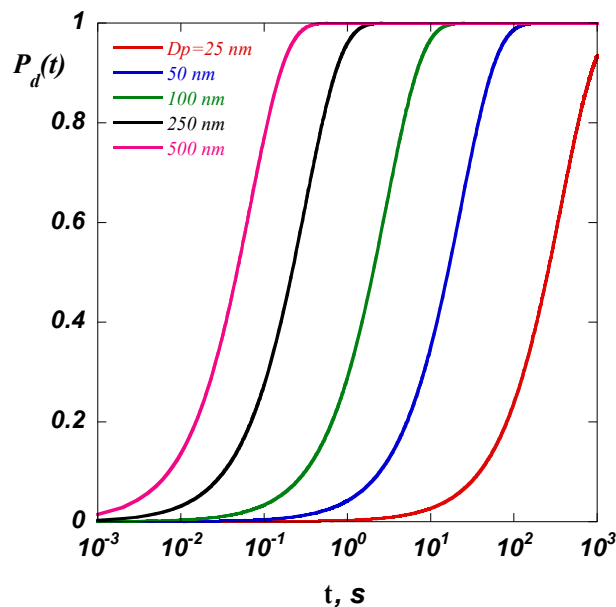


Figure 1.20: Activation probability as function of particle size.

### 1.4.3 Nucleation enabled by soluble particles

The formation and growth of a droplet on the surface of a soluble particle depends on the vapor pressure of an aqueous solution  $p'$  that is lower than that the one relative to pure water  $p$ . As well known in literature:

$$\frac{p'}{p} = \xi_w \quad (1.65)$$

where  $\xi_w$  is water molar fraction present in the solution. Considering a nucleus of solute with mass  $M_s$  of the substance of molecular weight  $m_s$  dissolved in water of molecular weight  $m_w$  that constitutes a drop of solution of radius  $r$  and density  $\rho'$ . The droplet contains  $n_w = (\frac{4}{3}\pi\rho' - M_s)/m_w$  moles of water and  $n_s = iM_s/m_s$  moles of solute,  $i$  is the van't Hoff factor that takes into account the dissociation of inorganic salts (Köhler, H., 1936). It follows

$$\xi_w = \frac{n_w}{n_s + n_w} = \frac{(\frac{4}{3}\pi\rho' - M_s)/m_w}{\frac{(\frac{4}{3}\pi\rho' - M_s)/m_w + iM_s/m_s} + iM_s/m_s} \quad (1.66)$$

Now using (1.66) and the Kelvin equation (1.16) it is obtained that:

$$\frac{p'_s(r)}{p_\infty} = \frac{p'_s(r)}{p_s(r)} \frac{p_s(r)}{p_\infty} = \xi_w \frac{p_r}{p_\infty} = \left[ \exp\left(\frac{2\sigma'}{n'_L k_B T r}\right) \right] \left[ 1 + \frac{iM_s m_w}{m_s (\frac{4}{3}\pi\rho' - M_s)} \right]^{-1} \quad (1.67)$$

Where the quantities with the apices refer to the solution containing the solute. In the case in which  $M_s \ll \frac{4}{3}\pi r^3 \rho$ , expanding the exponential in powers of  $1/r$  is obtained that the saturation ratio of S is:

$$S \equiv \frac{p'_s(r)}{p_\infty} \approx 1 + \left( \frac{2\sigma'}{n'_L k_B T r} \right) \frac{1}{r} - \frac{i M_s m_w}{\left( \frac{4}{3} \pi \rho' \right) m_s} \frac{1}{r^3} \equiv 1 + \frac{a}{r} - \frac{b}{r^3} \quad (1.68)$$

where

$$\begin{cases} a[\text{cm}] \approx \frac{3,3e-5}{T[\text{K}]} \\ b[\text{cm}^3] \approx 4,3 \frac{i M_s}{m_s} \end{cases} \quad (1.69)$$

being  $p'_s(r)$  the equilibrium vapor pressure of a drop of solution of radius  $r$ . A typical behavior of this function said Köhler function is shown in Figure 1.21.

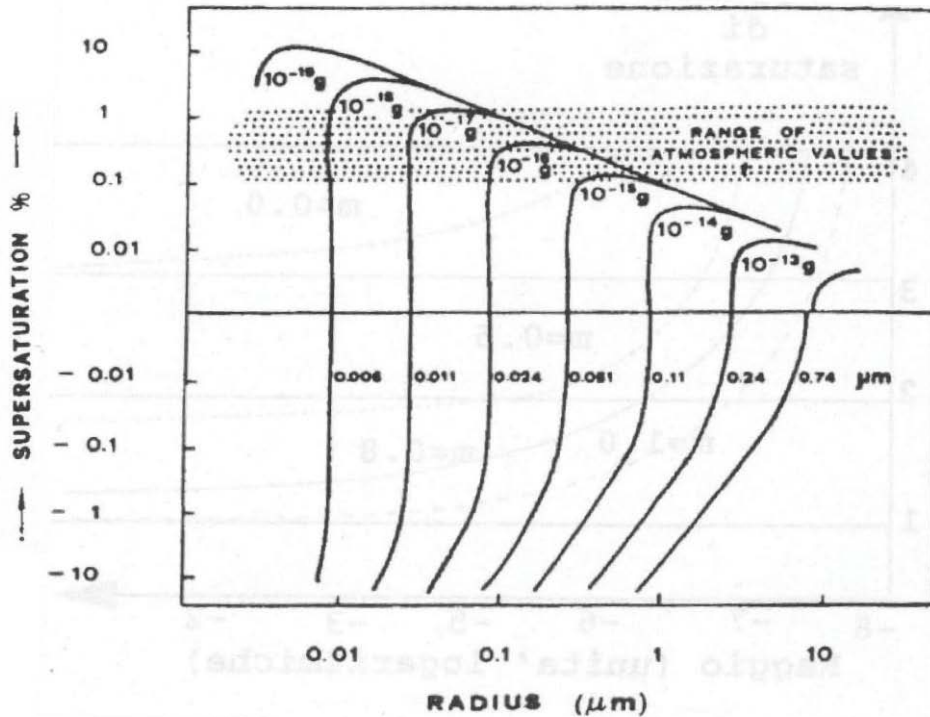


Figure 1.21: Köhler curves which show the relationship between the equilibrium size and critical supersaturation ratio  $S^*$  for nuclei of ammonium sulphate of different mass  $M_s$ .

The term  $-b/r^3$ , defined as solution term is the novelty compared to the case of homogeneous nucleation and has the effect of reducing the saturation vapor pressure, dominating at small radii. The first derivative of the (1.59) shows that the smaller radius  $r^*$ , for which condensation occurs at a given supersaturation  $S^*$ , is:

$$\begin{cases} r^* = \sqrt{\frac{3b}{a}} \\ S^* = S(r^*) = 1 + \sqrt{\frac{4a^3}{27b}} \end{cases} \quad (1.70)$$

By inverting (1.70) the values of a and b become:

$$\begin{cases} a = \frac{3}{2} S^* r^* \\ b = 3a(r^*)^2 \end{cases} \quad (1.71)$$

Thus very small drops of solution are in equilibrium with the vapor at a relative low humidity, also less than 100%, in contrast to what happens for the homogeneous nucleation. This process leads to the formation of mist particles. If the relative humidity increases slightly even drop will grow to reach a new equilibrium state. This process of growth of the relative humidity that allows the droplet to grow in conditions of equilibrium may proceed until a relative humidity of 100% and slightly higher, the "advantage" of the heterogeneous nucleation is just the fact that it can be done gradually and not so abrupt and sudden as in the case of homogeneous nucleation. But as soon as the humidity exceeds the critical supersaturation  $S^*$ , the droplet will grow over  $r^*$  without the saturation ratio rises further: the steam spreads naturally on the drop. While below  $r^*$  the droplet is in stable equilibrium above  $r^*$  the balance is unstable. The growth does not continue indefinitely because in every cloud there are many drops that compete for the available steam and tend to lower the supersaturation of the system, once the condensation rate exceeds that of supersaturation production. After the nucleation growth rate is fast, in just a few tenths of a second the process is complete allowing a separation between the activated do not activated particles.

#### 1.4.4 Nucleation activated by ions

The condensation is guided by the presence of ions and particles present in the vapor phase. (Wilson, 1897.1899) has found embryos for saturation ratios  $S = 4.2$  in contrast with the fog formed for of saturation ratios  $S > 7.8$  (homogeneous case). He attributed the difference to the presence of ions and verified this observation by ionizing a mixture of steam with X-ray. Subsequently, feeding separately positive ions and negative ions, he observed that the negatives one are active at  $p/p_\infty = 4$  and  $T = -6^\circ \text{C}$  and that the positive active a  $p/p_\infty = 6$ . Will lay the foundation for a theory that can explain the phenomenon, but there is not one well-established. Considering a vapor with a partial pressure  $p$ , in which is present an ion of charge  $Q$  and radius  $r_0$ . If a drop of radius  $r$  and dielectric constant  $\varepsilon$  condenses on the ion, the free energy change is:

$$\Delta G = -\frac{4}{3}\pi r^3 n_L k_B T \log \frac{p}{p_\infty} + 4\pi r^2 \sigma_{LV} + \frac{Q^2}{2} \left(1 - \frac{1}{\varepsilon}\right) \left(\frac{1}{r} - \frac{1}{r_0}\right) \quad (1.72)$$

Where  $r_0$  is the ion radius and the dielectric constant of the surrounding vapor  $\varepsilon = 1$ . To find the of equilibrium radius one proceeds as in the case of homogeneous nucleation, impose  $\partial G / \partial r = 0$  and is obtained

$$\log \left(\frac{p}{p_\infty}\right) = \frac{2\sigma_{LV}}{n_L k_B T r} - \frac{Q^2}{8\pi n_L k_B T r_0^4} \left(1 - \frac{1}{\varepsilon}\right) \quad (1.73)$$

This result was found by Thompson (1888). The saturation ratio is therefore lower than in the case of a drop  $r^4 = r_0^4$  in the second term of (1.73) or a charged particle compared to the homogeneous case, comparing the (1.16) with (1.73). To determine the nucleation rate it must

use the theory of fluctuation. Similarly to the treatment of homogeneous nucleation can be written:

$$J \simeq 10^7 N \exp\left(-\frac{\Delta G^*}{k_B T}\right) \quad (1.74)$$

#### 1.4.5 Nucleation activated insoluble solid charged particles

For charged particles, the nucleation occurs at a critical supersaturation  $S_{cr}$  lower than that on neutral particles, and the charge effect fades away as particle size increases. The charge effect is stronger than the theoretical predictions. In addition, a sign preference is detected, i.e., water vapor condenses more readily on negatively charged particle, a trend consistent with those observed on ions. However, both effects of charge and charge polarity on  $S_{cr}$  are stronger than that predicted by Volmer's theory for ion-induced nucleation. Condensation of a vapor onto charged particles is further influenced by the sign and the amount of charge and the dipole moment of the vapor molecules. Ions are believed to interact with the condensing vapor and change the energy barrier for nucleation (Chin-Cheng Chen and Hsiu-Chin Cheng, 2007). In the case of a charged particle treated as a perfectly wetted spherical ion of a radius  $R_0$  with the electric charge located at the center of the particle as shown in Figs. 1.22-a and 1.22-b, the change in Gibbs free energy required to form a critical embryo,  $\Delta G^*$ , can be written as (M. Volmer, 1939; K. C. Russell, 1969):

$$\Delta G = -\frac{4}{3M} \pi \rho_L R T \ln S (r_k^3 - r_i^3) + 4\pi \sigma_{LV} (r_k^2 - r_i^2) + \frac{q^2}{2} (k_0^{-1} - k^{-1}) \left( \frac{1}{r_k} - \frac{1}{r_i} \right) \quad (1.75)$$

Here  $\sigma_{LV}$  is the surface tension of water,  $k_0$  and  $k$  are the dielectric constants of gas phase and water,  $q$  is the electronic charge in Gaussian units,  $r_i$  is the radius that the charged particle has

when it is in stable equilibrium with the vapor, and  $r_k$  and  $r_a$  are the largest and the next smaller roots of  $\partial G/\partial r = 0$ :

$$\frac{\rho_L RT}{M} \ln S - \frac{2\sigma_{LV}}{r} - \frac{(r_k^2 - r_i^2)}{r} \frac{\partial \sigma_{LV}}{\partial r} + \frac{q^2}{8\pi r^4} (k_0^{-1} - k^{-1}) = 0 \quad (1.76)$$

To evaluate  $\Delta G^*$ ,  $r_i$  is set to  $R_0$  if  $r_a < R_0$  and it is set to  $r_a$  if  $r_a > R_0$ . For a given vapor pressure, a cluster of radius  $r_a$  is in stable equilibrium with the vapor, and any ion or charged particle with a radius  $R_0$  smaller than  $r_a$  will spontaneously grow up to  $r_a$ .

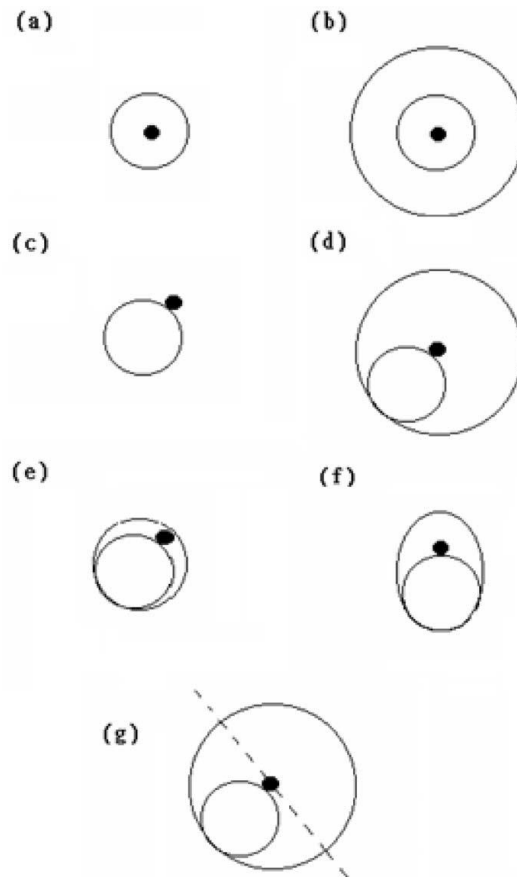


Figure 1.22: A schematic model for charge location in the particle and the growing embryo: (a) charge located at the particle center, (b) charge located at the center of concentric spheres of a particle and a growing embryo, (c) charge located on the particle surface, (d) charge located on particle surface and serving as the center of a growing spherical embryo, (e) charge located on the particle surface with a growing spherical embryo not concentric with the particle, (f) charge located on the particle surface with a growing nonspherical embryo, (g) volume of the embryo subjected to charge effect is more than a half of the embryo sphere as indicated by the dashed line for the case of charge located at the center of concentric spheres of particle and embryo.

However, in the case the electric charge is assumed to be to locate on particle surface as shown in Fig. 1.22-c and 1.22-d, there are more condensing water molecules strongly interacting with the charge compared to that shown in Figs. 1.22-a and 1.22-b due to the shorter interdistance between the charge and water molecules, leading to more lowering of the energy barrier. Equations (1.75) and (1.76) have to be modified to take into account the new charge distribution. Furthermore, the shape of the embryo may also vary with the amount of condensate as depicted by Figs. 1.22-e and 1.22-f and the charge may shift to a location more stable and having lower Gibbs free energy, both leading to an accurate evaluation of the charge effect becoming very complicated if not impossible. For simplicity, the embryo is assumed to be a spherical cap on the particle and the charge locates at the center as shown in Fig. 1.22-d, and we proposed a simplified modification as follows:

$$\Delta G = -\frac{4}{3M}\pi\rho_L RT \ln S(r_k^3 - r_i^3) + 4\pi\sigma_{LV}(r_k^2 - r_i^2) + V_q \frac{q^2}{2} (k_0^{-1} - k^{-1}) \left( \frac{1}{r_k} - \frac{1}{r_i} \right) \quad (1.77)$$

where  $r_i$  is the radius of an ion which is assumed to be a water molecule for the present case and  $V_q$  is a factor that takes into account the effect due to the exclusion of the embryo volume by the particle. The more the embryo volume excluded, the less the number of water molecules subjected to the charge interaction. And the ratio of embryo volume excluded by the particle varies with embryo size; consequently, the value of  $V_q$  changes accordingly. For an embryo growing to a radius equal to the diameter of the particle, the volume excluded by the particle is less than a half of the embryo as shown by the dashed line in Fig. 1.22-g ; thus, a value of 0.5 for  $V_q$  can be regarded as the lower limit, while for a very large embryo, the embryo volume excluded by the particle becomes negligible and  $V_q$  approaches 1. In the study here reported (Chin-Cheng Chen and Hsiu-Chin Cheng, 2007) the critical embryo at the critical supersaturation corresponding to each tested particle, calculated either by Volmer

theory for ion nucleation or by the Fletcher version of heterogeneous nucleation theory, is larger than the particle; thus, it is a reasonable approximation to use a value of 0.5–1 for  $V_q$  for the estimation of the charge effect. However, it is imperative to note that the accuracy of the approximation depends on the actual shape of the embryo and charge location, and there is no information available for the evaluation of an accurate charge effect yet. Further study is needed.

#### 1.4.6 *Physics of capillary condensation*

- Relevance in nano-system

As the size of systems go down, surface effect become increasingly important. Capillary condensation, which results from the effect of surfaces on the phase diagram of a fluid, is an ubiquitous phenomenon at nanoscale, occurring in all confined geometries, divided media, cracks, or contact between surfaces ( Bowden and Tabor, 1950). In divided media, capillary forces control the cohesion of the media, but also have dramatic influence on the ageing properties of materials. Since the condensation of liquid bridges is a first order transition, it gives rise to slow activated phenomena that are responsible for long time scale variation of the cohesion forces. Finally, the presence of capillary menisci and nanometric water film on solid highly rough surfaces has deep consequences on the surface physical and chemical properties, notably by permitting particular phenomena such as the activation of nanoscale recondensation.

- Physics of capillary condensation

Considering two parallel solid surfaces (area  $A$ ) separated by a distance  $D$ , in contact with a reservoir of vapor at a pressure  $P_v$ , and temperature  $T$ . If  $D$  is very large, the liquid-vapor equilibrium occurs at the saturating pressure  $P_v = P_{\text{sat}}$ . For a finite  $D$ , if the surface tension  $\sigma_{sl}$  of the wet solid surface is lower than the one  $\sigma_{sv}$  of the dry solid surface, the solid favors

liquid condensation. One should therefore ask if the solid can successfully stabilize a liquid phase when the vapor phase is stable in the bulk, i.e.  $P_v < P_{sat}$ . To answer this question, one must compare the grand canonical potential of two configuration: the “liquid filled interstice”, which we shall call the condensed state, and the “vapor filled interstice”, i.e. the non condensed state.



Figure 1.23:  $\Delta G_{non-condensed}(\mu) = 2A\sigma_{sv} - ADP_v(\mu)$        $\Delta G_{condensed}(\mu) = 2A\sigma_{sl} - ADP_l(\mu)$

with  $\mu = \mu_{sat} - \Delta\mu$  the chemical potential of the reservoir. Outside of coexistence, i.e. if  $\Delta\mu \neq 0$ , the pressure in the two phases are different and are given by the thermodynamic relation  $\partial(P_l - P_v)/\partial\mu = (\rho_l - \rho_v)$  (with  $\rho_l, \rho_v$  the number of molecules per unit volume in each phase). As the liquid is usually much more dense and incompressible than the vapour the pressure difference reduces to  $(P_l - P_v)(\mu) \simeq \rho_l \Delta\mu = \rho_l k_B T \ln(P_{sat}/P_v)$  if the vapour can be considered as an ideal gas. Thus, the condensed state is favoured if the confinement is smaller than the critical distance  $D_c(\mu)$ :

$$\rho_l \Delta\mu D_c(\mu) = 2(\sigma_{sv} - \sigma_{sl}) \quad (1.78)$$

The left side of eq. (1.78) represent the free energy required to condense the unfavorable liquid state, and the right hand side the gain in the surface energy.  $D_c(\mu)$  is thus the critical distance which balances the surface interactions and the bulk interactions to determinate the phase diagram of the fluid (Israelachvili, 1992). From the above equation it is clear that capillary condensation can occur if the liquid wets, at least partially, the solid surface. In the

case of partial wetting, the difference between the dry and wet surface tension is related to the contact angle  $\theta$  of the liquid onto the solid surface and the critical distance reduces to

$$D_c(\mu) = \frac{2\sigma_{lv}\cos\theta}{\Delta\mu} = 2\bar{r}_K\cos\theta \quad (1.79)$$

where  $\bar{r}_K$  is the Kelvin's radius associated to the under-saturation  $\Delta\mu$  so the radius of menisci curvature are evaluated from inside the gas ( $H = 2/\bar{r}_K < 0$  is the mean curvature of menisci evaluated inside the liquid).

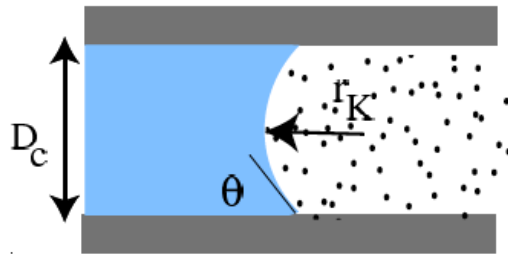


Figure 1.24: Coexistence of a liquid and its vapor across a curved surface

- Laplace - Kelvin equation

Another way to address capillary condensation is to consider the coexistence of a liquid and its vapour across a curved interface. Because of the Laplace law of capillarity the pressure in the two phases are not equal:  $P_{\text{int}} - P_{\text{ext}} = \sigma_{lv}/r$ , with  $r$  is the radius of mean curvature of the interface. The pressure is always higher on the concave side. Because of this pressure difference the chemical potential of coexistence is shifted as described in equation (1.8)  $(\mu_v - \mu_l) > 0$  if  $P_v < P_{\text{sat}}$ :

$$\mu_v(P_v) = \mu_l(P_l = P_v - \sigma_{lv}/r) = \mu_{\text{sat}} - \Delta\mu \quad (1.80)$$

we have assumed here that the liquid is on the convex side, a configuration compatible with and under-saturation. For an ideal vapour and an incompressible liquid:

$$\Delta\mu = k_B T \ln(P_{sat}/P_v); \quad P_l(\mu) \simeq \rho_l \Delta\mu + P_v(\mu) \quad (1.81)$$

From where we get the Laplace-Kelvin equation for the equilibrium curvature (Thomson, 1871):

$$\sigma_{lv}/\tilde{r}_K = P_v(\mu) - P_l(\mu) \simeq \rho_l \Delta\mu = \rho_l k_B T \ln(P_{sat}/P_v) \quad (1.82)$$

We check that in a flat slit, the critical confinement and the Kelvin's radius are related by (1.79). We see from the Laplace-Kelvin equation that the pressure in capillary condensates is usually very low: taking the example of water in ambient condition with relative humidity  $P_v/P_{sat}=40\%$ , the pressure in the condensates is  $P_l=-120\text{Mpa}$ , i.e. -1200 bar. With these severe negative pressures, condensates exert strong attractive capillary forces on the surfaces to which they are adsorbed. Furthermore, if the liquid phase wets totally the solid surfaces, the surface may be covered by a liquid film even in a non-confined geometry. In this case the critical distance for capillary condensation can be significantly enhanced at low humidity. In the case of water, the condensation of a liquid film has important consequences on surface chemistry as surface species can be dissolved in the liquid phase.

- Perfect wetting: the disjoining pressure

When the energy of the dry solid surface  $\sigma_{sv}$  is larger than the sum  $\sigma_{sl} + \sigma_{lv}$  of the solid-liquid and liquid-vapour interfaces ( $\theta \rightarrow 0^\circ$ ), the affinity of the solid for the liquid is such that it can stabilize a liquid film in equilibrium with an under-saturated vapour without any confinement. The existence of such wetting films must be taken into account when determining the liquid-vapour equilibrium in a confined space.



Figure 1.25: Stabilized liquid film in equilibrium with an under-saturated vapour without any confinement

In the theory of wetting, liquid film are described by the concept of interface potential (Derjaguin 1955, de Gennes 1985). The excess potential per unit area of a solid surface covered by a wetting film does not reduce to the sum  $\sigma_{sl} + \sigma_{lv}$  of the surface tension: a further excess must be taken into account corresponding to the fact that the molecular interactions which generate the surface tension do not operate over a thickness of liquid that can be considered infinite. The excess grand canonical potential of the humid solid surface of area  $A$  is then

$$\frac{G_{sv}}{A} = \widetilde{\sigma}_{sv} = \sigma_{sl} + \sigma_{lv} + W_{slv}(e) - e(P_l(\mu) - P_v(\mu)) \quad (1.83)$$

where the interface potential  $W_{slv}(e)$  vanishes for a macroscopic film. The excess potential  $\frac{G_{sv}}{A}$  describes the thermodynamic properties of the liquid film. It is minimum at equilibrium, so that the pressure in the liquid is not the same as in the vapour:

$$P_v(\mu) - P_l(\mu) = -\frac{dW_{slv}(e)}{de} = \Pi_d \quad (1.84)$$

the pressure difference  $\Pi_d$  is called disjoining pressure. The interface potential energy  $W_{slv}(e)$  and the wetting parameter  $\widetilde{\sigma}_{sv}(\Pi_d) - \sigma_{sl} - \sigma_{lv}$  are Legendre transform of each other:

$$W_{slv}(e) = \widetilde{\sigma}_{sv}(\Pi_d) - \sigma_{sl} - \sigma_{lv} - e\Pi_d \quad e = \frac{\partial \widetilde{\sigma}_{sv}}{\partial \Pi_d} \quad (1.85)$$

For instance in the case of van der Waals forces, the interface potential results from dipolar interactions going as  $1/r^6$  between molecules, and varies as  $1/e^2$

$$W_{slv}(e) = -\frac{A_{slv}}{12\pi e^2} \quad \Pi_d(e) = -A_{slv}/6\pi e^3 \quad \widetilde{\sigma}_{sv} = \sigma_{sl} + \sigma_{lv} + \left(\frac{-9A_{slv}}{16\pi}\right)^{1/3} \Pi_d^{2/3} \quad (1.86)$$

The Hamaker constant  $A_{slv}$  has the dimension of an energy (Israelachvili, 1992). It lies typically between  $10^{-21}$  and  $10^{-18}$  J and has negative sign when the liquid wet the solid ( $\theta < 90^\circ$ ), i.e. the interface potential is positive.

- Perfect wetting: the prewetting transition and capillary condensation

In a situation of perfect wetting, a liquid film condenses on a flat isolated solid surface if the humid solid surface tensions

$$\widetilde{\sigma}_{sv}(\Pi_d) - \sigma_{sl} - \sigma_{lv} + W_{slv}(e) + e\Pi_d \leq \sigma_{sv} \quad (1.87)$$

if the film exists, its thickness at equilibrium with the vapour is implicitly determinates by the analogue of the Laplace-Kelvin equation

$$\Pi_d(e) = \frac{\partial W_{slv}(e)}{\partial e} = P_v(\mu) - P_l(\mu) = \rho_l k_B T \ln \frac{P_{sat}}{P_v} \quad (1.88)$$

the thickness  $e^*$  realizing the equality in relation (1.86) is a minimum thickness for the wetting film, and the associated chemical potential  $\mu^*$  and vapour pressure  $P_v^*$  correspond to a prewetting transition. Above the transition the thickness of the adsorbed film increases with the vapour pressure until it reaches a macroscopic value at saturation.

In the case of van der Waals wetting for instance the vapour pressure at the prewetting transition is given by  $\Pi_d^*(e) = \rho_l k_B T \ln \frac{P_{sat}}{P_v^*} = \sqrt{16\pi S^3 / (-9A_{slv})}$  with  $S = \sigma_{lv}(\cos\theta - 1)$  the wetting parameter.

In a confined geometry such as a crack present on a rough surface, the grand canonical potential of the “non-condensed” state is shifted above the prewetting transition as the solid surface tension  $\sigma_{sv}$  has to be replaced by the humid value  $\widetilde{\sigma}_{sv}$ . The modified eq. (1.79) and the Laplace-Kelvin relation  $\sigma_{lv}/r_K = \Pi_d = \rho_l \Delta\mu$  give the critical distance

$$D_c = 2r_K + 2e + 2 \frac{W_{slv}(e)}{\Pi_d} \quad (1.89)$$

the difference with the partial wetting case is not simply to decrease the available interstice by twice the film thickness. In the case of van der Waals forces for example

$$D_c = 2r_K + 3e \quad \text{with} \quad e = (-A_{slv}/6\pi\rho_l\Delta\mu)^{1/3} \quad (1.90)$$

the effect of adsorbed films become quantitatively important for determining the critical size for capillary condensation in a perfect wetting situation.

- Effect of roughness on adhesion forces

The first order effect of roughness is to screen the interaction between surfaces, with an increased efficiency for the shorter range interaction. The molecular range solid-solid interaction are thus very efficiently screened by nanoscale roughness while the capillary interactions have more subtle behaviour. Three main regimes were identified by Halsey and Levine (Halsey and Levine, 1998) as function of the volume of liquid  $V$  available for the formation of a capillary bridge between two spheres: (1) the asperity regime prevails for small volumes, where capillary force is dominated by the condensation around single or a small number of asperities; (2) the roughness regime governs the intermediate volume range, where capillary bridges are progressively formed between a larger number of asperities and the

capillary force grows linearly with  $V$ ; (3) the spherical regime where a larger meniscus is recovered. The extension of the three domains is determined by the ratio between the characteristic scales of the gap distribution (height  $l_R$ , and correlation length  $\xi$ ) and the sphere radius  $R$ . when dealing with capillary bridges in equilibrium with under-saturated humidity, the roughness regime should be reduced to a narrow range of humidity values such that  $l_R = r_k$ , in which the capillary force jumps from a weak value to the spherical regime value. However, due to the first order nature of capillary condensation transition, the equilibrium condition may be preceded by a long time dependent region where the capillary bridges between asperities are progressively formed due to thermal activation. The energy barrier for the formation of a liquid bridge of volume  $v_d \approx hA$  between asperities of curvature radius  $R_c$  may be expressed as:

$$\Delta G = v_d \rho_l k_B T \log \frac{P_{sat}}{P_v} \quad (1.91)$$

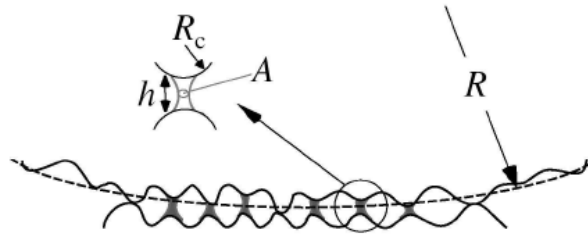


Figure 1.26: Formation of a liquid bridge between asperities present on particles surface

On the rough surface of a particle between the asperities will form a condensed stable liquid phase at under-saturation conditions through formation of a meniscus with negative curvature, which represent sites of nucleation and where it is generated a capillary force equal to  $2\sigma R_c$ . In the same way one can consider that also the valley between two asperities can acts as nucleation site since also in this case a stable liquid phase is present in under-saturation

condition. If on particles surfaces are present  $N_{tot}$  nucleation site, they should be particle activation site of the particle where a perfect wetting condition ( $\theta = 0$ ) is reached. In this case the reduction term of heterogeneous nucleation barrier  $f(\theta, x) = 0$  and this lead to the vanish of the nucleation barrier. Furthermore, the formation of liquid bridges increases the cohesion forces between the particles, leading to the formation of particle aggregates at sub-saturated vapour conditions.

- Vapor pressure over adhering spheres

The classical model that has been employed to describe condensation on a spherical particle (Fletcher, 1958), is a condensate in the form of a spherical cap on the aerosol particle's surface. The spherical morphology of the condensate is responsible for the well-known elevation of the equilibrium vapor pressure relative to its value over a plane results from the change in surface energy due to condensation which is evaluated via the well-known (Laplace) expression

$$P_l = P_v + \sigma_{lv} \left( \frac{1}{r_1} + \frac{1}{r_2} \right) \quad (1.92)$$

giving the pressure difference across a curved surface whose radii of curvature are  $r_1$  and  $r_2$ .

In heterogeneous condensation on aerosols, the presence of a soluble species is known to be responsible for the stability of aqueous particles at subsaturation humidities due to the term(s) that must be added to the Helmholtz function promoting condensation. A similar effect would occur for substrates without soluble deposits if  $P_v - P_l > 0$ . This condition, according to Eq.

(1.72), is fulfilled if  $\sigma_{lv} \left( \frac{1}{r_1} + \frac{1}{r_2} \right) < 0$  which is true if  $\left( \frac{1}{r_1} + \frac{1}{r_2} \right) < 0$  where the radii of

curvature are measured from inside the liquid. For a concave liquid surface,  $\left( \frac{1}{r_1} + \frac{1}{r_2} \right)$  can be

negative and this configuration pertains to the pendular ring of condensate that forms in the region where two adhering spheres make contact (Orr et al., 1975).

For aerosol particles whose radii are in the submicrometer range, the influence of the gravitational field is negligible. Within this domain, one can look at the problem from the mathematical standpoint and connect it to the well-known Plateau problem, which deals with minimum surfaces (surfaces of least area). The system that we want to examine, consists of three homogeneous phases: solid, liquid, and vapor. The solid phase is in the form of two particles of radii  $R_1$  and  $R_2$  in contact and these particles are assumed to be perfectly spherical, incompressible, and insoluble in both fluid phases, so that no exchange of matter occurs between the solid particles and either the liquid or vapor phase. Under these restrictions, the particles are defined as inert adsorbent. Any relative motion of the particles is ignored. On the other side, the liquid is in equilibrium with its vapor. Finally, all transformations are considered isothermal and reversible. Turning now to the hydrostatics of the condensate, introduce two geometrical parameters. The first is the mean curvature of a surface defined as the sum  $H=(1/r_1 + 1/r_2)$  where  $r_1$  and  $r_2$  are the local principal radii of curvature at a point of the surface. Here, the surface of interest is the liquid-gas interface. The second parameter is the contact angle  $\theta$ . The mean curvature, apart from being a geometrical quantity describing the meniscal profile, is also a fundamental parameter related to the vapor pressure over the liquid-vapor interface at equilibrium. This provides an important physical interpretation for the curves. As discussed above, the Kelvin equation relates the mean curvature to the equilibrium vapor pressure over the liquid-vapor interface and other physical properties like the temperature and the liquid-vapor interfacial tension. In the Kelvin equation,

$$P_H = P_0 \exp\left(\frac{M_w \sigma_{lv}}{\rho_l RT} H\right) \quad (1.93)$$

Here,  $P_H$  and  $P_0$  are respectively the equilibrium vapor pressures over surfaces of curvatures  $H$  and 0 (i.e., plane),  $M$ , is the molecular weight (molar mass) of the fluid,  $\rho$ , density of the liquid, and  $T$  the temperature of the system. Rewrite Eq. (1.73) by introducing the saturation ratio  $S$ :

$$S = \frac{P_H}{P_0} = \exp\left(\frac{M_w \sigma_{lv}}{\rho_l R T} H\right) \quad (1.94)$$

The sign of  $H$  specifies whether the vapor is subsaturated or supersaturated using the correspondence:

$H > 0 \Rightarrow$  supersaturation,

$H < 0 \Rightarrow$  subsaturation.

If the contact angle is greater than 90 degrees, condensation occurs only under conditions of supersaturation; due to the divergence to infinite positive values of the mean curvature at small filling angles, an extremely high supersaturation is consequently necessary to initiate condensation, so that any liquid phase that would be present at the point of contact between particles with such thermodynamic properties would evaporate completely. Therefore, such particles are not favorable sites for condensational growth. Conversely, for contact angles less than 90 degrees, the divergence to infinite negative values at small filling angles suggests that a small pendular ring could always exist in equilibrium, even at very low subsaturation levels. Then, start from a small amount of liquid already present in the interstitial region between the two particles and follow its evolution as the saturation slowly increases (quasistatic changes). As the surrounding vapor becomes increasingly saturated, its pressure becomes larger than the equilibrium vapor pressure corresponding to the curvature of the meniscus, so that condensation occurs. At one point, the system reaches a special configuration with zero mean

curvature: the vapor pressure becomes the same as the equilibrium vapor pressure over a plane.

The humidity of the medium next corresponds to supersaturated vapor. The corresponding point migrates towards still higher curvatures, following the curve, until the maximum is reached: there, any further increase results in the unconstrained condensational growth of the pair. The current saturation imposed on the system is thus called the critical supersaturation and is entirely analogous to the familiar Kohler curves for condensation on a drop containing a soluble salt. Then, the pendular ring increases in volume until both particles are enclosed by the liquid the evolution of the system then becomes that of a liquid droplet. The major consequence of capillary condensation on a pair of particles is the condensation nuclei activation at much lower supersaturations than the particles in isolation. Considering aerosol particles with contact angles less than  $90^\circ$  exposed to atmospheric conditions, a stable liquid ring can always exist in equilibrium at any subsaturation level, and that a critical supersaturation can be defined for which the system starts its unrestrained condensational growth.

- **Topographically structured surfaces**

The wetting properties of topographically structured surfaces have been discussed mainly in two contexts: filling transitions of grooves and wedges, and superhydrophobicity/superhydrophilicity. While the first is related to capillary condensation and drying, e.g., in slit pores, and to capillary filling (wicking) of thin tubes, research on the latter has been stimulated by the so-called lotus effect exhibited by many plant leaves. Both phenomena have many applications, ranging from simple bath sponges and water proof clothing to self-cleaning surface coatings. Capillary filling is a well known phenomenon and, e.g., in a cylindrical capillary or in a slit pore, driven by the Laplace pressure of the curved liquid-vapor interface. In this macroscopic view, the effect of intermolecular interactions is

summarized in the liquid-vapor surface tension and the equilibrium contact angle. In macroscopic systems, capillary forces are counteracted by gravity, which is the reason why water drips out of a wet sponge. Partial or complete capillary filling can occur only if the equilibrium contact angle  $\theta_{eq}$  at the capillary wall is smaller than  $\pi/2$  (see Figure 1.27(a)). Macroscopically, the wedge can be viewed as a generalization of a slit like capillary (which can be considered as the limiting case of a wedge with opening angle  $\alpha \rightarrow 0$ ) and the filling will occur if the contact angle equals half the wedge angle  $\alpha$  (see Figure 1.27(b)). In the absence of gravity and for  $\theta_{eq} > \pi/2 - \alpha/2$  the wedge is only filled with a film of microscopic thickness, while it is completely filled for  $\theta_{eq} < \pi/2 - \alpha/2$ . For most materials  $\theta_{eq}$  is a function of temperature and the filling of the wedge with a liquid in thermodynamic equilibrium with its vapor is a phase transition. Microscopic studies, which take intramolecular interactions into account, reveal the character of these filling transitions and the variation of the filling height as a function of the thermodynamic variables (K. Rejmer et al., 1999; Parry et al., 2000; J.M. Romero-Enrique and A.O. Parry, 2005; E.S. Hernández et al., 2006, M. Tasinkevych and S. Dietrich, 2007; M. Tasinkevych and S. Dietrich, 2007). The filling and emptying of one-sided capillaries represent continuous phase transitions (A.O. Parry, et al., 2007).

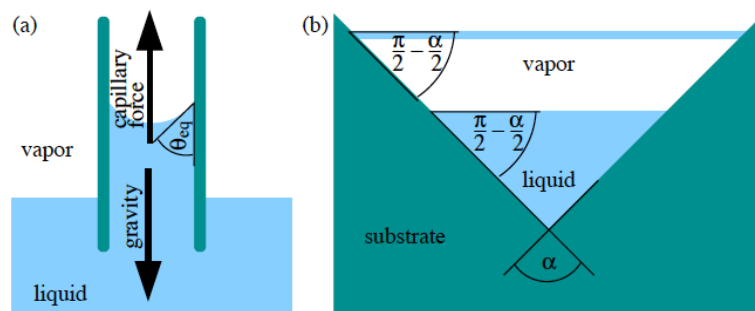


Figure 1.27: Wetting of topographically structured substrates. (a) A capillary in contact with a liquid. Capillary forces suck the liquid into the capillary if the equilibrium contact angle  $\theta_{eq}$  is smaller than  $\pi/2$ . (b) A macroscopically extended straight wedge with opening angle  $\alpha$

Case (b) can be viewed as a generalized slit-like capillary, which would be recovered in the limit  $\alpha \rightarrow 0$ . For  $\theta_{eq} > \pi/2 - \alpha/2$ , the wedge is dry on macroscopic scales, i.e., filled only with a film of microscopic thickness. It is completely filled for  $\theta_{eq} < \pi/2 - \alpha/2$ . For  $\theta_{eq} = \pi/2 - \alpha/2$  the liquid vapor interface is horizontally planar (as shown) and in a grand canonical ensemble all filling levels are (indicated are two) are thermodynamically equivalent.

#### ***1.4.7 Wetting and hydration of insoluble soot particles***

Hydration properties of black carbon aerosols are of increasing importance because they provide direct information about the amount of water on the soot surface and a pathway of its wetting. The water adsorption on black carbon is determined most of all by the chemical nature of the surfaces. Incorporation of soot aerosols into droplets depends on the wettability of their surface (Pruppacher H. K. and Klett J. D., 1978). However, the literature on the wettability of carbonaceous compounds yields a consistent picture of hydrophobicity. (Chen C.-C. et al., 1993 Schrader, M., 1975, Studebaker M. L. and Snow C. W., 1955). It means a non zero water droplet contact angle,  $\theta$ , which is traditionally associated with a poor ability to adsorb water and a low rate of heterogeneous nucleation. This is why there is a widespread assumption that fresh emitted soot particles should be hydrophobic and poor substrates for nucleating water embryos until they have undergone a chemical activation through the accumulation of soluble species or functional C-groups. (Brown R. C. et al. 1996, Karcher B., 1996). It is worth emphasizing that the factor influencing the soot wetting show a tremendous dependence on the surface chemical composition and microstructure. Wetting characteristics of soots are directly related to its hydrophilicity. The inverse Kelvin effect is considered as a mechanism of water nucleation which is facilitated by the soot agglomerated structure with

interparticle cavities in which condensation takes place on the insoluble surface. Irregular agglomerates of soot have micropores and mesopores between the primary particles which may be filled by water due to the inverse Kelvin effect. Since the water contact angles on soots were found to be less than  $90^\circ$ , mean curvature of the water meniscus inside interparticle cavities will start with negative values (i.e. for  $S < 1$ ) for small filling angles. As the surrounding vapor pressure becomes larger, the mean curvature increases reaching the final equilibrium curvature in correspondence with the relative humidity in the ambient atmosphere (Persiantseva et al. 2004).

However, according to the fundamental accepted mechanism of water adsorption on carbonaceous adsorbents (Dubinin M. M., , 1980 Gregg and S. J., Sing K. S. W, 1982, Vartapetian R. Sh. and Voloshuchuk A. M., 1995) the initial water adsorption on soot is via oxygen-containing polar groups which act as active sites. Primary adsorbed water molecules may then act as secondary sites for further water molecule adsorption to build up hydrogen bonded clusters on the soot surface. Oxygen containing groups on the surface of Palas soot have been observed using FTIR spectroscopy. They are attributed to the surface functionalities, such as a  $-C-O$ , aromatic  $-C=O$  and carboxylic  $C=O$  groups. Their existence can possibly be due to impurities in the graphite rod ( Kirchner et al., 2000) and/or the argon supply system (Kalberer et al., 1999a,b).

At present, different laboratory-made soot types with source-dependent properties are used for atmospherically-relevant studies (Chughtai, et al., 1996). Among those, soot generated by spark discharge between graphite electrodes has recently become subject of intensive studies (Kamm, et al., 1999; Weingartner, et al., 1997). This can be attributed to the convenience of operation and high reproducibility of the graphite spark generator, Palas GFG 1000, which produces soot particles without generation of undesirable combustion by-products. Determination of Palas soot hygroscopicity and its ability to act as condensation nuclei (Kotzick, et al., 1997; Nink, et al., 2001) requires knowledge on water adsorptivity over a

wide range of conditions. Furthermore also the bulk mechanical properties of particulate solids are often strongly influenced by the interaction with condensed vapors. Hydration of Palas soot particles in the humid atmosphere leading to changes in the structure of the particles (Weingartner et al. 1997). Water molecules may penetrate the micropores of the porous adsorbents present on particle surface, thereby increasing the surface area. In microporous materials, the adsorbate molecules are able to gain access to the adsorption space of micropores. Structure transformation is expected when the adsorbate molecule is of roughly the same size as the pore (or perhaps pore entrances) which may open up further during the structural change induced during the adsorption process. In a “rigid” solid, the displacements brought about by adsorption forces do not strain the material beyond its elastic limit. In a “less rigid” solid, an increase in the number of adsorbed molecules may cause the structure to “jump” to a new configuration of opened micropores that will give access to new micropores. Since such a transformation may be irreversible, some adsorbed molecules may be trapped inside micropores and desorb out with great difficulty until the temperature increases significantly (Popovitcheva et al. 2000). For these systems the low-pressure hysteresis is associated with the intercalation of the adsorbate molecules in the narrow pore spaces leading to irreversible changes in the pore structure in such a way soot agglomerates collapse to a more compact structure under the influence of capillary forces exerted by water condensed in the interstitial space of contacting particles. (Bailey et al., 1971; Gregg and Sing, 1982). Figure 1.28 shows a simplified swelling model for carbon particle.

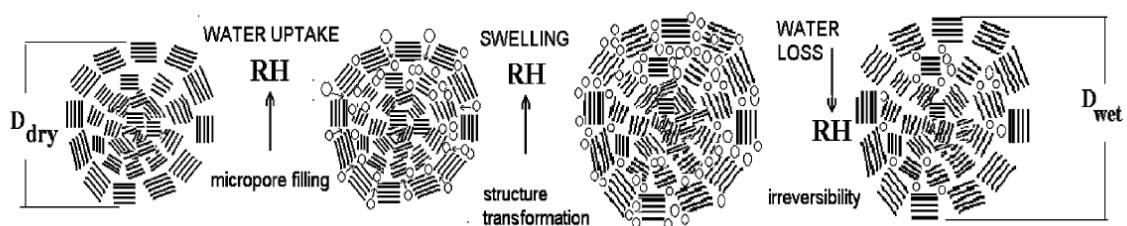


Figure 1.28 Simplified swelling model

The analysis of the adsorption/desorption isotherms in the first cycle is an useful tool to obtain information about the Palas soot porosity. A narrow high-pressure hysteresis in the adsorption and desorption parts of the first cycle that is a well-established characteristic of adsorbents with mesopores of radius larger than 2 nm (Bailey et al., 1971). The slope of the hysteresis is related to the form of the pore size distribution. The onset of the hysteresis loop at indicates capillary condensation in the micropores and mesopores of minimum radius which is estimated to be equal to 2.1 nm using the Kelvin–Thomson equation (Gregg & Sing, 1982).

The location of mesopores in the soot structure can be determined from electron microscopy analysis. It was observed that Palas soot consists of agglomerates with primary particle diameters between 5 and 10 nm (Weingartner et al., 1997; Helsper et al., 1993; Wentzel et al., 2003). while in this work their diameters ranges from 3-5 nm. The internal microstructure of the primary particles appears (Wentzel et al., 2003) to be totally amorphous without any distinctive micropores. This is different from the onion-like microstructure of combustor soot particles which determines their internal microporosity (Popovitcheva et al., 2000). Therefore, it is reasonable to conclude that the primary porosity of Palas soot is determined by micropores and mesopores to be identified with cavities between the primary particles.

Once produced the spark discharge soot particles will exhibit irreversible changes in surface area, porosity and hygroscopicity as a result of numerous humidity fluctuations until approaching a stable state of their microstructure due to exposure to saturated water vapor.

## **1.5 Diffusional Growth**

If an embryo has reached dimensions larger than the critical radius beyond which the pressure of saturated vapor on its surface is less than the pressure of the vapor in the bulk of the gaseous phase, it can grow until because there is a driving force that makes the vapor molecules diffuse from the gas phase to the surface of the embryo. It should be noted that, in general, as the drop grows it extracts humidity from the system and then the partial pressure of vapor in the system may decrease gradually; in a realistic case, the droplet cannot grow indefinitely.

Once created, the critical nuclei, they may develop larger and larger. In this phase the growth rate is limited by the mechanism by which atoms or molecules arrive at the surface of the embryo to make it increase in size. Depending on the case (nuclei in a gas, a liquid or a solid) will change the mechanism of the diffusion process. When a vapor species condenses on the particle, there is a variation of its diameter and consequently its size changes.

It has been demonstrated that the diameters of the small particles vary much faster than the diameters of the largest particles, then the condensation tends to reduce the size distribution of aerosols (Seinfeld and Pandis, 2006)

## **1.6 Coagulation**

It should be noted that, as mentioned earlier, as the drop grows it extracts humidity from the system and therefore the vapor pressure of the system could or should decrease gradually; in a realistic case, the droplet cannot grow indefinitely. Once reached the equilibrium condition the particle is no longer growing by diffusion but through the mechanism of coagulation.

The coagulation takes place by collision between two droplets and / or particles that move to thermal agitation, with formation of larger size droplets; following which it has globally a loss

in the number of drops, even if the mass concentration of the aerosol pollution remains unaffected. It is therefore a process that summarizes the steps of collision and adhesion.

The simulation of the coagulation process therefore requires in principle the calculation of the factor of collision, coalescence and their temporal variation. The coalescence is calculated using a of unitary adhesion coefficient: i.e. two particles which are in contact remain adherent to each other (without rebounds). This approximation leads to an overestimation of the coagulation factor, but there is no reliable information on the adhesion coefficient of atmospheric aerosols. Moreover, the kinetic energy of the particles is so low that the rebounds probability is small (Seinfeld, 1986). In a recent article states that between physical phenomena responsible for the formation and accretion of particles (coagulation, nucleation, condensation) that coagulation is the least important (Russell and Dennis, 2000). For this reason, some existing models, especially to decrease the computation time, neglect this phenomenon than others. This result was confirmed with reasons related to the characteristic times of each of the phenomena involved (Wexler et al., 1994) (Seinfeld and Pandis., 2006). Other studies say that coagulation has a significant influence on the number and volume of smaller particles (Jacobson, 1997a). Then neglecting the coagulation process in a model leads to erroneously predict a numerical concentration very high for smaller particles. The total mass of aerosols can always be predicted correctly, but will be distributed over a very large number of particles.

It is interesting to evaluate the characteristic time  $\tau_c$  of the coagulation process assessed through the following expression:

$$\tau_c = \frac{2}{KN_0} \quad (1.95)$$

where K is the of collision factor and  $N_0$  is the initial number concentration.

It represents the time required for the halving of the initial numerical concentration  $N_0$  (Seinfeld and Pandis, 2006).

### 1.7 Particles growth rate

From various studies present in literature, it is derived an analytical expression for the **condensation growth rate**. On the basis of this theory, has been obtained an analytical expression, approximate but accurate, of **growth the time** (T.Nieminen et al., 2010). It has been shown that the growth of the particulates is mainly due to the growth by condensation (Kulmala et al., 1998), and appears to be dependent on the size of the particles themselves (Hirsikko et al., 2005). The collision rate between particles of aerosol and vapor molecules into **kinetic regime** is:

$$K_{kin} = \frac{\pi}{4} (D_p + D_v)^2 (\bar{c}_p^2 + \bar{c}_v^2)^{\frac{1}{2}} C_v \quad (1.96)$$

where  $D$  is the diameter and  $\bar{c}$  is the average thermal speed.

The subscript "p" refers to the particle and "v" to the water molecule. The average thermal speed is expressed by:  $\bar{c}_i = \sqrt{8RT/\pi M_i}$ . Where R is the universal gas constant equal to  $R = 8.314 \text{ J/K}^{-1} \text{ mol}^{-1}$ , T is the absolute temperature,  $M_i$  is the molar mass in kg/mol,  $m_i$  is the molecular mass in atomic mass units ( $amu = 1.660 \times 10^{-27} \text{ kg}$ ). To describe the process in continuous regime, the equation (1.96) must be multiplied by a correction factor  $\gamma$ . This factor is obtained considering the generalized coagulation coefficient (Seinfeld and Pandis, 2006):

$$K = 2\pi(D_p + D_v)(\mathcal{D}_{iff,p} + \mathcal{D}_{iff,v})\beta_m \quad (1.97)$$

obtained by multiplying the equation (1.96) for  $\gamma$ ; where  $\mathcal{D}_{iff,p}$  e  $\mathcal{D}_{iff,v}$  are respectively the diffusivity of the particle and the vapor molecule;  $\beta_m$  is the correction factor of Fuchs-Sutugin in scheme transition for mass flow (Fuchs and Sutugin, 1971):

$$\beta_m = \frac{1 + K_n}{1 + \left(\frac{4}{3\alpha_m} + 0.337\right) K_n + \frac{4}{3\alpha_m} K_n^2} \quad (1.98)$$

where  $K_n$  is the **Kundsen number** and  $\alpha_m$  is the mass arrangement coefficient (assumed equal to unity in this work). In this way we obtain an expression for the of collision rate between vapor molecules and particles (Kulmala and Wagner, 2001):

$$K = \gamma K_{kin} = \gamma \frac{\pi}{4} (D_p + D_v)^2 (\bar{c}_p^2 + \bar{c}_v^2)^{1/2} C_v \quad (1.99)$$

where

$$\gamma = \frac{8(\mathcal{D}_{iff,p} + \mathcal{D}_{iff,v})}{(D_p + D_v)(\bar{c}_p^2 + \bar{c}_v^2)^{1/2}} \cdot \beta_m = \frac{4}{3} \cdot K_n \cdot \beta_m \quad (1.100)$$

For the evaluation of the collision factor of was used a modified form of the *Knudsen number* **Kn** (Lehtinen and Kulmala, 2003):

$$K_n = \frac{2\lambda}{(D_p + D_v)} \quad \lambda = \frac{3(\mathcal{D}_{iff,p} + \mathcal{D}_{iff,v})}{(\bar{c}_p^2 + \bar{c}_v^2)^{1/2}} \quad (1.101)$$

For the evaluation of the particles diffusion coefficient, in the case of multiply the molecular regime particle diffusivity is multiplied by Cunningham correction factor, and thus:

$$\mathcal{D}_{iff,p} = \frac{kT}{3\pi\mu D_p} C_c \quad (1.102)$$

where  $\mu$  is the dynamic viscosity of the gas present in the system, and the Cunningham correction factor is expressed by the following formula (Seinfeld and Pandis, 2006):

$$C_c = 1 + K_n \cdot [1,257 + 0,40 \exp(-1,10/K_n)] \quad (1.103)$$

The limiting behavior of  $C_c$  is

$$C_c = \begin{cases} 1 + (1.257) \frac{2\lambda}{d_p} & d_p \gg \lambda \\ 1 + (1.657) \frac{2\lambda}{d_p} & d_p \ll \lambda \end{cases} \quad (1.104)$$

The Cunningham correction is important only for aerosol particles much smaller than the micronic size. When this factor is taken into account, the definition of the Knudsen number is as follows:

$$K_n = \frac{2\lambda_v}{D_p} \quad \text{and} \quad \lambda_v = \frac{1}{\sqrt{2} D_v^2 \pi n_v} \quad (1.105)$$

that is the ratio between the mean free path of the molecules in the fluid and the particle radius. The term  $\lambda_v$  is the molecular mean free path where  $n_v$  is the density of the particle. Obtaining  $n_v$  the equation of the perfect gases  $pV = nRT = nN_A k_B T$ , we obtain the expression of the mean free path as a function of temperature and pressure:

$$\lambda_v = \frac{K_b T}{\sqrt{2} D_v^2 P \pi} \quad (1.106)$$

The value of  $K_n$  can vary from 0 to 1 and one can distinguish different regimes as shown schematically in Figure 1.28:

**$K_n \rightarrow 0$  (Continuum Regime)** The gas surrounding the particle can be considered as continuum; the particle has dimensions such as to influence the velocities distribution of the molecules close to it and the interaction is described by the equations of continuum mechanics;

**$K_n \rightarrow 1$  (Free molecular Regime).** In this region the velocity distribution of the gas molecules that affect the particle is not influenced by the presence of the latter. This is because the mean free path of the molecules is much larger than the radius of the particle ( $\lambda \gg r$ );

**$0 < K_n < 1$  (Transitional regime):** the intermediate region between the continuum regime and free molecular regime is called the transition region and the analysis of the interactions is very complex: no theoretical approach is really satisfactory. Unfortunately this is the situation in which we encounter in normal removal processes.

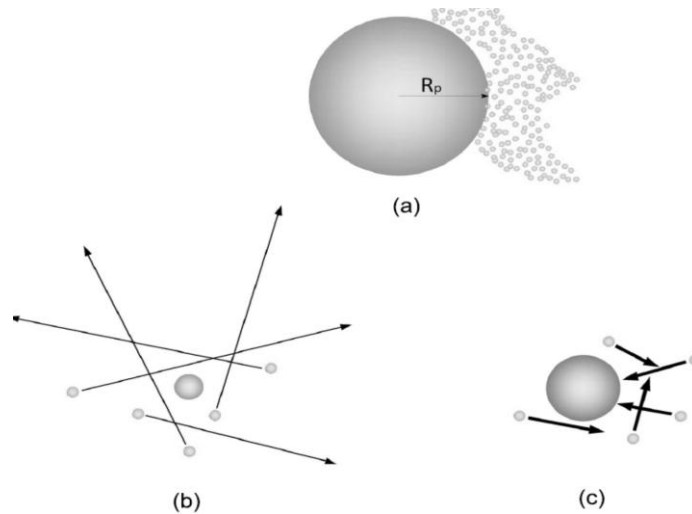


Figure 1.29: Schematic representation of the three regimes: (a) continuous regime ( $K_n \rightarrow 0$ ), (b) regime (kinetic) free molecular ( $K_n \rightarrow \infty$ ), (c) transition regime ( $K_n \sim 1$ ).

For vapor molecules the diffusion coefficient is calculated by a semi-empirical formula (Poling et.al., 2001):

$$D_{diff,v} = \frac{0.001T^{1.75}}{P(\Sigma_g^{1/3} + \Sigma_v^{1/3})^2} \sqrt{\frac{1}{m_g} + \frac{1}{m_v}} \quad (1.107)$$

Where  $m_g$  e  $m_v$  are molecular mass of gas and vapor phase and  $P$  is the pressure. The diffusion volume of gas and vapor phase,  $\Sigma_g$  e  $\Sigma_v$ , are obtained by summing atomic diffusion volume (listed in table 5 in Appendix B).

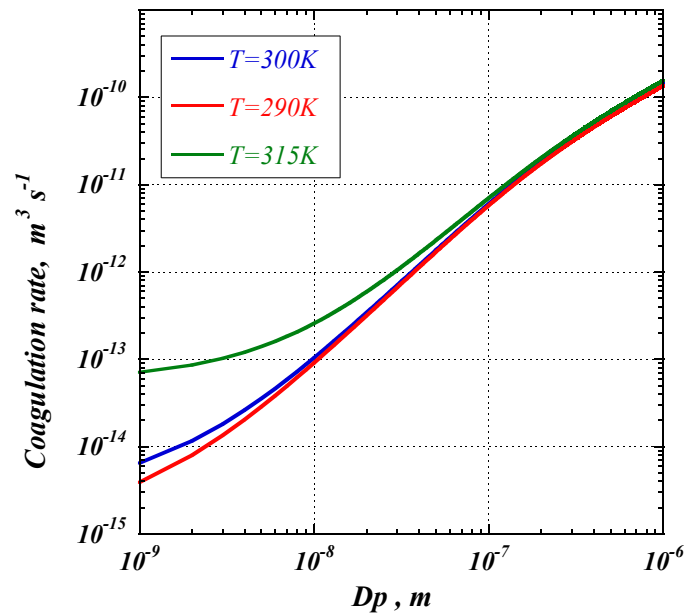


Figure 1.30: Trend of coagulation rate by varying particle diameter for fixed values of temperature

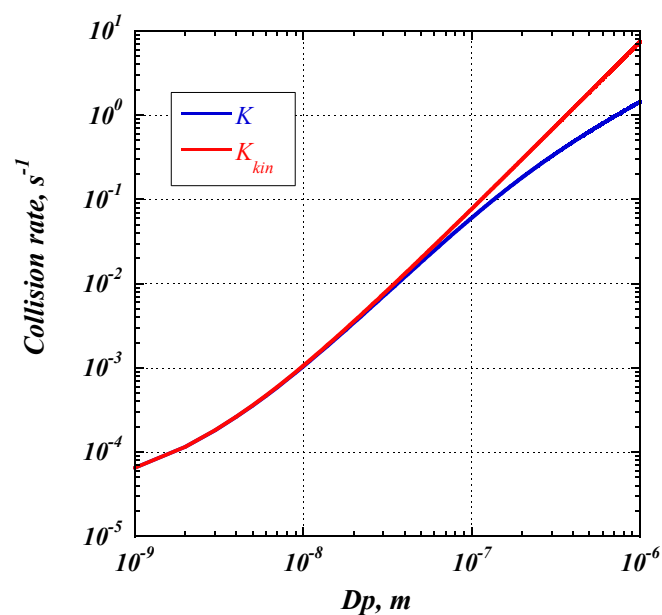


Figure 1.31. Trend of collision rate for kinetic (red line) and molecular regime (blue line)

The collision rate between vapor molecules and particles can be express in terms of mass flux. Combining the equations (1.99) e (1.100), and expressing the vapor molecule collision rate as function of its diameter, the particle growth rate can be formulated as follows:

$$GR = \frac{dd_p}{dt} = \frac{\frac{dm_p}{dt}}{\frac{dm_p}{dd_p}} = \frac{\gamma}{2\rho_p} \left(1 + \frac{D_v}{D_p}\right)^2 \left(\frac{8kT}{\pi}\right)^{1/2} \left(\frac{1}{m_v} + \frac{1}{m_p}\right)^{1/2} m_v C_v \quad (1.108)$$

Where  $\rho_p$  is particle density,  $m_p$  and  $m_v$  are respectively the molecular mass of particle and vapor,  $C_v$  is the vapor molecule number concentration. To get a prediction for the vapor concentration corresponding to a certain growth rate, the equation (1.104) must be integrated over the entire range of particle sizes where the growth rate has been determined. The equation (1.108) can not be analytically integrated. However, if the last term under the square root of Eq. (1.108) is substituted with its Taylor series expansion, we get:

$$\frac{dd_p}{dt} \approx \frac{\gamma m_v C_v}{2\rho_p} \left(\frac{8kT}{\pi m_v}\right)^{1/2} \left[1 + 2\frac{D_v}{D_p} + \left(\frac{D_v}{D_p}\right)^2 + \frac{1}{2}\frac{\rho_v}{\rho_p}\left(\frac{D_v}{D_p}\right)^3 + \left(2 + \frac{1}{2}\frac{\rho_v}{\rho_p}\right)\left(\frac{D_v}{D_p}\right)^4 + \frac{1}{2}\frac{\rho_v}{\rho_p}\left(\frac{D_v}{D_p}\right)^5\right] \quad (1.109)$$

where the masses of particles and droplets are expressed in terms of density and diameter.

An approximation with three terms of the Taylor series can be considered a good approximation in the range of size smaller than 10 nm. In addition to changing the term  $d_p$  in the derivative form  $dd_p/dt$  with the term  $d_v/d_p$ , we get:

$$\frac{d(D_v/D_p)}{dt} = \frac{-D_v}{D_p^2} \frac{dD_p}{dt} \approx \frac{\gamma m_v C_v}{2\rho_p D_p} \left(\frac{8kT}{\pi m_v}\right)^{1/2} \left(\frac{D_v}{D_p}\right)^2 \left[1 + 2\frac{D_v}{D_p} + \left(\frac{D_v}{D_p}\right)^2\right] \quad (1.110)$$

writing  $x = D_v/D_p$  e integrating, it follows:

$$C_v = \frac{2\rho_p D_v}{\gamma m_v \Delta t} \cdot \sqrt{\frac{\pi m_v}{8kT}} \cdot \left[ \frac{2x_1 + 1}{x_1(x_1 + 1)} - \frac{2x_0 + 1}{x_0(x_0 + 1)} + 2 \ln \left( \frac{x_1(x_0 + 1)}{x_0(x_1 + 1)} \right) \right] \quad (1.111)$$

In this expression placing  $x_1 = D_v/D_{p,final}$  and  $x_0 = D_v/D_{p,initial}$ , and considering the growth of the particles from  $D_{p,initial}$  to  $D_{p,final}$  time  $\Delta t$ , the equation (1.111) provides an easy-to-use relation between the rise time and the vapor concentration required.

Figure 1.32 shows the trend of the growth rate as a function of the vapor concentration for different values of the particle diameter, and can be observed as described above that the growth rate is greater for smaller particles.

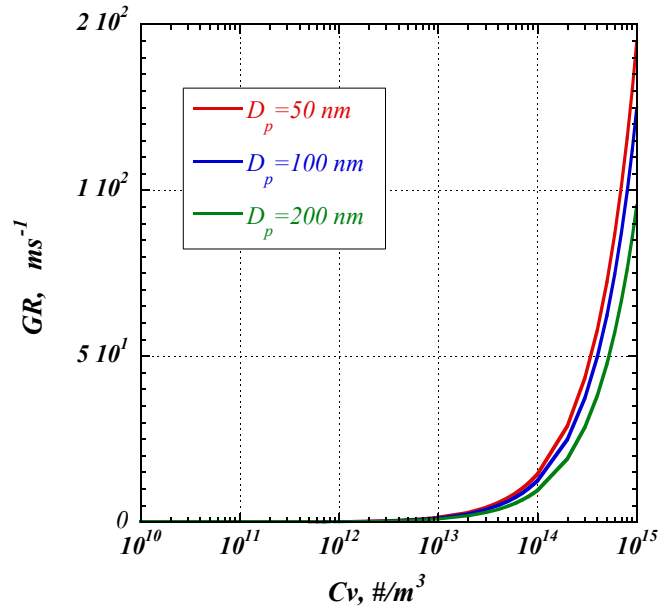


Figure 1.32: Trend of growth rate by varying the vapor concentration, for three different diameters of the particle.

From equation (1.111) it is possible to calculate the growth time by varying the vapor concentration in the same conditions in which it was assessed the growth rate. It can be seen that larger particles require a greater time for growth.

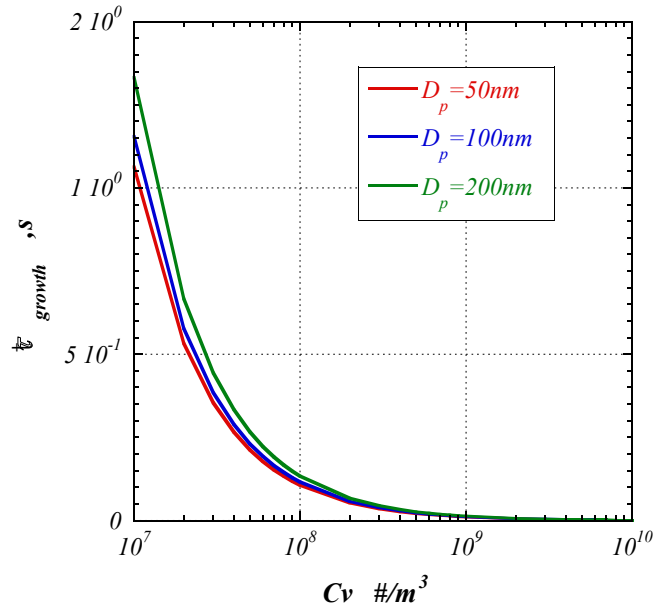


Figure 1.33: Trend of the growth time as a function of vapor concentration for three different diameters of the particle

Park and Lee find a relationship between supersaturation and particle growth rate can be expressed as (Park and Lee, 2010) formula presented by Kulmala:

$$\frac{dR_p}{dt} = (S - S_a) / \left\{ \rho R_p \left[ \frac{R_g T}{\left\{ \beta_m M_v D P_\infty \left[ 1 + \frac{(S + S_a) P_\infty}{2P} \right] \right\}} + \frac{S_a L^2 M_v}{\beta_t R_g K T^2} \right] \right\} \quad (1.112)$$

Where  $S$  is supersaturation,  $S_a$  is the supersaturation of particles surface under Kelvin effect,  $\rho$  is the density of particle,  $D$  is diffusion coefficient of vapor,  $R_g$  is gas constant,  $L$  is the latent heat of vaporization,  $K$  is heat conductivity,  $M_v$  is molar weight of water vapor,  $P_\infty$  is saturated vapor pressure,  $P$  is total pressure,  $\beta_m$  and  $\beta_t$  are mass flow and heat flow correction coefficients. Condensation rate and the formed diameter of dusty droplets increase with the improving of supersaturation. Particles stop growing when the supersaturation drop to  $S_a$  and the final diameter of dusty droplets can be derived from  $dR_p/dt=0$ .

Once evaluated the growth times of the drops it is possible to compare them with the characteristic times of the nucleation process. It can be seen that only under certain conditions

the characteristic time of the two processes are comparable. In particular, the time of nucleation is strongly dependent on the temperature.

The characteristic time of growth, being this controlled by the molecular diffusion of vapor, is very dependent on its concentration.

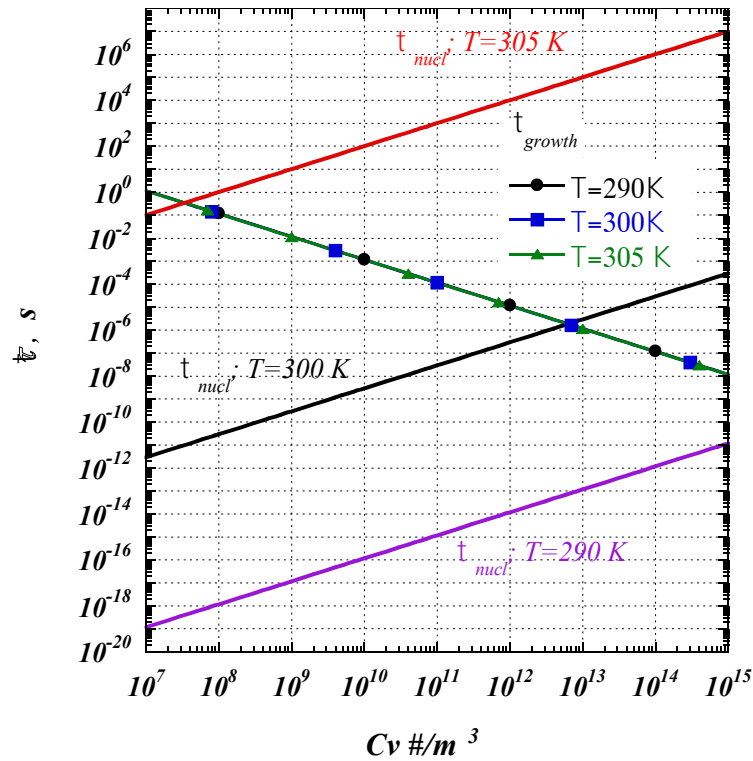


Figure 1.34: Comparison of the of growth time with nucleation time by varying the vapor number concentration, for three different temperatures.

It is to be noted that the numerical concentration  $C_v$  for the evaluation of the of nucleation time has been defined as  $P_s/k_B T$ , in fact  $C_v$  increases by increasing the temperature, at same time  $J^*$  (heterogeneous nucleation rate) strongly decreases and for this reason nucleation time increases by increasing vapor concentration.

Heidenreich (Heidenreich, 1994), in a review on the condensational droplet growth in the air–water system, demonstrated that heat flux between droplets and vapour can be related only to heat conduction and by diffusing molecules, neglecting the Dufour effect. The same author showed that the mass balance on a droplet in a binary air–water gas mixture can take in account only for the mass flux due to diffusion: the Stefan-flow and the Soret effect

contributions can be neglected since they account for less than 1.5% of the overall mass transfer rate. It was also found that heat and mass balances can be simplified by the assumptions that: (i) temperature inside the droplet is uniform;(ii) the gas is a continuous phase (i.e. droplet Knudsen number, Kn, is farless than 1); (iii) the droplets, if smaller than 5 $\mu$ m, are rigid non-deformable spheres (Clift etal.,1978); (iv) no-slip velocity condition for the gas flows at the droplet surface; (v) the binary air–water mixture has physical properties constant with temperature. Under these assumptions the heat and mass balance become (Heidenreich, 1994; Heidenreich andEbert,1995; Clift etal., 1978; Miller etal.,1998)

$$cm_d \frac{dT_d}{dt} + h_l I = Q \quad (1.113)$$

$$\frac{dm_d}{dt} = \frac{1}{2\pi\rho_l d^2 \frac{dd}{dt}} = -I \quad (1.114)$$

where Q is the total heat flux and I is the total mass flux to the droplet; T<sub>d</sub> is the temperature of the droplet and h<sub>l</sub>, c, m<sub>d</sub>, d are the specific enthalpy of the liquid, the specific heat capacity, the mass and the diameter of the droplet respectively. It was found that for S<2, the condensational growth of a droplet can be well described by the analytical solution provided by Fuchs(Fuchs, 1959) under the assumption of a pseudo-steady state droplet temperature. The expression of I was given first by Maxwell (see Fuchs(Fuchs, 1959))

$$I = \frac{2\pi d M_w D}{R_v T} (P_{v,a} - P_{v,\infty}) \quad (1.115)$$

where D is the diffusivity of water, T is assumed as the film temperature at the droplet surface estimated as (T<sub>∞</sub>+T<sub>d</sub>)/2, and P<sub>v,a</sub>, is the vapor pressure at the droplet surface, that can be related to the saturation vapor pressure over a flat liquid surface at temperature T<sub>d</sub> and radius according to the equation (Heidenreich and Ebert, 1995)

$$P_{v,a} = P^{\circ}(T_d) \exp\left(\frac{4\sigma M_w}{R_v T_d \rho_l d}\right) \quad (1.116)$$

Where  $\sigma$  is the particle surface tension (but if we consider that particle is a droplet or it is covered by a liquid layer  $\sigma = \sigma_{lv}$ ),  $M_w$  is water molecular weight,  $R_v$  ideal gas constant,  $\rho_l$  is the liquid density,  $d$  is the particle (droplet, particle water layer covered) diameter and  $T$  is the temperature.

The expression for the time course of droplet temperature  $T_d(t) = T_{\infty} - I\lambda/2\pi dK_w$  where  $\lambda$  is the specific heat of vaporization of water and  $K_w$  is the thermal conductivity. Eq.(1.116) is non-linear due to the dependence of  $I$  upon  $T_d$ , but is independent from  $d$ . Once  $T_d$  is calculated, Eq.(1.114) can be integrated overtime considering the initial condition:  $t=0$ ,  $d=d_0$  and  $T_d=T_{d,0}$ . Solution of Eq. (1.114) is not straight forward since both  $I$  and  $T_d$  are functions of time and numerical solutions are usually preferred.

Although the growth model is rigorously valid to describe the droplet growth in a continuous flow, this can be used also for heterogeneous condensation, assuming that the liquid–solid aerosol behaves as a homogeneous, isolated droplet with initial diameter  $d_0$  and temperature equal to that of the gas. Indeed, this approximation becomes reasonable only when the embryos enlarge enough to surround the particle, so that the model fails to describe the first instants of embryos growth. However, in practice, this time-lapse is very small and the model can be reasonably used to describe heterogeneous condensation (Heidenreich and Ebert, 1995), but it fails in the resolution of induction time of heterogeneous nucleation process. It is worth noticing that the models for nucleation and growth rates are strongly dependent on the assumptions that particles are spherical and that the gas is a continuous medium ( $K \ll 1$ ). These two assumptions allow a “geometric” view of the particle embryo system (Fletcher, 1958; Smorodin and Hopke, 2004) that fail to describe the actual physics of a nanometric, non spherical, rough, inhomogeneous “real particle” particle.

Also S. K. Friedlander and J. H. Seinfeld (S. K. Friedlander, 1977, J. H. Seinfeld, 1986) propose a similar expression for the calculation of saturation directly above a particle

$$P_{v,a} = P^\circ(T) a_i \exp\left(\frac{4\sigma_p v_i}{R_G T d}\right) \quad (1.117)$$

Where  $a_i$  is the activity of the particle species  $i$  in the particle,  $v_i$  is the partial molar volume of  $i$  in the particle  $\sigma_p$  is particle surface tension,  $R_G$  is the gas universal constant and  $T$  is the temperature. The traditional Köhler theory describes the saturation ratio of water vapor over a solution droplet of diameter  $d$  to depend on water activity ( $a_i$ ) and droplet curvature (Kelvin effect)

In the k- Köhler model  $a_i$  is given by

$$a_i = \frac{1}{1+k\frac{V_s}{V_w}} \quad (1.118)$$

where  $k$  is the effective hygroscopicity parameter or Raoult parameter, respectively (Petters and Kreidenweis, 2007; Mikhailov et al., 2009; Pöschl et al., 2009).  $V_s$  is the volume of dry particulate matter ( $V_s=4/3\pi r_s^3$ , with  $r_s$  the radius of the particles), and  $V_w$  is the volume of water in the aqueous particle/droplet ( $V_w=4/3\pi r_w^3$ , with  $r_w$  the radius of the wet fraction) Characteristic values of  $k$  are 0 for completely insoluble particles, 0.6 for  $(\text{NH}_4)_2\text{SO}_4$  and 1.28 for NaCl (Petters and Kreidenweis, 2007; Rose et al., 2008a). The hygroscopicity parameters of biomass burning aerosols range from 0.01 for freshly emitted smoke containing mostly soot particles to 0.55 for aerosol from grass burning, and the average value of  $k$  in polluted continental air is  $0.3\pm 0.1$  (Andreae and Rosenfeld, 2008; Rose et al., 2008b; Pöschl et al., 2009).

Köhler theory is an equilibrium theory neglecting the droplet growth kinetics. Furthermore, it is valid for soluble compounds, such as inorganic salts, but not for compounds with very low or zero solubility. For such compounds R. Sorjamaa and A. Laaksonen , (2007) suggest that adsorption is the phenomenon that causes particle to growth therefore, by substituting the  $a_i$  with that obtained from e.g. the FHH (Frenkel, Halsey and Hill) adsorption isotherm, the equilibrium saturation ratio for a solution droplet is obtained from :

$$P_{v,a} = P^\circ(T) \exp\left(\frac{4\sigma_p v_i}{R_G T d}\right) \exp(-A\Theta^{-B}) \quad (1.119)$$

Where  $\Theta$  is surface coverage  $\Theta = (D - D_{dry})/(2D_w)$ . The parameter A characterizes interactions between adsorbed molecules and between the surface and adjacent adsorbate molecules (i.e. those in the first monolayer). B characterizes the attraction between the solid surface and the adsorbate in subsequent layers.

Furthermore, the nucleation model and the same thermodynamics model of the heterogeneous condensations require the knowledge of surface tensions of the embryo–particle systems Eqs.(11),(22),(28). The problem is even more complicated if we consider any residual electrical charges, the presence of various functional groups, or soluble species, on the particles surface that can interact synergistically with the condensed vapor phase.

Considering the interactions of the solid phase with the gaseous and the liquid phase at nanoscale such as the interactions between these phases inside the porous and cracks present on the particles surface, one must consider some phenomenon such as the capillary condensation, and the forces of adhesion, resulting in the formation of liquids menisci and liquid bridges that can change the activation behavior of the particle by the water vapor. Furthermore the formation of such liquid structures on particles surface enhance the formation of particles aggregates at undersaturation conditions.

All these aspects affect the value and the critical saturation, that is a function of temperature and vapor concentration but also it his expected to be a complex function of the actual shape of the particle, its chemical nature, surface homogeneity and morphology.

## **CHAPTER 2**

### ***Experimental facility for condensational growth studies***

The studies concerning homogeneous and heterogeneous nucleation processes reported in the literature have been carried out on different types of systems. In this chapter the experimental facility used, for the characterization of condensational growth process, is presented in detail. The first part of the chapter describes the experimental configurations for the study of nucleation process, in order to identify the most useful configuration for the aim of this thesis. The choice of optimal configuration has been made taking into account some constraints considered during the design of the chamber, such as modulation and control of parameters controlling the process, spatially resolve the different phases of the process and optical accessibility. The experimental configuration that can meet these requirements is the laminar flow diffusion chamber.

The second part of the chapter describes in detail the core of experimental apparatus i.e. the condensation chamber, its characteristics and feeding configuration. Furthermore the auxiliary devices, for the generation of vapour gas mixture and for the dispersion of aerosol were described.

#### ***2.1 Experimental configurations for the study of nucleation process***

The studies concerning homogeneous and heterogeneous nucleation processes reported in the literature have been carried out on different types of systems. They can be divided into two main categories (expansion chamber or thermal diffusion chamber) based on the way in which the vapor gas mixture reaches the supersaturation conditions.

Figure 2.1 shows the different typologies of experimental facilities used for the study of the nucleation in relation to the ranges of nucleation rate that each configuration allow to study (Iland K. et al., 2004).

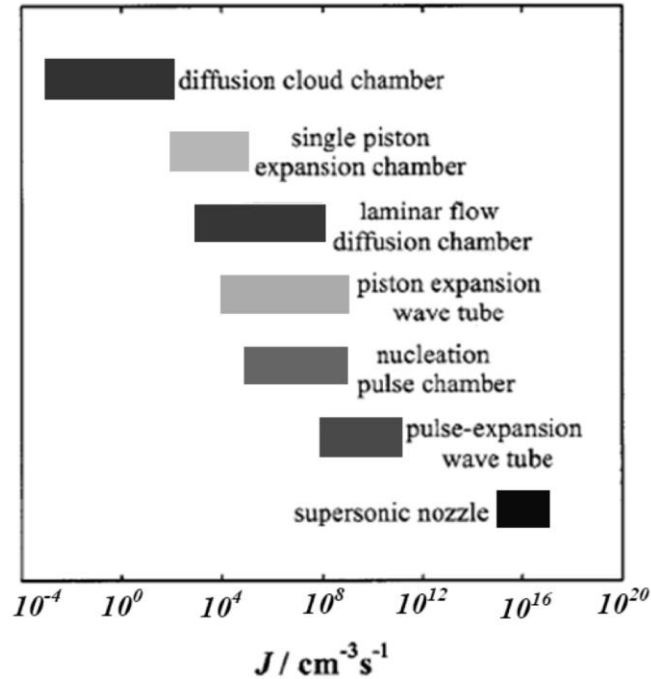


Figure 2.1: Different experimental facilities for homogeneous nucleation rate studies and their respective ranges of nucleation rates  $J$ .

There are several types of expansion cloud chambers, but they all rely rapid, adiabatic expansions to produce the desired degree of supersaturation and subsequent nucleation. Essentially, an expansion cloud chamber can be visualized as a cylinder/piston-like structure containing the vapour of interest and a background gas in the region above a cylinder and bounded by the piston walls. Initially, vapour/gas mixture is at the temperature of the piston walls and may or may not be saturated. Following an expansion, caused by the rapid withdrawal of the piston, the pressure of the vapour/gas mixture decreases somewhat while the temperature (away from the walls of the cylinder) decreases significantly due to adiabatic cooling. During this period (sensitive time), the vapour is supersaturated and the nucleation can occur. Normally shortly after the adiabatic expansion is complete a small recompression

pulse is issued to stop further nucleation and allow for growth of nucleated clusters. The length of sensitive time is of the order of milliseconds. Expansion cloud chambers are capable of generating large supersaturation. These chambers are not self-cleaning, and they require repeated expansion to cleanse the vapour/gas mixture of heterogeneous nucleation sites. The temperature and supersaturation conditions in the chamber are determined by using the thermodynamic relations for adiabatic cooling and often assuming ideal gas behaviour.

A rapid expansion can be achieved by means of two main configurations, i.e. shock tube and supersonic nozzles. Essentially, the shock tube consists of two sections, the driver and the driven sections, separated by a diaphragm. When the diaphragm is ruptured (as rapidly as possible), the higher pressure gas in the driver section sets up a nearly one dimensional, unsteady flow and a shock wave traveling to the driven section. At same time an expansion wave travels back into the driver section followed by an expansion fan that sets the gas initially at rest in the driver section in motion toward the driven section. The subsequent cooling of the rapidly expanding gas in the driver section is what is commonly used for nucleation studies. The supersonic nozzles rely upon adiabatic expansion of a vapour/gas mixture flowing through a converging/diverging or converging/straight nozzle. The vapour/gas mixture is first prepared and stored in a supply tank. One or more plenum chamber are often used to insure proper mixing, temperature and pressure conditions of the vapour/gas mixture prior to flow through the nozzle. The vapour/gas mixture flow is undersaturated prior to and slightly after entering the nozzle region. As the flow continues into the nozzle, the flow becomes saturated and then supersaturated. Nucleation of embryos followed by condensational growth occurs as the flow passes out of the throat region of the nozzle. As condensational growth occurs, the latent heat of condensation makes the local pressure raise. Pressure sensor records this pressure increase and allow for detection of the location of condensation onset. The onset of nucleation is usually associated with the onset of pressure

pulse, and if the latent heat of condensation is known and the pressure is measured carefully, an estimate of the amount of condensed phase can be made. Typical cooling rates associated with supersonic nozzle are quite large (1-10 K/ $\mu$ s) and nucleation rate are also large.

The thermal diffusion cloud chamber can be operated in either an upward or a downward mode. It consists of two parallel metal plates of cylindrical geometry separated by an optically transparent cylindrical ring. The region between the two plates, bounded by the inside of the transparent ring, forms the working region of the chamber. The working fluid is introduced as a shallow pool on the lower plate in the upward mode (as a moist pad or porous plate on the upper plate in the downward mode) and the chamber is filled with a stagnant, background gas. The lower (upper) plate is heated and the upper (lower) is cooled for the upward (downward) mode of operation. Imposing a temperature difference between the two plates results in temperature, mole fraction, and supersaturation profiles between the two plates. These profiles are obtained by solution of the appropriate mass and energy balance equations subject to an appropriate equation of state for the vapour/background gas mixture. The diffusion cloud chamber is a steady state, self-cleaning device. When the temperature difference between the two plates and the total pressure are such that the supersaturation in the chamber is sufficiently large, nucleated droplets are observed to form in the upper (lower) portion of the chamber for the upward (downward) mode of operation. Onset of nucleation and nucleation rates measurement can be made by light scattering techniques and particle counting methods.

The systems in which the condensation takes place by a temperature variation at constant pressure are less complex both in the management both in the interpretation of data that can provide. Such systems are efficient in the case of low nucleation rate.

The Laminar Flow Diffusion Chamber has generally used for homogeneous nucleation studies. During steady state operation, a heated, inert carrier gas flows is mixed with the condensable vapour of interest. This flowing vapour/gas mixture is often referred as core (or

main flow). The core is enveloped by a cooler flow of dry gas, often referred as confinement flow. This coaxial flow of the core and surrounding gas then enters in the chamber, where the mixing between the two streams takes place. The wall of the chamber is maintained at the confinement flow temperature. The ensuing energy and mass transfer from the core to the confinement region results in supersaturation and nucleation. If the core contains particles, heterogeneous nucleation is observed. The inert gas flow, externally fed to the mainstream prevents the diffusion of the droplets and particles toward the chamber walls, while simultaneously controlling the main-stream cooling. Detection of nucleation is done optically. Such systems can operate in a wide range of temperature and pressure thus assuring an high degree of versatility from the operational point of view.

- **Condensation chamber configuration**

The evaluation of the characteristics of the different typology of condensation chambers has led to the identification of most useful configuration for the aim of this thesis. In particular, the constraints considered during the design of the chamber have been:

- modulation and control of parameters controlling the process independently of each other (temperature, vapor concentration, flow velocity, particle concentration and typology)
- spatially resolve in the system regions in which the different phases of the process occur (nucleation, growth of the particles kinetically controlled and / or by diffusion, aging), in order to identify the characteristic times of the different sub-processes;
- optical accessibility in order to implement laser diagnostic technique that allow for in situ spatially and temporally resolved measurements
- flexibility with respect to plant modifications

From this point of view a configuration where the condensing stream pass trough the chamber in laminar conditions appears the most suitable flow conditions for the analysis of the

heterogeneous nucleation process. Thus a bi-dimensional axial-symmetric configuration has been chosen as reference configuration. It is possible to work with relatively low flow rate, consistent with the temporal resolution to be achieved in the characterization of the nucleation process. It is, however, necessary to appropriately assess the working conditions with respect to the carrier gas used. In fact, it is necessary that the Lewis number relative to the mixture flowing through the system is close to unity in such a way the process takes place in the entire section, and not on portions of it. The sizing of the chamber has been carried out assuming that the process takes place under conditions of pressure close to or slightly higher than atmospheric.

For the design of the system it was necessary to perform an evaluation of the characteristic times of the individual sub-processes that take place in series-parallel in the process of condensation of the vapour phase and as these times are influenced by both the operating parameters, such as temperature and pressure.

The Diffusion Laminar flow Chamber can meet these requirements. Such equipment is composed by a system where the cooling flow and saturation of the vapor gas mixture takes place or by the mixing between the feed streams to the chamber or by means of the local conditions of heat and mass transport. The chamber is also equipped with some auxiliary devices described in the following paragraphs.

The dimensions of the chamber have been chosen taking into account its critical points.

In particular was chosen a characteristic dimension of the chamber five times higher than that of the diameter of the injection tube of the main flow in order to avoid the diffusion and the formation of condensation on the walls. In addition, the chamber presents a square cross-section, to eliminate possible problems related to the curvature of the wall to the applicability of the various optical diagnostic techniques. The head of the chamber has 372 diffusers that guarantee a uniform distribution of the confinement gas flow.

- Project design

Through a series of fluid-dynamic simulations made using Fluent software it was possible to perform the design of the chamber used for the study of the particles growth process. Figure 2.2 shows the 3D-mesh used for the fluid-dynamic simulation and the qualitative velocity field on the axial plane of the chamber as well as the distribution of vapour concentration.

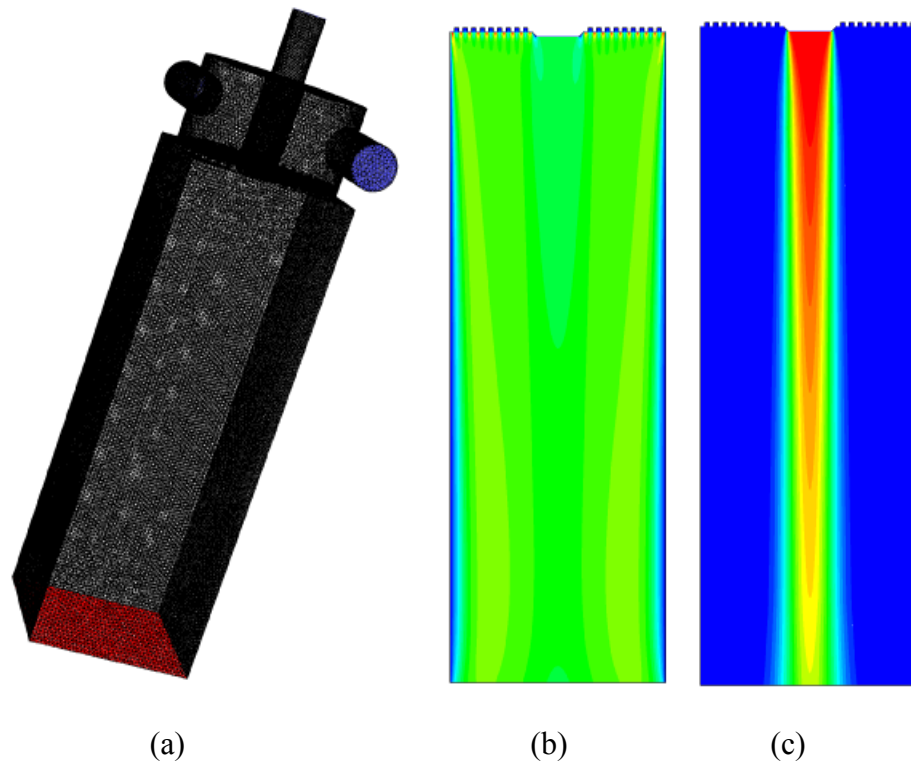
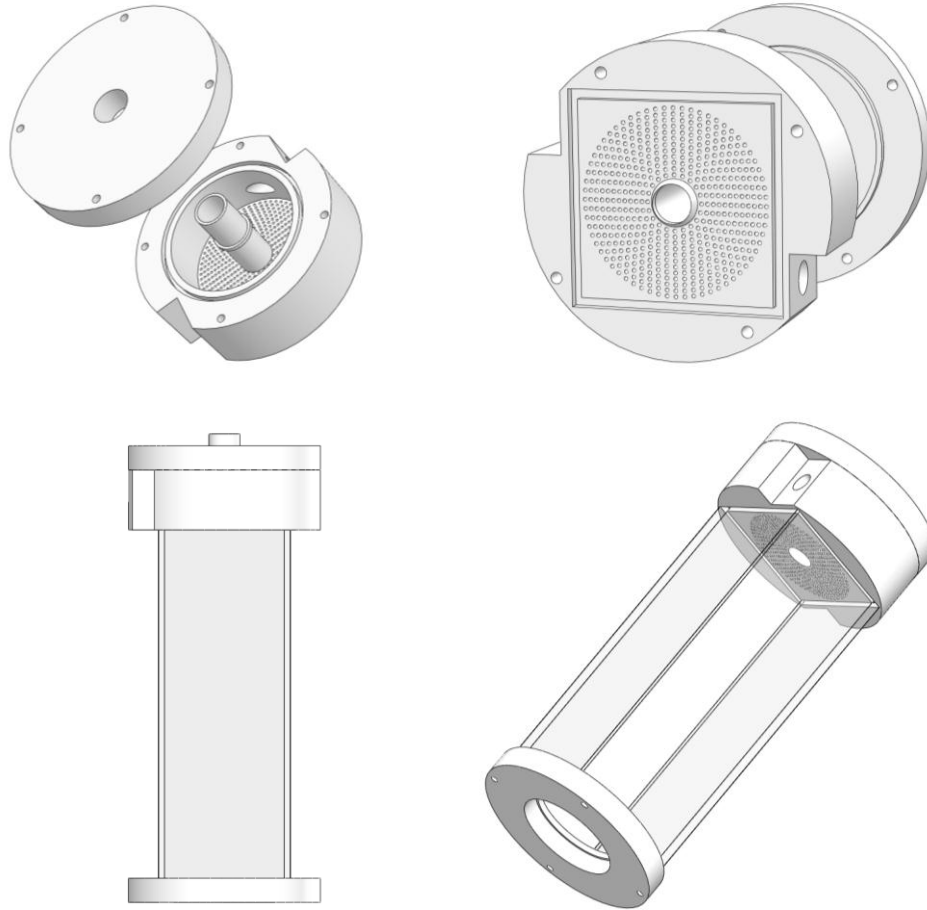


Figure 2.2 : (a) 3D mesh, (b) velocity field (c) vapor concentration

The project design is performed by a 3D cad software (SolidWork) Figure 2.3 shows a complete view of the chamber, and a detail of the upper part in which are installed the supply lines of the vapor and carrier gas containing the particles and the confinement flow.



*Figure 2.3: Overview of laminar diffusion chamber*

The main part of chamber are made in PTFE, while the chamber wall are in glass in order to make it optical accessible.

- Feeding Configuration

Experimental results have been obtained for four vapor inlet concentration  $X_v$  (0, 0.10, 0.25 and 0.35). Thus,  $X_v = 0$  corresponds to the case where only graphite (or iron or nickel) particles and carrier are fed to the flow chamber. By increasing the vapor concentration from 0 to 0.35, the percentage of the carrier gas has been changed in such way that the fluid-dynamic conditions are equivalent in all the condition considered. For each vapor concentration three inlet temperatures ( $T_{in} = 375K, 405K, 425K$ ) have been considered at a fixed confinement flow temperature  $T_c = 298K$ . The working conditions of particle generator have been chosen in such a way that a monodispersed particle distribution with the maximum

at 150nm (10nm C only) and with a number concentration of about  $2 \cdot 10^7$  #/cm<sup>3</sup> ( $6 \cdot 10^7$  ,  $1 \cdot 10^8$  #/cm<sup>3</sup> C only) has been fed to the flow chamber. The axial temperature profiles were measured by means a J-type thermocouple varying step by step the height of measurement.

Figure 2.4 shows the feeding configuration of laminar flow chamber

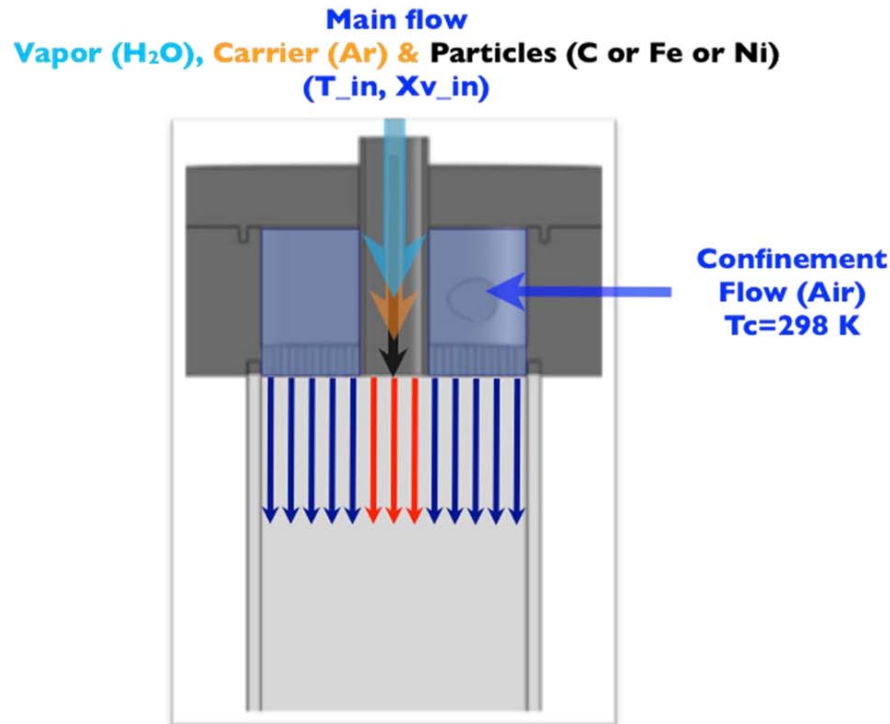


Figure 2.4: Supply configuration of laminar flow chamber

The chamber ends with a system for the collection of the gaseous flow, which is first analyzed, and then sent into suction hood. The outlet section of the chamber has been carefully designed. A first version of this part of chamber presented a sudden constriction in proximity outflow section ( $H=0.1$  m;  $D_{out}=0.01$ m) that induced disturbs on the fluid-dynamic field in the area of the chamber immediately above the outlet section. To work around these problems it was necessary to redesign the outlet section of the chamber. For the second configuration has been chosen a converging section and an characteristic size of outlet section six time greater with the respect to previous one ( $H=0.3$  m;  $D_{out}=0.06$ m).

## 2.2 Experimental lay-out

A general scheme of the experimental set-up is shown in Fig. 2.5 a 10 cm square cross section laminar flow chamber was used for the experimental tests. A carrier gas, steam and/or particles from a spark generator system (PALAS GFG1000) are axially fed into the chamber with a 2 cm injection tube. An inert gas flow is fed externally to the mainstream to prevent the diffusion of the droplets and particles toward the chamber walls, while simultaneously controlling the main-stream cooling.

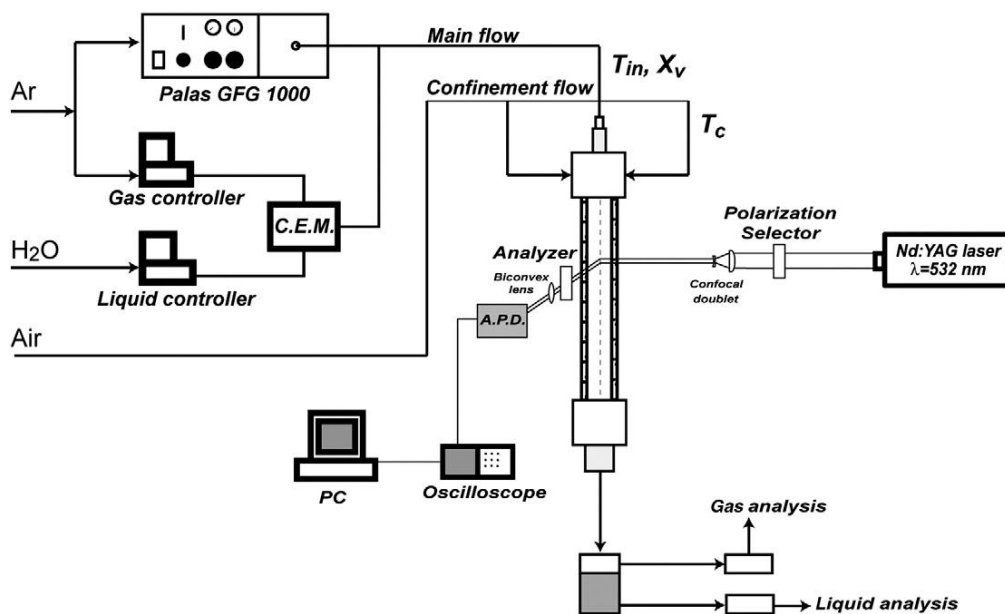


Figure 2.5: General scheme of the experimental set-up

In Figure 2.6 is shown an overall view of the experimental set-up where the main components of the system are highlighted along with the optical diagnostic apparatus which will be described in detail in next chapter.

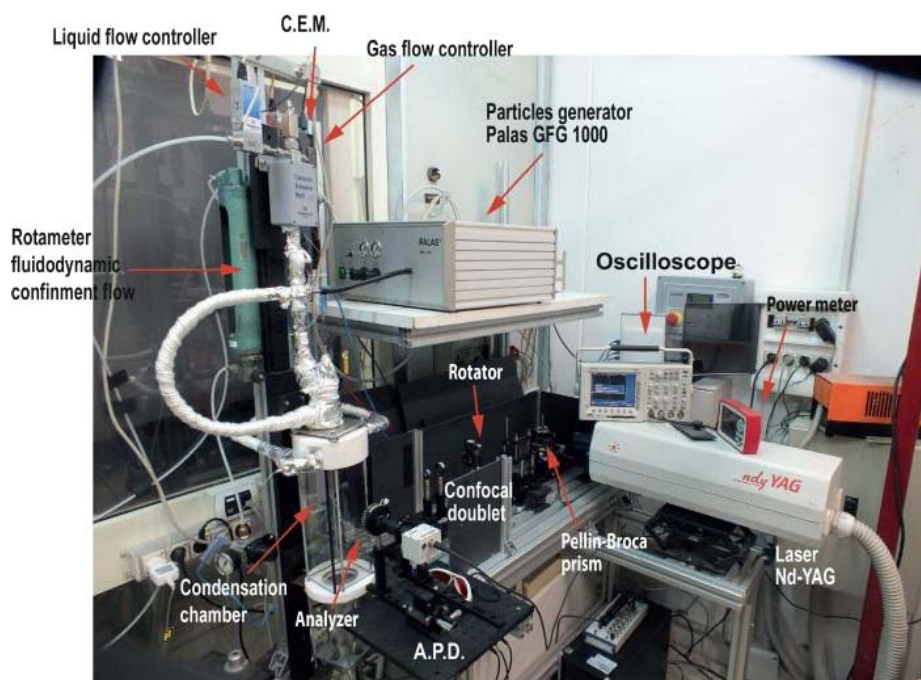


Figure 2.6: Overall view of the experimental apparatus

- **Laminar flow chamber**
- **Controlled Evaporator Mixer**

The steam is fed by means of an evaporator providing a controlled steam flow (Bronkhost C.E.M.). This device consists of three main components:

- a gas flow regulator (0.1 to 10 l / min- Ar);
- a liquid flow meter (1-100 g / h- H<sub>2</sub>O);
- a mixing valve of the two streams,

This system assures an accurately controlled gas/liquid mixture, fast response, high reproducibility, very stable vapour flow and a flexible selection of gas/liquid ratio, thereby it is possible to obtain a gas-steam mixture at a fixed temperature and concentration. Fig. 2.7 shows the connection scheme of controlled mixer evaporator

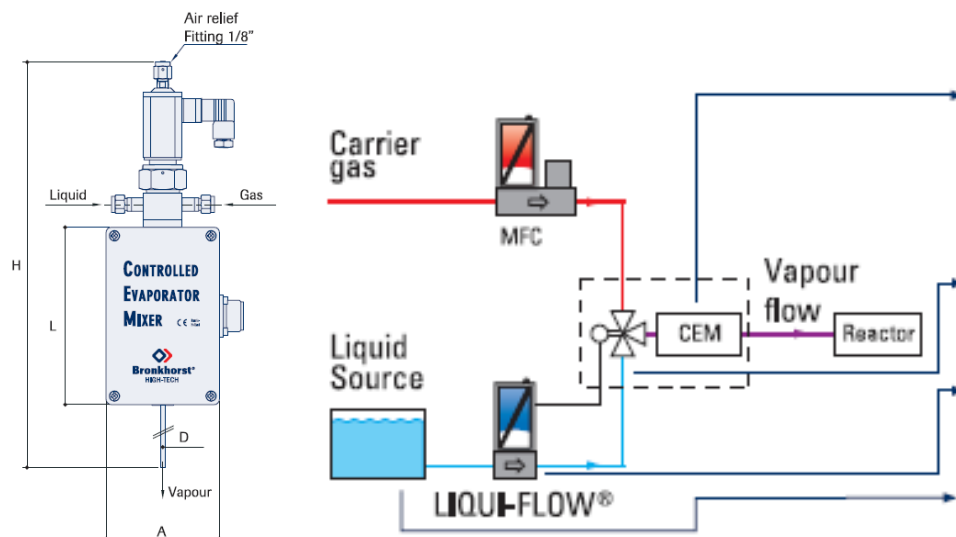


Figure 2.7: Scheme of the controlled mixer evaporator

The evaporator is controlled remotely through a PC by means of software developed using the application - object Labview. A remotely controlled heating system prevents the condensation of the steam along the feeding line and also allows to control the temperature of both streams (main and confinement flow) fed to the chamber. A J-type thermocouple placed in proximity of the outflow section of the main flow and one placed on the feeding line of confinement flow monitors the temperatures of working fluids. The automation of the plant management was a necessary step in order to regulate the flow rates needed, and the exact relationship between these and working temperatures and vapour concentration. The chamber is optically accessible in order to allow the implementation of different optical diagnostics techniques depending on the size of particles and or drops that must be detected.

- **Particulate dispersion System**

To analyze the evolution of heterogeneous nucleation process, it is necessary feed to the system submicronic particles. The manipulation of these substances is quite complex because of their particular characteristics. In this work the choice of particulate dispersion system for the study of the heterogeneous nucleation process must also satisfy requirements of

versatility, with respect to the nature of the particulate, production efficiency, reproducibility and provide an appropriate particle size distribution and concentration. With the development of nanotechnology a considerable number of techniques for the synthesis and / or the dispersion of submicron particles, extensively described in the literature have been developed. After thorough market research and comparison of individual parameters, the equipment that best meets the requirements is Palas GmbH Aerosol Generator GFG 1000, which provides for the generation of particles by means of vaporization of two electrodes between which is applied a suitable potential difference.

The generator produces pure carbon (metal, metal oxide) particles by spark discharge. Figure 2.8 show the mechanical set up of the generator. Two graphite electrodes of 6-mm diameter are mounted in brass collets. The flat ends of the electrodes are positionate at a distance of about 2mm in the middle of a plastic chamber. An argon stream is focussed through a narrow slit into the space between the electrodes.

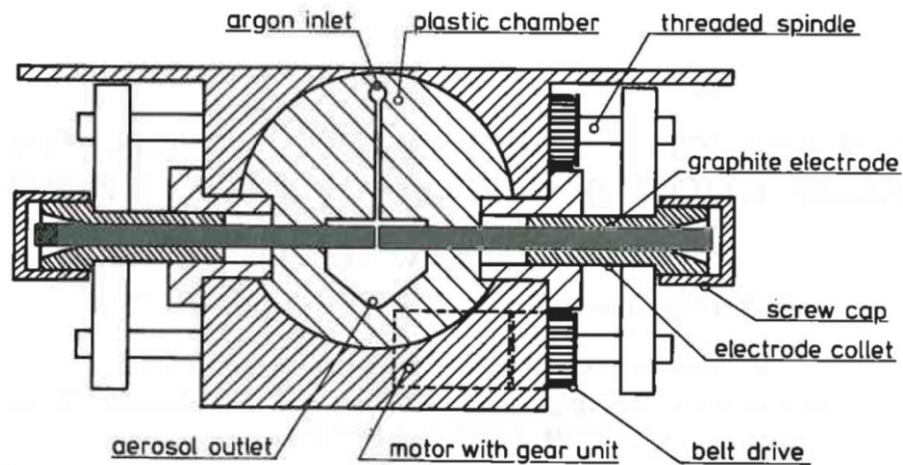


Figure 2.8: Mechanical arrangement of the spark aerosol generator (Helsper C. et al., 1993)

The distance between the electrodes can be varied automatically by means of a small electric motor that drives two threaded spindles connected to the electrode collets. The aerosol outlet is positioned about 15 mm downstream of the electrodes. The aerosol can be diluted at this point by air, which is mixed with the argon in a concentric annular nozzle. The electric supply

and control circuit is shown schematically in Fig. 2.9. A high-voltage capacitor with a capacitance of 20 nF connected to one of the electrode is charged by a high-voltage supply with adjustable output current. The breakdown voltage is monitored using a voltage divider and rectifier network. A d.c.-voltage proportional to the breakdown voltage is compared with a reference voltage and kept constant by adjusting the electrode distance. A constant energy release (40 mJ) in each spark is achieved. The repetition frequency of the sparks is controlled by adjusting the output current of the HV-supply. Current between 0.13 and 20 mA correspond to spark frequencies between 0 and 300 s<sup>-1</sup> (E. Evans, et al., 2004). An optimized flow geometry makes sure that all ions created in one spark are removed from the space between the electrodes before the onset of the next spark. This results in a constant breakdown voltage over the entire range of operation.

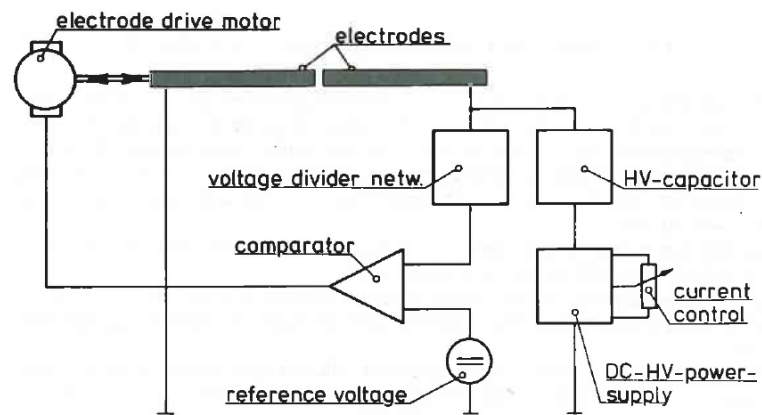


Figure 2.9: Electrical supply and control circuit of the carbon aerosol generator

The documentation provided by Palas GmbH, as well as the articles available in the literature demonstrate that, such device is the most versatile.

Two parameters can be adjusted to optimize particle production, namely the spark discharge frequency and the carrier gas flow rate. The spark discharge frequency,  $f$ , is determined by the charging current,  $I$ , of the capacitor which has a capacitance,  $C$ , and the discharge voltage,  $V_d$ ,

(S. Schwyn, et al., 1988) by  $f = \frac{I}{CV_d}$

It should be noted that the discharge voltage is not exactly equal to the breakdown voltage,  $V_b$ , but slightly higher since some time is required for the discharge conditions to develop (N. S. Tabrizi, et al. 2009). An additional overvoltage,  $V_o$ , is therefore introduced to balance the discharge and breakdown voltages:  $V_d = V_b + V_o$ . Increasing the spark discharge frequency results in an increase in the particle number concentration and a shift towards larger particle diameters (M. E. Messing et al., 2009), which is in good agreement with other reports on particles produced by spark discharge.

By adjusting these two parameters it is thus possible to choose the optimum operating condition for the purposes of the study should be conducted. The higher the spark discharge frequency, the greater the increase in the number of particles produced per second, since more electrode material is evaporated per second. The increase in evaporated particle material also leads to a higher coagulation rate, and hence faster growth of the particles, resulting in particles with larger diameters. The local temperature of the spark is high (R. Reinmann and M. Akram, 1997), resulting in evaporation of electrode material. Primary particles are formed by homogeneous nucleation of this supersaturated vapor, and coalesce into larger particles. The carrier flow rate can be adjusted between 2 and 8 l/min in order to obtain a reproducible and constant rate of particle generation. The flow rate must be high enough to remove all primary particles and ions between the electrodes before the next spark. Increasing the carrier flow rate from 3.4 to 5.9 l/min resulted in a slight decrease in particle number concentration, but had no effect on particle diameter. However, specific carrier flow rates combined with specific spark discharge frequencies resulted in more stable particle production.

Figure 2.10a shows the curves of the size distribution of the particles produced, parametric in the frequency. Figure 2.10b shows the distribution curves obtained varying the dilution of the system at a predetermined operating frequency, relating to such equipment. The two diagrams

show that, although the distribution curves show a size range relatively extended, they are single-mode and dependent on the regulation parameters of the system such as the spark frequency and dilution of the output current from the system. (Helsper C. et al., 1993)

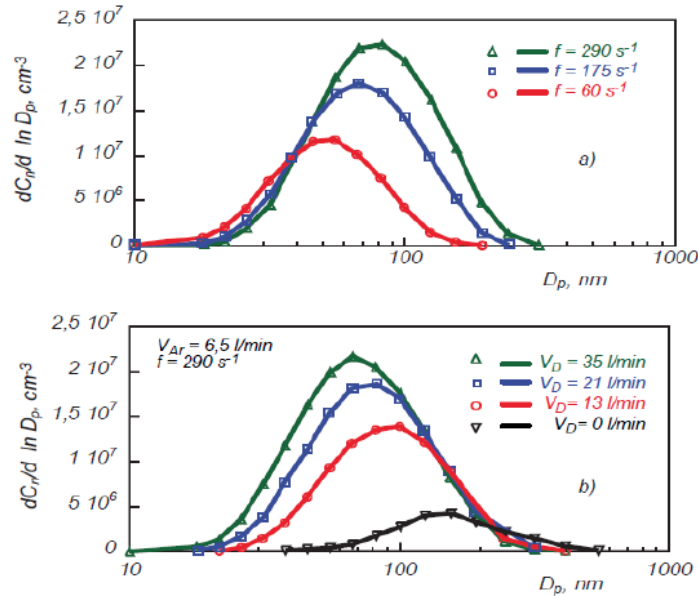


Figure 2.10 (a) Particle number distribution of the carbon aerosol for different spark repetition frequencies. Argon flow rate, (b) particle number distribution of the carbon aerosol for different dilution air flow rate (Helsper C. et al., 1993)

The spark aerosol generator produces particles with a structure similar to the soot particles produced by combustion systems.

To analyze the effect of particle nature on heterogeneous nucleation activation process, particles of different chemical nature can be produced by using different rods material.

Metals and metal oxides particles, which may be of particular interest for this scope can be produced by such equipment. For this purpose electrodes of the desired chemical nature must be replaced to the electrodes of graphite.

Metallic aerosols were produced by replacing the graphite electrodes within the Palas GFG 1000 aerosol generator with those of pure metals (99,999 %). The metals were purchased in pure rod form with diameters in excess of the 6.35mm required. The rods were then machined to their final diameter and cut to a length of 98 mm. In this work were used electrodes of iron

and nickel, in addition to graphite rod shown in Figure 2.11 together with that of graphite.

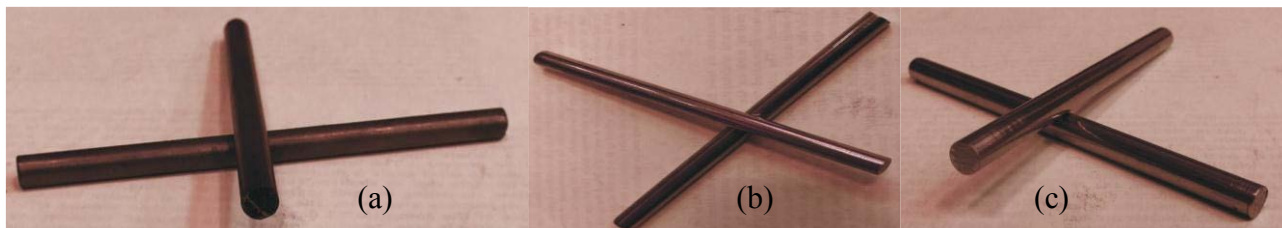


*Figure 2.11: (a) Graphite rods, (b) Iron rods, (c) Nickel rods*

These electrodes can be individually positioned within brass collets and then inserted in the aerosol production chamber of the spark generator, as shown in Figure 2.12.

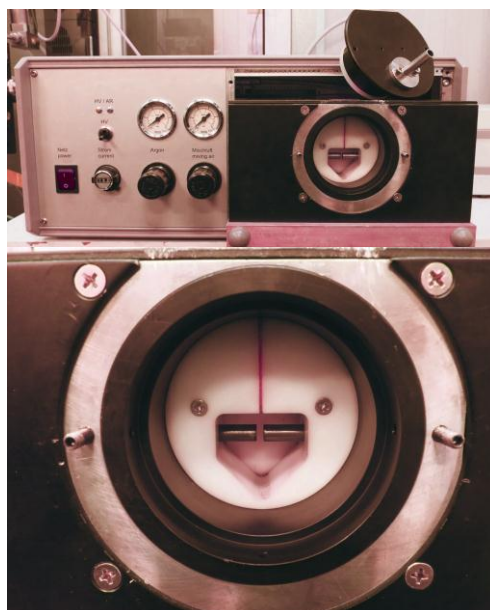


*Figure 2.12: Aerosol production chamber*

In this way it is possible to obtain graphite, iron, nickel, and mixed material particles. A mixed aerosol could therefore be produced by inserting two electrodes of differing composition into the GFG 1000 aerosol generator. The chemical physic characteristics of the selected species used, are summarized in Table 2.1 and refer to literature data.

Specie	density Kg/m <sup>3</sup>	Thermal conductivity W/m K	Electrical conductivity ( $\Omega\text{m}$ ) <sup>-1</sup>	T <sub>melting</sub> K	T <sub>boiling</sub> K
Graphite (C)	2200	129	500 $\perp$ 3 $10^6$ $\parallel$	3773	5100
Iron	7847	80.2	$9.96 \cdot 10^6$	1808	3273
Nickel	8908	90.2	$14.3 \cdot 10^6$	1728	3186

Table 2.1. Chemical –physical properties of selected rods for particulate production

The density, melting and boiling temperatures, electrical and thermal conductivity influence the production efficiency of aerosols, thus for each type of material the optimum operation conditions of the particles generator, which guarantee size distributions and number concentration comparable for the different types of particles considered, have to be found. The most efficient aerosol formation from spark discharge appeared to broadly result from the least thermally and electrically conductive material (i.e., graphitic carbon), with diminishing efficiency observed with increases in both of these physical properties for the other materials studied. Iron and Nickel have similar physical chemical properties so the respective aerosol production efficiency is very similar.

## **CHAPTER 3**

### ***Diagnostics and diagnostic set-up***

The choice of diagnostic methods to be used for fundamental studies in experimental facilities has to guarantee an exhaustive evaluation of parameters to be analyzed. In present work the main requirement that the diagnostics tools have to satisfy is the need of the carrying on in situ measurements with a significant spatial resolution while limiting as much as possible the perturbation of the control volume. The nucleation of droplets on submicronic particles and their growth are very sensitive to the local parameters and are characterized by very low characteristic time. In this perspective, laser based optical diagnostic techniques can satisfy such requirements with high level of reliability. A general schematization of laser-based optical diagnostic scheme is reported in Figure 3.1. A laser beam of a proper wavelength passes through the system to be studied. The scattered light is collected from an optical detection system placed at a fixed angle with respect to the incident beam. The dimension of the control volume is identified by the intersection of laser beam and the axis of the optical detection system.

The typology of both the light source and the detection system strongly depend on the characteristic of the specific laser-based diagnostic technique considered. Elastic light scattering technique has been used in this work due to its high sensitivity in multi phase systems for the characterization of number and dimension of physical discontinuity.

In this chapter the basic theory of elastic light scattering has been described with particular regards to the tools used to carry out the experimental measurements and their interpretation.

In this framework, evaluation of quantities useful to follow the dimension increase of condensed phase in relation to its properties has been reported. In addition, the characteristics of the diagnostic set-up have been described in detail.

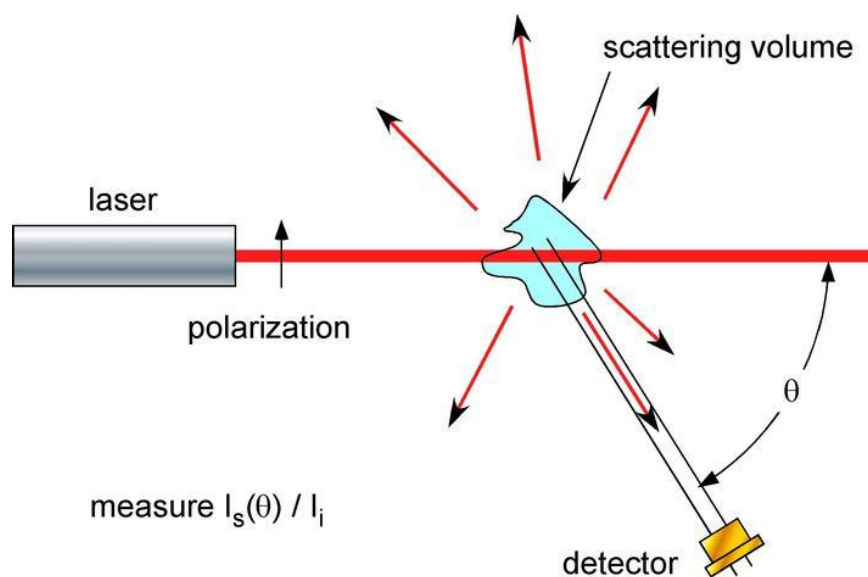


Figure 3.1: Schematization of laser-based optical diagnostics apparatus

### 3.1 Laser Light Scattering

The light scattering is a technique for the characterization of morphological and dimensional wide variety of macromolecules and particles. It allows for the determination of the molar mass and particle size. The physical principle is the diffusion of the incident light by the particles that absorb energy and re-emit in all directions. The manner in which the scattering occurs depends mainly on the ratio between the linear dimensions of the particles and the wavelength of the incident radiation.

The scattering of light may be thought of as the redirection of light that takes place when an electromagnetic (EM) wave (i.e. an incident light ray) encounters an obstacle or non-homogeneity, for example the scattering particle. As the EM wave interacts with the discrete particle, the electron orbits within the particle's constituent molecules are perturbed periodically with the same frequency ( $\nu_0$ ) as the electric field of the incident wave. The oscillation or perturbation of the electron cloud results in a periodic separation of charge within the molecule, which is called an induced dipole moment. The oscillating induced dipole moment is manifest as a source of EM radiation, thereby resulting in scattered light as

shows in Fig. 3.2. The majority of light scattered by the particle is emitted at the identical frequency ( $\nu_0$ ) of the incident light, a process referred to as elastic scattering. In summary, the above comments describe the process of light scattering as a complex interaction between the incident EM wave and the molecular/atomic structure of the scattering object; hence light scattering is not simply a matter of incident photons or EM waves “bouncing” off the surface of an encountered object.

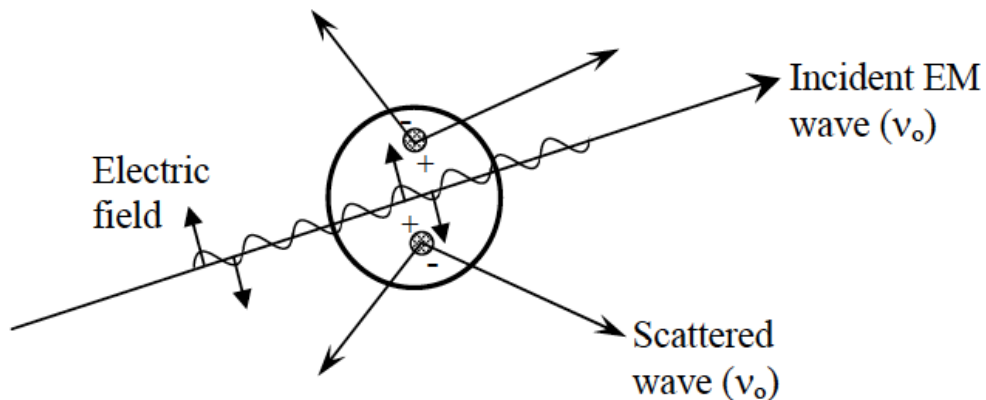


Figure 3.2: Light scattering by an induced dipole moment due to an incident EM wave.

Formal light scattering theory may be categorized in terms of two theoretical frameworks. One is the theory of Rayleigh scattering that is, strictly speaking as originally formulated, applicable to small, dielectric (non-absorbing), spherical particles. The second is the theory of Mie scattering that encompasses the general spherical scattering solution (absorbing or non-absorbing) without a particular bound on particle size. Accordingly, Mie scattering theory has no size limitations and converges to the limit of geometric optics for large particles. Mie theory, therefore, may be used for describing most spherical particle scattering systems, including Rayleigh scattering. However, Rayleigh scattering theory is generally preferred if applicable, due to the complexity of the Mie scattering formulation. The criteria for Rayleigh scattering is that  $\alpha \ll 1$  and  $|m| \alpha \ll 1$ , where  $\alpha$  is the dimensionless size parameter given by the expression

$$\alpha = \frac{2\pi a}{\lambda} \quad (3.1)$$

where  $a$  is the spherical particle radius, and  $\lambda$  is the relative scattering wavelength defined as

$$\lambda = \frac{\lambda_0}{m_0} \quad (3.2)$$

where  $\lambda_0$  is the incident wavelength with respect to vacuum, and  $m_0$  represents the refractive index of the surrounding medium. Finally,  $m$  is the refractive index of the scattering particle, and is commonly represented by the complex notation defined as

$$m = n - ik \quad (3.3)$$

In this notation,  $n$  indicates the refraction of light (i.e.  $n$  equals the speed of light in vacuum divided by the speed of light in the material), while the complex term is related to absorption.

The commonly used absorption coefficient of the material ( $\text{cm}^{-1}$ ) is related to the complex part of the refractive index via the relation absorption coefficient

$$\text{Absorption} = \frac{4\pi k}{\lambda} \quad (3.4)$$

It is noted that the value of  $k$  is never exactly zero for any material, but materials with a value approaching zero are termed dielectrics. The magnitude of the refractive index,  $m$ , as needed for the Rayleigh criteria, is given by the expression

$$|m| = (n^2 + k^2)^{1/2} \quad (3.5)$$

The Rayleigh criteria as related above,  $\alpha \ll 1$ , correspond physically to the assumptions that

the particle is sufficiently small such that the particle encounters a uniform electric field at any moment, accordingly the time for penetration of the electric field is much less than the period of oscillation of the EM wave.

Figure 3.3 shows the spherical coordinate scattering geometry used for Mie and Rayleigh light scattering corresponding to a single incident light ray on a single spherical particle. Using this coordinate system, the scattering parameters may be defined for the Rayleigh and Mie solutions.

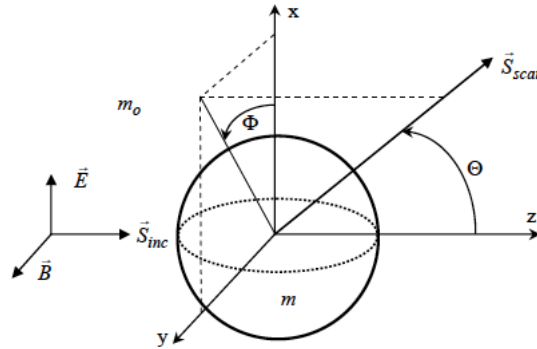


Figure 3.3: Coordinate geometry for Rayleigh and Mie scattering.

For each scattering angle  $(\phi, \theta)$ , the Equations (6) and (7) represent the intensities (W/cm<sup>2</sup>) of scattered radiation vertically and horizontally polarized with respect to the scattering plane, respectively, which is defined by the incident ray (of intensity  $I_0$ ) and the scattered ray, noting the polarization state of the incident ray as shown in Figure 3.3

$$I_{\phi} = I_0 \frac{\lambda^2}{4\pi^2 r^2} i_1 \sin^2 \phi \quad (3.6)$$

$$I_{\theta} = I_0 \frac{\lambda^2}{4\pi^2 r^2} i_2 \cos^2 \phi \quad (3.7)$$

$r$  is the distance from the scatterer.

For perfectly spherical particles, polarized incident radiation produces similarly polarized scattered radiation; hence the scattering problem may be redefined in terms of the polarization states with respect to the scattering plane. Accordingly, equations (6) and (7) may be recast in terms of the differential scattering cross sections ( $\text{cm}^2/\text{sr}$ ), namely

$$I_{\mathbf{VV}} = I_0 \frac{1}{r^2} \sigma_{\mathbf{VV}} \quad (3.8)$$

$$I_{\mathbf{HH}} = I_0 \frac{1}{r^2} \sigma_{\mathbf{HH}} \quad (3.9)$$

In these two equations, the subscripts refer to the state of polarization of the incident and scattered light, respectively, with orientation defined by the scattering plane. Specifically, the subscripts  $\mathbf{VV}$  refer to both vertically polarized incident light and vertically polarized scattered light with respect to the scattering plane (i.e.  $\phi = 90^\circ$ ). Similarly, the subscripts  $\mathbf{HH}$  refer to both horizontally polarized incident light and horizontally polarized scattered light with respect to the scattering plane (i.e.  $\phi = 0^\circ$ ). For unpolarized incident light, the scattering is given by the following

$$I_{\mathbf{scat}} = I_0 \frac{1}{r^2} \sigma_{\mathbf{scat}} \quad (3.10)$$

where  $\sigma_{\mathbf{scat}}$  is the average of  $\sigma_{\mathbf{VV}}$  and  $\sigma_{\mathbf{HH}}$ , and noting there is no dependence on  $\phi$ . Finally, it is noted that the dependency of the above quantities on the scattering angle  $\theta$  is through the differential cross sections, as detailed below. Equations 8-10 provide an expression for the intensity of light about a single scattered ray. These equations may also be reconsidered in terms of the rate of scattered energy into a defined solid angle, as shown in Figure 3.4

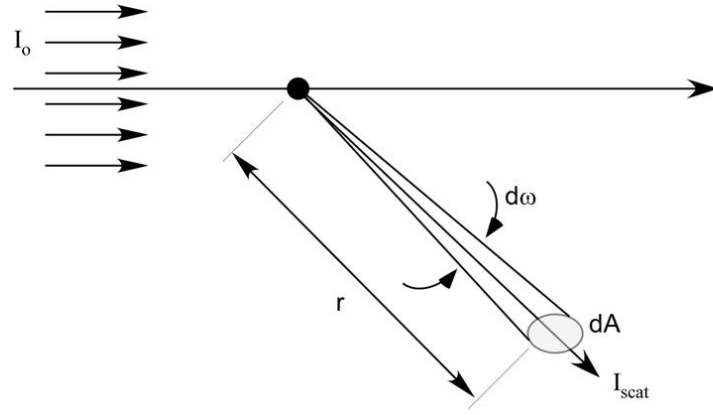


Figure 3.4: Angular scattering intensity.

Using the differential scattering cross section, the total scattered energy rate (W) striking  $dA$  is

$$E_{scat}^{\dot{}} = I_0 \dot{\sigma}_{scat} d\overline{\omega} \quad (3.11)$$

where the solid angle  $d\omega$  is related to the subtended area by  $d\omega = dA/r^2$ . The units of equation (11) are readily apparent. Substitution of  $dA/r^2$  for the solid angle and division of both sides by

$dA$  yields equation (10); hence the scattered intensity about the scattered ray  $I_{scat}$ .

While the above equations account for the redistribution of incident radiation due to light scattering, incident radiation may also be absorbed by the particle. The rate of the total amount of incident energy abstracted from the incident beam due to interactions with a single particle is calculated directly from the extinction cross section ( $\text{cm}^2$ ),

$$E_{removed}^{\dot{}} = I_0 \dot{\sigma}_{ext} \quad (3.12)$$

The extinction cross section represents loss of energy from the incident beam due to both scattering and absorption; hence the extinction cross section may be expressed as

$$\sigma_{ext} = \sigma_{abs} + \sigma_{scat} \quad (3.13)$$

where  $\sigma_{abs}$  and  $\sigma_{scat}$  are the absorption and total scattering cross sections ( $\text{cm}^2$ ), respectively.

The latter quantity is calculated by integrating the differential cross section over  $4\pi$

steradians. While the above equations allow calculation of the relevant scattering and extinction quantities based on the incident light intensity, it now falls to the Rayleigh and Mie theories to provide the appropriate expressions for calculation of the various cross-sections expressed above.

### 3.1.1 Rayleigh Theory

In the Rayleigh regime, the differential scattering cross sections can be readily calculated from

the following equations:

$$\sigma_{VV} = \frac{\lambda^2}{4\pi^2} \alpha^6 \left| \frac{m^2-1}{m^2+2} \right|^2 \quad (3.14)$$

$$\sigma_{HH} = \sigma_{VV} \cos^2 \theta \quad (3.15)$$

Examination of equations (14) and (15) reveals several interesting items. Functionally, the differential scattering cross sections are proportional to the 6<sup>th</sup> power of particle size, and are inversely proportional to the 4<sup>th</sup> power of wavelength (Bahcall, J. N., 1964). This latter dependency gives rise to the blue color of our sky, as the air molecules (e.g. N<sub>2</sub> and O<sub>2</sub>) are well within the Rayleigh regime; hence the shorter blue light of the sun is more efficiently redirected out of the direct path of sunlight and subsequently redirected from all directions as scattered light. In addition, note that the vertical differential scattering cross section is independent of the observation angle  $\theta$ , while the horizontal-horizontal differential scattering cross section has a minimum at 90°. This implies that unpolarized light will be strongly polarized at 90° observation for Rayleigh particles. The total scattering cross section (cm<sup>2</sup>) and

absorption cross section (cm<sup>2</sup>) are defined as

$$\sigma_{scat} = \frac{2\lambda^2}{3\pi} \alpha^6 \left| \frac{m^2-1}{m^2+2} \right|^2 \quad (3.16)$$

$$\sigma_{abs} = \frac{-\lambda^2}{\pi} \alpha^3 \text{Im} \left\{ \frac{m^2-1}{m^2+2} \right\} \quad (3.17)$$

Finally, the total extinction cross section (cm<sup>2</sup>) is defined as a sum of the scattering and absorption cross sections, namely,

$$\sigma_{ext} = \sigma_{sca} + \sigma_{abs} \quad (3.18)$$

As represented in equations (16) and (17), the scattering cross section scales with  $\alpha^6$ , while the absorption cross section is proportional to  $\alpha^3$ . In the Rayleigh regime, the size parameter must be much less than unity, therefore the contribution of scattering (i.e.  $\sigma_{sca}$ ) to the total extinction cross section is generally neglected for an absorbing particle ( $k \neq 0$ ), and it is therefore assumed that  $\sigma_{ext} = \sigma_{abs}$ . However, for a dielectric particle ( $k = 0$ ), then  $\sigma_{ext} = \sigma_{scat}$ , as the contribution of absorption is identically zero ( $\sigma_{abs} = 0$ ).

### 3.1.2 Mie Theory

Based on the theory of Mie, the differential scattering cross sections are defined in terms of the angular intensity functions  $i_1$  and  $i_2$ , as given by the expressions

$$\sigma_{VV} = \frac{\lambda^2}{4\pi^2} i_1 \quad (3.19)$$

$$\sigma_{HH} = \frac{\lambda^2}{4\pi^2} i_2 \quad (3.20)$$

As before, the above two equations are averaged to define the differential scattering cross section

for unpolarized incident light, which gives the relation

$$\sigma_{scat} = \frac{\lambda^2}{8\pi^2} (i_1 + i_2) \quad (3.21)$$

In this formulation, the intensity functions are calculated from the infinite series given by

$$i_1 = \left| \sum_{n=1}^{\infty} \frac{2n+1}{n(n+1)} [a_n \pi_n(\cos\theta) + b_n \tau_n(\cos\theta)] \right|^2 \quad (3.22)$$

$$i_2 = \left| \sum_{n=1}^{\infty} \frac{2n+1}{n(n+1)} [a_n \tau_n(\cos\theta) + b_n \pi_n(\cos\theta)] \right|^2 \quad (3.23)$$

In the equations (22) and (23), the angular dependent functions  $\pi_n$  and  $\tau_n$  are expressed in terms of the Legendre polynomials by

$$\pi_n(\cos\theta) = \frac{P_n^{(1)}(\cos\theta)}{\sin\theta} \quad (3.24)$$

$$\tau_n(\cos\theta) = \frac{P_n^{(1)}(\cos\theta)}{d\theta} \quad (3.25)$$

where the parameters  $\mathbf{a}_n$  and  $\mathbf{b}_n$  are defined as

$$a_n = \frac{\psi_n(\alpha)\psi_n'(m\alpha) - m\psi_n(m\alpha)\psi_n'(\alpha)}{\xi(\alpha)\psi_n'(m\alpha) - m\psi_n(m\alpha)\xi'(\alpha)} \quad (3.26)$$

$$b_n = \frac{m\psi_n(\alpha)\psi_n'(m\alpha) - \psi_n(m\alpha)\psi_n'(\alpha)}{m\xi(\alpha)\psi_n'(m\alpha) - \psi_n(m\alpha)\xi'_n(\alpha)} \quad (3.27)$$

The size parameter  $\alpha$  is defined using Equations (1) and (2) as

$$\alpha = \frac{2\pi a m_0}{\lambda_0} \quad (3.28)$$

The Riccati-Bessel functions  $\Psi$  and  $\xi$  are defined in terms of the half-integer-order Bessel

function of the first kind ( $J_{n+1/2}(z)$ ), where

$$\psi_n(z) = \left(\frac{\pi z}{2}\right)^{1/2} J_{n+1/2}(z) \quad (3.29)$$

Equation (30) describes the parameter  $\xi_n$

$$\xi_n(z) = \left(\frac{\pi z}{2}\right)^{1/2} H_{n+1/2}(z) = \psi_n(z) + iX_n(z) \quad (3.30)$$

where  $H_{n+1/2}(z)$  is the half-integer-order Hankel function of the second kind, where the parameter

$X_n$  is defined in terms of the half-integer-order Bessel function of the second kind,  $Y_{n+1/2}(z)$ , namely

$$X_n(z) = -\left(\frac{\pi z}{2}\right)^{1/2} Y_{n+1/2}(z) \quad (3.31)$$

Finally, the total extinction and scattering cross sections are expressed as

$$\sigma_{ext} = \frac{\lambda^2}{2\pi} \sum_{n=0}^{\infty} (2n+1) \text{Re}\{a_n + b_n\} \quad (3.32)$$

$$\sigma_{scat} = \frac{\lambda^2}{2\pi} \sum_{n=0}^{\infty} (2n+1) (|a_n|^2 + |b_n|^2) \quad (3.33)$$

noting that the absorption cross section is readily calculated from the above two.

### 3.1.3 Polarization ratio

The experimental polarization ratio is the ratio of the intensities of the horizontally to vertically polarized scattered light and was obtained with a selector and an analyzer appropriately oriented, in both the incident and scattered beams. There was no depolarization by the aerosol in the sense that when these polarizator were crossed there was complete extinction. The reproducibility of successive polarization ratio determinations on the same

aerosol was such that the average deviation was about 1 to 2 %. The solid angle subtended by the photometer receiver (photomultiplier tube) was sufficiently small so that no appreciable error would be encountered from this factor. Light-scattering intensity functions  $I_i(\theta, \alpha, m)$  and  $I_j(\theta, \alpha, m)$  which are functions of particle index of refraction  $m$ , angle of observation  $\theta$ , and the quantity  $\alpha = 2\pi a/\lambda$  where  $a$  is the particle radius and  $\lambda$  is the wavelength of the light in the medium. These functions are proportional, respectively, to the intensity of the vertically and horizontally polarized components of the scattered light (E. MATIJEVMI et al., 1960). If the aerosol is characterized by a size distribution  $P_a da$  which is the fraction of particles with values of  $r$  between  $r$  and  $a+da$ , then the polarization ratio is given by:

$$\gamma = \frac{\int I_{HH}(\theta, \alpha, m) p_a da}{\int I_{VV}(\theta, \alpha, m) p_a da} \quad (3.34)$$

It can therefore calculate the ratio of polarization, for an average size of particle, as follows:

$$\gamma = \frac{I_{HH}}{I_{VV}} \quad (3.35)$$

where

$$I_{VV} = NC_{VV} = \frac{\pi^4}{4\lambda^4} \left| \frac{m^2-1}{m^2+2} \right|^2 N d_{scat}^6 ; I_{HH} = NC_{HH} \quad (3.36)$$

- $C_{VV}$  : scattering cross section of vertically polarized light
- $C_{HH} = C_{VV}(1 + \cos^2(\theta))$  : scattering cross section of horizontally polarized light
- $m=n-ik$ : complex refractive index
- $d_{scat}$  : scattereres' diameter

The polarization ratio is independent from the number of scatterers present in the measurement volume, it gives information on the average diameter of the particles.

### 3.2 Scattering by a composite sphere with an absorbing inclusion

By varying the particles nature present in the control volume it results in a different response of the system due to the different solicitations induced by laser illumination with regard to the intensities of the signals relating to elastic scattering of light.

In the present work the materials considered for the particle production have a different refraction index, as shown in Table 3.1 where has been included also the refractive index of water, used as a condensing substance for the particles capture.

Specie	Refractive index
C	$1.56 + i 0.56$
Ni	$1.88 + i 3.5$
Fe	$2.9 + i 2.92$
H <sub>2</sub> O*	$1.33 + i 0$

Table 3.1: Refractive index of selected material used for particles production  
([www.Luxpop.it](http://www.Luxpop.it))

For these value of refraction indices, the components  $I_{VV}$  and  $I_{HH}$  of elastically scattered light were calculated by varying the diameter of the particle for an incident radiation equal to that used in the experimental tests (532nm) and with an angle of view equal to 5 steradians. In

particular a calculation program derived from the one proposed by Bohren and Huffmann (Bohren, C.F. and Huffman, D.R., “, 2007): has been used for this evaluation.

From the calculation  $I_{VV}$  and  $I_{HH}$  is thus then possible to evaluate the polarization ratio of the different material as  $\gamma = I_{HH} / I_{VV}$ .

Figure 3.5 shows the trend of  $I_{VV}$ ,  $I_{HH}$  and  $\gamma$  for graphite particles. It is possible to see that  $I_{VV}$  and  $I_{HH}$  decrease by increasing  $D$  from 10 nm up to 50 nm, keeping constant their ratio (particle diameter), as shown by  $\gamma$  value which has a constant value with diameter up to  $D=100$  nm. For higher value of the diameter both light intensities and  $\gamma$  sharply increase up to  $D=400$  nm. Then  $\gamma$  oscillates between values of about 0.1 and 1 up to  $D=2 \mu\text{m}$  after that it reaches an almost constant value for whole range of dimensions considered.

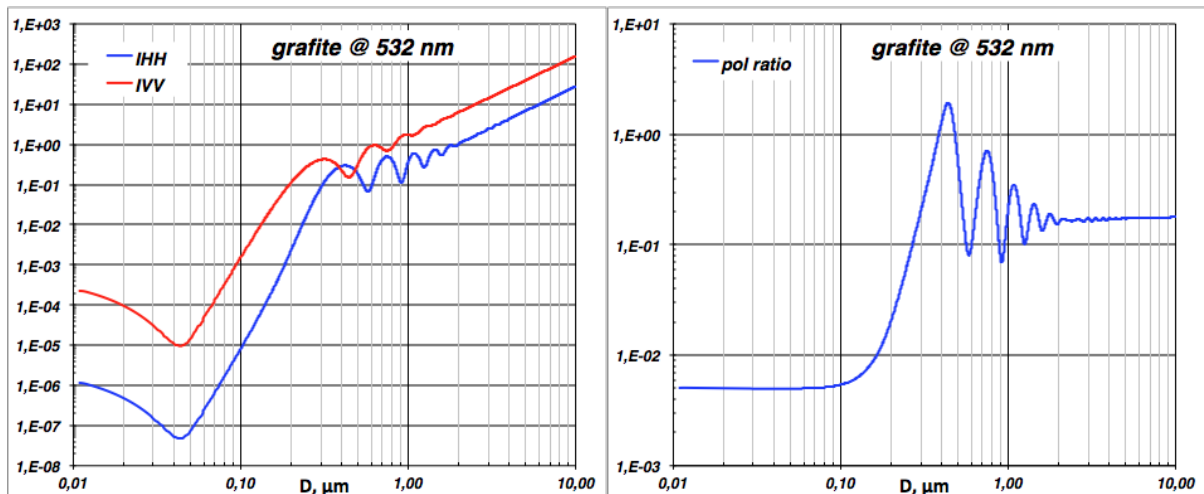


Figure 3.5:  $I_{VV}$  ed  $I_{HH}$  (left side) and  $\gamma = I_{HH}/I_{VV}$  (right side) evaluated for graphite particles

The trend of  $I_{VV}$  and  $I_{HH}$  and  $\gamma$  evaluated for water droplets have a similar trend with the respect of graphite particles, even if their absolute values are different, as shown in figure 3.6.

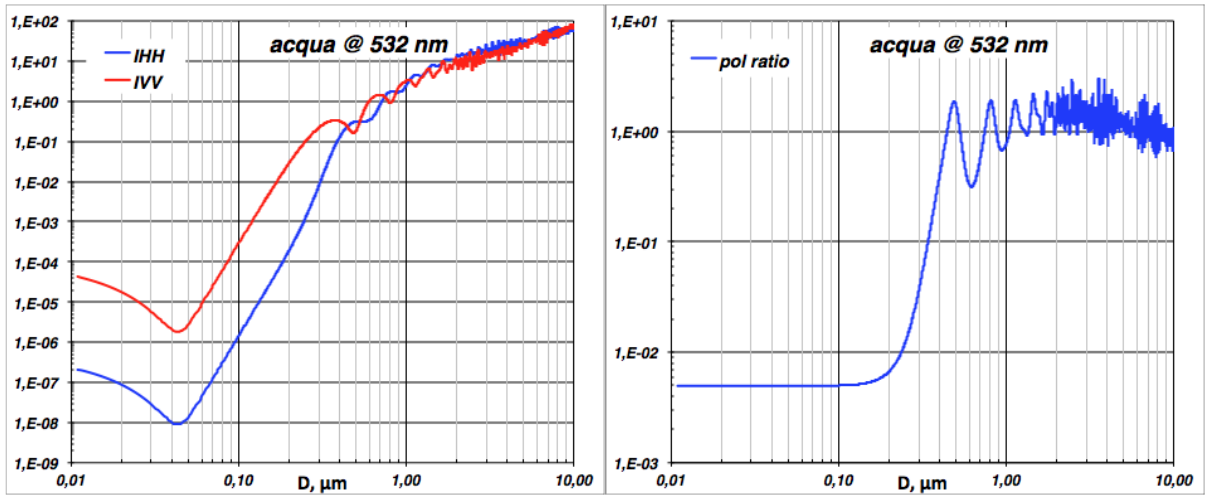


Figure 3.6:  $I_{VV}$  ed  $I_{HH}$  (left side) and  $\gamma = I_{HH}/I_{VV}$  (right side) evaluated for water droplets

Different considerations must be made for iron and nickel particles. For such particles the decrease of  $I_{HH}$  in the range of diameter from 10nm up to 100nm is greater than the decrease of  $I_{VV}$  component. This is reflected in a decrease of polarization ratio for diameters up to about 30nm. This decrease is followed by a rapid increase for  $D$  greater than 30nm. This behavior is highlighted by the diagrams in Figure 3.7 and Figure 3.8.

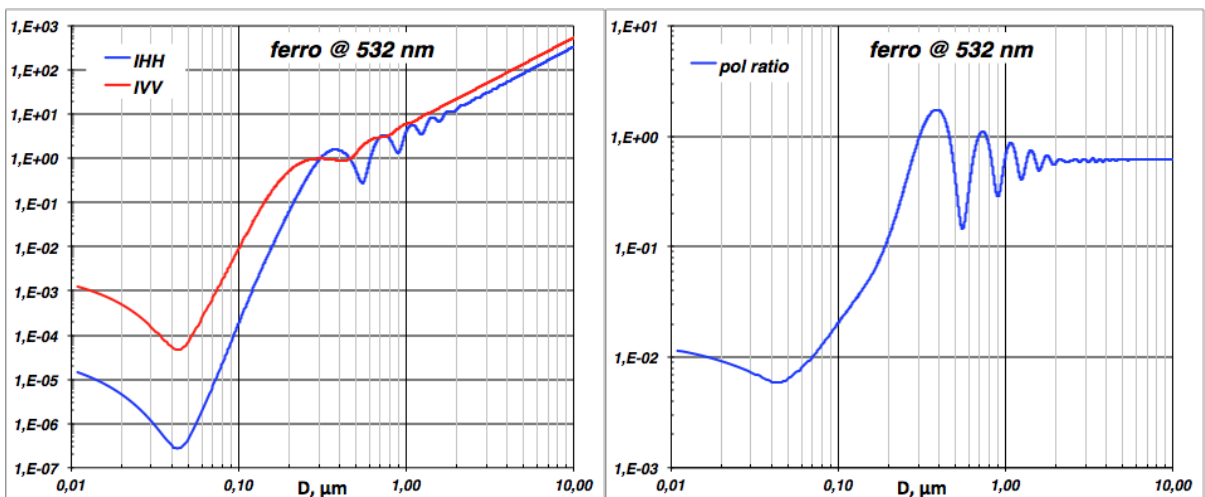


Figure 3.7:  $I_{VV}$  ed  $I_{HH}$  (left side) and  $\gamma = I_{HH}/I_{VV}$  (right side) evaluated for iron particles

Furthermore, the variation of the polarization ratio between  $D = 300\text{nm}$  and  $2\mu\text{m}$  occurs in a range of narrower values of  $\gamma$ . It then reaches a constant value equal to approximately 0.6 and

0.7 for iron and nickel, respectively, higher than that achieved in the case of graphite particles, that are equal to about 0.2.

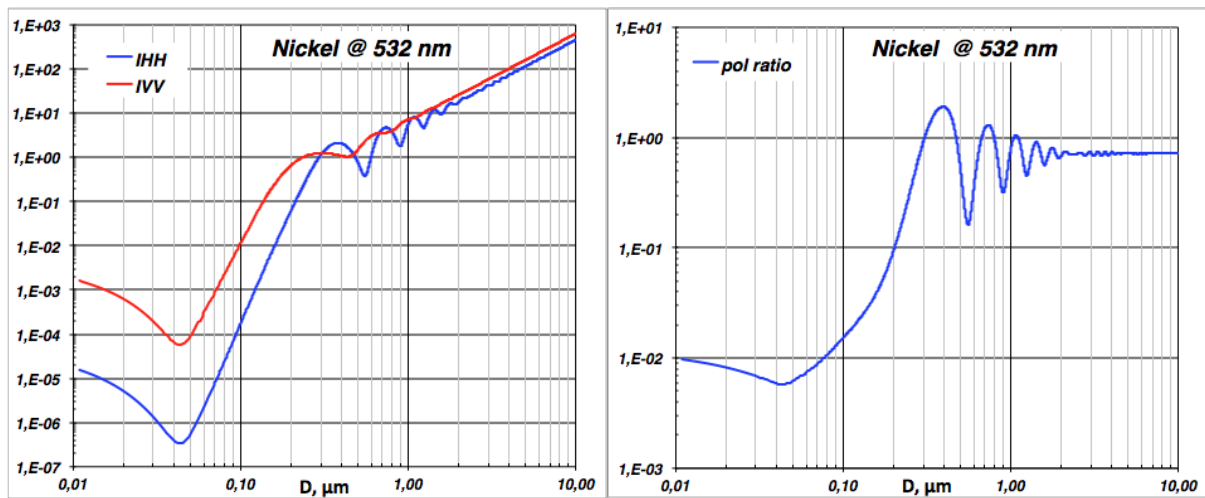


Figure 3.8:  $I_{VV}$  ed  $I_{HH}$  (left side) and  $\gamma = I_{HH}/I_{VV}$  (right side) evaluated for nickel particles

As just shown an estimation of size evolution of particle is possible by the evaluation of the polarization ratio. This is a complex function, which depends on the particle size and on its optical properties. This dependence becomes more complicated if the particle involved in the growth process, varies its size because of a water layer deposition, due to vapor condensation, on its surface. In this case the optical properties of the particle will vary depending on the relative size (i.e. relative volume) between the particle and the covering liquid layer and on the optical properties of particle and the coating material. A model for the estimation of refractive index of a liquid sphere, which presents an absorbent inclusion (composite sphere) is required for evaluation of the optical properties of this inhomogeneous scatterer and for the evaluation of the polarization ratio of such system. Only by the knowledge of the optical properties of an absorbent solid particle covered by a liquid layer, it is possible to estimate its final size, by the evaluation of the polarization ratio. Furthermore, in such a way, it is possible to compare the final dimensions reached by water coated particles.

Knowledge of the scattering and absorption of electromagnetic radiation by heterogeneous particles is important in remote sensing and radiation transfer of planetary atmospheres whose

constituent particles may contain cloud droplets formed on condensation nuclei, scavenged aerosols, melting snowflakes, and hailstones. For these and many other applications, an exact solution of the electromagnetic boundary conditions is impossible to find, not only because of the sheer number of different particle geometries and compositions which the electromagnetic field encounters, but also because the geometries and compositions of the particles are largely unknown. For this reason, statistical and approximation methods have been developed (Chy'lek P. al., 1988). One method of calculating the scattering properties of heterogeneous particles is to find an equivalent homogeneous particle of the same geometry composed of an effective medium and calculate its scattering properties.

This methodology has been around since the turn of the century. Depending on the type of particle system and the scattering properties of interest, different prescriptions for finding an equivalent homogeneous particle have been derived. In using these methods, it should keep in mind that an equivalent homogeneous particle, which can be used to predict all the scattering properties of a heterogeneous system, does not exist. As for any approximation method, it is relatively easy to trivialize or even discredit effective medium approximations by considering cases for which the methods were not derived. Much of the recent research has focused on providing estimates on the accuracy of effective medium approximations. It will be examined a specific scattering properties of a common atmospheric particle, a water droplet containing a carbon nucleation site (adsorbing inclusion). The occurrence of carbon in cloud droplets is of interest as an absorber of atmospheric radiation and as a possible contributor to the cloud absorption anomaly. Whereas the effect of aerosols on radiation and climate is a decrease in the global temperatures, the presence of black carbon in the atmosphere serves to increase the absorption of solar radiation and decreases the reflection albedo ( R.J. Charlson, et al., 1992., J.T. Kiehl, and B.P. Briegleb, 1993). The extended effective medium approximation developed by Chy'lek and Srivastava (P. Chy'lek, and V. Srivastava, 1983) is based on the extension of the Bruggeman (D.A.G. Bruggeman, 1935) effective medium

approximation developed by Stroud and Pan (D. Stroud, and F.P. Pan, 1978.). Whereas Stroud and Pan kept the electric and magnetic dipole terms in their partial wave expansion, Chy'lek and Srivastava retained all the terms in their expansions. Comparisons of effective medium results with those obtained using dipole superposition methods suggest that the extended effective medium approximation of Chy'lek and Srivastava can be used for inclusion sizes larger than the wavelength when calculating extinction (J.M. Perrin and P.L. Lamy, *Astrophys. J.*, 1990). Ossenkopf also noted that the accuracy increases with increasing inclusion absorbance (V. Ossenkopf, 1991). The accuracy of effective medium approximations in predicting the absorption efficiencies has previously been explored for a spherical water host containing a spherical highly absorbing inclusion, since it is carbon's absorbing properties that are of primary interest for atmospheric science applications (G. Videen et al., 1995. P. Chy'lek and G. Videen, 1998). Effective medium results were compared with the absorption calculated by solving the boundary conditions exactly from a spherical host containing a spherical carbon inclusion averaged over all inclusion locations. The basic goal of extended effective medium approximations is to extend the validity of effective medium approximations to cases where the grain sizes are no longer small compared to the wavelength. Such an effective medium is constructed by setting the forward-scattering amplitude of all particle constituents in the effective medium equal to zero:  $S(0)=0$ . Stroud and Pan extended Bruggeman's results, by including the magnetic dipole terms in the partial wave expansions (D. Stroud and F.P. Pan, 1978). Their results can be summarized as follows. The effective refractive index  $m_{\text{eff}}$  of a composite medium is obtained by an iterative solution of the equation:

$$(m_{\text{eff}}^2)_{k+1} = m_2^2 \frac{A_k(1-f) + fB_k}{A_k(1-f) - 2fB_k} \quad (3.37)$$

where

$$A_k = -\frac{12i\pi^2 m_{eff}^3}{\lambda^3} \quad (3.38)$$

and

$$B_k = \frac{3}{4\pi r^3} \sum_n (2n+1) [a_n(r, m_1/m_{eff}) + b_n(r, m_1/m_{eff})] \quad (3.39)$$

where  $m_1$ ,  $r$ , and  $f$  are the refractive index, radius and volume ratio of the inclusions, and  $a(r, m_n)$  and  $b(r, m_n)$  are the Mie scattering coefficients of a radius  $r$ , refractive index  $m$  sphere, and a time dependence of  $\exp(-i\omega t)$  is assumed. Furthermore in following are proposed other numerical methods for the evaluation of composite sphere refraction index.

Bruggeman approximation, whose effective refractive index can be obtained by solving the following equation:

$$(1-f) \frac{m_1^2 - m_{eff}^2}{m_1^2 + 2m_{eff}^2} + f \frac{m_2^2 - m_{eff}^2}{m_2^2 + 2m_{eff}^2} = 0 \quad (3.40)$$

Another method to calculate the composite sphere refractive index is obtained using the Maxwell-Garnett approximation, whose effective refractive index is given by

$$m_{eff}^2 = m_1^2 \frac{m_2^2 + 2m_1^2 + 2f(m_2^2 - m_1^2)}{m_2^2 + 2m_1^2 - f(m_2^2 - m_1^2)} \quad (3.41)$$

by comparing the effective-medium results with those obtained using an exact solution to Maxwell's equations obtained by solving the boundary conditions on the two spherical surfaces (J.G. Fikioris and N.K. Uzunoglu, 1979, F. Borghese et al., 1992, K.A. Fuller, 1995, N.C. Skaropoulos et al., 1994, G. Videen et al., 1995). Since the scattered field of the individual composite sphere depends on the position of the inclusion within the host sphere, it is calculated the average scattering properties as the position of the inclusion is varied

throughout the host sphere.

First it is examined the gross scattering results. The model calculations show good agreement with all effective-medium calculations up to an inclusion volume ratio of  $10e-3$ , corresponding to an inclusion radius of  $r/R=10$ . At this point the effective medium calculations begin to diverge. The Bruggeman and Maxwell-Garnett mixing rules show slightly better agreement with the model calculations of extinction and absorption for inclusion radii around  $r/R=0.2$ , but as the inclusion size is further increased, the extended effective medium approximation shows better agreement. The agreement of the Bruggeman and Maxwell-Garnett results with the model results for extinction is due in part to a cancellation of errors: these mixing rules tend to overestimate the absorption cross section and underestimate the scattering section. The extended effective medium approximation shows excellent agreement with the scattering efficiencies regardless of the inclusion size.

The differential scattering cross sections contain the angular distribution of scattering intensities. For small size inclusions  $r < 0.5$ , there is very little difference between the differential cross sections predicted using the different effective medium approximations and the model calculations. As the inclusion size approaches that of the wavelength inside the host sphere, differences become apparent. As the inclusion size is further increased, greater divergence is seen in the effective medium results. This shift in the differential cross sections is the result of an increase in the real part of the refractive index of the composite sphere, which favors higher order modes in the sphere. Table 3.2 shows the real parts of the refractive index calculated using the different effective medium approximations. As the inclusion size increases, both the Bruggeman and Maxwell-Garnett show a much greater change in the refractive index of the composite sphere than the extended effective medium approximation. Physically, the Bruggeman and Maxwell-Garnett approximations assume the inclusions within the host scatter light as Rayleigh particles. The forward-scattering amplitude of a Rayleigh particle is proportional to the particle volume; whereas, for larger particles, the

forward-scattering amplitude is proportional to the particle size parameter. Since these effective medium approximations are calculated from the forward-scattering amplitudes, the Bruggeman and Maxwell-Garnett mixing rules place a greater weight on the inclusion than is approximation is calculated from the entire partial wave expansion of the inclusions, the weighting of the inclusions is more realistic. The resulting extended effective medium calculations more closely resemble model calculations as the inclusion size becomes comparable to the wavelength. Figure 3.5 shows the trend of polarization ratio as function of particle dimension for carbon and water particles.

Volume ratio	Eq. (3.36)	Eq. (3.40)	Eq. (3.41)
$10^{-4}$	$1.335 + i5.52 \cdot 10^{-5}$	$1.335 + i5.07 \cdot 10^{-5}$	$1.335 + i5.07 \cdot 10^{-5}$
$10^{-3}$	$1.336 + 6.66 \cdot 10^{-4}$	$1.335 + i5.07 \cdot 10^{-4}$	$1.336 + i5.07 \cdot 10^{-4}$
$10^{-2}$	$1.337 + 6.07 \cdot 10^{-3}$	$1.341 + i5.05 \cdot 10^{-3}$	$1.341 + i5.07 \cdot 10^{-3}$
$10^{-1}$	$1.337 + 3.67 \cdot 10^{-2}$	$1.398 + i5.37 \cdot 10^{-2}$	$1.399 + 5.15 \cdot 10^{-2}$

*Table 3.2 Refractive index values calculated using the extended effective medium approximation given by Eq. (3.36), Bruggeman (Eq. 3.40), and Maxwell-Garnett (Eq.3.41). effective medium approximations of a water ( $m_1=1.335$ ).  $R=\lambda$  host sphere containing a carbon  $m_2=1.94 + 0.66i$ . inclusion (Chy'lek P., et al., 1988)*

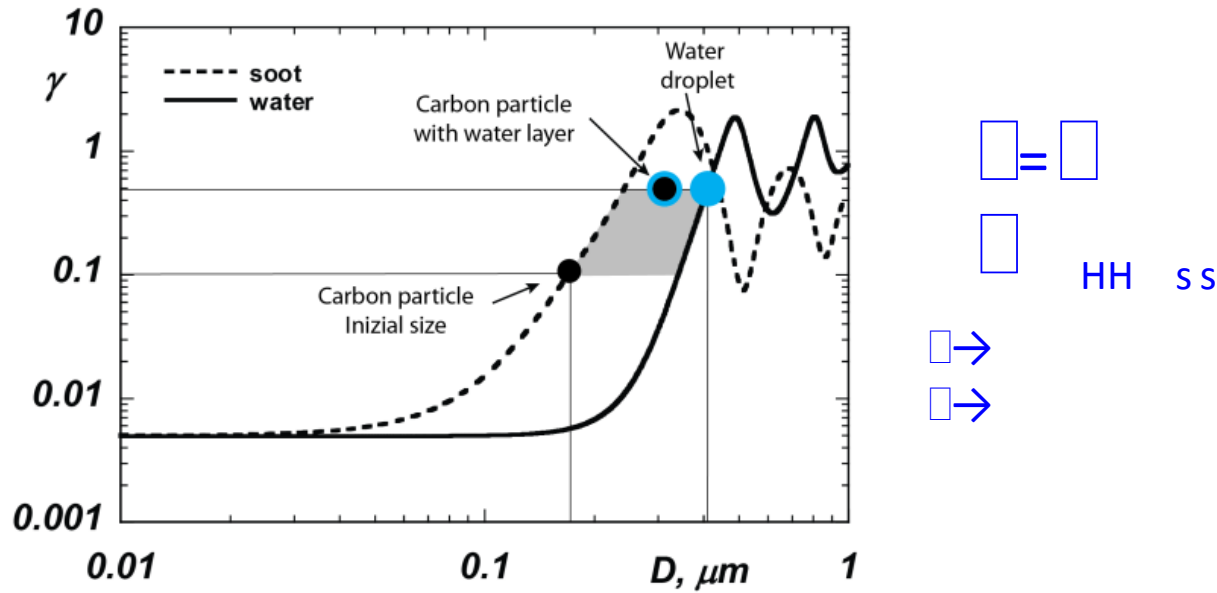


Figure 3.9: Trend of polarization ratio of water (solid line) and carbon particle (dashed line) as function of particles diameter

In this work the Bruggeman approximation was used to evaluate the refractive index of composite sphere formed by an adsorbing host sphere (graphite, iron and nickel) in a water droplet by varying the volume ratio of the inclusion. The results are summarized in the table 3.3. The values of refractive index calculated by Bruggeman approximation are useful to values the evaluation of polarization ratio of a composite sphere.

Volume ratio, f	C	Fe	Ni
<b>1 (particle)</b>	$1.92 + i0.66$	$2.92 + i2.92$	$1.88 + i3.5$
<b>0.1</b>	$1.33 + i3.67 \cdot 10^{-2}$	$1.54 + i1.04 \cdot 10^{-1}$	$1.53 + i1.73 \cdot 10^{-1}$
<b>0.01</b>	$1.33 + i6.07 \cdot 10^{-3}$	$1.35 + i6.33 \cdot 10^{-3}$	$1.36 + i7.87 \cdot 10^{-3}$
<b>0.001</b>	$1.33 + i6.66 \cdot 10^{-4}$	$1.33 + i6.024 \cdot 10^{-4}$	$1.33 + i7.29 \cdot 10^{-5}$
<b>0.0001</b>	$1.33 + i5.52 \cdot 10^{-5}$	$1.33 + i5.99 \cdot 10^{-5}$	$1.33 + i5.99 \cdot 10^{-5}$
<b>0 (water)</b>	$1.33 + i0$	$1.33 + i0$	$1.33 + i0$

Table 3.3 : refraction index of composite sphere for the selected material by varying volume ratio

### 3.3 *Description of the optical diagnostic system*

The facility has been provided with all the equipment for the realization of measures of elastic scattering of light. The illumination is performed through the second harmonic (wavelength 532 nm) of a Nd-YAG laser (YAG Handy 101) that is focused by means of a confocal doublet ( $f = 100$   $f = -25$ ). The elastically scattered light is focused by means of a biconvex lens with a focal length of 50 mm on a pin-hole which has a diameter of 2mm. and then focused on a photomultiplier tube using a biconvex lens with a focal length of 100 mm. this assures for a field of view with a characteristic dimension of 2 mm and an angle of collection equal to about 5 degrees. This system allows a significant reduction of the stray light due to the presence of the glass walls of the chamber.

The magnification ratio of the collection system is equal to 1 so it realizes a measurement volume that is substantially a cylinder (orthogonal to the incident laser beam) with a diameter of 2 mm. The depth of the measurement volume is approximately equal to 1 mm (diameter of the laser beam). Before the collection lens is placed a filter holder in which is mounted an interferential filter at 532 nm (FWHM 10nm) for measurements of scattered light. in order to eliminate possible interferences.

The signal collected by the photomultiplier tube. which has a rise time equal to 2000 picoseconds. is recorded by means of an oscilloscope Tektronix with a sampling frequency of 1 Gs / sec ( $10^9$  samples per second). For each laser pulse a track that is the time evolution of scattered light signal is recorded. and at the same time is also recorded a second track. collecting by means of an APD illuminated. by means of a partial reflection foil (1 % of the incident intensity). from the incident laser beam. In this way it is possible to fix. for each laser pulse. the intensity of the collected light to the fluctuations of intensity of the incident light.

Temporal profiles collected (typically in number of 2000 for each test) are processed by means of a suitable procedure. fully automated and operates in real time. written in

LabVIEW. In particular the signals are filtered by means of a numerical filter (low-pass filter type of fifth-order Butterworth) in order to remove any impulsive noise and are then realigned (in the case of scattering signals) temporally with respect to the signal collected by the photodiode of calibration.

The magnitude of the time lag between the two signals is due to propagation delays on the coaxial cables used for transmitting the signal from optical sensors to the oscilloscope. This phase shift is constant for all the tests performed elastic scattering and its value has been used to correctly determine the amount of delay of the signal compared to incandescent signal excitation laser.

The filtered signals are then evaluated by means of a routine that, after determining the time interval over which extends the peak of light collected through the calculation of the autocorrelation time, evaluates the integral (extended on that interval) by means of a numerical integration algorithm based on the method of trapezoids. Finally, the filtered and realigned temporally traces and integral values of light widespread are stored for future processing. In particular, using the polarization rotator and polarization analyzers were measured intensity of diffused light elastically  $I_{VV}$  and  $I_{HH}$  along the axis of the chamber. In this way it was evaluated the polarization ratio  $\gamma = I_{HH}/I_{VV}$  of the particles in order to assess their size and their coverage degree by the condensing vapor specie. Figure 3.6 shows the scheme of optical diagnostic system

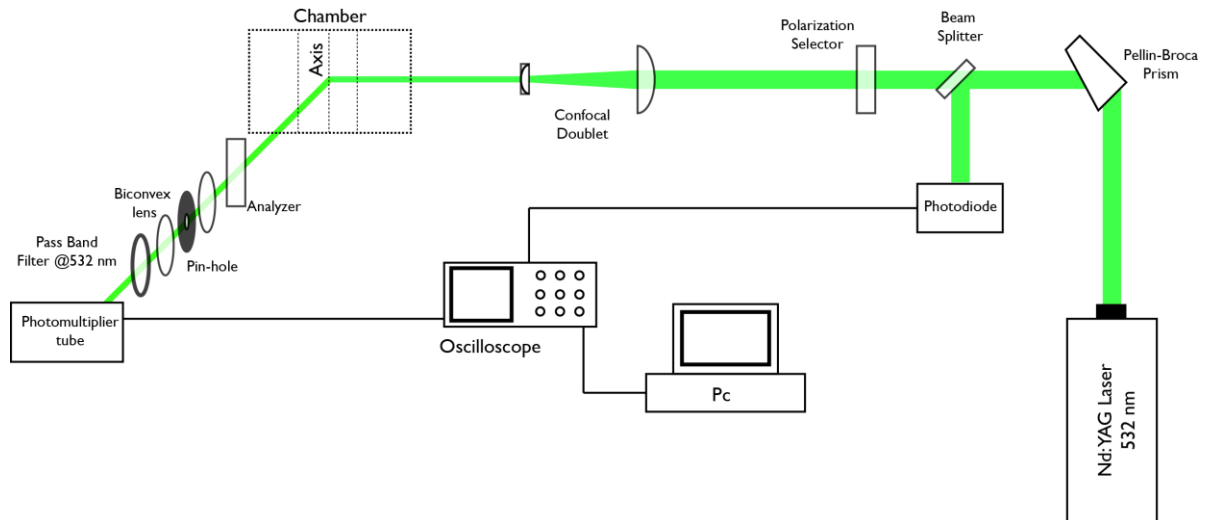


Figure 3.10: General scheme of optical diagnostic system

light and was obtained with a selector and an analyzer appropriately oriented. in both the incident and scattered beams. There was no depolarization by the aerosol in the sense that when these polarizer were crossed there was complete extinction. The reproducibility of successive polarization ratio determinations on the same aerosol was such that the average deviation was about 1 to 2 %. The solid angle subtended by the photometer receiver (photomultiplier tube) was sufficiently small so that no appreciable error would be encountered from this factor.

### 3.4 Dynamic Light Scattering

Dynamic Light Scattering (sometimes referred to as Photon Correlation Spectroscopy or Quasi-Elastic Light Scattering) is a technique for measuring the size of particles typically in the sub micron region. Light scattering methodologies allow for both real-time and on line monitoring of aerosols. The intensity of the elastically scattered light varies as the sixth power of diameter for nanoparticles. Because of this, the scattered light signals from nanoparticles

are very small and cannot be detected reliably. Nonelastic light scattering methodologies, such as dynamic light scattering, have been used for measuring nanoparticles. Dynamic light scattering, also called photon correlation spectroscopy, is the spectral broadening of the signal because of Brownian motion of the particles. In this method, the diffusion coefficient of the particles is determined by interpretation of the dynamically scattered light signal, and with knowledge of the temperature, an estimate of the particle size can be obtained. Clearly, this poses challenges several because of the difficulties in an accurate determination of temperature, for example, in combustion systems. Moreover, the optics are rather complicated, and, hence, the technique is not extensively used for in situ monitoring. However, there are several commercial instruments that are used offline to determine the fractional size distributions of particles in the nanometer-size regime (Malvern Z-sizer 90 series).

DLS measures Brownian motion and relates this to the size of the particles. Brownian motion is the random movement of particles due to the collision with by the solvent molecules that surround them. Normally DLS is concerned with measurement of particles suspended within a liquid. The larger the particle, the slower the Brownian motion will be. Smaller particles are “kicked” further by the solvent molecules and move more rapidly. An accurate measure of temperature is necessary for DLS since knowledge of the viscosity is required. The temperature also needs to be stable, otherwise convection currents in the sample will cause non-random movements that will ruin the correct interpretation of size. The velocity of the Brownian motion is defined by a property known as translational diffusion coefficient (usually given the symbol,  $D$ ).

The size of a particle is the hydrodynamic diameter and is calculated from the translational diffusion coefficient by using the Stokes-Einstein. The diameter that is measured in a DLS is considered the hydrodynamic diameter. The diameter that is obtained by this technique is the diameter of a sphere that has the same translational diffusion coefficient as the particle. The

translational diffusion coefficient will depend not only on the size of the particle “core”. but also on any surface structure. as well as the concentration and type of ions in the solvent. The factors that affect the diffusion speed of particles are the strength of the solvent; the particle surface structure and the particle sphericity.

The ions in the solvent and the total ionic concentration can affect the particle diffusion speed by changing the thickness of the electric double layer. which is named Debye length. Thus a low conductivity solvent will produce an extended double layer of ions around the particle. reducing the diffusion speed and resulting in a larger. apparent hydrodynamic diameter. Conversely. higher conductivity media will suppress the electrical double layer and reduces the measured hydrodynamic diameter. The performance of a DLS instrument is normally verified by measurement of a suitable polystyrene latex standard. If the standard needs to be diluted prior to measurement. then dilution in an appropriate solvent is important. The International Standard on DLS (ISO13321 Part 8 1996) says that dilution of any polystyrene standard should be made in 10mM NaCl. This concentration of salt will suppress the electrical double layer and ensure that the hydrodynamic diameter reported will be the same as the hydrodynamic diameter on the certificate or the expected diameter.

Any change to the surface of a particle that affects the diffusion speed will correspondingly change the apparent size of the particle. An adsorbed polymer layer projecting out into the solvent will reduce the diffusion speed more than if the polymer is lying flat on the surface. The nature of the surface and the polymer. as well as the ionic concentration of the solvent can affect the polymer conformation. which in turn can change the apparent size by several nanometres.

All particle-sizing techniques have an inherent problem in describing the size of nonspherical particles. The sphere is the only object whose size can be unambiguously described by a single figure. Different techniques are sensitive to different properties of the particle. e.g. projected area. density. scattering intensity. and in general will produce different mean sizes

and size distributions for any given sample. Even the size in a microscope image will depend on parameters set, such as edge contrast etc. It is important to understand that none of these results are inherently “correct”.

The hydrodynamic diameter of a nonspherical particle is the diameter of a sphere that has the same translational diffusion speed as the particle. If the shape of a particle changes in a way that affects the diffusion speed, then the hydrodynamic size will change. For example, small changes in the length of a rod-shaped particle will directly affect the size, whereas changes in the rod's diameter, which will hardly affect the diffusion speed, will be difficult to detect. The conformation of proteins and macromolecules are usually dependent on the exact nature of the dispersing solvent. As conformational changes will usually affect the diffusion speed, DLS is a very sensitive technique for detecting these changes.

If the particles are small compared to the wavelength of the laser used (typically less than  $d = \lambda/10$  or around 60nm for a He-Ne laser), then the scattering from a particle illuminated by a vertically polarized laser will be essentially isotropic, i.e. equal in all directions.

The Rayleigh approximation tells us that ( $I \propto d^6$ ) and also that ( $I \propto 1/\lambda^4$ ), where

- $I$  = intensity of light scattered.
- $d$  = particle diameter
- $\lambda$  = laser wavelength.

The  $d^6$  term tells us that a 50nm particle will scatter  $10^6$  or one million times as much light as a 5nm particle. Hence there is a danger that the light from the larger particles will swamp the scattered light from the smaller ones. This  $d^6$  factor also means it is difficult with DLS to measure, for example, a mixture of 1000 nm and 10 nm particles because the contribution to the total light scattered by the small particles will be extremely small. The inverse relationship to  $\lambda^4$  means that a higher scattering intensity is obtained as the wavelength of the laser used decreases.

When the size of the particles becomes roughly equivalent to the wavelength of the

illuminating light. then a complex function of maxima and minima with respect to the scattering angle is observed. Figure 3.7 shows the theoretical plot of the log arithmetic of the relative scattering intensity versus the particle size at angles of  $173^\circ$  (the detection angle of the Zetasizer Nano S and Nano ZS in aqueous media) and  $90^\circ$  (the detection angle of the Nano S90 and Nano ZS90) assuming a laser wavelength of 633nm. real refractive index of 1.59 and an imaginary refractive index of 0.001. Mie theory is the only theory that explains correctly the maxima and minima in the plot of intensity with angle and will give the correct answer over all wavelengths. sizes and angles. Mie theory is used in the Nano software for conversion of the intensity distribution into volume.

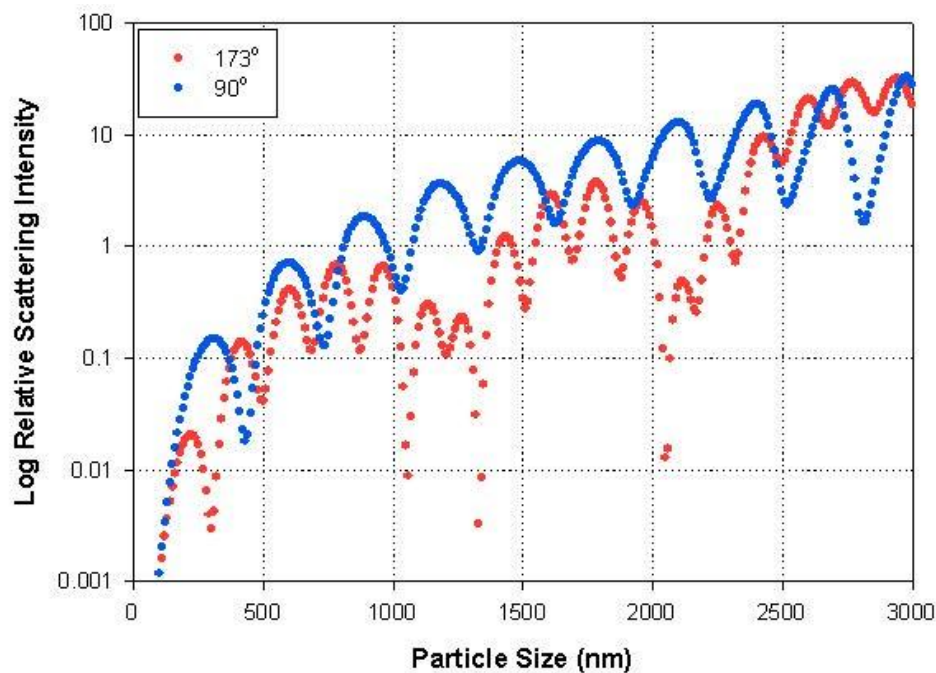


*Figure 3.11: Theoretical plot of the log of the relative intensity of scattering versus particle size at angles of  $173^\circ$  (in aqueous media) and  $90^\circ$*

In dynamic light scattering, the speed at which the particles are diffusing due to Brownian motion is measured. This is done by measuring the rate at which the intensity of the scattered light fluctuates when detected using a suitable optical arrangement. When a liquid sample that contains stationary particles is illuminated by a laser and a frosted glass screen to view the

sample cell is used, a classical speckle pattern would be seen (Figure 3.8).

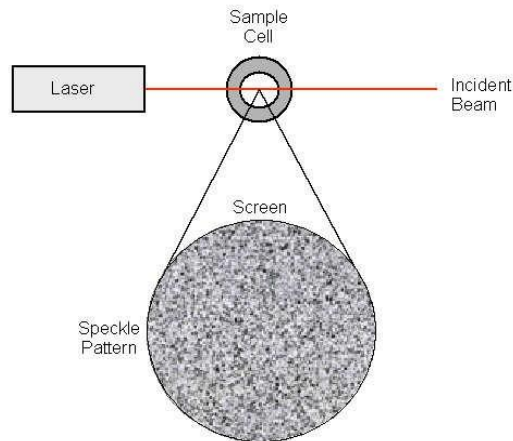


Figure 3.12: Schematic representation of a speckle pattern

The speckle pattern will be stationary both in speckles size and position, because the whole system is stationary. The dark spaces are where the phase additions of the scattered light are mutually destructive and cancel each other out (Figure 3.9A). The bright “blobs” of light in the speckle pattern are where the light scattered from the particles arrives with the same phase and interfere constructively to form a bright patch (Figure 3.9B).

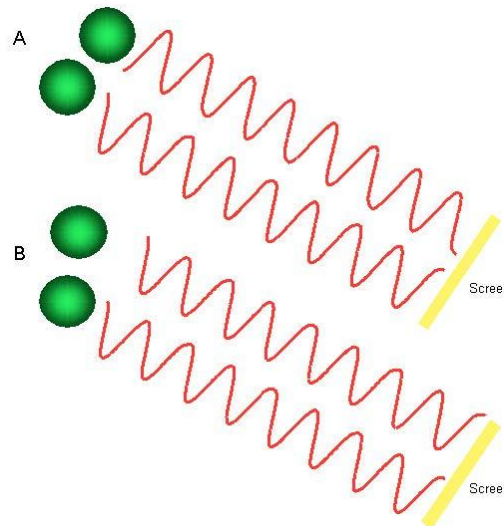


Figure 3.13: The observed signal depends on the phase addition of the scattered light falling on the detector. In example A, two beams interfere and ‘cancel each other out’ resulting in a decreased intensity detected. In example B, two beams interfere and ‘enhance each other’ resulting in an increased intensity detected.

For a system of particles undergoing Brownian motion, a speckle pattern is observed when the position of each speckle is seen to be in constant motion. This is because the phase addition from the moving particles is constantly evolving and forming new patterns. The rate at which these intensity fluctuations occur will depend on the size of the particles. Figure 3.10 schematically illustrates typical intensity fluctuations arising from a dispersion of large particles and a dispersion of small particles. The small particles cause the intensity to fluctuate more rapidly than the large ones.

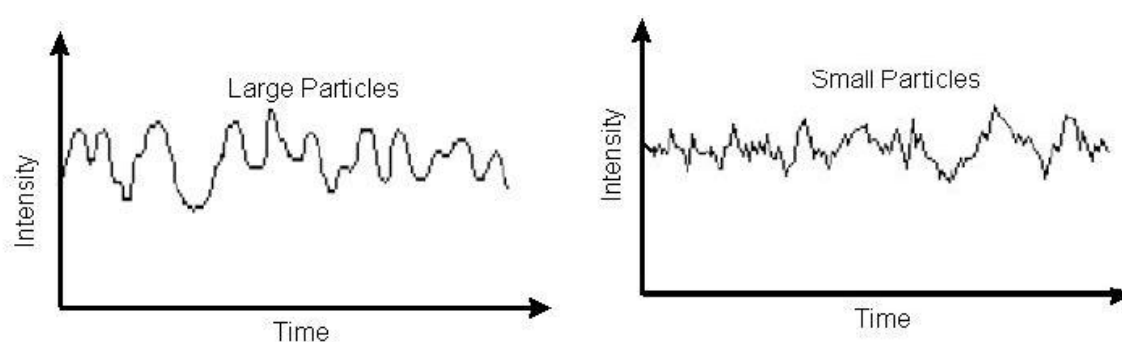


Figure 3.14: Typical intensity fluctuations for large and small particles

A correlator is basically a signal comparator. It is designed to measure the degree of similarity between two signals, or one signal with itself at varying time intervals. If the intensity of a signal is compared with itself at a particular point in time and a time much later, then for a randomly fluctuating signal it is obvious that the intensities are not going to be related in any way, i.e. there will be no correlation between the two signals (Figure 3.11). Knowledge of the initial signal intensity will not allow the signal intensity at time  $t \rightarrow \infty$  to be predicted. This will be true for any random process such as diffusion. However, if the intensity of signal at time  $t$  is compared to the intensity a very small time later ( $t + \delta t$ ), there will be a strong relationship or correlation between the intensities of two signals. The two signals are strongly or well correlated. If the signal, derived from a random process such as Brownian motion at  $t$ , is compared to the signal at ( $t + 2\delta t$ ), there will still be a reasonable comparison or correlation between the two signals, but it will not be as good as the comparison at  $t$  and ( $t + \delta t$ ). The

correlation efficiency is reducing with time. The period of time  $\delta t$  is usually very small, maybe nanoseconds or microseconds and is called the sample time of the correlator. If the signal intensity at  $t$  is compared with itself there is perfect correlation as the signals are identical.

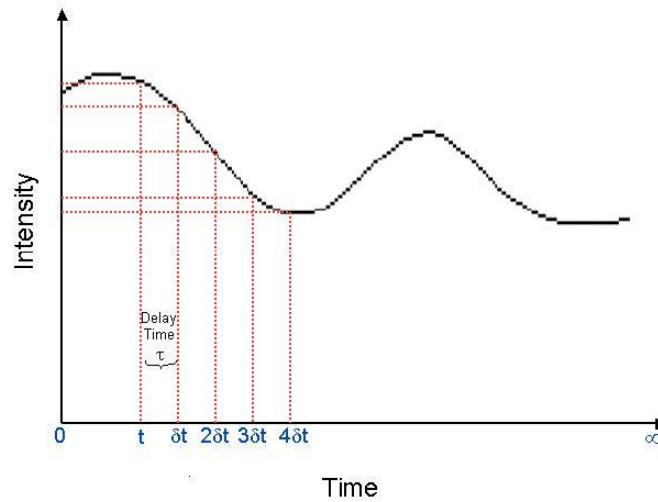


Figure 3.15: Schematic showing the fluctuation in the intensity of scattered light as a function of time

Perfect correlation is indicated by unity (1.00) and no correlation is indicated by zero (0.00). If the signals at  $t+2\delta t$ ,  $t+3\delta t$ ,  $t+4\delta t$  etc. are compared with the signal at  $t$ , the correlation of a signal arriving from a random source will decrease with time until at some time, effectively  $t = \infty$ , there will be no correlation. If the particles are large, the signal will be changing slowly and the correlation will persist for a long time (Figure 3.11). If the particles are small and moving rapidly, then correlation will reduce more quickly (Figure 3.12).

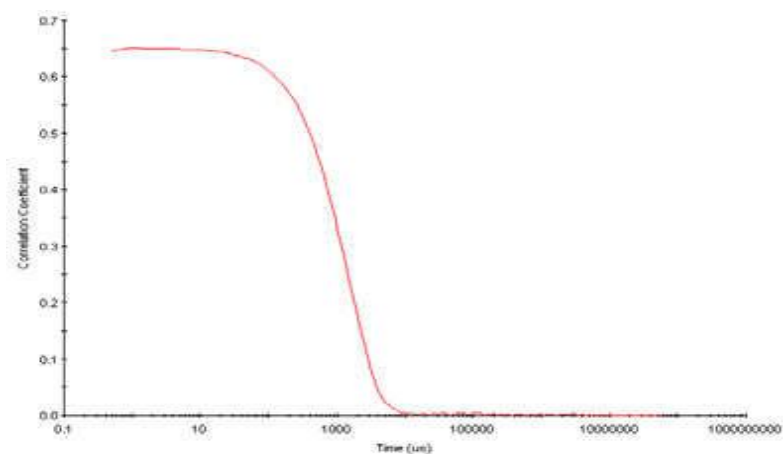


Figure 3.16: Typical correlogram from a sample containing large particles in which the correlation of the signal takes a long time to decay

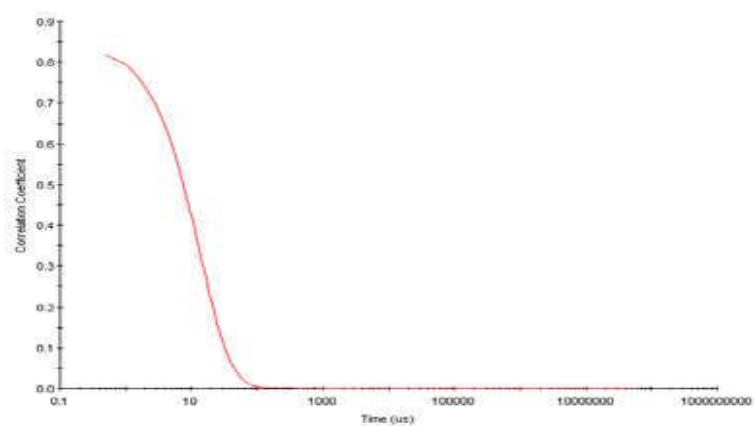


Figure 3.17: Typical correlogram from a sample containing small particles in which the correlation of the signal decays more rapidly

### 3.5 TEM and HRTEM

In the TEM only thin samples, which allow a fraction of the incident electron beam to go through the sample can be studied. When an accelerated beam of electrons impinges upon a sample a rich variety of interactions takes place (Fig 3.13). The versatility of electron microscopy and x-ray microanalysis is derived in large measure from this variety of interactions that the beam electrons undergo in the specimen.

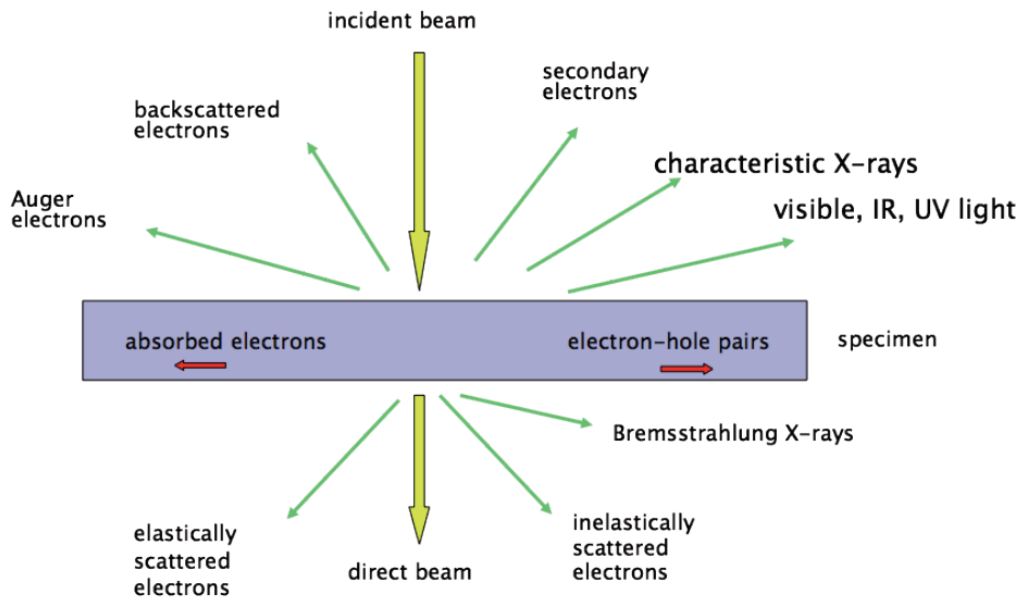


Figure 3.18: Variety of interactions that the beam electrons undergo in the specimen

Transmission electron microscopy TEM is capable of displaying magnified images of a thin specimen, typically with a magnification in the range  $10^3$  to  $10^6$ . In addition, the instrument can be used to produce electron-diffraction patterns, useful for analyzing the properties of a crystalline specimen. This overall flexibility is achieved with an electron-optical system containing an electron gun (which produces the beam of electrons) and several magnetic lenses, stacked vertically to form a lens column. It is convenient to divide the instrument into three sections.

The illumination system comprises the electron gun, together with two or more condenser lenses that focus the electrons onto the specimen. Its design and operation determine the diameter of the electron beam (often called the “illumination”) at the specimen and the intensity level in the final TEM image. The specimen stage allows specimens to either be held stationary or else intentionally moved, and also inserted or withdrawn from the TEM. The mechanical stability of the specimen stage is an important factor that determines the spatial resolution of the TEM image.

The imaging system contains at least three lenses that together produce a magnified image (or a diffraction pattern) of the specimen on a fluorescent screen, on photographic film, or on the

monitor screen of an electronic camera system. How this imaging system is operated determines the magnification of the TEM image, while the design of the imaging lenses largely determines the spatial resolution that can be obtained from the microscope.

High-resolution transmission electron microscopy (HRTEM) is an imaging mode of the transmission electron microscope (TEM) that allows the imaging of the crystallographic structure of a sample at an atomic scale. (Spence, John C. H., 1988). Because of its high resolution, it is a valuable tool to study nanoscale properties of crystalline material such as semiconductors and metals.

For TEM observations, thin samples are required due to the important absorption of the electrons in the material. High acceleration voltage reduces the absorption effects but can cause radiation damage (estimated at 170 kV for Al). At these acceleration tensions, a maximum thickness of 60 nm is required for TEM and HREM observations and quantifications.

Conventional TEM uses only the transmitted beams or some of the forward scattered beams to create a diffraction contrast image. HREM uses the transmitted and the scattered beams to create an interference image. As it will be detailed in the following parts, the TEM microscope must have a high performance (low spherical aberrations and high stability of the high tension, of the lens currents and of the energy of the electron beam). The understanding of the image formation must take into account the two following steps: (1) the propagation of the incident wave through the object, (2) the transfer of the scattered wave by an optical system of the microscope (the objective lens). The propagation of the incident wave through the sample is usually treated with one of these two different methods: the Bloch waves method or the multislice method. Both are applicable to perfect crystals, but in addition the multislice method is also applicable to crystals with defects or to non-periodic structures. As usual in transfer theory, the wave transferred through the optical system (the image wave) is the convolution between the object wave (exit wave) and a transfer function .

### 3.6 Absorption (UV-Vis)

Absorption of visible and ultraviolet (UV) radiation is associated with excitation of electrons. in both atoms and molecules. from lower to higher energy levels. Since the energy levels of matter are quantized. only light with the precise amount of energy can cause transitions from one level to another will be absorbed. UV-vis spectroscopy is the measurement of the wavelength and intensity of absorption of near-ultraviolet and visible light by a sample. Ultraviolet and visible light are energetic enough to promote outer electrons to higher energy levels. UV-vis spectroscopy is usually applied to molecules and inorganic ions or complexes in solution. The uv-vis spectra have broad features that are of limited use for sample identification but are very useful for quantitative measurements. The concentration of an analyte in solution can be determined by measuring the absorbance at some wavelength and applying the Beer-Lambert Law.

Absorption of visible and ultraviolet (UV) radiation is associated with excitation of electrons. in both atoms and molecules. from lower to higher energy levels.

Since the energy levels of matter are quantized. only light with the precise amount of energy can cause transitions from one level to another will be absorbed.

UV-visible spectrometers can be used to measure the absorbance of ultra violet or visible light by a sample. either at a single wavelength or perform a scan over a range in the spectrum. The UV region ranges from 190 to 400 nm and the visible region from 400 to 800 nm. The technique can be used both quantitatively and qualitatively. The light source (a combination of tungsten/halogen and deuterium lamps) provides the visible and near ultraviolet radiation covering the 200 – 800 nm. The output from the light source is focused onto the diffraction grating which splits the incoming light into its component colours of different wavelengths. like a prism but more efficiently. For liquids the sample is held in an optically flat. transparent cuvette. The reference cell contains the solvent in which the sample is dissolved and this is commonly referred to as the blank. For each wavelength the intensity of light

passing first through both a reference cell ( $I_0$ ) and then the sample cell ( $I$ ) is measured. If  $I$  is less than  $I_0$ , then the sample has absorbed some of the light. The absorbance ( $A$ ) of the sample is related to  $I$  and  $I_0$  according to  $A = \log(I/I_0)$

The detector converts the incoming light into a current, the higher the current the greater the intensity. The chart recorder usually plots the absorbance against wavelength (nm) in the UV and visible section of the electromagnetic spectrum. The diagram below shows a simple UV-visible absorption spectrum for buta-1,3-diene. Absorbance (on the vertical axis) is just a measure of the amount of light absorbed. One can readily see what wavelengths of light are absorbed (peaks), and what wavelengths of light are transmitted (troughs). The higher the value, the more of a particular wavelength is being absorbed.

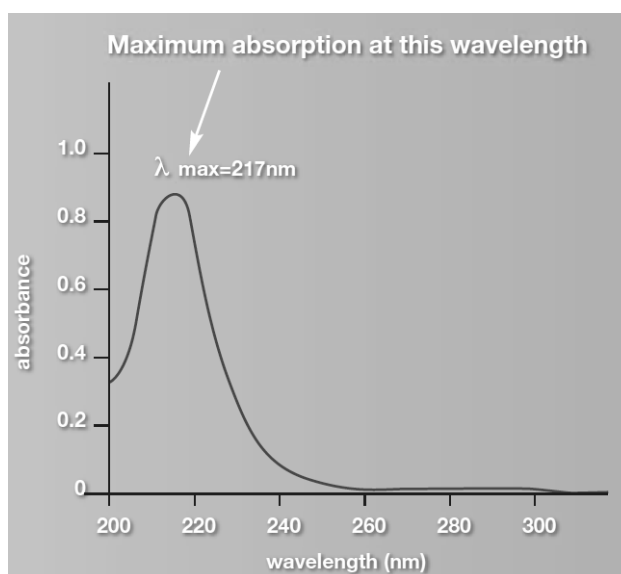


Figure 3.19: Absorption spectra

The absorption peak at a value of 217 nm, is in the ultraviolet region, and so there would be no visible sign of any light being absorbed making buta-1,3-diene colourless. The wavelength that corresponds to the highest absorption is usually referred to as "lambda-max" ( $\lambda_{\text{max}}$ ).

According to the Beer-Lambert Law the absorbance is proportional to the concentration of the substance in solution and as a result UV-visible spectroscopy can also be used to measure the

concentration of a sample. The Beer-Lambert Law can be expressed in the form of the following equation:

$$A = \varepsilon \cdot c \cdot l$$

Where

$A$  = absorbance

$l$  = optical path length. i.e. dimension of or cuvette (cm)

$c$  = concentration of solution (mol dm<sup>-3</sup>)

$\varepsilon$  = molar extinction. is constant for a particular substance at a particular  $\lambda$  (dm<sup>3</sup> mol<sup>-1</sup> cm<sup>-1</sup>)

If the absorbance of a series of sample solutions of known concentrations are measured and plotted against their corresponding concentrations, the plot of absorbance versus concentration should be linear if the Beer-Lambert Law is obeyed. This graph is known as a calibration graph.

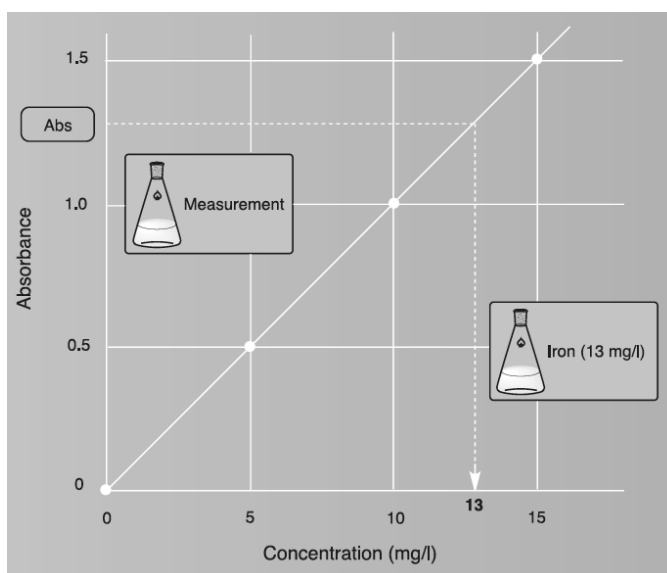


*Figure 3.20: Calibration graph*

A calibration graph can be used to determine the concentration of unknown sample solution by measuring its absorbance. In environmental fields the quantification of organic materials and heavy metals in fresh water can be carried out using UV-visible spectroscopy.

### **3.7 Electrical Low Pressure Impactor - E.L.P.I**

These measurements were performed by means of Electrical Low Pressure Impactor (ELPI). It is a real-time particle size spectrometer for real-time monitoring of aerosol particle size distribution. The main components of the instrument are a corona charger, low-pressure cascade impactor and multichannel electrometer. In ELPI the sample first passes through a unipolar positive polarity charger where the particles in the sample are charged electrically by small ions produced in a corona discharge. After the charger, the charged particles are size classified in a low-pressure impactor. The charged particles collected in a specific impactor stage produce an electrical current, which is recorded by the respective electrometer channel. A larger charge correlates to a higher particle population. The current value of each channel is proportional to the number of particles collected, and thus to the particle concentration in the particular size range.

It is possible to measure the charge present on particle surface by means of a specific measure protocol. If the ELPI charger is turned off, a reading of negative currents indicates that the particles have a negative charge state. In most cases the original charge of the particles does not affect the ELPI results (when the charger is ON). If the original charge of the particles is negative, the ELPI charger produces a sufficient amount of positive ions to first neutralize and then charge the particles normally, therefore no neutralizer is needed. It is possible to measure the residual charge of particles by comparing the measurements obtained when the charger is switched off and those obtained with the charger switched on, elaborating such data by means of a specific spreadsheet.

### 3.8 B.E.T.

The tendency of all solid surfaces to attract surrounding gas molecules gives rise to a process called gas sorption. The gas sorption process provides a wealth of useful information about the characteristics of solids. These molecules can either bounce off or stick to the surface. Gas molecules that stick to the surface are said to be adsorbed. The strength with which adsorbed molecules

interact with the surface determines if the adsorption process is to be considered physical (weak) or chemical (strong) in nature. Physical adsorption (physisorption) is the most common type of adsorption. Physisorbed molecules are fairly free to move around the surface of the sample. As more gas molecules are introduced into the system, the adsorbate molecules tend to form a thin layer that covers the entire adsorbent surface. Based on the well-known Brunauer, Emmett and Teller (BET) theory, one can estimate the number of molecules required to cover the adsorbent surface with a monolayer of adsorbed molecules,  $N_m$ . Multiplying  $N_m$  by the cross sectional area of an adsorbate molecule yields the sample's surface area. Continued addition of gas molecules beyond monolayer formation leads to the gradual stacking of multiple layers (or multilayers) on top of each other. The formation of multilayers occurs in parallel to capillary condensation saturation pressures at equilibrium, and convert them to cumulative or differential pore size distributions. As the equilibrium adsorbate pressures approach saturation, the pores become completely filled with adsorbate. Knowing the density of the adsorbate, one can calculate the volume it occupies and, consequently, the total pore volume of the sample. If at this stage one reverses the adsorption process by withdrawing known amounts of gas from the system in steps, one can also generate desorption isotherms. Since adsorption and desorption mechanisms differ, adsorption and desorption isotherms rarely overlay each other. The resulting hysteresis leads to isotherm shapes that can be mechanistically related to those expected from particular pore-shapes. In

contrast to physisorption, chemical adsorption (chemisorption) involves the formation of strong chemical bonds between adsorbate molecules and specific surface locations known as chemically active sites. Chemisorption is thus used primarily to count the number of surface activesites which are likely to promote chemical and catalytic reactions.

### **3.9 FT-IR**

Fourier transform infrared spectroscopy (FTIR) is a technique which is used to obtain an infrared spectrum of absorption, emission, photoconductivity or Raman scattering of a solid, liquid or gas. An FTIR spectrometer simultaneously collects spectral data in a wide spectral range. The main difficulty was the slow scanning process. A method for measuring all of the infrared frequencies simultaneously, rather than individually, was made employing a very simple optical device called interferometer. The interferometer produces a unique type of signal which has all of the infrared frequencies “encoded” into it. The signal can be measured very quickly. Thus, the time element per sample is reduced to a matter of a few seconds. Most interferometers employ a beam-splitter which takes the incoming infrared beam and divides it into two optical beams. One beam reflects off on a flat mirror which is fixed in place. The other beam reflects off on a flat mirror which is on a mechanism which allows this mirror to move a very short distance (typically a few millimeters) away from the beam-splitter. The two beams reflect off of their respective mirrors and are recombined when they meet back at the beamsplitter. Because the path that one beam travels is a fixed length and the other is constantly changing as its mirror moves, the signal which exits the interferometer is the result of these two beams “interfering” with each other. The resulting signal is called an interferogram which has the unique property that every data point (a function of the moving mirror position) which makes up the signal has information about every infrared frequency which comes from the source. This means that as the interferogram is measured, all frequencies are being measured simultaneously. Thus, the use of the interferometer results in

extremely fast measurements. Because the analyst requires a frequency spectrum (a plot of the intensity at each individual frequency) in order to make an identification, the measured interferogram signal can not be interpreted directly. A means of “decoding” the individual frequencies is required. This can be accomplished via a well-known mathematical technique called the Fourier transformation. This transformation is performed by the computer which then presents the user with the desired spectral information for analysis.

### ***3.10 Thermogravimetry***

Thermogravimetry (TG) or thermogravimetric analysis (TGA) measures the mass loss of a sample as the temperature of the sample is increased in a controlled manner. The temperature is controlled in a pre-programmed temperature/time profile, or in the rate-controlled mode, where the pre-programmed value of the weight changes imposes the temperature change in the way necessary to achieve and maintain the desired weight-change rate. TG is inherently quantitative, and therefore an extremely powerful thermal technique, but gives no direct chemical information. The gaseous environment of the sample can be: ambient air or inert gas. The commonly investigated processes are: thermal stability and decomposition, dehydration, oxidation, determination of volatile content and other compositional analysis.

## **CHAPTER 4**

### ***Experimental Results***

Several off-line measurement systems were employed to analyze particles fed into the chamber; DLS was used for the evaluations of particles dimension collected on a filter trap, UV-Vis Spectroscopy for the determination of particles concentration, TEM and HRTEM images for characterization of particle surface morphology. Furthermore an estimation of residual charge on particles surface is obtained by means an electrostatic low pressure impactor.

#### ***4.1 Characterization of the solid particulate***

The particulate matter produced by the Palas generator was collected using a trap consisting of a PTFE filter (Millipore, Fluoropore 0.45  $\mu\text{m}$  porosity or Whatman anodisk 0.025  $\mu\text{m}$  porosity), immediately located downstream of the generator, for a sampling time of 30 min.

The particulate samples were produced by varying:

- a) spark frequency (from 300 to 50  $\text{s}^{-1}$ );
- b) carrier gas flow rate (argon)
- c) the flow rate and dilution gas type (air, argon).
- d) the chemical nature of the particles

Operating conditions are listed in the Table 4.1

#	s <sup>-1</sup>	Ar (l/min)	Air (l/min)	Ar (l/min)	yield (mg/h)
1a	300	5.5			
2a	200	5.5			
3a	100	5.5			
1	50	4.1	0		1.88
2	50	6	0		1.76
3	50	7	0		1.88
4	50	7	12		1.92
5	50	7	30		2.12
6	50	7	43		2.2
7(6bis)	50	7		31 <sup>a</sup>	1.56
8(5bis)	50	7		21 <sup>b</sup>	1.84
<sup>a</sup> correspond to 43 l/min air			<sup>b</sup> correspond to 30 l/min air		

Table 4.1 Operating condition of aerosols spark generator (PALAS GFG 1000)

The particulate samples, collected on a filter, were extracted with dichloromethane (DCM) to verify the absence of adherent molecules on the particles and soluble in DCM. The particulate samples were weighed using a high precision analytical balance ( $\pm 0.01$ mg) Mettler; the yield of particulate matter was reported in Table 4.1

The particulate matter was suspended in N-methylpyrrolidinone (NMP) with use of an ultrasonic bath to be subsequently subjected to dimensional analysis (dynamic scattering, DLS and size exclusion chromatography, SEC) and spectroscopic (UV-Visible spectroscopy).

- **(Size Exclusion Chromatography, SEC)**

The SEC chromatography allows to obtain information on the molecular weight distribution of the particles in suspension. The chromatographic analysis was performed using a chromatographic column suitable for exploring a range of molecular weights between 1E5 - 1E10 u (assuming density of 1.8g/cm<sup>3</sup> and spherical shape, and an hydrodynamic particle diameter up to approximately 100 nm). The chromatographic column (Jordi Gel

divinylbenzene, DVB) was exerts in isocratic conditions in a stream of NMP (1 mL/min) and at room temperature.

The SEC chromatograms of Palas particulate matter samples, suspended in NMP, do not present significant differences. The particulates produced by Palas are monodisperse and distributed almost entirely in the area of molecular weights of approximately  $1E10$  u. The exclusion limit of the column ( $1E10$  u) does not allow to reliably assessing the distribution greater than  $1E10$  u.

The monodispersion of Palas particulate matter suspension, was confirmed by subjecting the suspension to successive filtrations using an aluminum filters (Anopore, Whatman of 0.1 and 0.025  $\mu$ m porosity) and analyzing the filtrate by SEC chromatography. At the operating conditions of the aerosol generator considered in table 4.1, was not observed a size distribution below 100 nm for any particulate matter sample.

- **(Dynamic Light Scattering, DLS)**

The dynamic scattering measurements allow measuring the diffusion coefficients of particles suspended in a fluid (gas or solution). Thus is possible to estimate the hydrodynamic diameter of the particles measuring the diffusion coefficient.

The DLS measurements were performed with an Argon laser - water cooled operating at 488 nm, perpendicular polarized with the respect to the scattering plane and collimated by a convex glass lens of focal length  $f = 400$  mm.

The signal acquisition system consists of Glann-Thomson polarizer placed at  $90^\circ$  with respect to the direction of the incident light. The collected signal is sent, by means an optical fiber to a detector ALV / SO-Schuban that uses two photomultipliers and a beam-splitter cube to perform a PSUDO CROSS acquisition type in order to increase the detection accuracy for very rapid processes. The correlator is digital (ALV-6010/200 multiple tau) allowing a real

time sampling with a pulse pair resolution of 5 ns. The signal was analyzed by mean of an acquisition program. Small volume quartz cuvettes were used (1 ml, 1 cm light path). All solvents used for DLS analysis were prefiltered on filters of 0.02 microns porosity (Anotop 10 from Whatman Int Ltd) to eliminate interference from dust.

The hydrodynamic diameters measured with the DLS are shown in Figure 4.1. Smaller diameters (110-120 nm) were obtained, as expected, using the maximum dilution with lower spark frequency ( $50\text{s}^{-1}$ ). It worthwhile to note that the diluent gas type does not influence the particle size.

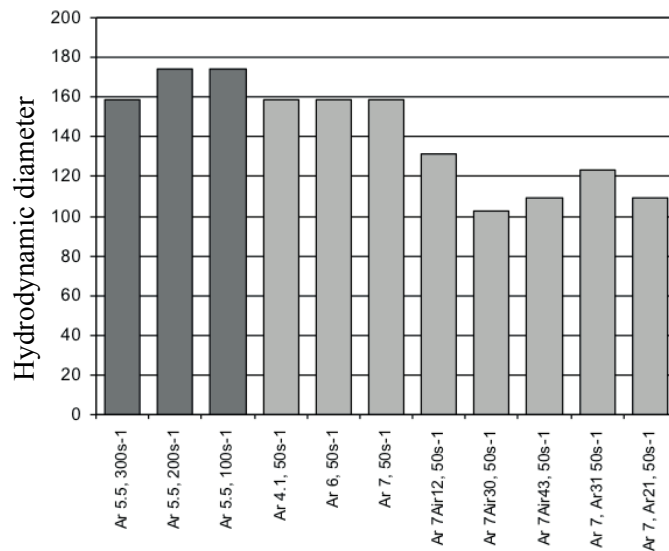


Figure 4.1: Mean hydrodynamic diameter (DLS) of particulate matter produced by Palas

Particle size distribution are shown in Fig. 4.2 ( $300\text{-}200\text{-}100\text{s}^{-1}$ ) e 4.3 ( $50\text{ s}^{-1}$ ).

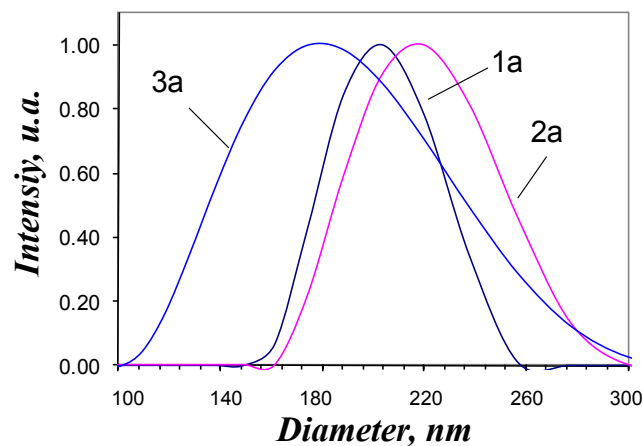


Figure 4.2: Mean hydrodynamic diameter (DLS) of particulate matter produced by Palas ( $300\text{-}200\text{-}100\text{s}^{-1}$ ).

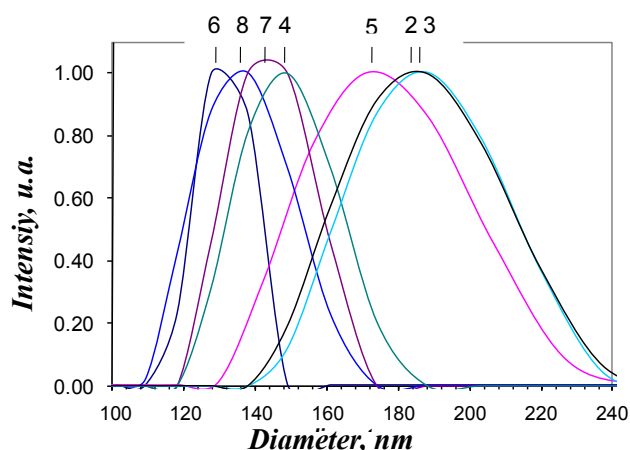


Figure 4.3 : Mean hydrodynamic diameter (DLS) of particulate matter produced by Palas ( $50s^{-1}$ ).

- **Spectroscopy (UV-Visible)**

The UV-Vis spectra of particulate samples suspended in NMP were acquired on a HP 8452A diode array spectrophotometer in the region between 260-800 nm using a quartz cuvette of 1 cm path length.

UV-VIS spectra show that the specific absorption of the particulate matter, expressed on the weight basis ( $m^2/g$ ), shown in Figure 4.4, present a decreasing trend from ultraviolet to the visible region. This trend is typical of carbonaceous particulates. The spectra have a trend very similar both in terms of specific absorption (Figure 4.4) both in the spectrum shape (Figure 4.5). There were no significant differences in absorption profiles using argon as the diluent gas instead of air.

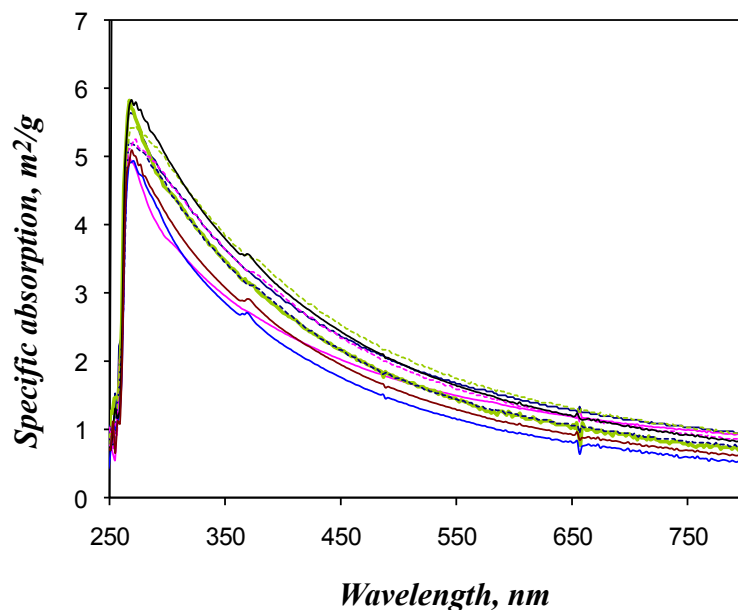


Figure 4.4: UV-Visible absorption spectra of particulates matter produced by Palas, expressed on the weight basis ( $m^2/g$ )

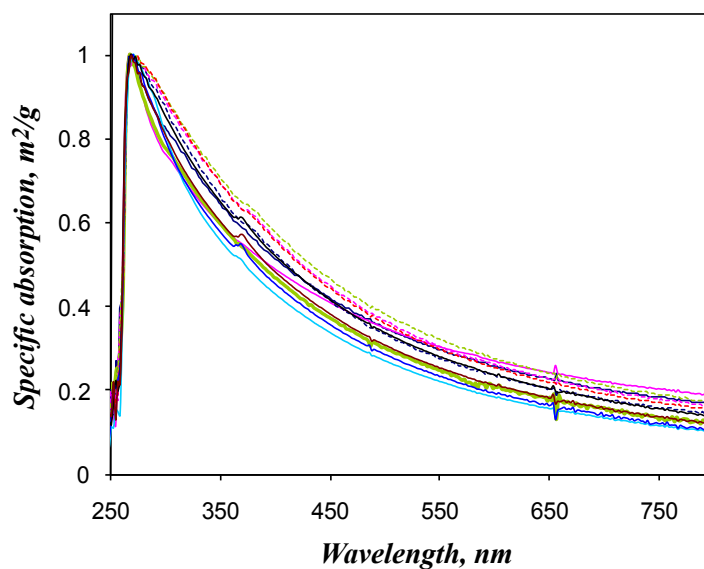


Figure 4.5: Absorption spectra of particulates matter produced by Palas normalized to the maximum value of the absorption.

The specific absorptions of the particulate at 300 nm and 500 nm were compared (Figure 4.6) with the specific absorptions of the particulate produced in flames under fuel rich conditions ( $C/O > 0.7$ ) using aliphatic (ethylene and hexane) and aromatic fuels (benzene). The absorptions are related to particulate matter collected within the area of nucleation (inception,

I), in the area of maximum formation of soot (maximum formation rate, MFR) and in the area end of flame (EOF).

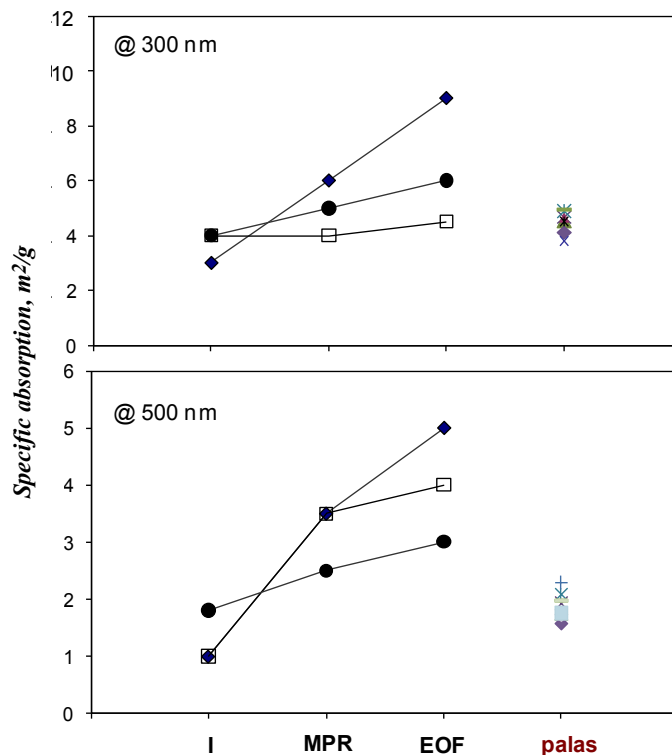


Figure 4.6: Comparison of the specific absorption at 300 nm and 500 nm of particulate matter produced by Palas and particulate sampled in rich flames exercised with aliphatic (hexane (●) ethylene (□)) and aromatic (benzene (◆)).

The values of specific absorption of Palas particulate matter are similar to those of the particulate matter collected at the beginning of flame.

Such values are in the range between those of a soot resulting from aromatic fuel (benzene) flame under fuel rich condition and of a soot produced with aliphatic fuel (hexane), sampled in the area of maximum formation of soot (EOF).

For the analyzed samples was not detected any fluorescence phenomenon, unlike the particulate matter produced by aliphatic and aromatic flames. This confirms the absence of adsorbed/adherent molecules on particles surface, released in NMP after sample sonication.

In Figure 4.7 the absorption spectra of the Palas particulate matter were compared with those of particulate matter produced in a premixed flames, of aliphatic (ethylene) and aromatic

(benzene) fuel, under fuel rich conditions. This comparisons was made in the area of "young-soot" and "mature-soot" formation (end of flame zone).

It is observed that the spectroscopic characteristics of the Palas particulate matter are very similar to those of young soot produced in an aromatic flame.

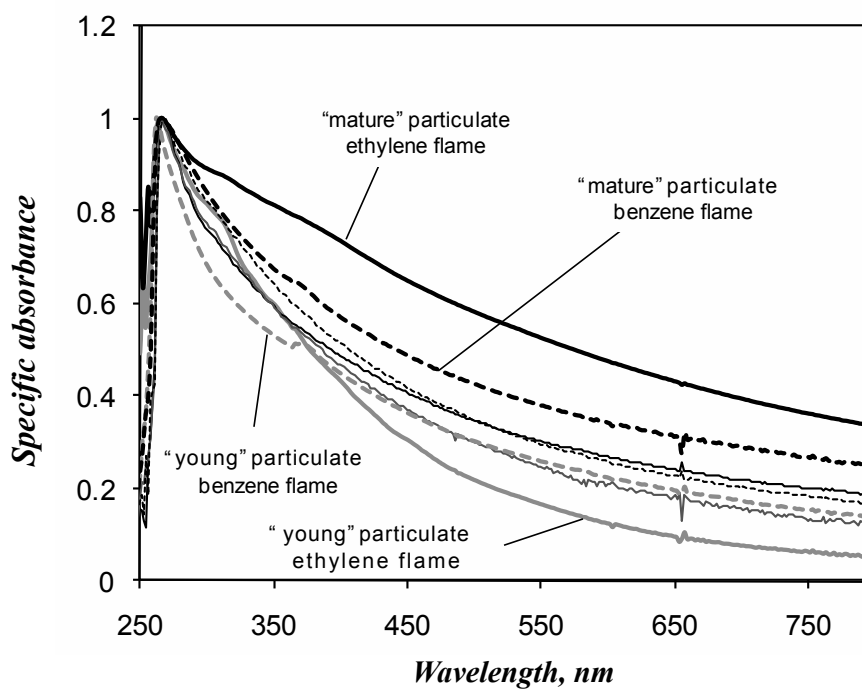


Figure 4.7: Absorption of particulate matter produced by Palas normalized to the maximum value of the absorption and compared with the normalized absorption of the particulates collected in rich flames of ethylene and benzene.

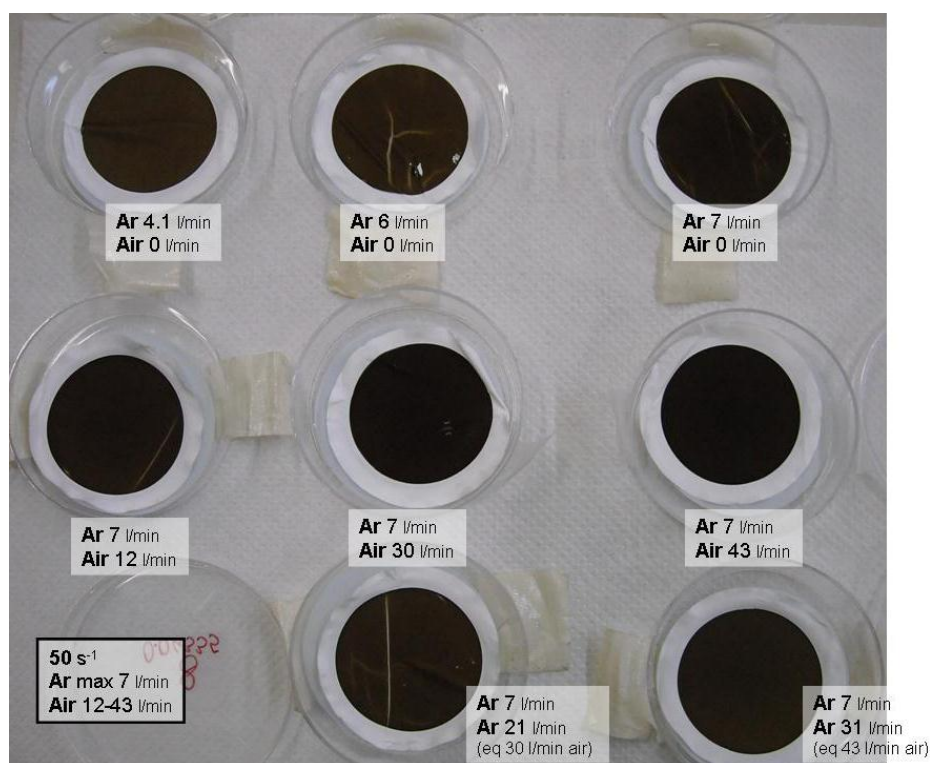


Figure 4.8: Overview of carbon samples

A further characterization of the particulate matter has been carried out in different operating conditions of the spark generator summarized in the Table 4.2

#	$s^{-1}$	Material	Ar (l/min)	$\overline{D_p}$ , nm
9	33	C	3.5	~150
10	3	C	3.5	~10
11	180	Fe	3.5	~150
12	210	Ni	3.5	~150

Table 4.2 Operating condition of aerosols spark generator (PALAS GFG 1000)

The flow rate of carrier gas (Ar) has been set equal to 3.5 l/min for all conditions considered, while the spark frequency of generator was varied from 3 up to 210  $s^{-1}$  by varying the chemical nature of particle or to obtain the desired size distribution.

Due to the different aerosols production efficiency, which depends on the chemical-physical characteristics of the electrodes used for particles generation (strongly from electrical

conductivity), different spark frequency were used.

The operating condition of aerosol generator to produce a very similar particle size distribution for graphite, iron and nickel particles are listed in table 4.2

As described in the previous chapter, the aerosol production efficiency decreases from graphite to nickel, higher spark frequency was used to produce nickel particles. In order to obtain a graphite particle distribution with the maximum at  $D_p=10$  nm was chosen a frequency equal to  $3\text{ s}^{-1}$ .

The particulate matter produced (condition 9,11,12) was collected, using a trap consisting of a filter (Millipore, Fluoropore  $0.45\text{ }\mu\text{m}$  porosity), located immediately downstream the generator.

The particulate samples, collected on a filter, were extracted with ethanol. The particulate matter was suspended in ethanol by sonication to be subsequently subjected to dimensional analysis (dynamic scattering, DLS ). Small volume quartz cuvettes were used (1 ml, 1 cm light path). All solvents used for DLS analysis were prefiltered on filters of porosity  $0.02$  microns (Anotop 10 from Whatman Int Ltd) to eliminate interference from dust.

In order to detect the ultrafine particles produced using a spark frequency of  $3\text{ s}^{-1}$  an aluminum filter ( $0.025\text{ }\mu\text{m}$  porosity) is used as a trap. Furthermore to avoid sticking phenomena due to the deposition of the particles on the filter, the sampling time (condition 10) was 10 min instead of 30 min. The hydrodynamic diameters was observed after analyzing with a Z-Sizer Nano (Malvern) and shown in Figure 4.9.

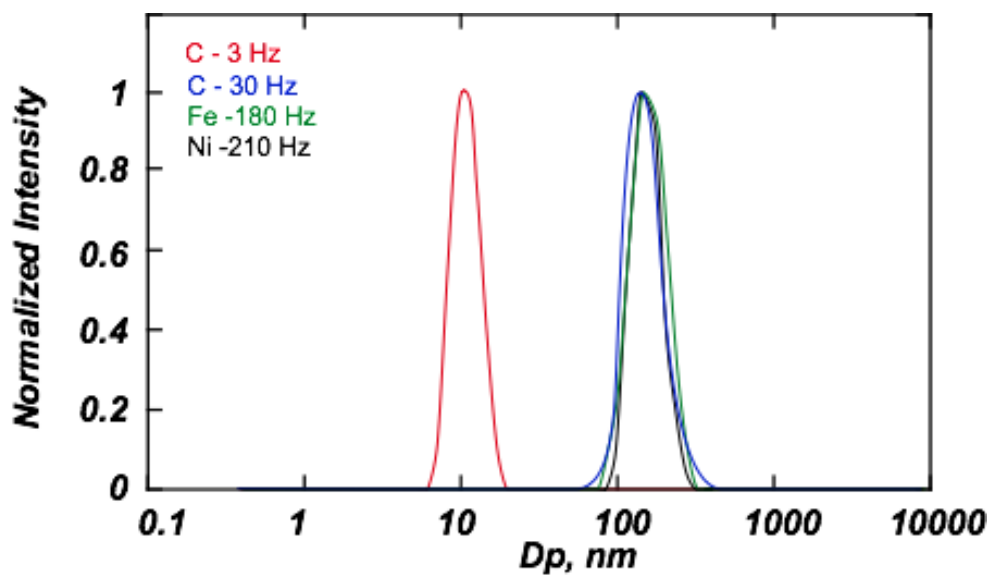


Figure 4.9: Mean hydrodynamic diameter (DLS) of particulate matter produced by Palas

- **Measure of particle charge**

Figure 4.10 shows the number of elementary charge present on graphite and iron particles.

These results were carried out using E.L.P.I and following the measure protocol presented in chapter III.

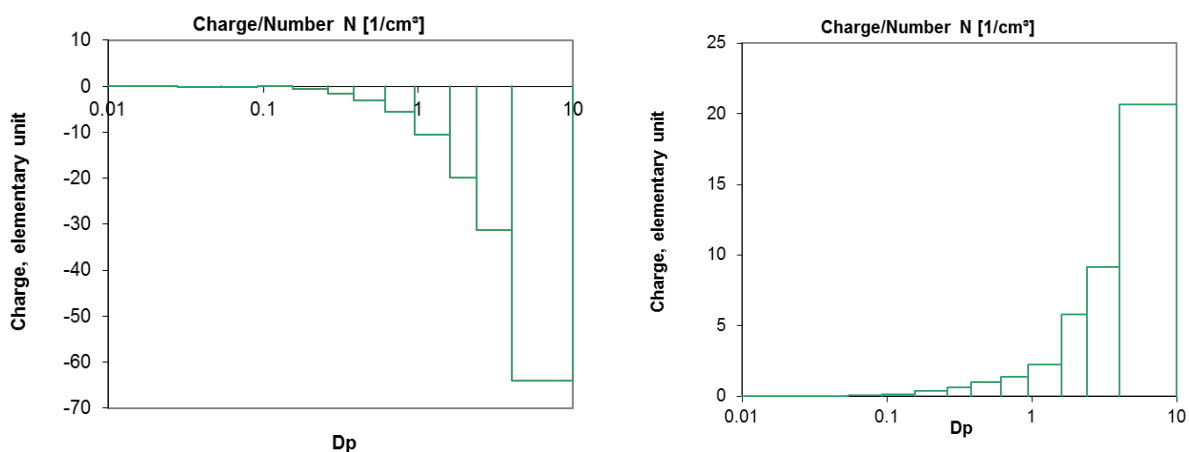
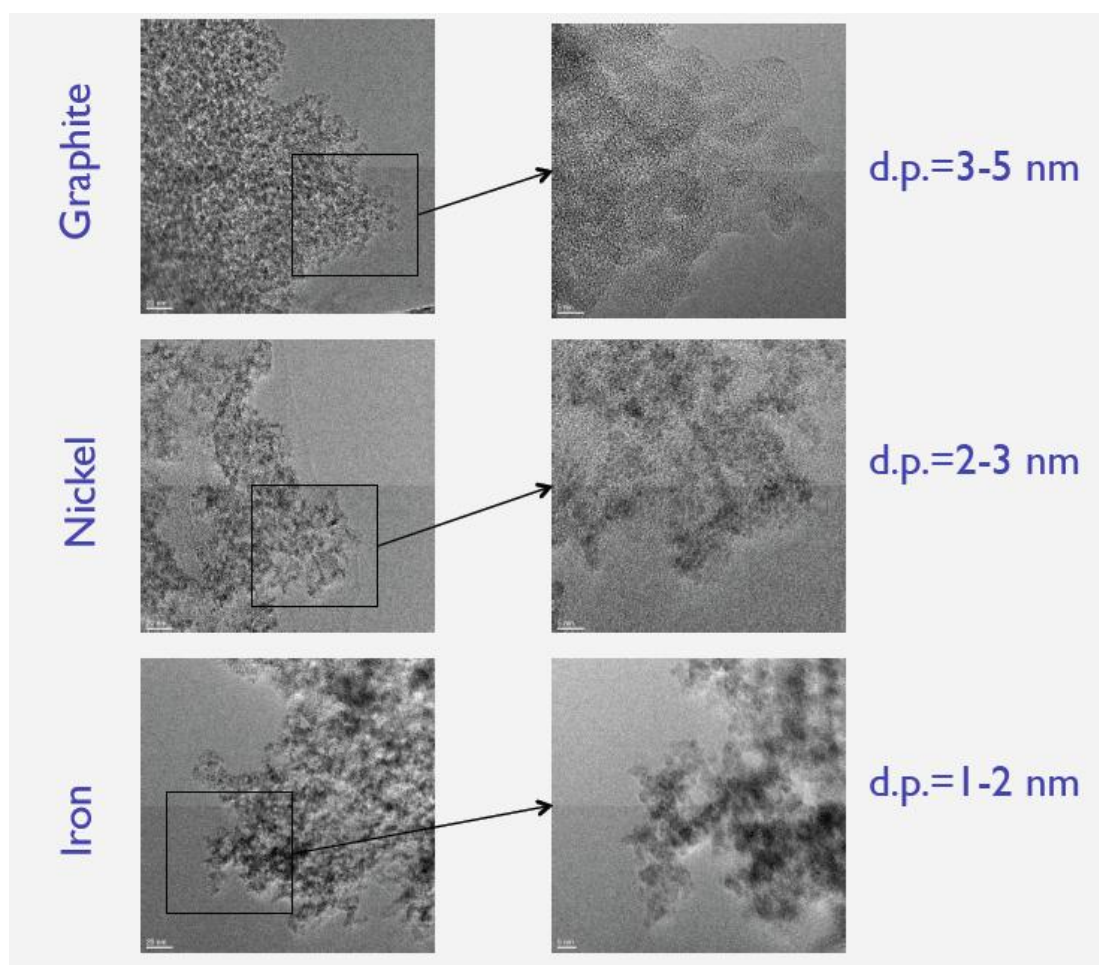


Figure 4.10: Number of elementary charge as function of particles diameter (left side) graphite, (right side) iron particles

These results show that in the size range of interest (10 - 150 nm) the charge present on the particles surface is negligible. Furthermore, these results show that graphitic particles have a negative charge, while iron particles have a positive charge, same consideration apply for nickel particles.

- **TEM and HRTEM**



*Figure 4.11: TEM and HRTEM of nanoparticulates obtained from graphite (up) nickel (middle) and iron electrodes (down).*

In Figure 4.11 TEM and HRTEM images of the three nanoparticulates are reported. All the particles present a common microtexture consisting of rather spheroidal primary particles agglomerated in chain-like compact structure. The microtexture of the three palas-generated particulates is similar to the particulate produced in sooting flame and carbon black, although

their averaged primary particle size is much smaller than those soot whose average is 20–40 nm. As a general consideration, the primary particles appear rounded with a narrow size distribution. The nanoparticulate generated from iron electrodes has a smaller primary particle size (1 - 2 nm) with respect to the nickel-generated nanoparticulate (2 - 3 nm). In both case the primary particles surface is rather smooth and does not exhibit a core-shell structure.

The nanoparticulate generated from graphite electrodes exhibits the largest primary particles (3 - 5 nm) in which short graphene segments are discernible, arranged concentrically and parallel to the particle perimeter. Structurally, the nanoparticulate generated from graphite electrodes is more fullerenoid presenting several closed carbon shells. Moreover HRTEM images reveal a highly defective non-smooth surface, associated with a high oxygen content, as confirmed by infrared spectroscopy.

- B.E.T

The solid phase was subjected to analysis for the evaluation of specific surface BET using the strumento Autosorb-1 (Quantachrome).

The amount of sample to be analyzed has been fixed equal to approximately 15 mg, to optimize the instrument performance that requires the presence in the analysis cell of a surface comprised between 1 and 5 m<sup>2</sup>. Before performing gas sorption experiments, solid surfaces must be freed from contaminants such as water and oils so the analysis comprises a step of sample degassing in vacuum conditions at a temperature  $T = 60\text{ }^{\circ}\text{C}$  for a time of 24 h. Subsequently, the sample is moved into the analysis station of the instrument and is subjected to a measurement of the specific surface area by BET (Brunauer Emmett and Teller) method. The measurement is carried out at low temperatures ( $-200\text{ }^{\circ}\text{C}$ ) and pressures. Then, small amounts of a gas (N<sub>2</sub>- the adsorbate) are admitted in 11 steps into the evacuated sample chamber. The evaluation of the volume of gas (N<sub>2</sub>) adsorbed by the solid at various pressures, (lower than the saturation pressure) allows to calculate the theoretical volume of a

monomolecular layer adsorbed and on the basis surface area of the gas molecules, it extrapolates the value of the specific surface area of the sample. The results obtained are summarized in Table 4 Appendix A

- FTIR

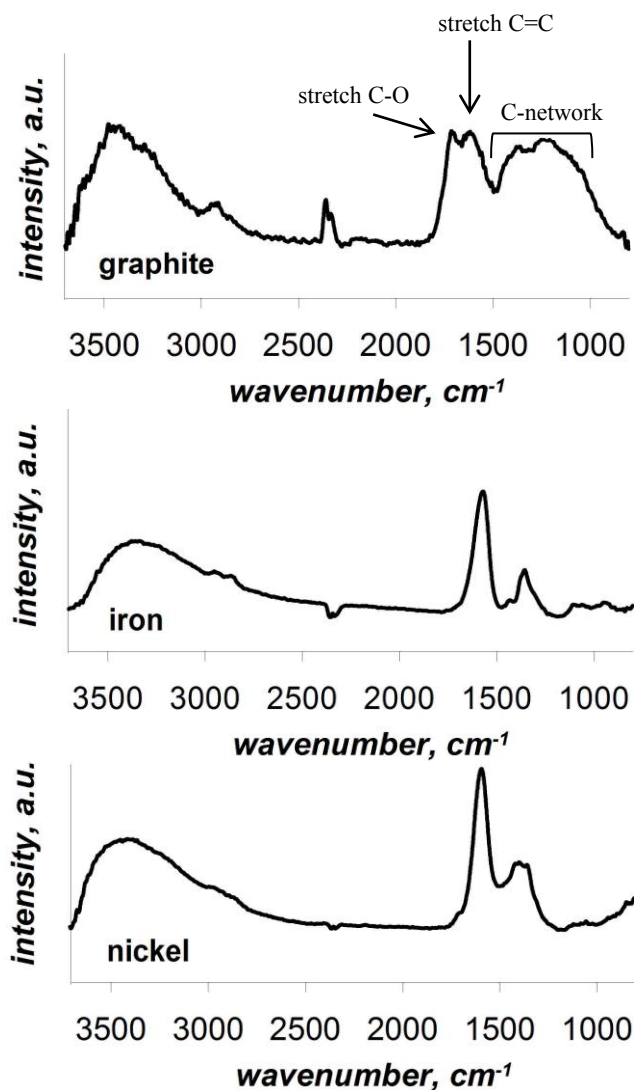


Figure 4.12 FTIR spectra of nanoparticles obtained from graphite (up) iron (middle) and nickel electrodes (down).

In Figure 4.12 FTIR spectra of the three nanoparticles are reported. From the analysis of FTIR spectra results that all the particles present oxygenated functional groups in the region of wave number between  $1850\text{-}1500\text{ cm}^{-1}$ .

- Thermogravimetry

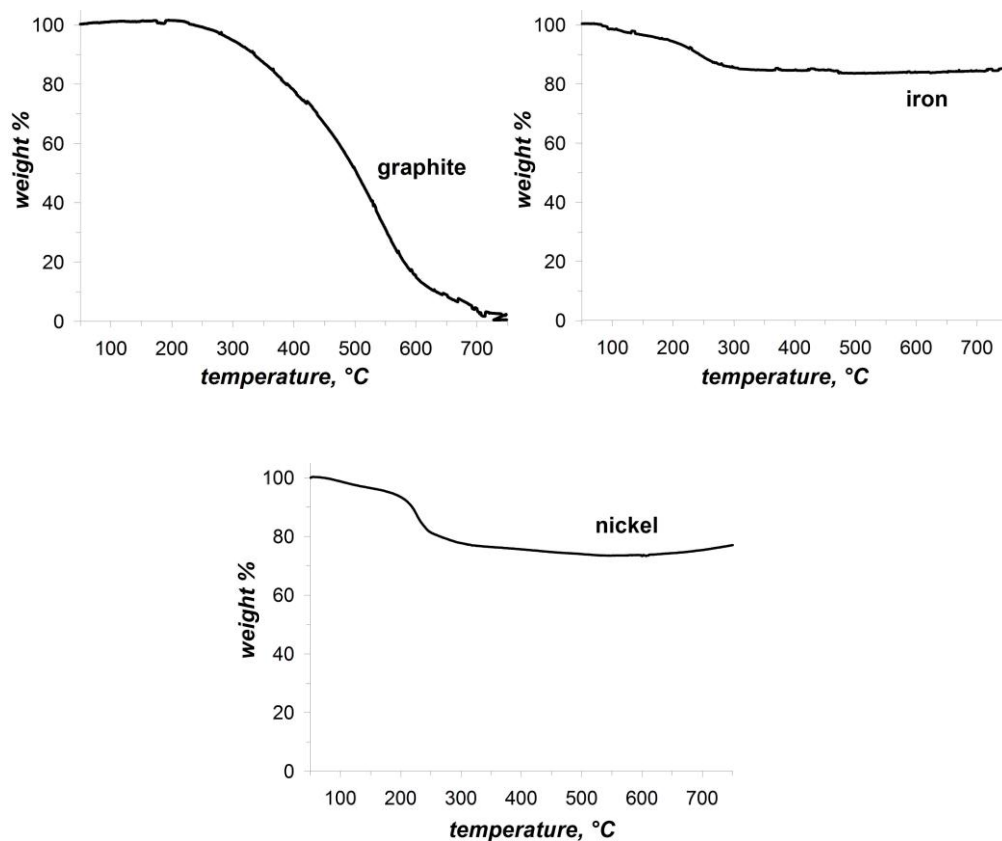


Figure 4.13: Thermogravimetry obtained from graphite (up) iron (middle) and nickel electrodes (down).

In Figure 4.13 thermogravimetric measurement (obtained in air) of the three nanoparticulates are reported. The weight loss of about 20% of the metal particulate is due to the devolatilization of metal oxides for temperature higher than approximately 200 °C after that they show a constant weight (80% of initial weight) up to the maximum temperature reached in the system. For graphite the weight loss is associated to a complete devolatilization of the sample starting from 250 °C.

- ***In situ Measurement***

The nucleation process of droplet on a particle and its further growth has been experimentally followed in the laminar diffusion chamber described in Chapter 2 for a wide range of parameters. As described in the previous chapter, the working parameters of the experimental test chamber can be varied independently from each other thus allowing for exploring the effect of a single parameter on the whole process. The experimental conditions in which the tests have been carried out are summarized in table 4.3. These represent in working conditions that are potentially typical of practical applications and cover values outside the range of interest of fundamental studies on nucleation. The experimental results will be presented by dividing them into paragraphs according to the investigated parameters considered, which Experimental tests were performed by varying some characteristic parameters that affect the particles growth process.

<b><i>Inlet temperature</i></b>	<b><i>T<sub>in</sub>, K</i></b>	<b><i>375 - 405 - 425</i></b>
<b><i>Inlet vapor concentration</i></b>	<b><i>X<sub>v</sub></i></b>	<b><i>0 - 0.1 - 0.25 - 0.35 - 0.5 - 0.7</i></b>
<b><i>Contact angle</i></b>	<b><i>θ°</i></b>	<b><i>20 - 50 - 85</i></b>
<b><i>Particles number concentration</i></b>	<b><i>N, #/cm<sup>3</sup></i></b>	<b><i>2.0e7 - 6e7 - 1.0e8</i></b>
<b><i>Particle Diameter</i></b>	<b><i>D<sub>p</sub>, nm</i></b>	<b><i>10-150</i></b>

*Table 4.3 Explored parameter*

The condensation process were analysed using the temporal profiles of the polarization ratio for the examined operating conditions summarized in table 5.1. During the first session of tests the inlet temperature of vapor/gas mixture fed to the chamber was varied to shows the effect of this parameter on the characteristics time of the particles growth process. The polarization ratio was measured as a function of axial coordinate and reported as function of the residence time,  $t$ , with the axial flow velocity,  $v$ , being constant and equal to 0.4 m/s for all reported conditions. A residence time,  $t_{res}$ , was defined as  $z_{max}/v$ . with  $z_{max} = 0.1m$ . Temporal profiles of  $\gamma$  were obtained for some value of vapor inlet concentrations,  $X_v$  (0, 0.10, 0.25 and 0.35). When  $X_v=0$ , only particles and carrier are fed to the flow chamber. By increasing the vapor concentration from 0 to 0.35, the percentage of the carrier gas was changed in such a way that the fluid-dynamic conditions are equivalent for all conditions studied. For each vapor concentration, three inlet temperatures ( $T_{in}=375$  K, 405 K, 425 K) were examined at a fixed confinement temperature,  $T_c = 298$  K. Afterwards, further tests were made to evaluate the effect of inlet vapor concentration, particle wettability (i.e. contact angle), particle number concentration and particle size. These tests are necessary for a full characterization of the particles growth process, and are also required to assess repeatability and validity of the characteristic times evaluated. The polarization ratio of propane was measured with the same experimental apparatus as a reference value to determine the limits of the detection system. Possible sources of measurement error are the electronic noise introduced by the detection system and the noise produced by the stray light. The first contribution was considered negligible by verifying that in absence of laser illumination, the collected signal was well below two orders of magnitude of the minimum detected signal. The error of the averaged measured values was estimated by computing the ratio of the value of polarized light component signals in each spatial/temporal position to the value of the depolarized component in the same position/time. It should be stressed that this approach is, in general, an overestimation of the error. In fact, the depolarization of incident light is due

not only to the stray light contribution but also to the irregular shape and surface of the particulates. This last contribution is not relevant in the case of nucleated droplets. Accounting for these possible contributions, the value of the error was verified to be below 10% for every experimental condition with values below 8% for distances from the chamber inlet greater than 20 mm.

## 4.2 Effect of inlet Temperature

- **Graphite Particles**

The chemical nature of the particle (i.e. contact angle or that the same particles wettability) is one of the most important parameter that affects particles growth process. In this first section, tests were carried out by feeding to the chamber graphite particles. The characteristic contact angle of graphite is  $\theta=85^\circ$ . The aerosol generator was operated with graphite electrodes with a spark discharge frequency of 30 Hz and a carrier feed of Ar of 3.5 l/min. At these conditions, a mono-dispersed particle distribution with the maximum at  $D_p=150$  nm was observed after analyzing with a Z-Sizer Nano (Malvern). This diameter corresponds to a particle number density of  $2 \cdot 10^7$  particles/cm<sup>3</sup>.

Figure 4.14 shows the value of  $\gamma$  measured at  $T_{in}=375$  K for the four values of  $X_v$ .

For  $X_v=0$  the value of  $\gamma$  is almost constant with the residence time of approximately 0.1, consistent with the particle size of the feed stream. This trend suggests that coagulation occurring among the carbon particles is negligible. Although the theoretical value of the polarization ratio should be equal to zero for particle light scattering described by the Rayleigh model, the experimental literature values of the polarization ratio collected at  $90^\circ$  range between 0.01 and 0.1, due to the finite collecting angle of the diagnostic system. The  $\gamma$

values reported in Fig. 4.14 are consistent with the calculated values after accounting for the collection system characteristics and the generated particle properties and size distributions.

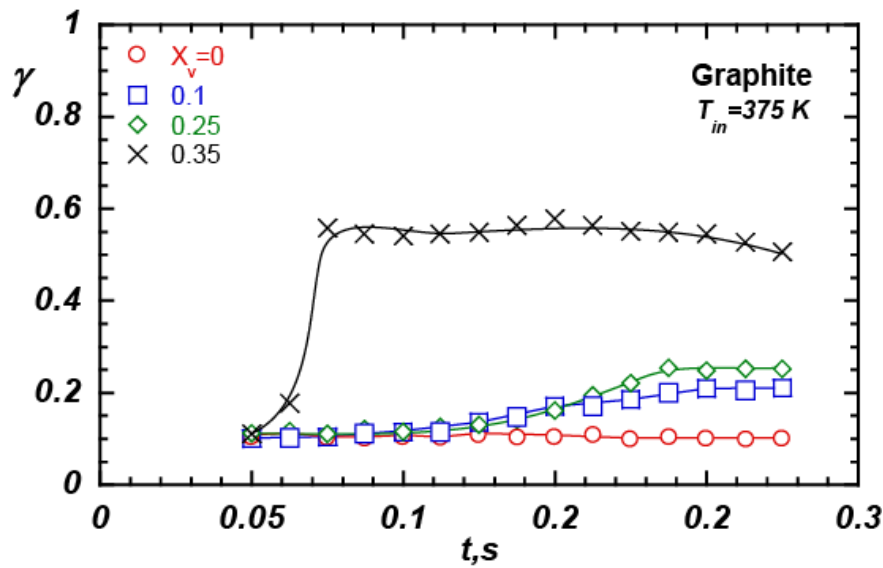


Figure 4.14: Polarization ratio as a function of residence time at  $T_{in}=375\text{ K}$

The condensation process was clearly present, as suggested by the profile of the polarization ratio measured in the presence of vapor. For  $X_v=0,35$  at  $t=0,05\text{ s}$  polarization ratio value was slightly higher than that measured for  $X_v=0$ . This trend suggests that there was no significant change in the scatterers' dimensions. At  $t$  higher than  $0,05\text{ s}$   $\gamma$  sharply increased and reached a value of  $0,558$  at  $0,075\text{ s}$  with little variation with respect to this value for  $t > 0,075\text{ s}$  suggesting that the scatterers' diameters significantly increased. This behavior indicates that the nucleation process was suddenly activated, and the surface growth leads to the formation of larger droplets.

For  $X_v=0,25$  the profiles shown in Fig 4.12 indicate that the value of polarization ratio remained at approximately  $0,11$ , slightly higher than the value of the soot particles up to  $0,1\text{ s}$ . At  $t$  higher than  $0,1\text{ s}$  polarization ratio slowly increased and reached the value of  $0,22$  at  $0,1875\text{ s}$ , then reaching a plateau of  $0,24$  at  $t=t_{res}$ . These data suggest that, while heterogeneous nucleation occurred, the increase in droplet size was limited compared with higher vapor concentrations case.

Different considerations apply to data collected at  $X_v=0.1$ . At these conditions,  $\gamma$  monotonically increased, reaching a plateau of 0.2 at  $t=0.225$  s. The absence of a sudden increase in signal and the presence of a plateau suggest that the nucleation and growth processes are slow, leading the system to an equilibrium condition where no further change in droplet diameter can occur.

An increase in the inlet temperature delayed the collection mechanism, as seen from profiles shown in Figs. 4.15 and 4.16, where  $\gamma$  measured for a  $T_{in}$  of 405 K and 425 K were reported. Fig 4.13 shows the value of  $\gamma$  evaluated at  $T_{in}=405$  K for the four values of  $X_v$ . As expected, an increase of  $T_{in}$  from 375 K to 405 K increased the induction time. More specifically, for  $T_{in}=405$  K, and  $X_v=0.35$   $\gamma$  increased for  $t$  higher than 0.075 s and reached a maximum of approximately 0.35, remaining nearly constant up to  $t=t_{res}$ . The polarization ratio trend at  $X_v=0.25$  did not demonstrate the step increase seen for higher vapour concentration condition. Instead, it increased smoothly, reaching a maximum value of approximately 0.2 at  $t=t_{res}$ . Additionally, the  $\gamma$  curve corresponding to  $X_v=0.1$  was delayed compared with the curve at  $T=375$  K, while retaining nearly the same shape and values. A further increase in temperature to 425 K shifted the curves toward higher times, as shown in Fig. 4.16

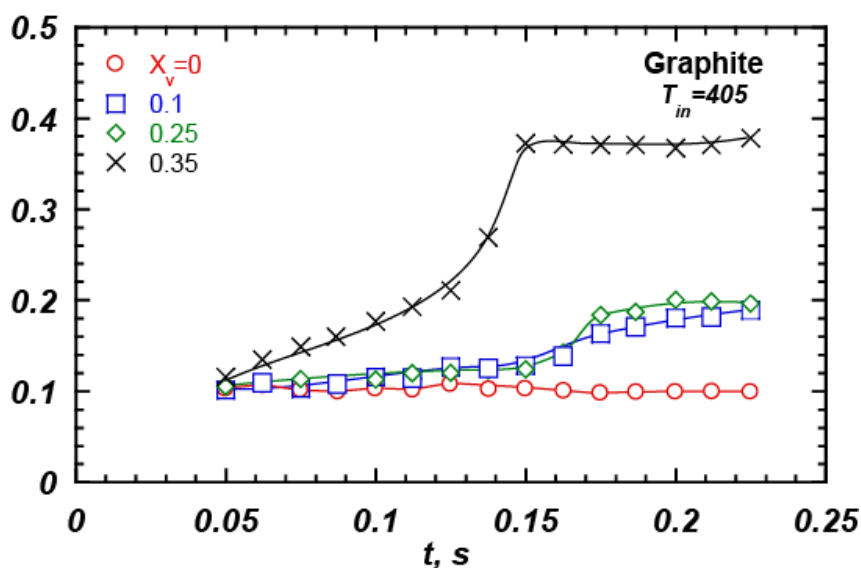


Figure 4.15: Polarization ratio as a function of residence time at  $T_{in}=405$  K

Figure 4.16 shows the value of  $\gamma$  evaluated at  $T_{in}=425$  K for the four values of  $X_v$ .

For  $X_v=0,35$  from  $t=0.05$ s to  $t=0.1$ s polarization ratio was constant a value slightly higher than that measured for  $X_v=0$ . This trend suggests that there was no significant change in the scatterers' dimensions. For  $t$  higher than  $0.01$  s  $\gamma$  increased and reached a value of  $0.36$  at  $0.2$  s, showing then a quite constant value up to  $t=t_{res}$ .

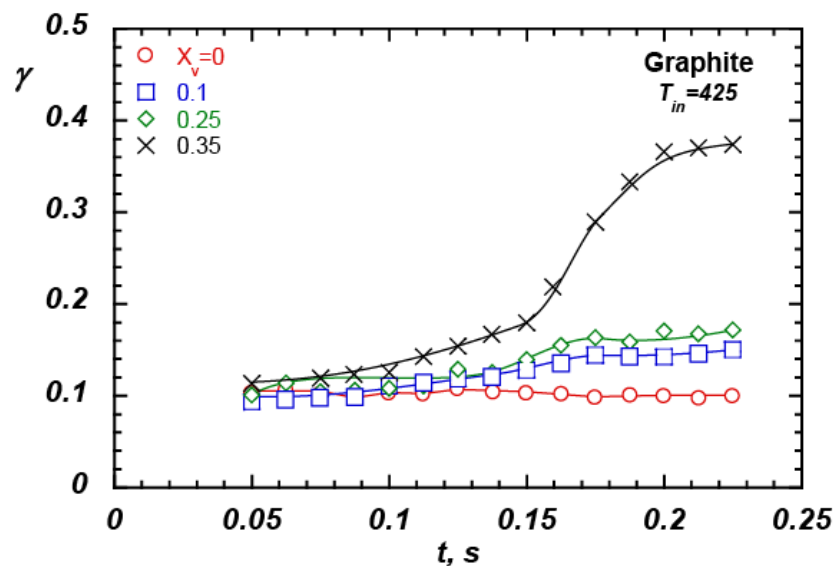


Figure 4.16: Polarization ratio as a function of residence time at  $T_{in}=425$  K

For  $X_v=0.25$  from  $t=0.05$  s to  $t=0.125$ s  $\gamma$  value was approximately equal to that measured for soot particles. At times higher than  $t=0.125$ s  $\gamma$  slowly increased and reached its maximum value of  $0.18$  at  $0.2$ s and then retains this value up to  $t=t_{res}$ . Additionally, both the  $\gamma$  curve corresponding to  $X_v=0.25$  and  $X_v=0.1$  was delayed compared with the curve at  $T=375$  K, and  $405$  K while retaining nearly the same shape and values.

- **Iron Particles**

In order to assess the effect of particle wettability on the characteristic time of the nucleation process, in this section, tests were carried out by feeding iron particle to the chamber. Such particle show a contact angle  $\theta=50^\circ$ . The aerosol generator was operated with iron electrodes with a spark discharge frequency of 180 Hz and a carrier feed of Ar of 3.5 l/min. At these conditions, a mono-dispersed particle distribution with the maximum at  $D_p=150$  nm was observed after analyzing with a Z-Sizer Nano (Malvern). This diameter corresponds to a particle number density of  $2 \cdot 10^7$  particles/cm<sup>3</sup>. Further tests were carried out by feeding nickel particles to the chamber. Fig 4.17 shows the value of  $\gamma$  evaluated at  $T_{in}=375$  K for the four values  $X_v$ .

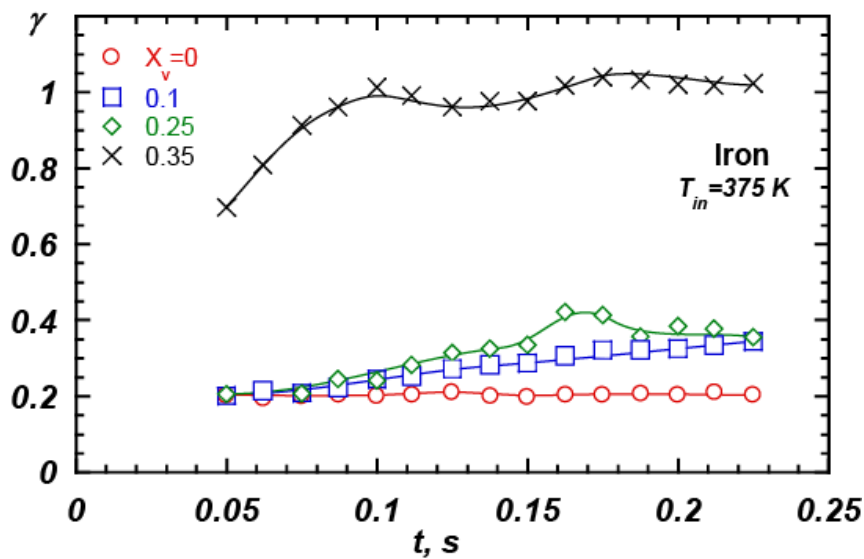


Figure 4.17: Polarization ratio as a function of residence time at  $T_{in}=375$  K

For  $X_v=0$  the value of  $\gamma$  is almost constant with a residence time of approximately 0.2, consistent with the particle size of the feed stream. This trend suggests that coagulation occurring among the iron particles is negligible. Although the theoretical value of the polarization ratio should be equal to zero for particle light scattering described by the Rayleigh model, the experimental literature values of the ratio collected at  $90^\circ$  range between

0.01 and 0.1, due to the finite collecting angle of the diagnostic system. This deviation from the theoretical value is due to the optical properties of the iron and internal stray-light.

The condensation process was clearly present, as suggested by the profile of the polarization ratio measured in the presence of vapor. For  $X_v=0.35$  at  $t=0.05$ s polarization ratio value was 0.69 higher than that measured for iron particles. This behavior indicates that the nucleation process is already activated, and the surface growth and coalescence led to the formation of larger droplets. At  $t$  higher than 0.05 s polarization ratio reached its maximum value of approximately 1, then showing a plateau of 1 up to  $t=t_{res}$ . This behavior suggest that the system is in an equilibrium condition where no further changes in the droplet occurs.

For  $X_v=0.25$  from  $t=0.05$  s to 0.075 s  $\gamma$  was constant at value of 0.2, this trend suggests that there is no significant change in the scattereres dimension. For  $t$  higher than  $t=0.075$ s polarization ratio slowly increased and reached a value of 0.42 at  $t=0.1625$ s. At  $t$  higher than 0.1625 s  $\gamma$  presents little variation around its maximum value and reached the value of 0.35 at  $t=t_{res}$ . For  $X_v=0.10$  polarization ratio monotonically increased with the residence time from 0.2 up to 0.34. The absence of a sudden increase in signal suggest that the nucleation and growth processes are slow. Again as shown in the previous section, an increase in the inlet temperature delayed characteristics time of particles growth process, as seen from profiles shown in Figs. 4.18 and 4.19, where  $\gamma$  measured for a  $T_{in}$  of 405 K and 425 K are reported.

Fig 4.18 shows the value of  $\gamma$  evaluated at  $T_{in}=405$  K for the four values of  $X_v$ . As expected, an increase of  $T_{in}$  from 375 K to 405 K increased the induction time of the growth process.

For  $X_v=0.35$  from  $t=0.05$  to  $t=0.125$ s s  $\gamma$  value was slightly higher than 0.2 this trend suggests that there is no significant change in the scatteres' dimension. At  $t$  higher 0.125 s  $\gamma$  increased rapidly and reached the value of 0.55 at  $t=0.1625$  s, then showing a slight decrease up to 0.48 at  $t=t_{res}$ .

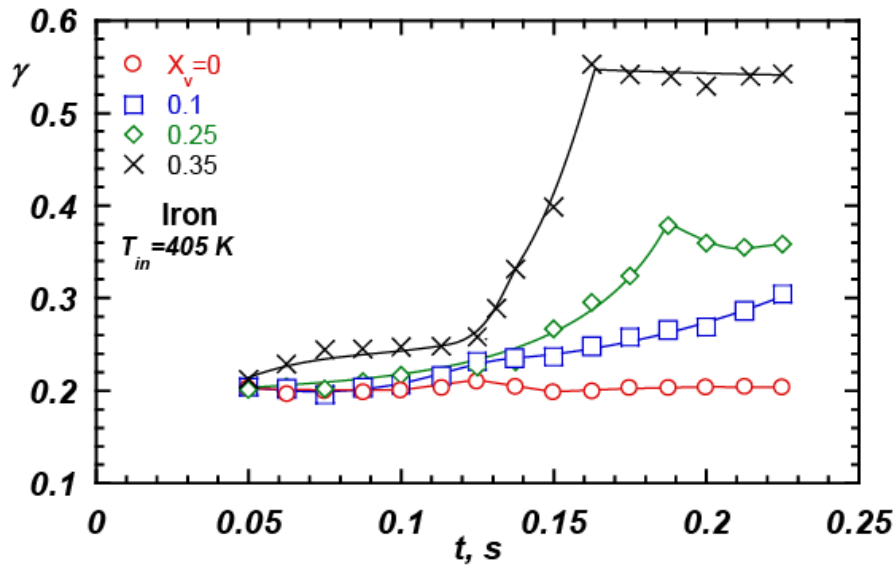


Figure 4.18: Polarization ratio as a function of residence time at  $T_{in}=405\text{ K}$

For  $X_v=0.25$  from  $t=0.05\text{ s}$  to  $t=0.1375\text{ s}$   $\gamma$  was almost constant at value of about 0.2. For  $t$  higher than 0.1375 s polarization ratio increased and reached a value of 0.39 at  $t=0.1875\text{ s}$

For  $X_v=0.10$   $\gamma$  showed a monotonically increase with the residence time and reached a value of 0.3 at  $t=t_{res}$ . Additionally, the  $\gamma$  curve corresponding to  $X_v=0.1$  was delayed compared with the curve at  $T=375\text{ K}$ , while retaining nearly the same shape and values. A further increase in temperature to 425 K shifted the curves toward higher times, as shown in Fig. 4.19

Figure 4.19 shows the value of  $\gamma$  evaluated at  $T_{in}=425\text{ K}$  for the four values of  $X_v$ .

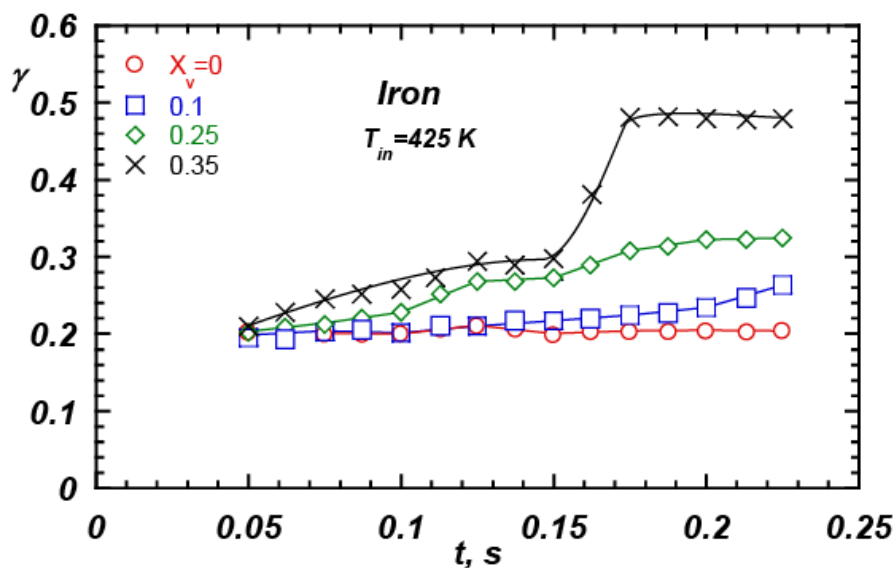


Figure 4.19: Polarization ratio as a function of residence time at  $T_{in}=425\text{ K}$

For  $X_v=0.35$  from  $t=0.05s$  to  $t=0.15s$   $\gamma$  value was slightly higher than that measured for iron particles. At  $t$  higher than  $0.15s$  polarization ratio increased and reached a value of  $0.48$  at  $t=0.175s$  showing then a plateau of  $0.48$  up to  $t = t_{res}$

For  $X_v=0.25$   $\gamma$  increased continuously with residence time and reaches a value of  $0.3076$  at  $t=t_{res}$ .

For  $X_v=0.10$  polarization ratio was constant at a value slightly higher than iron particle for  $t$  higher than  $0.15$  s. The absence of a sudden signal increase testifies that the nucleation and growth processes are very slow.

The polarization ratio trend at  $X_v=0.25$  and  $X_v=0.1$  did not demonstrate the step increase seen for lower inlet temperature condition cases. Instead, it increased smoothly, reaching a maximum value for a  $t=t_{res}$ . Additionally, these  $\gamma$  profiles reported in figure 5.6 were delayed compared with the curve at  $T=405K$ , while retaining nearly the same shape and values.

- **Nickel Particles**

To further characterize the effect of particles wettability on the onset of particles growth process nickel particles, which present the lower contact angle ( $\theta=20^\circ$ ), with the respect to iron and graphite particles, are fed to the chamber. In this case the aerosol generator was operated with nickel electrodes with a spark discharge frequency of  $210$  Hz and a carrier feed of Ar of  $3.5$  l/min. At these conditions, a mono-dispersed particle distribution with the maximum at  $D_p=150$  nm was observed after analyzing with a Z-Sizer Nano (Malvern). This diameter corresponds to a particle number density of  $2 \cdot 10^7$  particles/cm<sup>3</sup>. Figure 4.20 shows the value of  $\gamma$  evaluated at  $T_{in}=375$  K for the four values  $X_v$ .

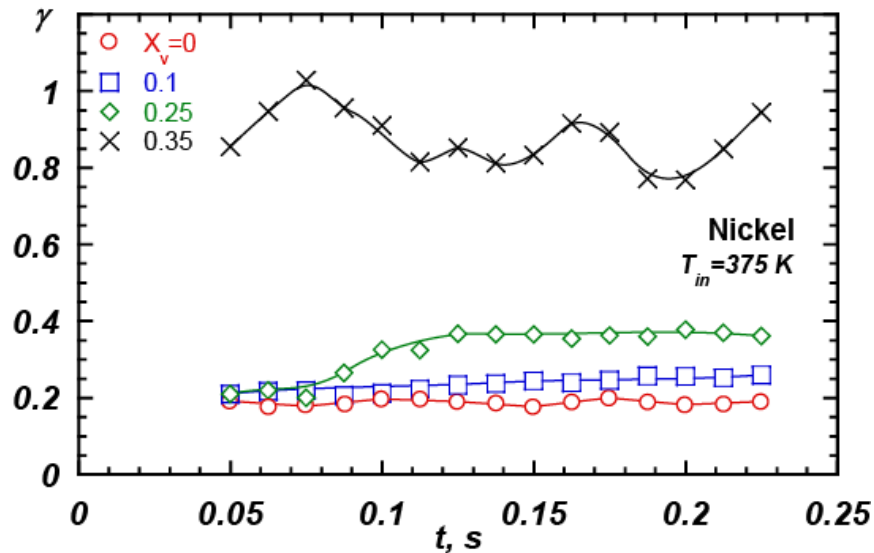


Figure 4.20: Polarization ratio as a function of residence time at  $T_{in}=375$  K

For  $X_v=0$  the value of  $\gamma$  is almost constant with the residence time of approximately 0.2, consistent with the particle size of the feed stream. This trend suggests that coagulation occurring among the nickel particles is negligible. Although the theoretical value of the polarization ratio should be equal to zero for particle light scattering described by the Rayleigh model, the experimental literature values of the ratio collected at  $90^\circ$  range between 0.01 and 0.1, due to the finite collecting angle of the diagnostic system. This deviation from the theoretical value is due to the optical properties of the nickel particles.

For  $X_v=0.35$  at  $t=0.05$ s polarization ratio value was 0.85 very higher than that measured for nickel particles (i.e.  $x_v=0$  case). At  $t$  higher than 0.05s  $\gamma$  sharply increased and reached the value of 1.028 at  $t=0.075$ s. This behaviour indicates that the nucleation process was already activated at  $t$  lower than 0.05s. At  $t$  higher than 0.075 s polarization ratio showed an oscillating trend up to  $t=t_{res}$ . As showed for the iron particles, nickel particles have an induction time lower than carbon particles. This behaviour suggest that particles wettability improves the interaction between the condensing water vapour and solid substrate.

For  $X_v=0.25$  from  $t=0.05$ s to 0.075s  $\gamma$  was constant at value of approximately 0.21. This trend suggests that there is no significant change in the scatteres' dimension. At  $t$  higher than

0.075 s  $\gamma$  slowly increased and reached its maximum value of 0.36 at  $t=0.125$  s, showing a plateau of 0.36 up to  $t=t_{res}$ . This trend suggests that the system is reaching an equilibrium condition where no further change in droplet diameter can occur.

For  $X_v=0.10$   $\gamma$  value was slightly higher than that measured for nickel particles. In this condition polarization ratio slowly increased and reached the value of 0.255 at  $t=0.187$  s.

An increase in the inlet temperature delayed characteristics time of particles growth process, as seen from profiles shown in Figs. 4.21 and 4.22, where  $\gamma$  measured for a  $T_{in}$  of 405 K and 425 K are reported.

Figure 4.21 shows the value of  $\gamma$  evaluated at  $T_{in}=405$  K for the four values of  $X_v$ .

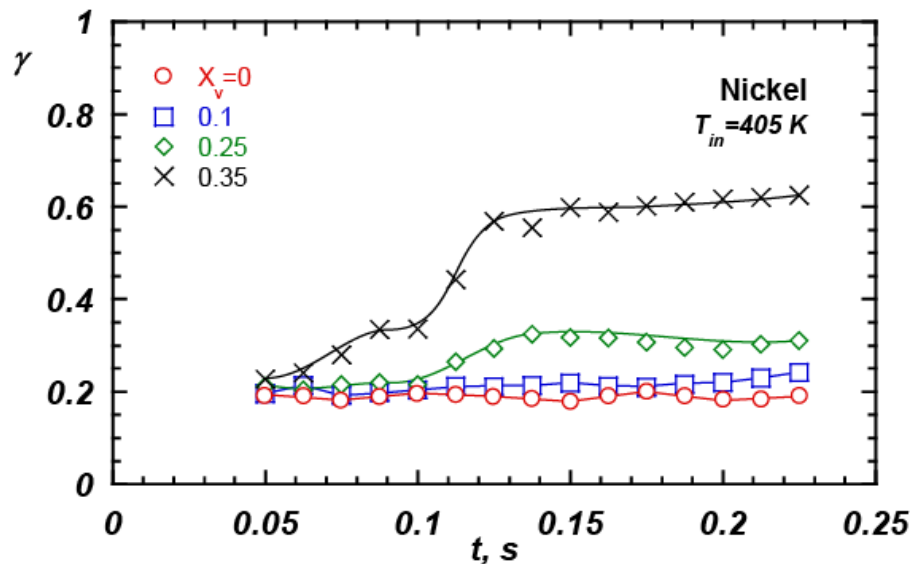


Figure 4.21: Polarization ratio as a function of residence time at  $T_{in}=405$  K

For  $X_v=0.35$  from  $t=0.05$  s to  $t=0.06$  s  $\gamma$  was quite constant a value slightly higher than that measured at  $x_v=0$ . At  $t$  higher than 0.6 s  $\gamma$  rapidly increased and reached a value of 0.55 at  $t=0.135$  s with an additional slight increase up to  $t=0.225$  s. This behavior indicates that the nucleation process was suddenly activated, and the surface growth and coalescence lead to the formation of larger droplets.

For  $X_v=0.25$  from  $t=0.05$  s to  $t=0.1$  s  $\gamma$  was almost constant at a value of about 0.21. At  $t$  higher than  $t=0.1$   $\gamma$  slowly increased and reached its maximum value of 0.32 at 0.1375 s, showing then a plateau of 0.3 up to  $t=t_{res}$ . This trend suggests that the nucleation and growth

processes are slow leading the system to an equilibrium condition where no further change in droplet diameter can occur.

Different consideration apply to profile collected at  $X_v=0.1$ . In this case  $\gamma$  monotonically increased reaching a plateau of 0.24 at  $t=0.225$ . The absence of a sudden signal increase and the presence of a plateau testify that the nucleation and growth processes are very slow and the change in droplet size is much smaller with respect to the cases with higher vapor concentration.

Figure 4.22 shows the value of  $\gamma$  evaluated at  $T_{in}=425$  K for the four values of  $X_v$ .

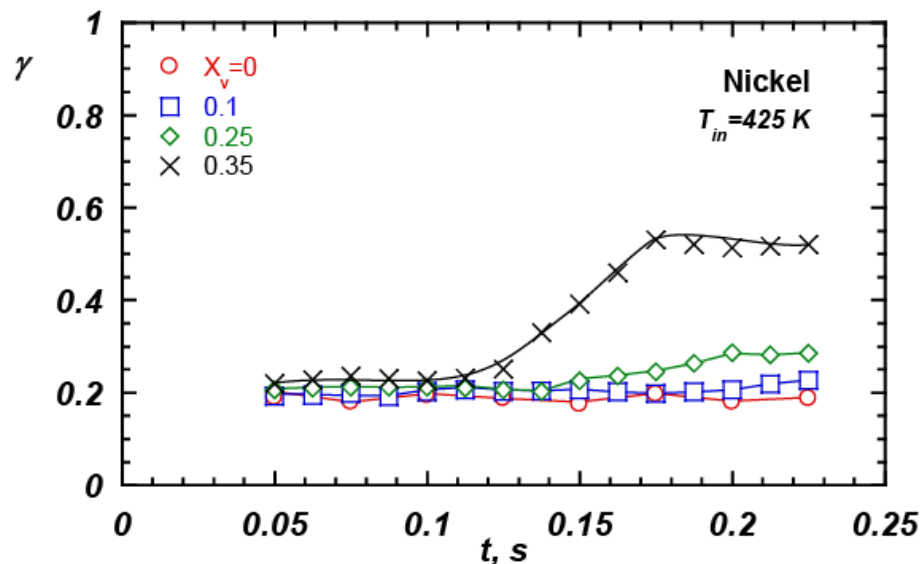


Figure 4.22: Polarization ratio as a function of residence time at  $T_{in}=425$  K

For  $X_v=0.35$ , from  $t=0.05$  s to  $t=0.135$  s,  $\gamma$  was constant at a value slightly higher than that measured for  $X_v=0$ . This trend suggests that up to  $t=0.135$  s there is no significant change in the scatterers dimension. For  $t$  higher than 0.135 s, the polarization ratio increased and reached a value of about 0.53 at  $t=0.175$  s, testifying that the scatterer diameters significantly increased. This behaviour indicates that the nucleation process was activated and the surface growth and coalescence lead to the formation of larger droplets. At  $t$  higher than 0.175 s polarization ratio showed a plateau of about 0.5 suggesting that the system is reaching an equilibrium condition where no further change in droplet diameter can occur.

For  $X_v=0.25$  polarization ratio monotonically increased with residence time and reached a value of 0.285 at  $t=0.2$  s. The polarization ratio trend at  $X_v=0.25$  did not demonstrate the step increase seen for higher vapour concentration condition. Same consideration for  $X_v=0.10$  condition, but in this case polarization ratio reached a maximum value of approximately 0.226.

### 4.3 Effect of particles number concentration

- Graphite particles

In order to analyse the effect of particles number concentration on characteristic time of particle growth process, experimental tests were carried out by varying particles number concentration fed to the chamber. The aerosol generator was operated with graphite electrodes with a spark discharge frequency of 90 Hz and 150 Hz respectively, and a carrier feed of Ar of 5 l/min. At these conditions, a mono-dispersed particle distribution with the maximum at  $D_p=150$  nm was observed after analyzing with a Z-Sizer Nano (Malvern). This diameter corresponds to a particle number density of  $6 \cdot 10^7$  and  $1 \cdot 10^8$  particles/cm<sup>3</sup> respectively. In order to assure the same fluid-dynamic condition with the respect to the previous tests only a fraction of carrier gas from the spark generator is send to the chamber. Further more the increment of spark frequency does not influence the particles dimension as shown from the linear profile of  $I_{VV}$  reported in Figure 4.23

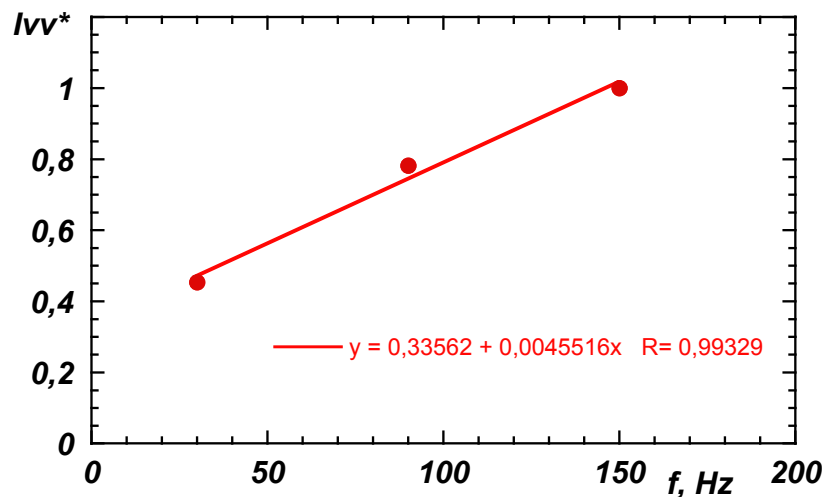


Figure 4.23: trend of the vertical component of the elastically scattered light as function spark frequency of particles generator (i.e. particles number concentration)

In the following diagram, showed in Figure 4.24, the experimental values of polarization ratio are reported for four value of vapour molar fraction, for  $T_{in}=405$ K and for a spark frequency of aerosol generator  $f=90$  Hz

For  $X_v=0$  the value of  $\gamma$  was almost constant with the residence time at a value of approximately 0.1, consistent with the particle size of the feed stream. This trend suggests that coagulation occurring among the carbon particles is negligible.

For  $X_v=0.35$  from  $t=0.05$  s to  $t=0.1375$  s  $\gamma$  was almost constant at value of approximately 0.1. At  $t$  higher than  $t=0.1375$  s polarization ratio increased and reached a value of 0.29 at  $t=0.1625$  s. This behaviour indicates that the process was activated and surface growth and coalescence lead to the formation of larger droplets. It is worth noting that for the same operating conditions, ( $T_{in}=405$  K  $X_v=0.35$ ) an increase of particle number concentration results in a their lower coverage degree from water vapour. The maximum value of polarization ratio reached in this condition is lower than that measured for graphite particles at  $f=30$  Hz.

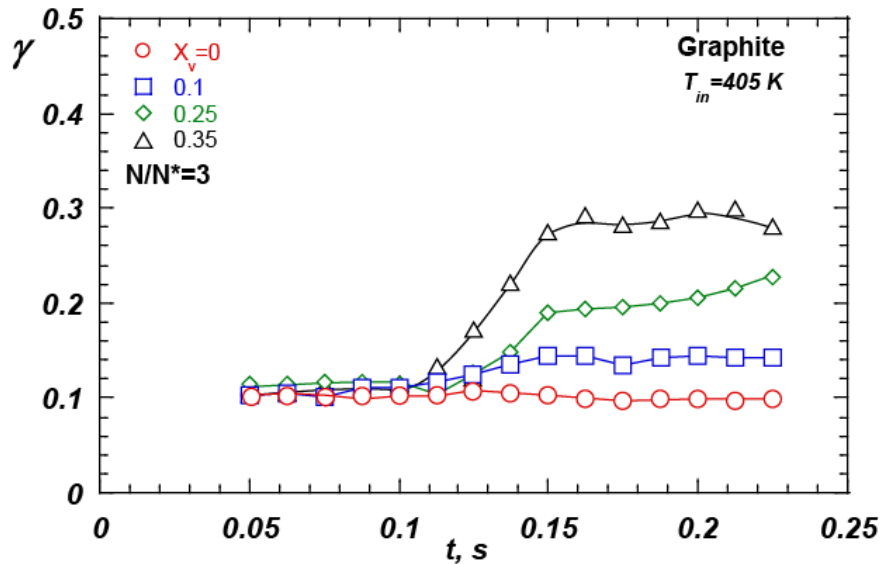


Figure 4.24: Polarization ratio as a function of residence time at  $T_{in}=405$  K ( $f=90$ Hz)

For  $X_v=0.25$  from  $t=0.05$  s  $\gamma$  value was slightly higher than 0.1 up to  $t=0.1125$  s. At  $t$  higher than 0.1125 s  $\gamma$  continuously increased and reached the maximum value of 0.22 at  $t=t_{res}$ . The absence of a sudden increase in signal suggests that the nucleation and growth processes are slow.

For  $X_v=0.10$   $\gamma$  slowly increased with the residence time and reached a plateau of circa 0.15 at  $t=t_{res}$ . Figure 4.25 shows the polarization ratio values obtained at  $T_{in}=405$  K for four values of vapour concentration and for a spark frequency  $f=150$  Hz

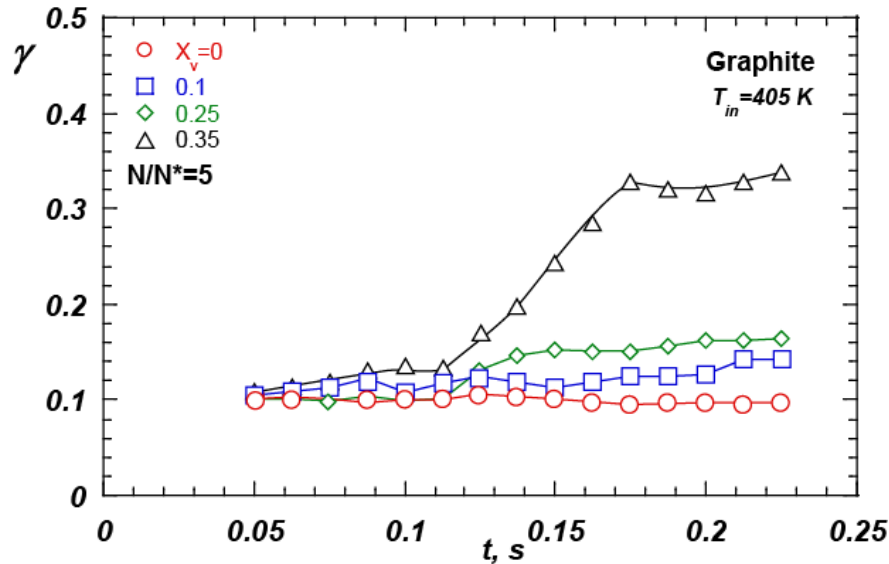


Figure 4.25: Polarization ratio as a function of residence time at  $T_{in}=405$  K ( $f=150$ Hz)

For  $X_v=0$  the value of  $\gamma$  is almost constant with the residence time of approximately 0.1, consistent with the particle size of the feed stream.

For  $X_v=0.35$  from  $t=0.05$  to  $t=0.1375$  s  $\gamma$  was almost constant at value of approximately 0.1. At  $t$  higher than  $t=0.1375$  s polarization ratio rapidly increased and reached the value of 0.32 at  $t=0.175$  s. This behaviour indicates that the growth process was activated, and surface growth and coalescence lead to the formation of larger droplets.

For  $X_v=0.25$  from  $t=0.05$  s to  $t=0.1125$  s  $\gamma$  was constant at a value slightly higher than that measured at  $x_v=0$ , then it smoothly increased and reached a value of 0.16 at  $t=t_{res}$ . It is worth noting that for the same operating conditions, an increase of the numerical concentration of the particles results in a their lower coverage degree from water vapour. This trend is particularly noticeable observing the polarization ratio profile for  $X_v=0.25$  at  $f=90$  and  $f=150$  Hz respectively.

For  $X_v=0.10$   $\gamma$  was constant with the residence time at a value very close to that measured for graphite particle and reached the maximum value of 0.13 at  $t=t_{res}$ .

#### **4.4 Effect of particle dimension**

- Graphite particles

In order to assess the effect of particle dimensions on collection mechanism, in particular to analyze the effect that this parameter has on the characteristic time of particles growth process graphite particles with a mono-dispersed particle distribution with the maximum at  $D_p=10$  nm is fed to the chamber. To achieve these particle size distribution the aerosol generator was operated with graphite electrodes with a spark discharge frequency of 3 Hz and a carrier feed of Ar of 3.5 l/min.

Figure 4.26, shows  $\gamma$  values obtained for three different value of vapour fraction ( $X_v=0,0.25,0.35$ ) and for  $T_{in}=375$  K.

For  $X_v=0$   $\gamma$  is quite constant with the residence time of approximately 0.1, consistent with the particle size of the feed stream. This trend suggests that coagulation occurring among the carbon particles is negligible.

At  $X_v=0.35$  for  $t$  higher then 0.05 s  $\gamma$  rapidly increased from 0.2 up to of 0.79 at  $t=0.1$  s. This behaviour indicates that the process was suddenly activated, and surface growth and coalescence lead to the formation of larger droplets.

For  $X_v=0.25$  from  $t=0.05$ s  $t= 0.1875$ s.  $\gamma$  value was slightly higher than 0.21 up to At  $t$  higher 0.1875 s  $\gamma$  increased and reached the value of 0.4 at  $t=0.2$  s. Then  $\gamma$  reached a plateau of 0.4

up to  $t=t_{res}$ . This behaviour suggest that the system is reaching an equilibrium condition where no further change in droplet diameter can occur.

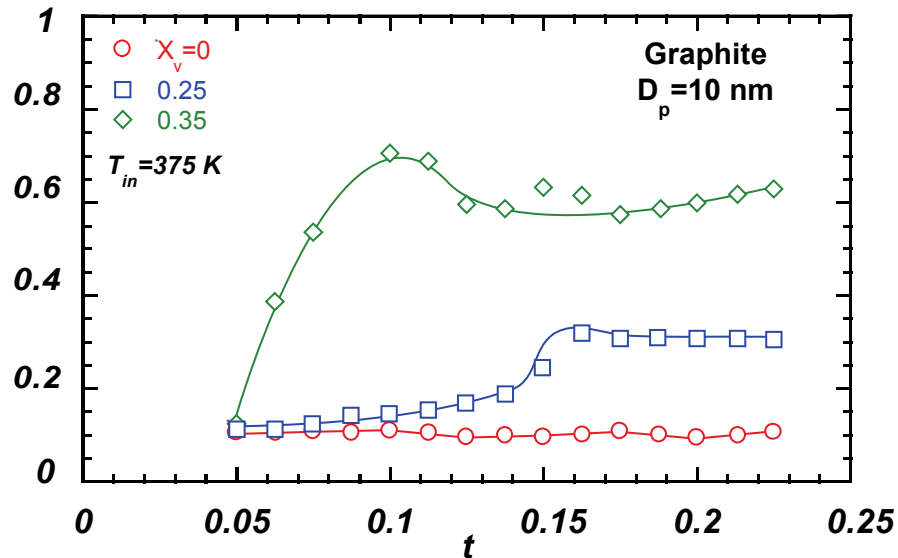


Figure 4.26: Polarization ratio as a function of residence time at  $T_{in}=375$  K ( $f=3$ Hz)

#### 4.5 Effect of vapour concentration

- *Graphite particles*

In order to assess the effect of vapor concentration on particles activation and coverage, i.e. effect of vapor concentration on characteristic time of the particle growth process and final droplet size. Experimental tests were carried out by varying the inlet vapor concentration from  $X_v=0$  up to  $X_v=0.7$ , keeping constant the others parameter such as inlet temperature, particles diameter and particles number concentration. Figure 4.27 shows the polarization ratio values as function of residence time obtained for  $T_{in} = 405$  K,  $D_p=150$ nm and  $N=2 \cdot 10^7$  #/cm<sup>3</sup>

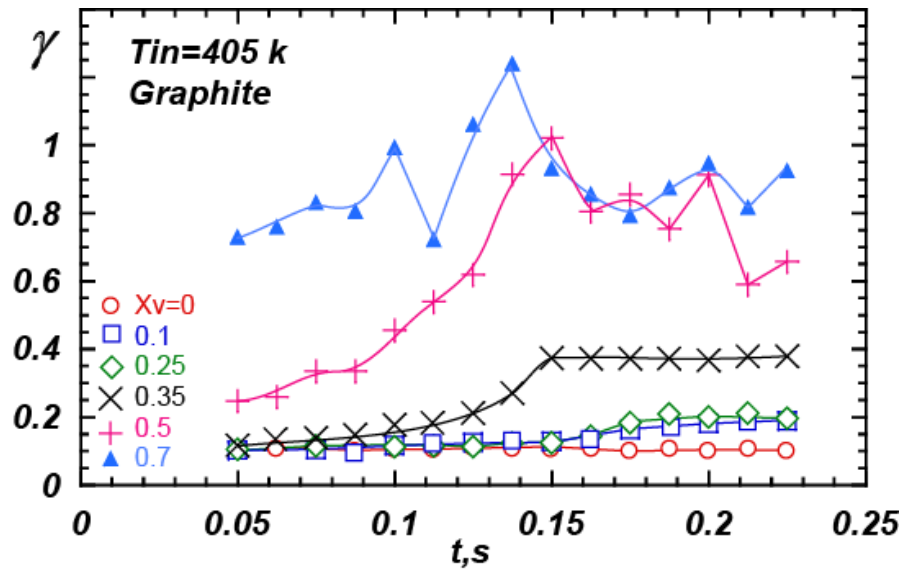


Figure 4.27: Polarization ratio as a function of residence time at  $T_{in}=405$  K

For  $X_v=0$  the value of  $\gamma$  is almost constant with the residence time approximately of 0.1, consistent with the particle size of the feed stream. This trend suggests that coagulation occurring among the carbon particles is negligible.

For  $X_v=0.1$ ,  $\gamma$  monotonically increased, reaching a plateau of 0.18 at  $t=0.225$  s. The absence of a sudden increase in signal and the presence of a plateau suggest that the nucleation and growth processes are very slow, leading the system to an equilibrium condition where no further change in droplet diameter can occur.

For  $X_v=0.25$   $\gamma$  value was very similar to that soot particles from  $t=0.05$  s to  $t=0.15$  s. At  $t$  higher than 0.1 s polarization ratio slowly increased and reached a value of 0.2 at  $t=t_{res}$ .

The condensation process was clearly present, as suggested by the profile of the polarization ratio measured in the presence of higher vapor concentration.

For  $X_v=0.35$  from  $t=0.05$  s to  $t=0.1$  s polarization ratio value was slightly higher than that measured for  $X_v=0$ . This trend suggests that there was no significant change in the scatterers' dimensions. For  $t$  higher than 0.1 s  $\gamma$  sharply increased and reached a value of 0.36 at 0.15 s then showing a plateau up to  $t=t_{res}$ .

For  $X_v=0.5$  At  $t=0.05$ s polarization ratio value was 0.2 slightly higher than that measured for graphite particles then it continuously increased up to  $t=0.15$  s and reached a value of approximately 1. At  $t$  higher than  $t=0.15$  s polarization ratio showed an oscillation trend while it decreased to a value of about 0.6 at  $t=t_{res}$ .

This behavior suggests that the nucleation process is active leading to the formation of larger droplet with the respect to lower vapor concentration cases.

For  $x_v=0.7$  at  $t=0.05$  s polarization ratio value was of about 0.7 very higher than that measured for graphite particles. This suggest that the nucleation process is already activated. At  $t$  higher than 0.05 s polarization ratio continuously increased and reached a value of approximately 1 at  $t=0.125$  s, then again, it shows as in the previous case, an oscillating behaviour while it decreased, and reached a value of 0.95 a  $t=t_{res}$ .

Figure 4.28 shows the polarization ratio profiles as function of residence time obtained for  $T_{in}=375$  K,  $D_p=150$ nm,  $N=2 \cdot 10^7$  #/cm<sup>3</sup> and varying vapor inlet concentration to  $x_v=0$  up to  $x_v=0.7$ .

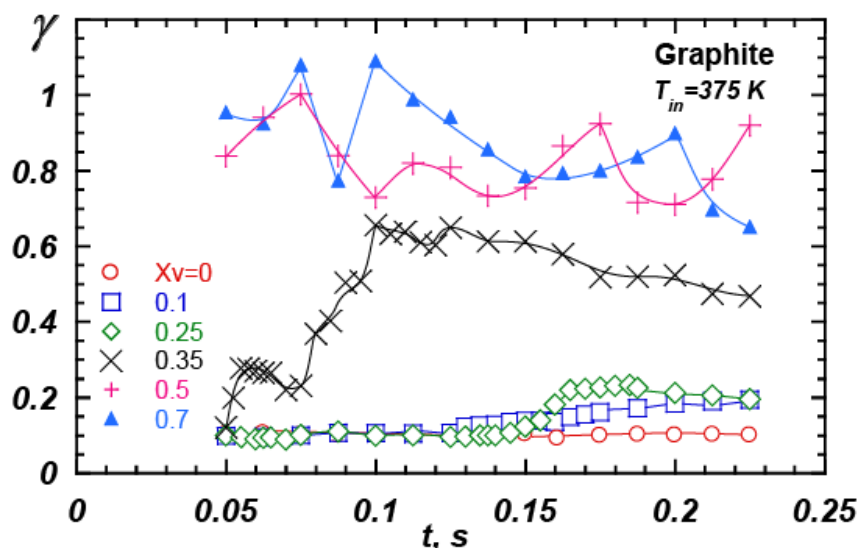


Figure 4.28: Polarization ratio as a function of residence time at  $T_{in}=375$  K

For  $X_v=0$  the value of  $\gamma$  is almost constant with the residence time approximately of 0.1, consistent with the particle size of the feed stream. This trend suggests that coagulation occurring among the carbon particles is negligible.

For  $X_v=0.1$ ,  $\gamma$  monotonically increased, reaching a plateau of 0.2 at  $t=0.225$  s. The absence of a sudden increase in signal and the presence of a plateau suggest that the nucleation and growth processes are very slow, leading the system to an equilibrium condition where no further change in droplet diameter can occur.

For  $X_v=0.25$   $\gamma$  value was very similar to that measured for soot particles up to  $t=0.125$ s. At  $t$  higher than 0,125 s polarization ratio increases slowly and reaches the value of 0.24 at  $t=t_{res}$ . The condensation process was clearly present, as suggested by the profile of the polarization ratio measured in the presence of higher vapor concentration. For  $X_v=0,35$  at  $t=0.05$ s polarization ratio value was very similar to that measured for  $X_v=0$ . For  $t$  higher than 0.05 s  $\gamma$  sharply increased and reached a value of 0.558 at 0.075 s then it presents an almost constant value up to  $t=t_{res}$ .

For  $X_v=0.5$  At time equal to 0.05s polarization ratio have a value of 0.8 higher than graphite particles. At time higher than 0.05 s polarization ratio grows and reaches a value of approximately 1 at  $t=0.07$ , then it shows an oscillating behavior with residence time and reaches a value approximately of 0.95 at  $t=t_{res}$ .

This behavior suggests that the nucleation process is already active at  $t=0.05$ s, leading to the formation of larger droplet with the respect to lower vapor concentration cases.

For  $x_v=0.7$  at  $t=0.05$  s value of about 0.95 higher than graphite particles. This suggest that the nucleation process is already active. For  $t$  higher than 0.05 s polarization ratio grows continuously and reached a value of approximately 1 at  $t=0.07$  s, then it shows an oscillating behaviour while it decreased and reaches a value of 0.65 a  $t=t_{res}$ .

Figure 4.29 shows the polarization ratio profiles as function of residence time obtained for  $T_{in}=375\text{ K}$ ,  $D_p=150\text{nm}$  (iron particles),  $N=2 \times 10^7\text{ \#/cm}^3$  and varying vapor inlet concentration to  $x_v=0$  up to  $x_v=0.7$ . For  $x_v=0$  the value of  $\gamma$  is almost constant with the residence time approximately of 0.2, consistent with the particle size of the feed stream. This trend suggests that coagulation occurring among the carbon particles is negligible.

For  $x_v=0.1$ ,  $\gamma$  monotonically increased, reaching a plateau of approximately 0.36 at  $t=0.225\text{ s}$ . The absence of a sudden increase in signal and the presence of a plateau suggest that the nucleation and growth processes are very slow, leading the system to an equilibrium condition where no further change in droplet diameter can occur.

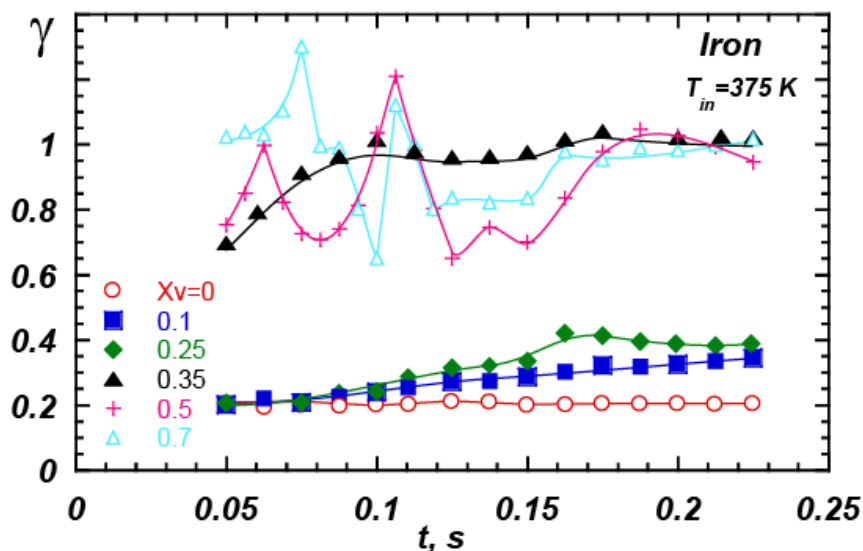


Figure 4.29: Polarization ratio as a function of residence time at  $T_{in}=375\text{ K}$

For  $x_v=0.25$   $\gamma$  value was very similar to that measured for iron particles up to  $t=0.1\text{ s}$ . At  $t$  higher than  $0.1\text{ s}$  polarization ratio increases slowly and reaches the value of 0.4 at  $t=t_{res}$ .

The growth process was clearly present, as suggested by the profile of the polarization ratio measured in the presence of higher vapor concentration. For  $x_v=0.35$  at  $t=0.05\text{ s}$  polarization ratio value was 0.62. For  $t$  higher than  $0.05\text{ s}$   $\gamma$  increased and reached a value of 0.98 at  $0.09\text{ s}$  then it presents an almost constant value up to  $t=t_{res}$ .

For  $X_v=0.5$  At time equal to 0.05s polarization ratio have a value of 0.7 higher than iron particles. At time higher than 0.05 s polarization ratio grows and reaches a value of approximately 1 at  $t=0.06$ , then it shows an oscillating behavior with residence time and reaches a value approximately of 0.995 at  $t=t_{res}$ .

This behavior suggests that the nucleation process is already active at  $t=0.05s$ , leading to the formation of larger droplet with the respect to lower vapor concentration cases.

For  $x_v=0.7$  at  $t=0.05$  s value of about 1 higher than iron particles. This suggest that the nucleation process is already active. For  $t$  higher than 0.05 s polarization ratio shows an oscillating behaviour up to  $t=0.15$  s while it disappears and reaches a value of 1 a  $t=t_{res}$ .

Figure 4.30 shows the polarization ratio profiles as function of residence time obtained for  $T_{in}=375$  K ,  $D_p=150nm$  (nickel particles),  $N=2*10^7$  #/cm<sup>3</sup> and varying vapor inlet concentration to  $x_v=0$  up to  $x_v=0.7$ .

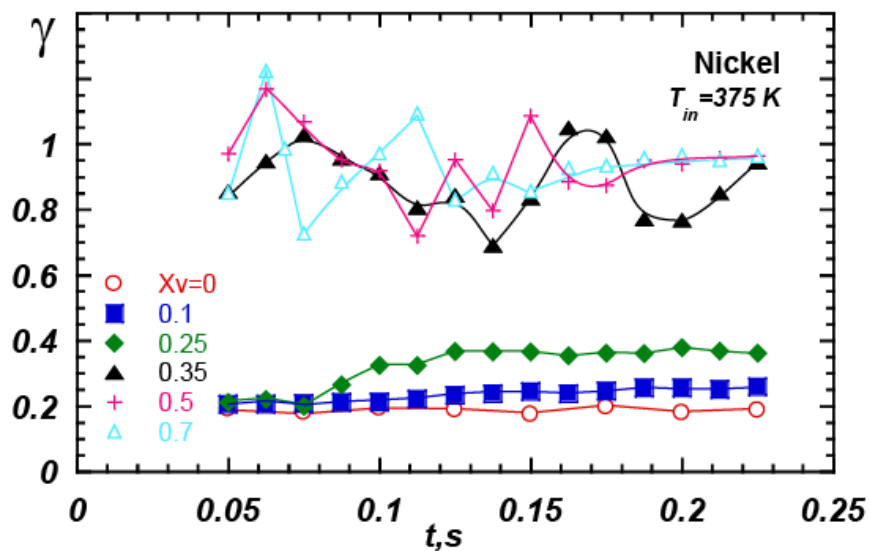


Figure 4.30: Polarization ratio as a function of residence time at  $T_{in}=375$  K

For  $X_v=0$  the value of  $\gamma$  is almost constant with the residence time approximately of 0.2, consistent with the particle size of the feed stream. This trend suggests that coagulation occurring among the carbon particles is negligible.

For  $X_v=0.1$ ,  $\gamma$  monotonically increased, reaching a plateau of approximately 0.22 at  $t= 0.225$  s. The absence of a sudden increase in signal and the presence of a plateau suggest that the nucleation and growth processes are very slow, leading the system to an equilibrium condition where no further change in droplet diameter can occur.

For  $X_v=0.25$   $\gamma$  value was very similar to that measured for iron particles up to  $t= 0.075$ s. At  $t$  higher than 0,075 s polarization ratio increases slowly and reaches the value of 0.38 at  $t=t_{res}$ . The growth process was clearly present, as suggested by the profile of the polarization ratio measured in the presence of higher vapor concentration. For  $X_v=0,35$  at  $t=0.05$ s polarization ratio value was 0.8. For  $t$  higher than 0.05 s  $\gamma$  increased and reached a value of approximately 1 at 0.75 s then it presents an almost oscillating behaviour up to  $t=t_{res}$ .

For  $X_v=0.5$  At time equal to 0.05s polarization ratio have a value of 0.82 higher than nickel particles. At time higher than 0.05 s polarization ratio grows and reaches a value of approximately 1 at  $t=0.06$ , then it shows an oscillating behavior with residence time and reaches a value approximately of 0.95 at  $t=t_{res}$ .

This behavior suggests that the nucleation process is already active at  $t=0.05$ s, leading to the formation of larger droplet with the respect to lower vapor concentration cases.

For  $x_v=0.7$  at  $t=0.05$  s value of about 1 higher than nickel particles. This suggest that the nucleation process is already active. For  $t$  higher than 0.05 s polarization ratio shows an oscillating behaviour up to  $t=0.125$  s while it disappears and reaches a value of 1 a  $t=t_{res}$ .

#### ***4.6 Effect of local conditions***

It is worthwhile to note that  $T$  and  $X_v$  local values are strictly correlated to the local fluid-dynamics field. In order to assess the combined effect of local temperature and vapor concentration conditions on particle growth process, experimental tests were carried out by

measuring the polarization ratio as function of residence time for three values of radial coordinate ( $r=0, 5$  and  $10$  mm). For this purpose the field of view of the signal collection system is reduced by introducing a  $2$ mm pin-hole on the path-length of collected light.

These tests are necessary for a full characterization of the particles growth process, and are also required to assess repeatability and validity of the characteristic times evaluated.

Figure 4.31 shows the polarization ratio profiles as function of residence time for  $T_{in}=375$  K,  $X_v=0.7$  evaluated for three values of radial coordinate  $r=0, 5, 10$  mm. The overall trend of polarization ratio is quite similar with residence time for the three radial coordinate considered. This behavior suggests that by varying radial coordinate the local temperature and vapor concentration conditions change but the evolution of nucleation process is similar for the three condition considered.

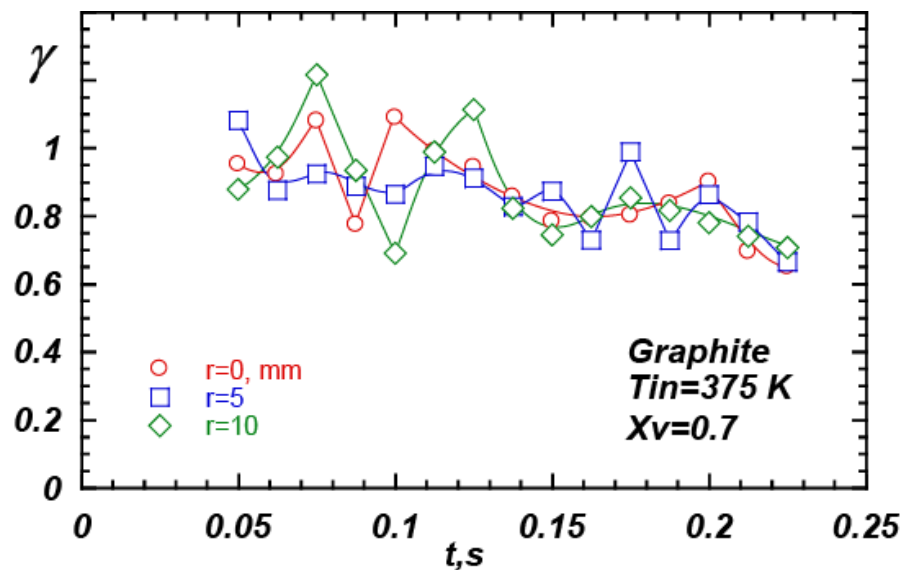


Figure 4.31: Polarization ratio as a function of residence time at  $T_{in}=375$  K and  $X_v=0.7$  by varying radial position of measurement

Same considerations apply to data collected at  $X_v=0.5$ . Figure 4.32 shows the polarization ratio profiles as function of residence time for  $T_{in}=375$  K and  $X_v=0.5$  evaluated for the three values of.

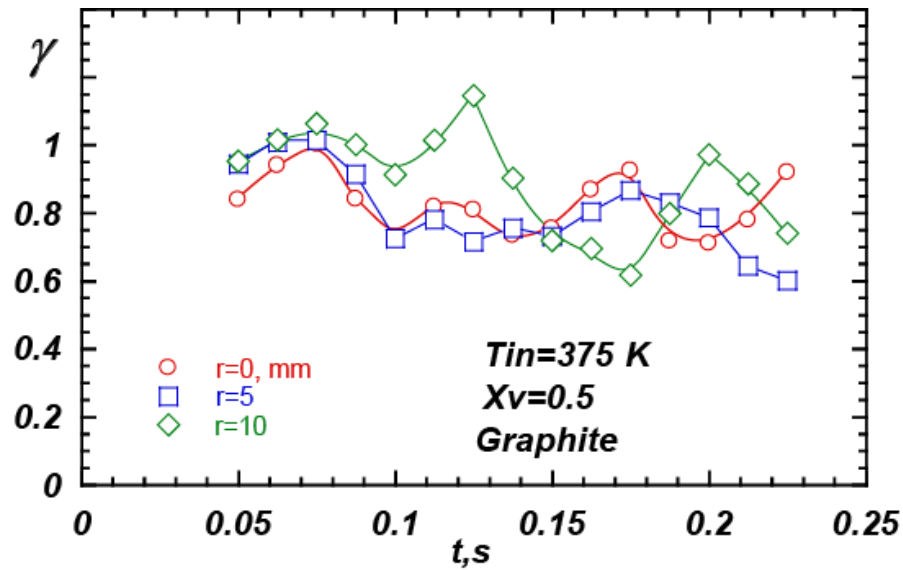


Figure 4.32: Polarization ratio as a function of residence time at  $T_{in}=375$  K and  $X_v=0.5$  by varying radial position of measurement

Figure 4.33 shows the polarization ratio values as function of residence time for  $T_{in}=375$  K,  $X_v=0.35$  evaluated for the three values of radial coordinate  $r=0, 5, 10$  mm. The polarization ratio profile related to  $r=5$  mm showed the minimum induction time and the maximum value of approximately 0.8 at  $t=0.12$  s. Also in this case the overall trend of the particle growth process is similar with residence time for the three radial coordinate considered.

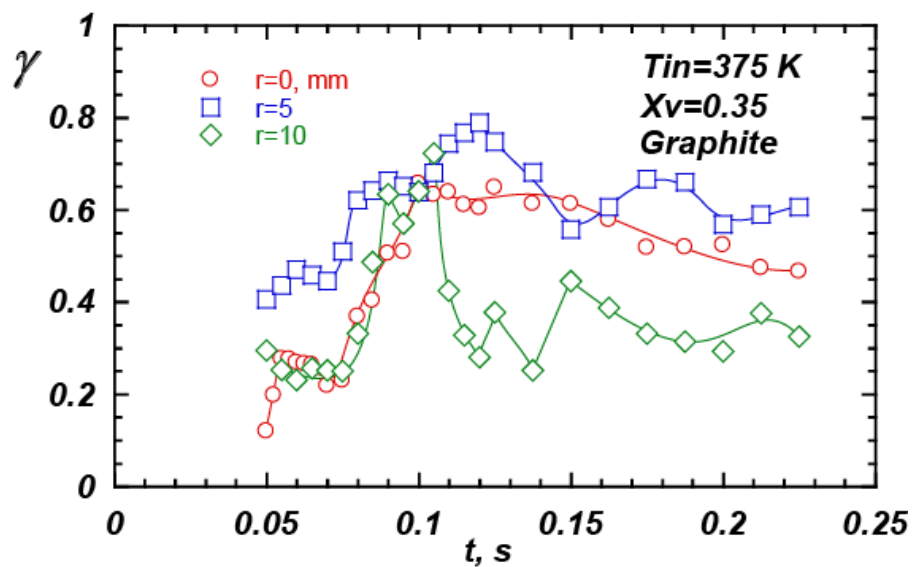


Figure 4.33: Polarization ratio as a function of residence time at  $T_{in}=375$  K and  $X_v=0.35$  by varying radial position of measurement

Figure 4.34 shows the polarization ratio values as function of residence time for  $T_{in}=375$  K,  $X_v=0.25$  evaluated for the three values of radial coordinate  $r=0, 5, 10$  mm. The polarization ratio profile related to  $r=10$  mm shows the minimum induction time and reached the maximum value of approximately 0.35 at  $t=t_{res}$  with the respect to the other polarization ratio profiles reported. Also in this case the overall trend of the particle growth process could be considered quite similar with residence time for the three radial coordinate considered.

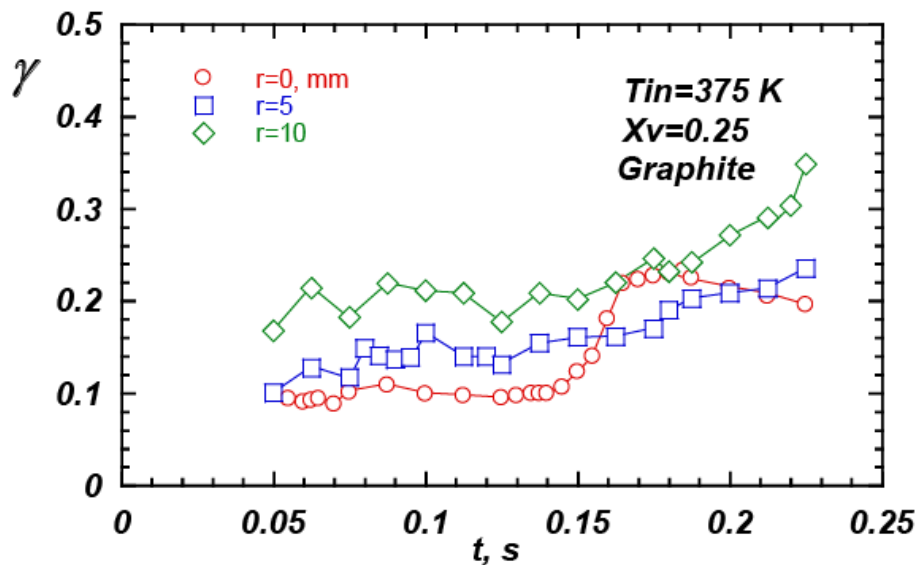


Figure 4.34: Polarization ratio as a function of residence time at  $T_{in}=375$  K and  $X_v=0.25$  by varying radial position of measurement

Figure 4.35 shows the polarization ratio profiles evaluated at  $T_{in}=375$  K and  $X_v=0.1$ . From  $t=0.05$  s up to  $t=0.125$  s polarization ratio profiles related to the three radial coordinate do not show any appreciable difference. At  $t$  higher than  $t=0.125$  s the polarization ratio profile measured at  $r=0$  overcame the polarization ratio profiles evaluated at  $r=5$  and  $r=10$  mm respectively up to  $t=t_{res}$ .

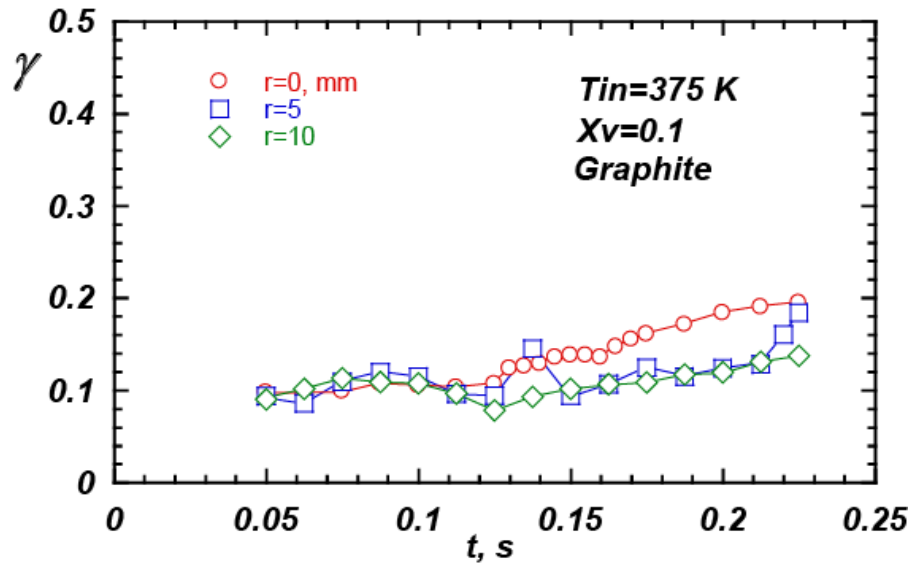


Figure 4.35: Polarization ratio as a function of residence time at  $T_{in}=375$  K and  $X_v=0.1$  by varying radial position of measurement

## ***CHAPTER 5***

### ***Discussion***

In this chapter the main experimental results obtained during this thesis are summarized and discussed. The experimental work was carried out with the aim to characterize the heterogeneous nucleation and growth process of droplets from phenomenological point of view under typical conditions of a practical application that aims to eliminate the particulate present in a flue gas of an industrial process.

Due to the highly specific configurations of the experimental facilities or to highly specific working conditions, the results present in the literature are not easily generalizable to a range of parameters wide enough to be interesting in fields different from the one related to atmospheric issues. In addition, the dependencies of the heterogeneous nucleation and growth of droplet on the single process parameters as well as the evaluation of the characteristic condensation process time are often overestimated. The ranges of parameters of interest in this work are the ones that can be potentially interesting as working condition of a pollutant abatement unit placed downstream a combustion process or a main industrial processes. More specifically, higher temperature and lower vapor concentration conditions with respect to the one analyzed in literature have been taken in to account.

The system used for the study of the evolution of the nucleation and growth process of particles is a laminar flow diffusion chamber. Such configuration was properly chosen because it allows for modulating and controlling the parameters driving the process independently of each other (temperature, vapor concentration, flow velocity, particle concentration and typology) and for spatially resolve in the system regions in which the different phases of the process occur (nucleation, growth of the particles kinetically controlled

and/or by diffusion, aging), in order to identify the characteristic times of the different sub-processes.

So that, implementing the proper diagnostic techniques, it is possible to resolve in time and/or space the process and obtain useful information on the effect of working conditions and particles characteristics on droplet formation and growth process finalized to the optimization of an abatement particle unit.

In the following the results presented in the previous chapter, are discussed on the basis of a phenomenological interpretation allowing for the identification of different steps of condensational growth process. In particular, heterogeneous nucleation on seed particles and its growth with corresponding characteristic times have been identified as function of inlet and local parameters values as well as function of particulate chemical nature.

### ***5.1 Polarization ratio and evolution of condensation process: a scheme of interpretation***

Figure 5.1 shows the trend of polarization ratio of the different particles species (C or Fe or Ni) fed to the chamber as function of axial coordinate for  $X_v=0$ . The trend of polarization ratio profiles showed in Fig. 5.1 suggests that any phenomenon relative to particles size variation, such as coagulation, occurring among the graphite, iron and nickel particles can be neglected negligible.

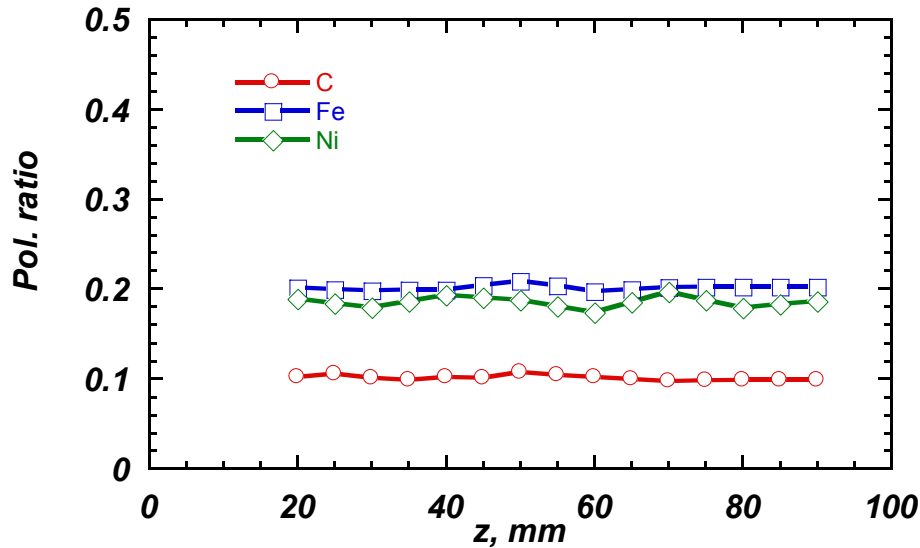


Figure 5.1: Polarization ratio of graphite, iron and nickel particles for  $X_v=0$

Although the theoretical value of the polarization ratio should be equal to zero for particle light scattering described by the Rayleigh model, the experimental literature values of the ratio collected at  $90^\circ$  range between 0.01 and 0.1, due to the finite collecting angle of the diagnostic system. The  $\gamma$  values reported in Fig. 5.1 are consistent with the calculated values after accounting for both the collection system characteristics and the generated particle properties and size distributions. Different considerations apply for iron and nickel particles. The scattered light is influenced by the different optical properties of materials considered i.e. different refractive index.

In the evaluation of evolution of nucleation and growth process, the polarization ratio profiles related to each type of particle, represent a reference condition. By comparing them with polarization ratio profiles measured by varying inlet conditions, any changes of values of polarization ratio with respect to its initial value indicates a size variation of scatterers.

### 5.1.1 Comparison of polarization of particles with a liquid layer.

As described in Chapter 3 the polarization ratio is a complex function of both particle size and its optical properties. This dependence becomes more complicated if the particle involved in

the growth process, varies its size because of a water layer deposition on its surface. In this case the optical properties of the scatterers vary depending on the relative size (i.e. relative volume) between the particle and the covering liquid layer and on the optical properties of particle and the coating material. The comparison among the polarization ratios, related to different typologies of scatterers need of an interpretative scheme that take into account the evolution of the single scatterer itself. The first step is to consider a model for the evaluation of the optical properties of composite particles in order to clarify whether the comparative evaluation of polarization ratios can be effective. As summarized in Table 3. In this work the Bruggeman approximation (Eq 3.40) has been used to evaluate the refractive index of the composite sphere formed by an adsorbing sphere (in this case graphite, iron and nickel) in a water droplet by varying the volume ratio  $f$  of the inclusion.

The values of refractive index calculated by Bruggeman approximation have been used for the evaluation of polarization ratio of the composite sphere potentially present in the control volume.

Figure 5.2 shows the trends of the polarization ratio as function of scatterer diameter consisting of a water droplet hosting an absorbent particle, in this case a graphite particle. These profiles are parametric in the volume ratio  $f$  of the particle included in the water droplet. As comparison Figure 5.2 also shows polarization ratio profiles of graphite (host particle) and water (coating species).

It appears that starting from a value of  $f = 0.1$  the polarization profiles of the composite particle coincide with that of the water in the range of size considered. This means that for a particle of 150 nm, a layer approximately of 90 nm makes the composite sphere optically behave as a water droplet.

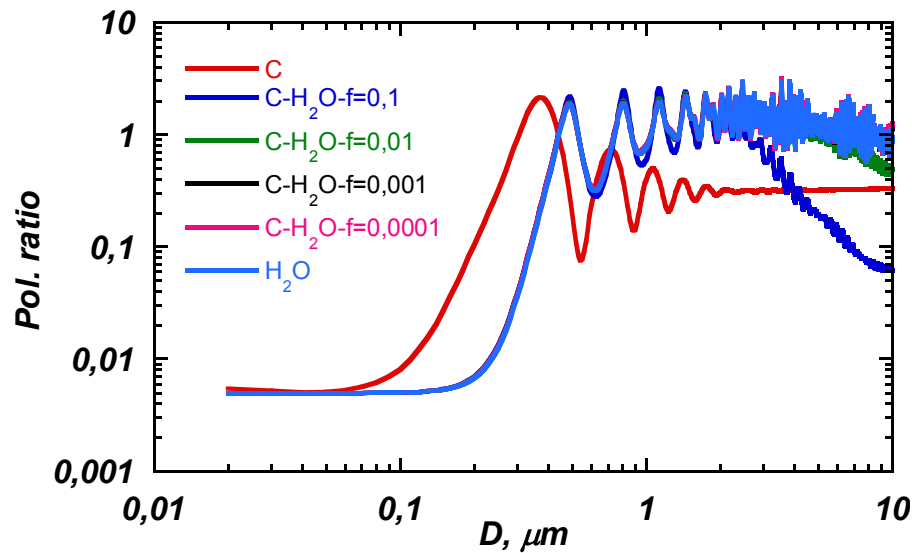


Figure 5.2:  $\gamma$  evaluated for water droplets, graphite particle and composite sphere

Figure 5.3 shows the trends of the polarization ratio as function of scatterer diameter consisting of a water droplet that hosts an iron particle. These profiles are parametric in the volume ratio  $f$  of the particle included in the water droplet. Figure 5.3 also shows polarization ratio profiles of iron (host particle) and water (coating species).

It clearly appears that from a value of  $f = 0.01$  the polarization ratio profiles of the composite particle coincide with those of the water in the range of dimensions considered. Again these results show that the composite sphere optically behaves as a water droplet for a volume ratio value  $f$  higher with the respect of graphite particle. This behavior is essentially due to different refractive index of iron with respect to graphite.

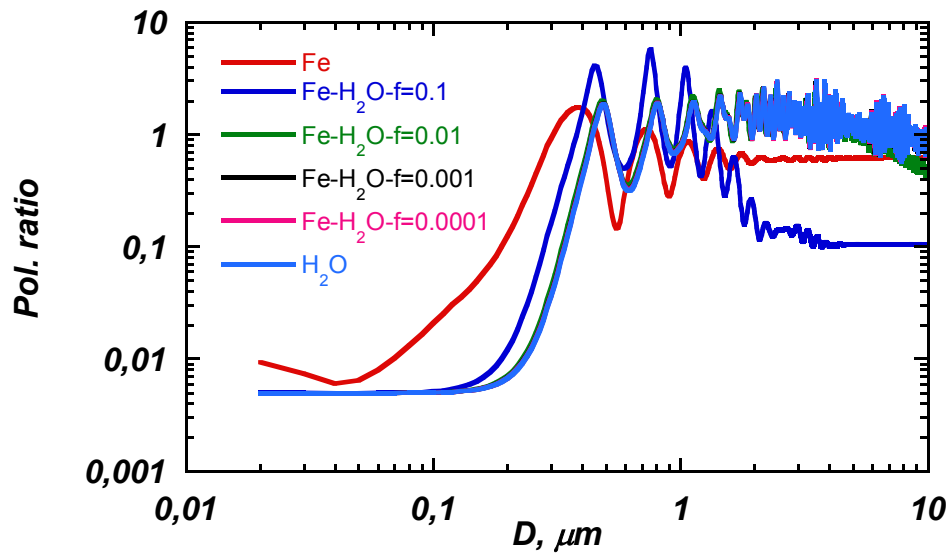


Figure 5.3:  $\gamma$  evaluated for water droplets, iron particle and composite sphere parametric in  $f$

Same considerations apply to a composite sphere constituted by an nickel host particle in a water droplet. In Figure 5.4 the trends of the polarization ratio as function of scatterer diameter water droplet hosting a nickel particle have been reported.

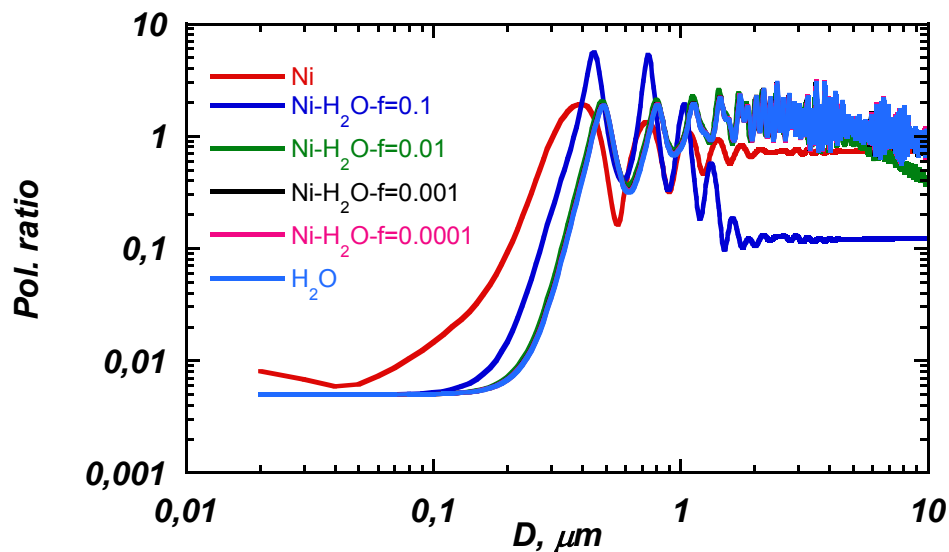


Figure 5.4:  $\gamma$  evaluated for water droplets, nickel particle and composite sphere parametric in  $f$

The results shows in Figure 5.2, 5.3 and 5.4 are summarized in Figure 5.5.

Figure 5.5 shows the polarization ratio profiles of water droplet in comparison with those of composite sphere constituted by a water drop hosting a graphite, iron and nickel particle respectively for a value of  $f=0.01$ .

The results show that for a volume ratio of the inclusion of 0.01, the solid particles coated by a water layer presents optical properties very similar to a water droplet. This result has great implication because it allows for comparing the size of the droplets regardless of the nature of host particle present in the water drops if the volume ratio of inclusion is equal or higher than 0.01.

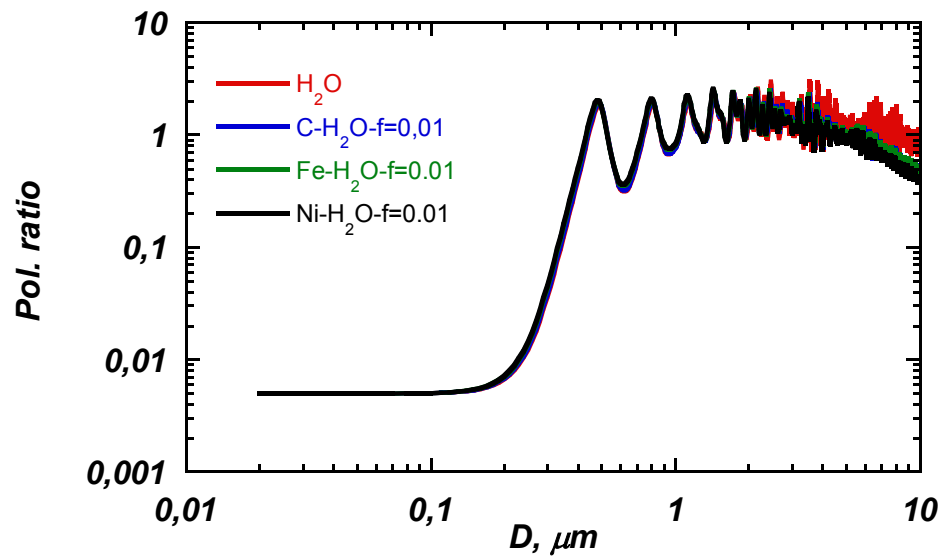


Figure 5.5  $\gamma$  evaluated for water droplets, and composite sphere for  $f=0.01$

This behavior is due to the dependence of refractive index of layer thickness, as shown in Figure 5.6 and 5.7. Figure 5.6 and 5.7 report respectively the trends of the real and the imaginary part of the complex refractive index of a composite sphere evaluated by Bruggeman approximation (Eq 3.40). For  $f=1$  the values reported in the figure correspond to the refractive index of particles, by varying  $f$  from 1 to 0.0001 the real part of the refractive index of particles tends to that of water droplet, while the imaginary part tends to zero. This behavior indicates that the optical properties of particles approach optical properties of water droplet when the particles are coated by a liquid layer.

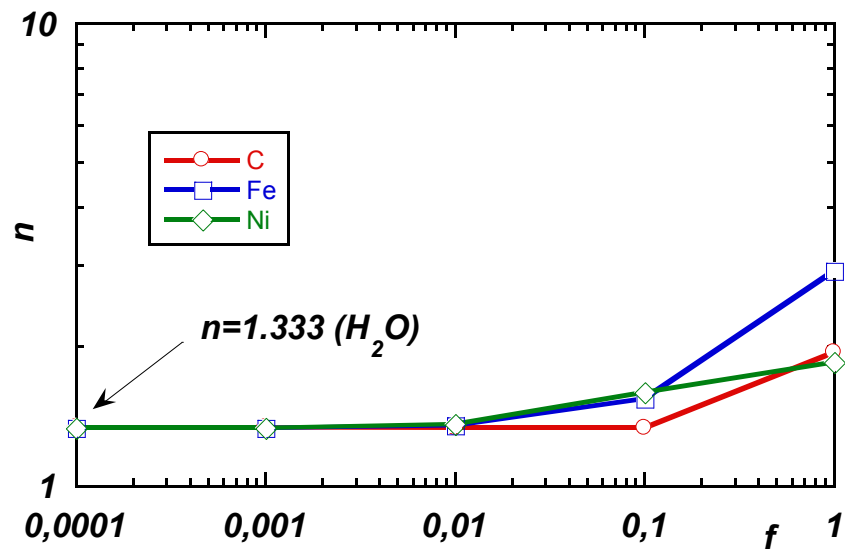


Figure 5.6: Real part of complex refractive index for composite sphere

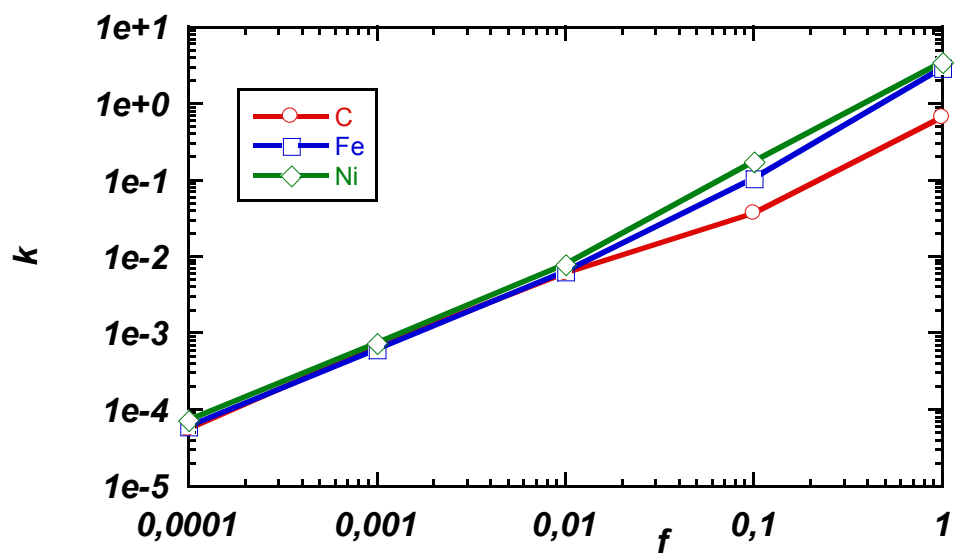


Figure 5.7: Imaginary part of complex refractive index for composite sphere

### 5.1.2 Qualitative spatial/temporal evolution of condensation process

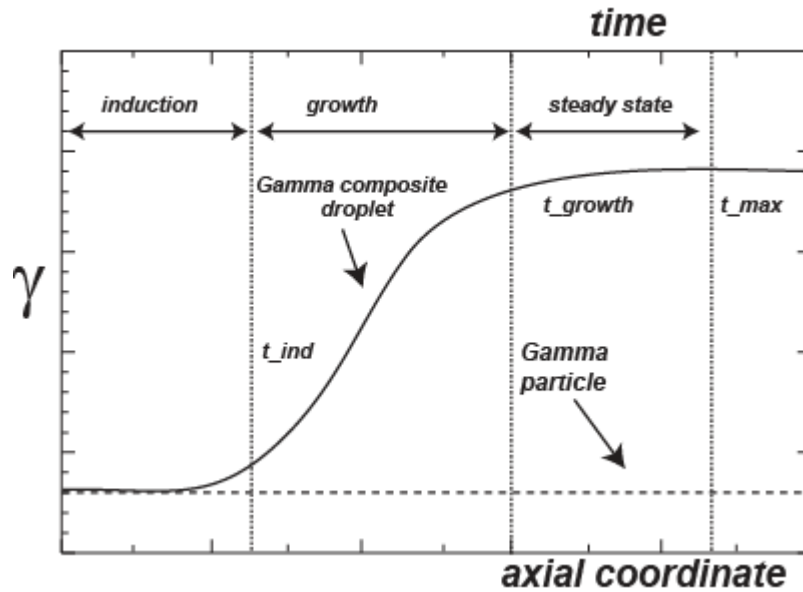


Figure 5.8: Qualitative trend of polarization ratio of a particle (dashed line) and a activated particle condensation (solid line)

The Figure 5.8 shows qualitatively a typical spatial trend of the polarization ratio in two different conditions. The dashed profile shown corresponds to the case when only the particles and the carrier gas are fed to the chamber. As commented before, in this case any phenomenon relative to particles size variation is negligible because the polarization ratio is almost constant in the spatial range considered. The secondary abscissa represents the time axis corresponding to the spatial coordinate, giving that the flow velocity is kept constant at 0.4 m/s

The profile reported by a solid line shows the polarization ratio measured in the case that water vapor is fed to the laminar flow chamber with particles. This trend suggest that scatterer enlarges with respect to its initial dimension because the formation of a liquid layer on particle surface is occurring in the control volume.

Different steps of condensation process can be identified by following the polarization ratio profiles. By analyzing the polarization ratio profile obtained for  $X_v > 0$  and comparing it with that relative to  $X_v = 0$  condition, it is possible to identify an induction step where the

polarization ratio is equal to the one obtained at  $X_v=0$ . The polarization ratio then start to increase at a time (or space) identified as the induction time  $t_{ind}$ , that corresponds to the characteristic time at which the growth process starts. After the nucleation inception, the polarization ratio increases, either steeply or smoothly depending on the condition considered. This trend is related to a complete covering of the particle and/or to an increase of droplet dimension. This occurs up to a time identified as growth time  $t_{growth}$ . Then, the polarization ratio generally reaches a maximum value at steady-state condition at  $t_{max}$ .

For the identification of the characteristic times of the process a general criterion for all conditions tested has been defined. If  $\gamma_{V+P}$  is the polarization ratio measured at  $X_v \neq 0$  and  $\gamma_P$  is the polarization ratio of the particle measured at  $X_v=0$ , the induction time  $t_{ind}$  has been defined as the time (i.e. axial coordinate) in correspondence of which the following condition is satisfied :

$$\frac{\gamma_{V+P} - \gamma_P}{\gamma_{V+P}^{MAX} - \gamma_P} > 0.15 \quad (5.1)$$

where  $\gamma_{V+P}^{MAX}$  is the maximum value reached by polarization ratio measured at  $X_v \neq 0$ . Such threshold values of 0.15 has been chosen on the basis of the mean error value of 10% that affect the light scattering measurement. In a similar way a criterion for identification of the growth time was defined. The growth time is the time at which the following condition is satisfied :

$$\frac{\gamma_{V+P} - \gamma_P}{\gamma_{V+P}^{MAX} - \gamma_P} > 0.9 \quad (5.2)$$

Finally  $t_{max}$  is the time at which the following condition is verified :

$$\frac{\gamma_{V+P}}{\gamma_{V+P}^{MAX}} > 0.95 \quad (5.3)$$

A further condition which must always be checked for a correct interpretation of the characteristic times extrapolated from the analysis of the polarization ratio profiles is the following:

$$t_{ind} < t_{growth} \leq t_{max} \quad (5.4)$$

$t_{max}$  is the less indicative characteristic time of the whole process because in some conditions it is equal to  $t_{growth}$ . These conditions is reached when the polarization ratio profiles shows an oscillating behavior, or when the polarization ratio profiles presents a plateau after reaching its maximum value (step increase), or when the growth time is relatively high and reaches its maximum value at  $t=t_{res}$  (monotonically increase)

## ***5.2 Effect of local conditions: activation processes and saturation conditions***

In the previous chapter the polarization ratios measured along the axial coordinate have been presented in dependence of inlet conditions. However, it is interesting to compare the experimental profile with respect to the local temperature or vapor concentration profiles that are affected by radial heat and mass transport.

Figure 5.9 shows the temperature values measured along chamber axis ( $r=0$ ) for an inlet temperature  $T_{in}=373$  K.

The fluid dynamic conditions typical of coaxial jet in laminar flow condition configuration, present in the chamber permits to evaluate the mixing degree between the core flow and confinement flow. It is a function of the local temperature of the two stream fed into the system. Assuming a constant confinement flow temperature of  $T_c=298$ K, it is possible to approximate the mixing degree  $\phi$  as :

$$\phi(T) = (T - T_c)/(T_{in} - T_c) \quad (5.5)$$

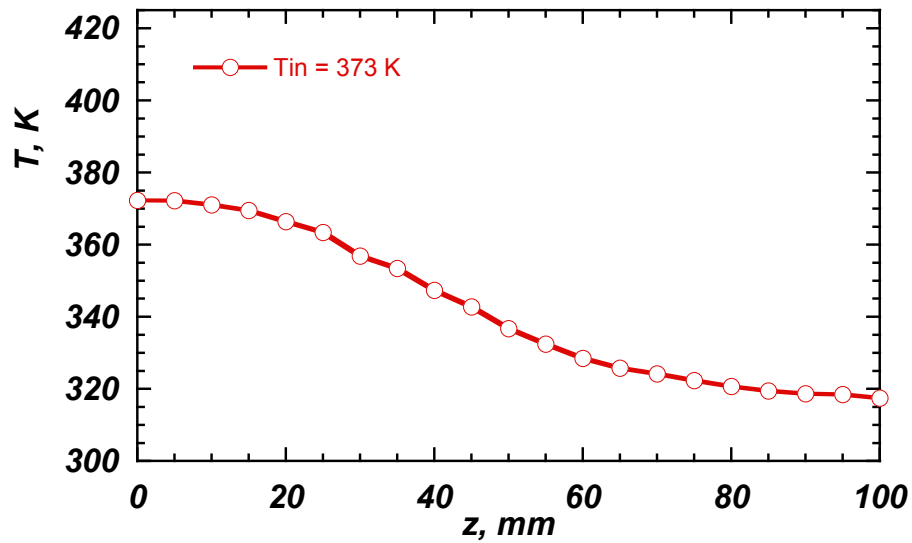


Figure 5.9: Axial temperature profile measured at  $T_{in}=373$  K

For every point of the axis where the temperature is measured, the mixing degree of the two flow is known.

Thus, it is possible to evaluate the local vapor concentration once the mixing degree is evaluated as:

$$X_v = \phi(T) \cdot X_{v_{in}} \quad (5.6)$$

thus the vapor local concentration may be reported as a function of the axial coordinate.

Figure 5.10 show the values of vapor molar fraction as function of axial coordinate varying the inlet vapor concentration from  $X_v=0.1$  up to  $X_v=0.7$

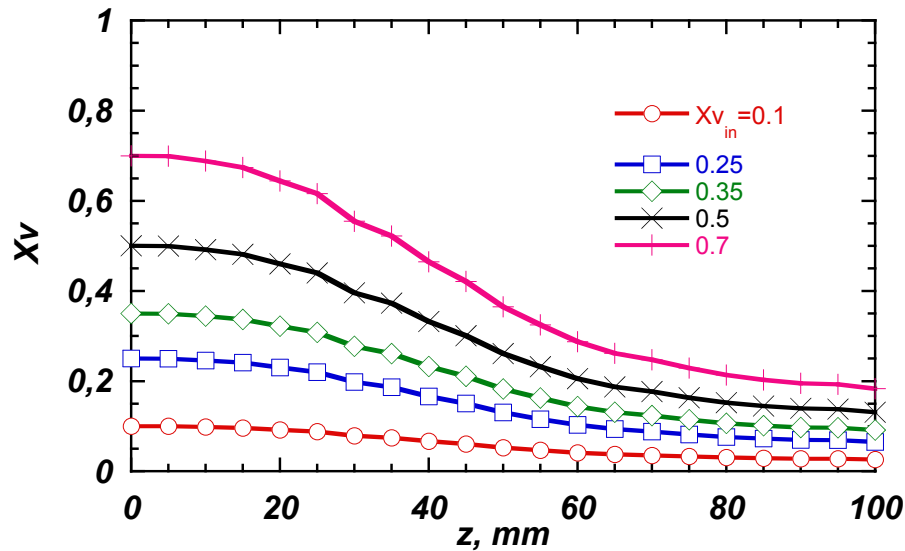


Figure 5.10: Axial vapor concentration profile evaluated at  $T_{in}=375$  K

Figure 5.11 shows polarization ratio trends evaluated at  $T_{in}=375$  K for  $X_v$  from 0 up to 0.7 measured in presence of graphite particles.

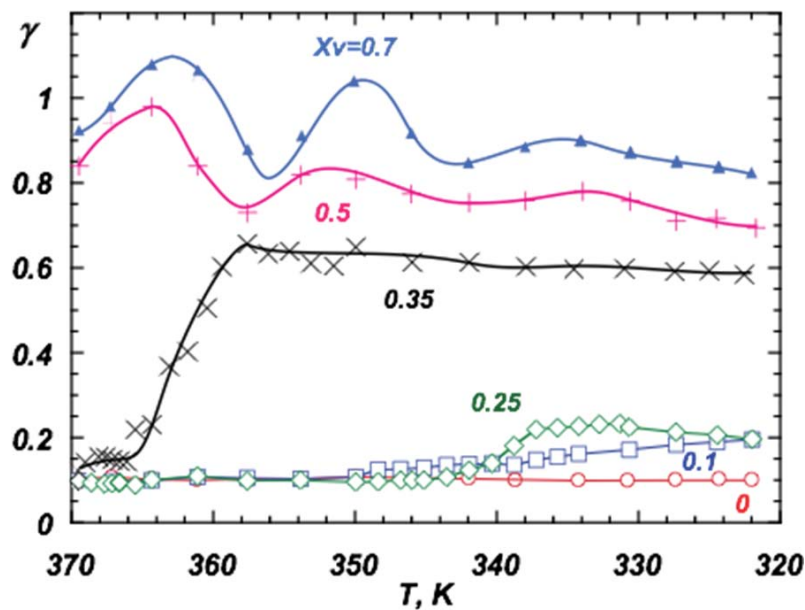


Figure 5.11: Polarization ratio profiles as function of axial temperature evaluated at  $T_{in}=375$  K and  $X_v=0$  up to 0.7 (graphite particles)

As already discussed, for  $X_v=0$ , (only particles and carrier fed into the chamber) the value of  $\gamma$  is almost constant with axial coordinate i.e. local temperature. For  $X_v=0.1$  to  $X_v=0.25$  polarization ratio profile shows a value slightly higher than that measured at  $X_v=0$  only for a temperature value less than 340K. This behavior suggests that scatterers dimensions slightly

increases. Furthermore the absence of a sudden increase in signal and the presence of a plateau suggest that, the system reaches an equilibrium condition where no further change in scatterers diameter occurs. For  $X_v=0.35$ , from  $T = 365$  K,  $\gamma$  the polarization ratio sharply increases and reaches a value of approximately 0.58 at  $T=358$ K, suggesting that the scatterers' diameters significantly increased. Then polarization ratio slowly decreased up to 0.58 at  $T=324$ K. For  $X_v=0.5$  the polarization ratio profiles shows a value much higher than that measured at  $X_v=0$  and reached a value of approximately 1 at  $T=364$  K. Then it shows an oscillator behavior up to  $T=324$  K. As seen from numeric polarization ratio showed in Figure 6.2, this behavior assures that the scatterer dimension reaches micronic size. Same considerations apply to  $X_v=0.7$  condition. The data reported in Figure 5.11 as function of the local temperature can be also analyzed as function of local vapor concentration, as shown in Figure 5.12, where polarization ratio profiles as function of local vapor concentration, measured in presence of graphite particles and water vapor, at  $T_{in}=375$ K e for  $X_v=0$  up to 0.7 have been reported.

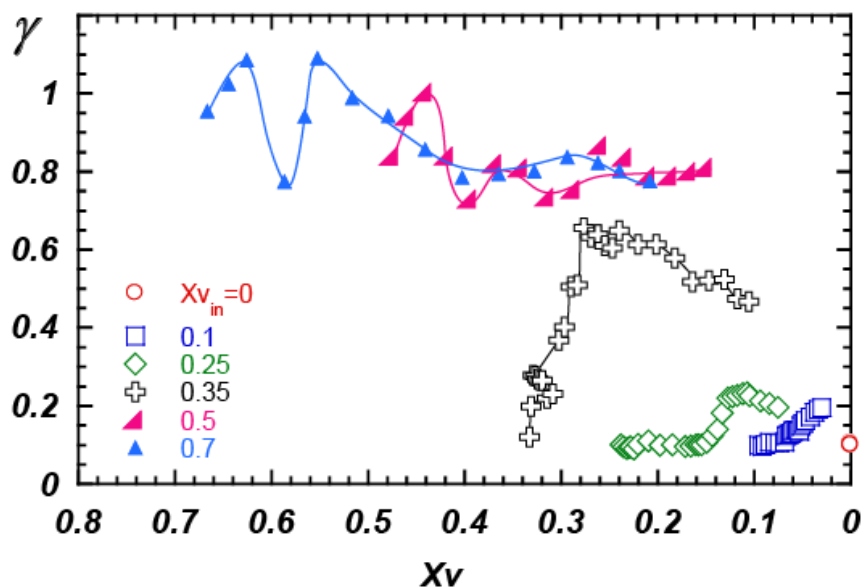


Figure 5.12: Polarization ratio profiles as function of axial vapor concentration evaluated at  $T_{in}=373$  K and  $X_v=0$  up to 0.7 (graphite particles)

From the results presented in figure 5.12 it is possible to follow the evolution of scatterers size variation increasing inlet vapor concentration. For  $X_v=0$  up to  $=0.7$  the mean value of polarization ratio and also its maximum value increases. This behavior suggest that higher is the vapor concentration higher is the scatterer size variation. To confirm this trend in the Figure 5.13 are shown the mean values of polarization ratio as a function of the corresponding local vapor concentration  $X_v$

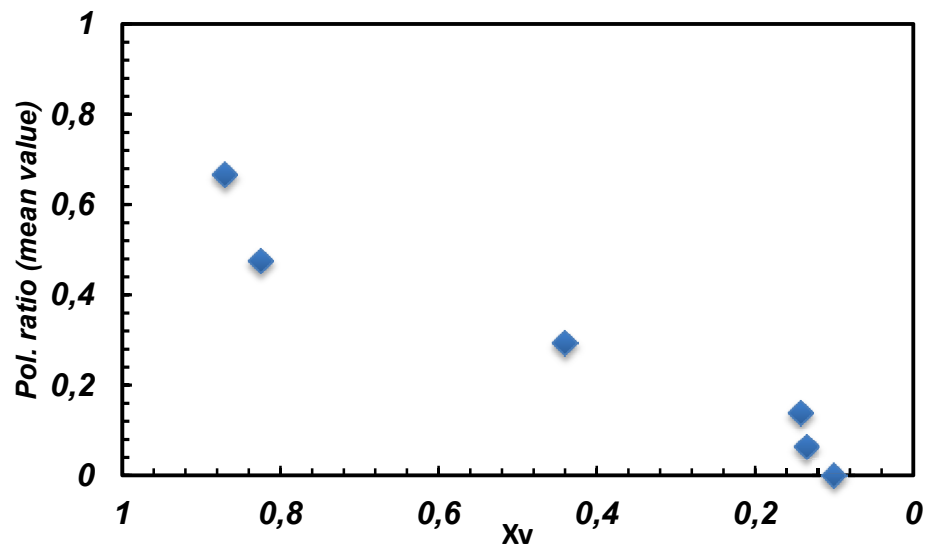


Figure 5.13: Mean values of polarization ratio for  $T_{in}=375$  K an  $X_v=0$  up to 0.7

In order to get information on the mechanisms that control the nucleation and growth process the trend of polarization ratio measured in a fixed condition along the axial coordinate has been compared with the trend of saturation profiles evaluated under different hypotheses and the trend of local vapor concentration.

The profiles reported in Figure 5.14 represent local conditions of vapor concentration and temperature at which the polarization ratio varies with respect to  $X_v=0$  condition of an amount that the criterion 5.1 is satisfied. , i.e. the system reaches the induction time.

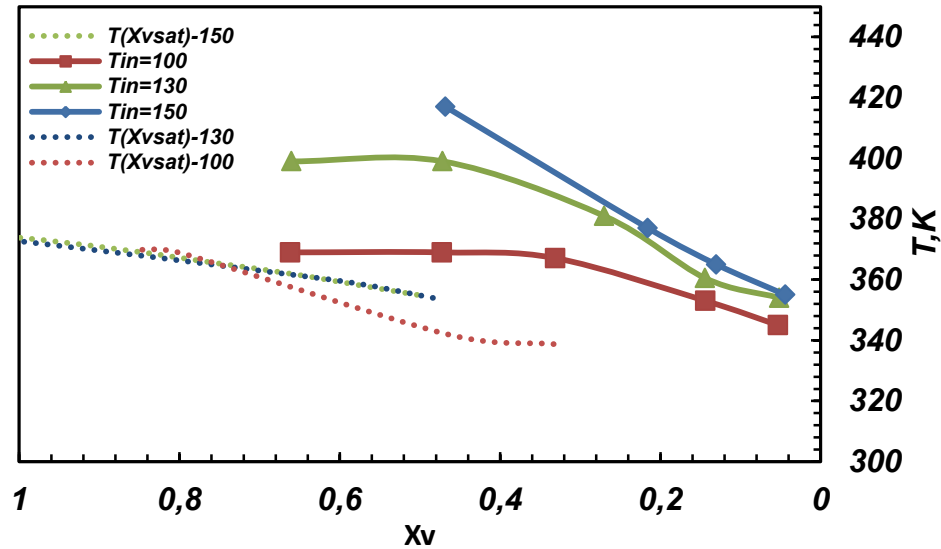


Figure 5.14:  $(X_v, T)$  and  $(X_{v\_sat}, T)$  values evaluated at  $t=t_{ind}$

Figure 5.14 shows both  $X_v, T$  and  $X_{v\_sat}, T$  values pairs evaluated at  $t=t_{ind}$ .  $X_{v\_sat}$  is the saturation vapor concentration of the vapor bulk phase evaluated at  $T(t_{ind})$ . Profiles showed in Figure 5.14 suggests that the local conditions of temperature and vapor concentration, at which the polarization ratio vary with the respect to  $X_v=0$  condition is far from equilibrium condition of bulk phase. Same considerations is valid if the equilibrium vapor concentration is evaluated from heterogeneous nucleation theory (eq. 1.63). The equilibrium vapor concentration evaluated over particles surface, by classical nucleation theory, does not take into account the fact that particles, that acts as condensation nuclei present in real, a very rough surface where phenomenon of capillary condensation could take place. It is possible to evaluate the equilibrium vapor concentration on a rough surface considering the formation of a liquid meniscus in the pores of particle by means of equation  $P_H = P_0 \exp\left(\frac{M_w \sigma_{lv}}{\rho_l RT} H\right)$ . In such a case, as shown by HRTEM figure presented in the previous chapter a graphite particles is formed by primary particles in a size range between (3-5 nm). The space between two primary particles, represent sites where capillary condensation process could take place.

Figure 5.15 shows the  $(X_v, T)$  and  $(X_{v\_sat}(H), T)$  values evaluated a  $t=t_{ind}$ . In this case the equilibrium vapor concentration on a liquid meniscus of curvature  $H=1/2rk < 0$  evaluated a

$t=t_{ind}$  showed a trend quite similar to  $(X_v, T)$  experimental values. These results show that capillary condensation process take place at system condition far from saturation condition of vapor bulk phase.

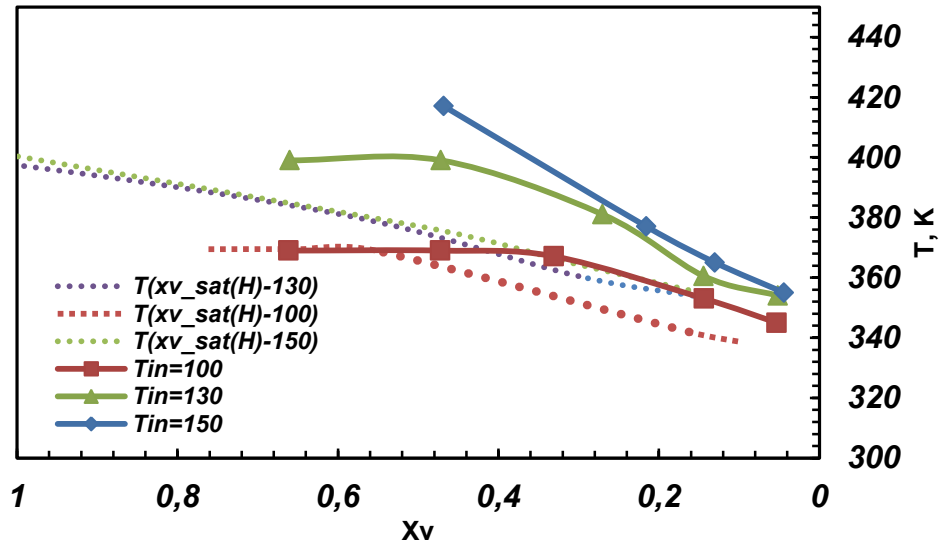


Figure 5.15:  $(X_v, T)$  ans  $(X_{v\_sat}(H), T)$  value evaluated a  $t=t_{ind}$

Thus, in Figure 5.16 the profiles of vapor concentration evaluated according equation (5.6) and the values of  $X_{v\_sat}$  that is the saturation vapor concentration of vapor bulk phase evaluated at local measured  $T=T(Z)$  according to the equation have been also reported (in Appendix B).

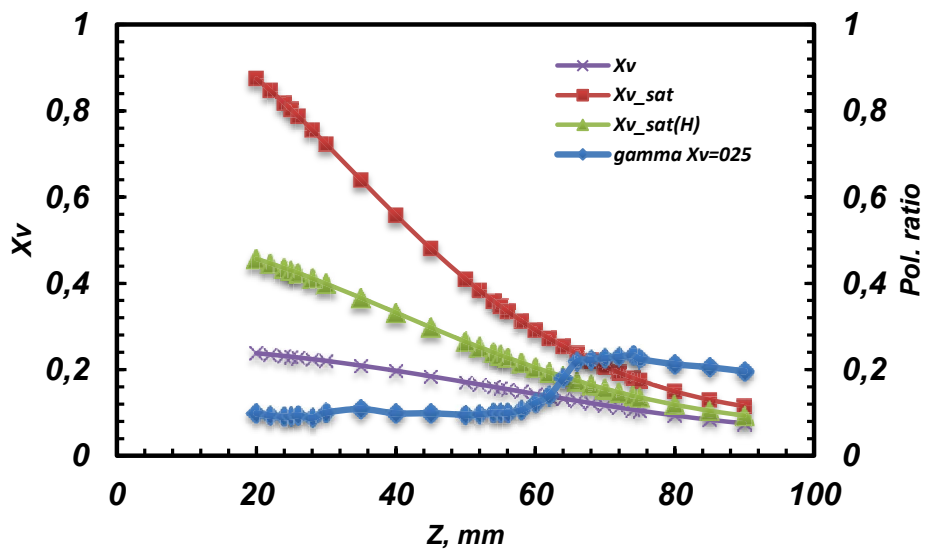


Figure 5.16: Trend of polarization ratio and  $X_v$  as function of axial coordinate  $Z$  evaluated at  $T_{in}=375$  K and  $X_v=0.25$

The value of  $X_{v\_sat}$  is very close to the one evaluated by equation (1.63) according to classical nucleation theory that represent the value of saturation vapor concentration over a spherical, smooth surface particle (covered by a water layer) with diameter  $D=150$  nm. Therefore, it has not been showed. Furthermore the value of  $X_{v\_sat}(H)$  is reported. The latter represents the equilibrium vapor concentration (i.e. vapor pressure) over a surface with negative curvature  $H$  equation from the following equation  $P_H = P_0 \exp\left(\frac{M_w \sigma_{lv}}{\rho_l RT} H\right)$ . The theory related to this approach has been already reported in the chapter 1.

It is a function of local temperature and vapor concentration. It is worth to note that the value of  $X_{v\_sat}(H)$  strongly depends on surface morphology, chemical and physical properties (surface tension of vapor liquid interface, contact angle between solid and liquid phase) of both particles and condensing vapor specie that rigorously should be evaluated according nano-thermodynamic or fluctuation theory. Such knowledge goes beyond the aims of this PhD thesis. For our purpose  $X_{v\_sat}(H)$  was evaluated as function of macroscopic physical properties of phases involved in the formation and growth process of droplets on particles surface. Thus it represents a useful tool and not a rigorous approach for the interpretation of experimental results carried out from polarization ratio measurements.

The trends of such vapor concentration profiles have been compared with the polarization ratio profile (secondary axis) measured for inlet condition of temperature and vapor concentration of  $T_{in}=375$  K and  $X_v=0.25$ , feeding graphite particles into system.

It is clearly shown in the figure that the local vapor concentration is very low with respect to the saturation concentration needed for nucleation process as derived from Fletcher approximation (Fletcher, 1958), widely used in literature for heterogeneous condensation (Giechaskiel et al., 2011) in the whole range considered. As deeply described in the chapter 1, the Fletcher approximation however is not able to proper reproduce the behavior of nucleation process in the case the particles considered are soluble or partially soluble in the condensing

species. In this case, the Köhler equation is able to reproduce experimental data, even though several corrective coefficients have been tentatively evaluated in different conditions. On the other hand, the Köhler theory is inadequate in the case of wettable and insoluble or slightly soluble particle (Sorjamaa et al., 2007). As a matter of fact, Huff Hartz et al. (2006) reported that some organic particles exist as liquid droplets at very low relative humidity. Sorjamaa et al. (2007) by means of a theoretical analysis suggested that the process occurs due to adsorption of condensing species on particles even though no clear experimental identification of this process was available. Persiantseva et al. (2004) considered the adsorption of water as potential process of water uptake on hydrofobic particles. Popovicheva et al. (2008) report on water uptake on carbonaceous particle produced by Palas GFG1000 related also to a small increase of particle dimension at relative humidity lower than 100%. The authors associate this finding to the swelling occurring after the water uptake on particles.

In Figure 5.16, the comparison of local concentration value and the saturation vapor concentration computed taking into account for adsorption process shows that they are relatively close especially in the spatial region where a change in polarization ratio occurs.

Due to the complex morphology of particle, as shown from figure of TEM and HRTEM reported in the previous chapter, graphite particle surface is very far from to be a spherical homogeneous smooth surface. The particle is composed by primary particles in the size range between 3-5 nm so its shape results to be very irregular (not spherical) and its surface present a fractal dimensions (not smooth or homogeneous) of approximately  $2.0 \pm 0.1$  (M. Wentzel, et al., 2003). It can be assessed that the particle surface is dotted by cracks and pores where the capillary condensation process could occurs. On such a type of nano-structured surface the formation of liquid meniscus can be stabilized at under-saturation conditions with the respect of vapor bulk phase. This process has characteristic time in the order of water vapor molecules transition time on particle surface ( $\tau_0=10^{-16}$  s) so it appears to be the first and fastest process occurring in series during the formation and growth of droplet on particles surface.

When the local vapor concentration in the bulk phase  $X_v$  approaches to equilibrium vapor concentration  $X_{v\_sat}(H)$  the liquid begins to cover the particle so that an increase of scatterers' dimension is observed. This phenomenon allows to identify the induction time ( $t_{ind}$ ) of the process, in correspondence of polarization ratio value variation. It begins to increase in correspondence of such conditions. The droplet growth continues until the system reaches an equilibrium condition due to vapor depletion in the bulk phase, as showed from polarization ratio value that present a plateau up to  $Z=90$  mm.

Indeed, the experimental data reported in this work represent the first clear indication of particle activation toward droplet nucleation and growth at low relative humidity.

The polarization ratio profile reported in Figure 5.14 is typical of a small size variation in scatteres dimension due to low local relative humidity conditions Different considerations apply for higher local relative humidity conditions.

Figure 5.17 shows the trend of polarization ratio as function of axial coordinate evaluated at  $T_{in}=375$  K and  $X_v=0.7$  for a radial coordinate  $r=10$ mm and feeding into the system graphite particles.

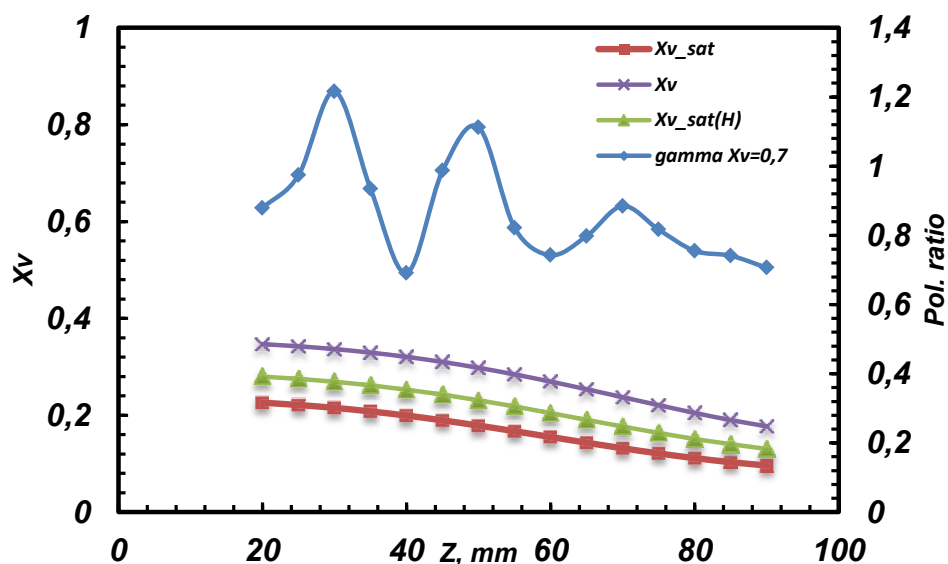


Figure 5.17: Trend of polarization ratio and  $X_v$  as function of axial coordinate  $Z$  evaluated at  $T_{in}=375$  K and  $X_v=0.7$  and  $r=10$ mm

This condition represents a case of lower local temperature and higher local vapor concentration with respect to previous one. In such a case the local vapor concentration  $X_v$  is higher than  $X_{v\_sat}$  and  $X_{v\_sat}(H)$ . The polarization ratio profile related to this working condition shows a value very higher with the respect  $X_v=0$  case showed in Figure 5.1 (graphite particles), furthermore it shows an oscillating behavior along axial coordinate. This trend suggests that in this case the particles have been activated by water vapor condensation for a time  $t_{ind}$  smaller than previous case.

Furthermore assuming a mono-disperse narrowed particle size distribution the oscillating behavior suggests that particles reach micronic size as supported by numeric polarization profiles showed in Figure 5.2.

The polarization ratio oscillations depend on the width of the size distribution function. In Fig 5.18 a computation, assuming the refractive index of water, of the polarization ratio is reported for different values of the width of normal size distributions. The curves relative to a certain percentage have been computed by assuming a width of the distribution at each size value equal to that percentage (e.g. for a computation at  $D \mu m$  and a width of 10 % corresponds to a normal size distribution with a mean value equal to  $D$  and a sigma equal to  $D*0.1$ ). The position of the polarization ratio oscillations does not depend on the width of the size distribution function. However, as it can be easily seen, up to a value of 10% it is possible to observe at least the first three oscillations. At wider size distribution functions the oscillation (apart from the first one) can no longer be observed. In other words the observation of three or more oscillations in correspondence of the drop size growth, due to water deposition on the surface, is a clear indicator of a relatively narrow size dispersion of the droplets. As a consequence, it is possible to affirm that the activation of nucleation and growth occur contemporaneously on all particles (unitary activation efficiency). This consideration can be extended to all condition where an increase of polarization ratio is detected. In addition, the maximum values of polarization ratio occur at fixed scatterers

diameters independent of particle dispersion, as shown in Figure 5.18. It is possible to show that it is also independent of imaginary part of refractive index. Thus the occurrence of maxima in the experimental profile of polarization ration can be used to evaluate the final dimension reached by droplets.

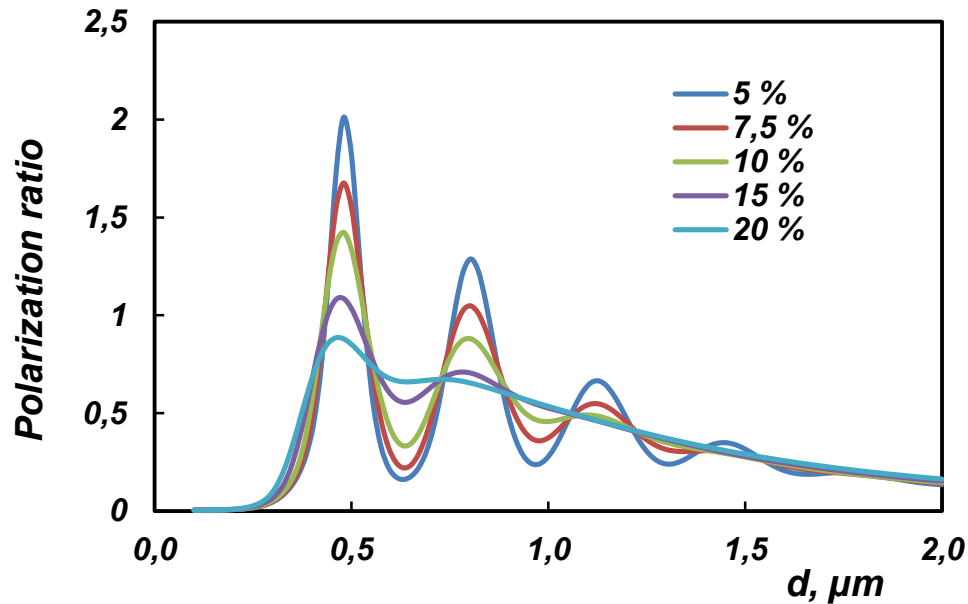


Figure 5.18: Polarization ratio profiles assuming the refractive index of water, for different values of the width of normal size distributions.

In order to summarize the behavior of the condensation process with respect to the local temperature and vapor concentration in all experimental conditions considered, on a  $T, X_v$  plane the points corresponding to the conditions at which the induction of the process occurs have been reported along with the points indicating the saturation condition computed according to the equation (see Appendix B).

Figure 5.19 shows the  $X_v, T$  values evaluated at  $t=t_{ind}$ , (i.e. axial coordinate) for three values of inlet temperature  $T_{in}=375, 405, 425$  K, and  $X_v$  varying from 0.1 up 0.7. This time value corresponds to the time at which the condition (5.1) is satisfied.  $X_v$  is calculated from equation (5.6) once that  $T(t_{ind})$  is identified.

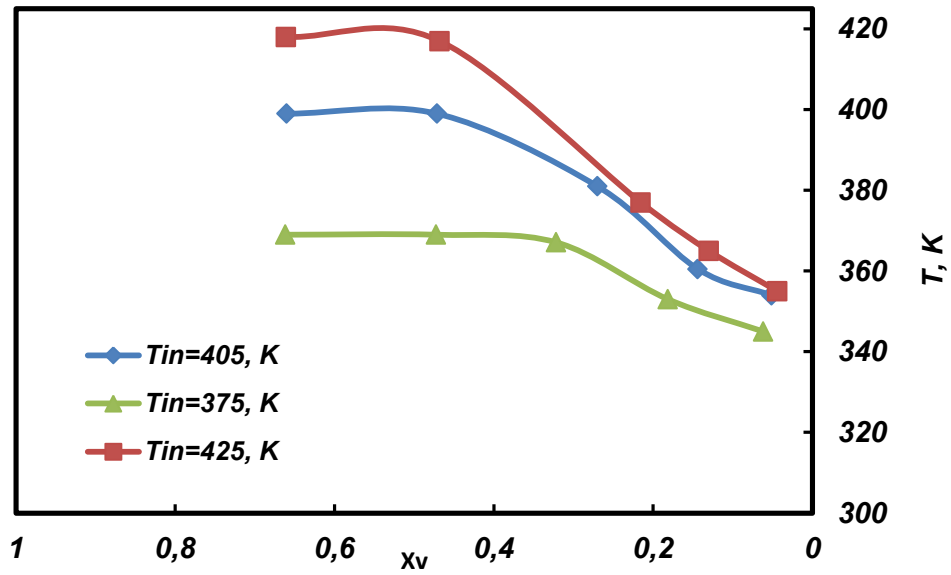


Figure 5.19:  $(X_v, T)$  values evaluated at  $t=t_{ind}$

Figure 5.20 shows the  $(X_v, T)$  values for inlet temperature condition of  $T_{in}=375$  K and  $X_v=0$  up to 0.7 by varying radial coordinate of measurement, and Re number (i.e. increasing confinement flow rate).

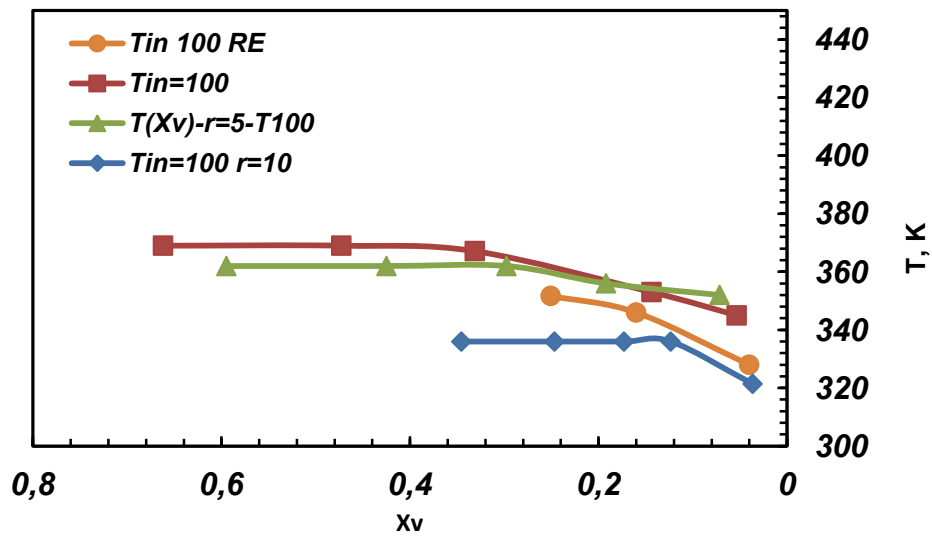


Figure 5.20:  $(X_v, T)$  values for  $T_{in}=375$ , varying axial coordinate of the measurement and confinement flow rate

### 5.3 Effect of particles chemical nature

Figure 5.21 shows the polarization ratio trends evaluated at  $T_{in}=405K$  for four value of vapor concentration  $X_v=0, 0.1, 0.25, 0.35$  and fed into the chamber graphite particle ( $\theta=85^\circ$ ), iron particles ( $\theta=50^\circ$ ) and nickel particles ( $\theta=20^\circ$ ) respectively with a mean diameter  $D_p=150$  nm. These data are the reported in Figure 5.9 as function of residence time.

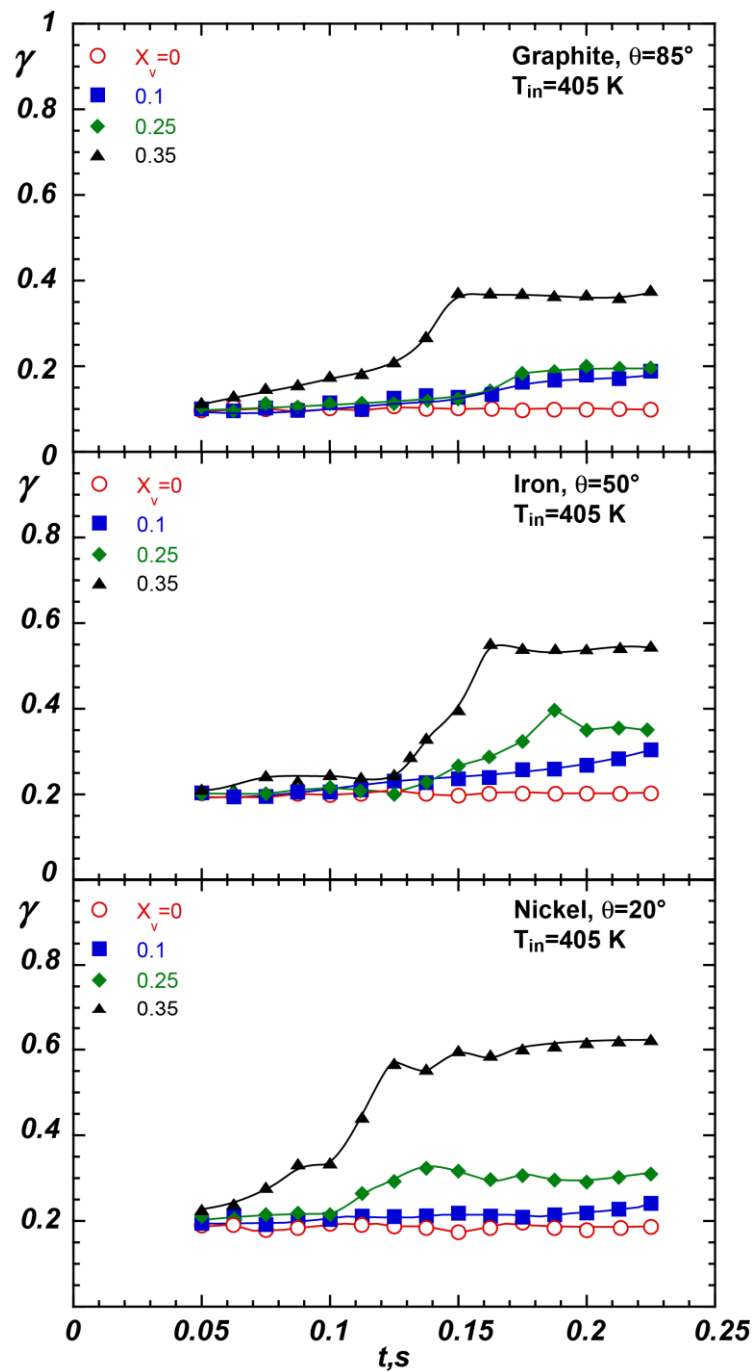


Figure 5.21: Polarization ratio trends for  $T_{in}=405$  K,  $X_v=0, 0.1, 0.25, 0.35$ , varying the chemical specie of particle (i.e. contact angle) feeding to the system.

The results highlight that passing from graphite to nickel particles, (i.e. increasing particles wettability) the characteristics time of the process, for the same working conditions, decreases as suggested from polarization ratio profiles related to the different particles specie. For  $X_v=0.35$  the induction time varies from  $t_{ind}=0.15$  s for graphite, to 0.125 s, for iron and to 0.11s for nickel particles respectively. Furthermore higher particles wettability leads to higher coverage degree of particles by water layer. Again passing from graphite to nickel particles, polarization ratio reaches a maximum value of 0.4 for graphite, 0.58 for iron and 0.62 for nickel particles respectively.

#### 5.4 Effect of particles number concentration

Figure 5.22 shows the trend of polarization ratio a function of residence time (i.e. axial coordinate) to emphasize the fact that particles number concentration does not affect the occurrence of induction time and only influences the final size of particles as suggests from the maximum value reached by polarization ratio that correspond to the case  $N/N^*=1$  ( $N^*=2.0 \cdot 10^{-7}$  #/cm<sup>3</sup>)

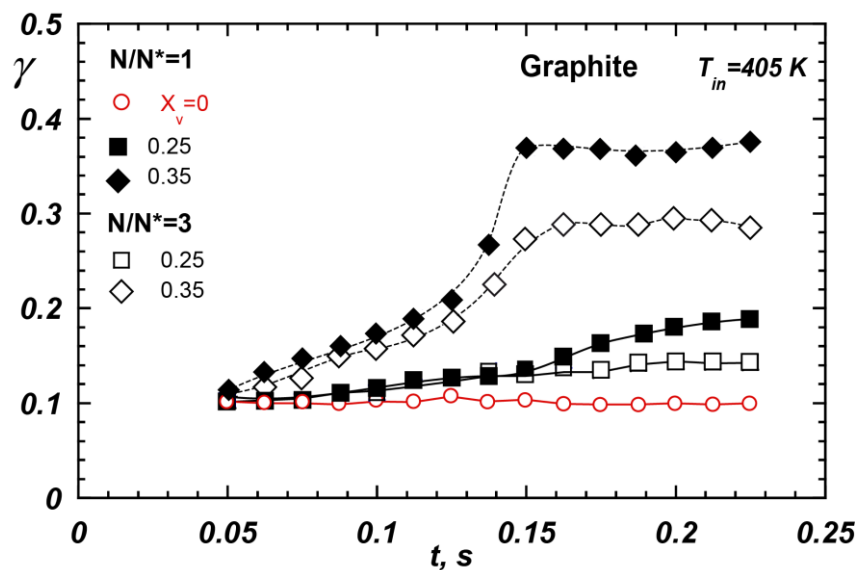


Figure 5.22: comparison of polarization ratio profiles measured for  $T_{in}=405$  K  $X_v=0, 0.25, 0.35$  and for two values of particles number concentration.

As shown by the polarization ratio profile for  $X_v=0.35$  evaluated for  $N/N^*=1$  and  $N/N^*=3$  respectively the trend of polarization presents a very similar slope from  $t=0.05$  s up to  $t=0.1$  s that is the induction time evaluated for the  $N/N^*=1$  condition. For  $t$  higher than  $0.1$  s both the profiles show an increase up to  $0.15$  s that represent the growth time. The main difference between polarization ratio profiles evaluated for the two different values of particles number concentration is the maximum value of polarization ratio reached at  $t=t_{\text{growth}}$ . For  $N/N^*=1$  polarization ratio maximum value is approximately of  $0.38$  while for  $N/N^*=3$  the polarization ratio reaches a value of approximately  $0.3$ .

### 5.5 Effect of initial particles dimension

Figure 5.23 shows the polarization ratio profile as function of residence time (i.e. axial coordinate) measured for  $T_{in}=375$  K and  $X_v=0, 0.25$  and  $0.35$ , feeding into the system graphite particle with a diameter  $D_p=150$  and  $D_p=10$  nm respectively.

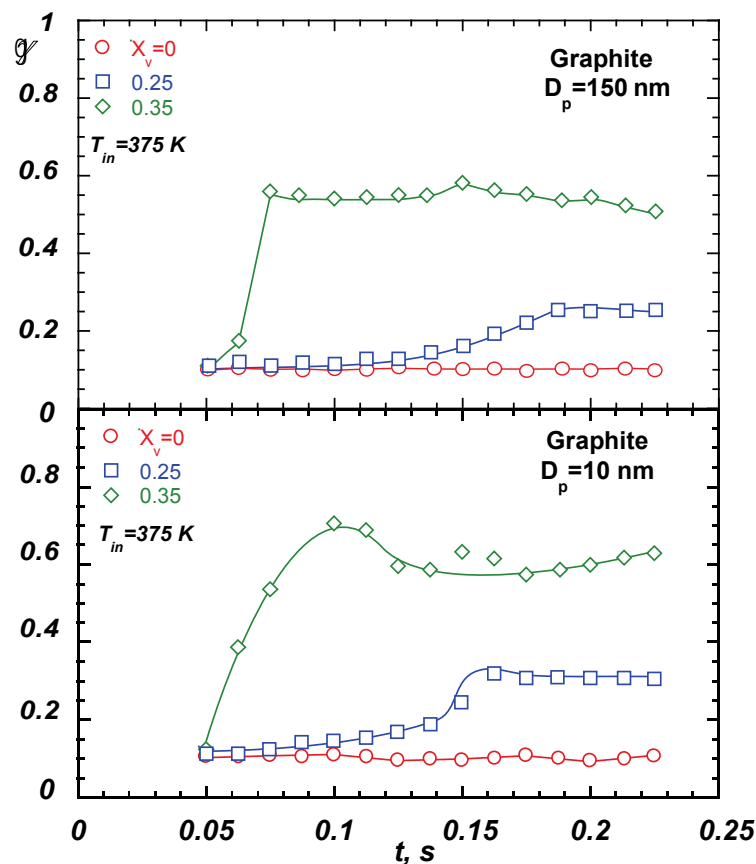


Figure 5.23: Comparison of polarization ratio profiles measured for  $T_{in}=375$  K  $X_v=0, 0.25, 0.35$  and for two values of particles diameter.

From polarization ratio profiles showed in Figure 5.23 results that ultrafine particles ( $D_p=10$  nm) presents a slight lower induction time, and a higher covering rate with respect to larger particles  $D_p=150$  nm. This behavior appears clear comparing the values of polarization ratio measured at  $t=0.06$  s. At this time the polarization ratio value of ultrafine particles is approximately of 0.4, while for larger particles it is about of 0.2. Same consideration apply to  $X_v=0.25$  condition. Also in this case polarization ratio profile relative to  $D_p=10$  nm shows an induction time lower than that measured at  $D_p=150$  nm.

### ***5.6 Characteristic times of the condensation process***

On the basis of given definitions the characteristic times have been evaluated from the experimental polarization ratios profiles reported in chapter IV and have been summarized in the Figure 5.9. In particular, Figure 5.24 shows the induction time, growth time and time needed for reaching a steady state conditions as function of  $X_v$  (from 0.1 to 0.35) varying inlet temperature from  $T_{in}=375$  K up to 435 K, for the different typology of particles fed to the laminar condensation chamber. More specifically, the first row refers to graphite particles, the second row to iron particles and the last row to the nickel particles respectively. The data refer to particle dimension of 150nm. The dashed represents the time at the axial coordinate  $Z = 20$ mm i.e. the lower time that could be detected.

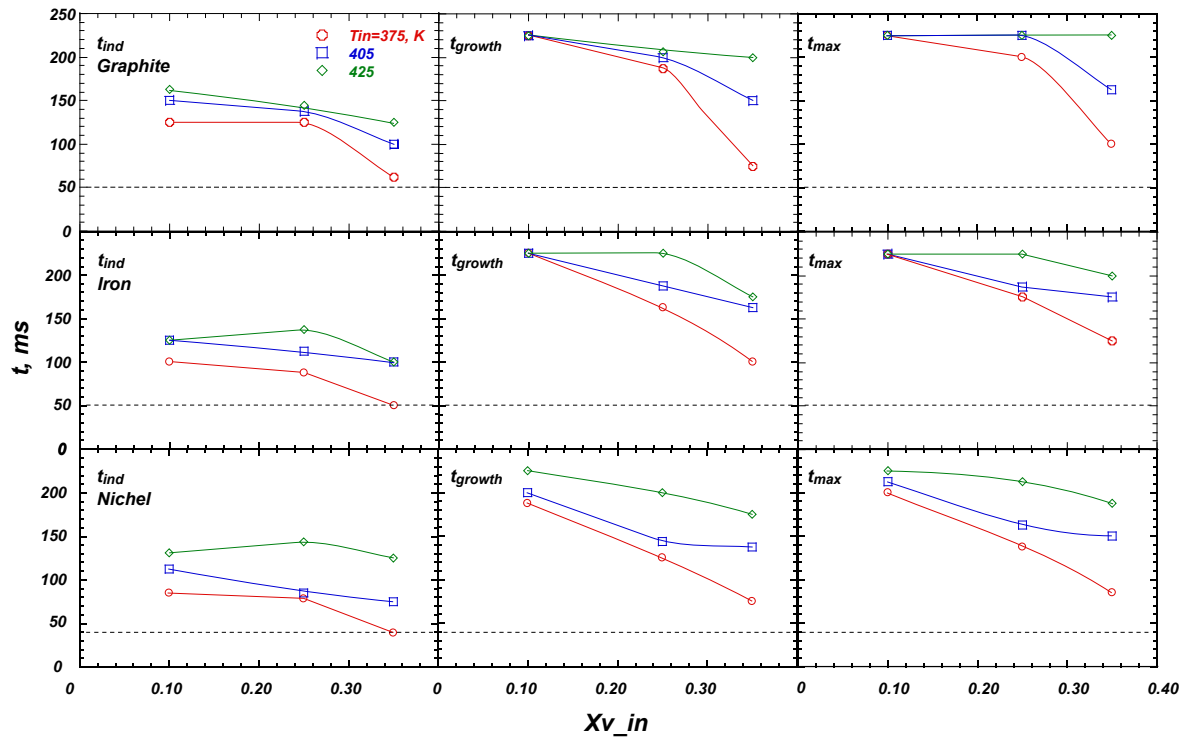


Figure 5.24: Characteristic times evaluated for of graphite, iron and nickel particles respectively

The analysis of experimental results shows that higher inlet vapor concentration as well as lower working temperature reduce the induction time. For graphite particles, at  $T_{in}=375K$ ,  $t_{ind}$  decreases from 120ms to 60ms for a inlet vapor concentration increase from 0.1 to 0.35. The same behavior has been obtained for higher inlet temperature.  $t_{growth}$  is more sensitive to inlet vapor concentration. As a matter of a fact,  $t_{growth}$  decreases from 225ms to 75ms for  $Xv$  variation from 0.1 to 0.35. In this case, the dependence of  $t_{growth}$  on  $Xv$  is less pronounced at higher temperatures. Furthermore higher particles wettability anticipates the occurrence of the induction time. At  $T_{in}=375K$  and  $Xv=0.1$  it decreases from 125 ms for graphite to 100 ms for iron to 85 ms for nichel particles. These differences decrease at higher vapor concentrations. The same considerations apply for the growth time. In the operative condition considered, the induction and growth time experimentally evaluated, are comparable with practical application and useful for the design of a real abatement unit.

Figure 5.25 (a) shows the characteristics time of droplet formation on graphite particles evaluated at  $T_{in}=375$  K varying  $X_v$  from 0.1 up to 0.7 and for three different values of axial coordinate  $r=0, 5, 10$  mm.

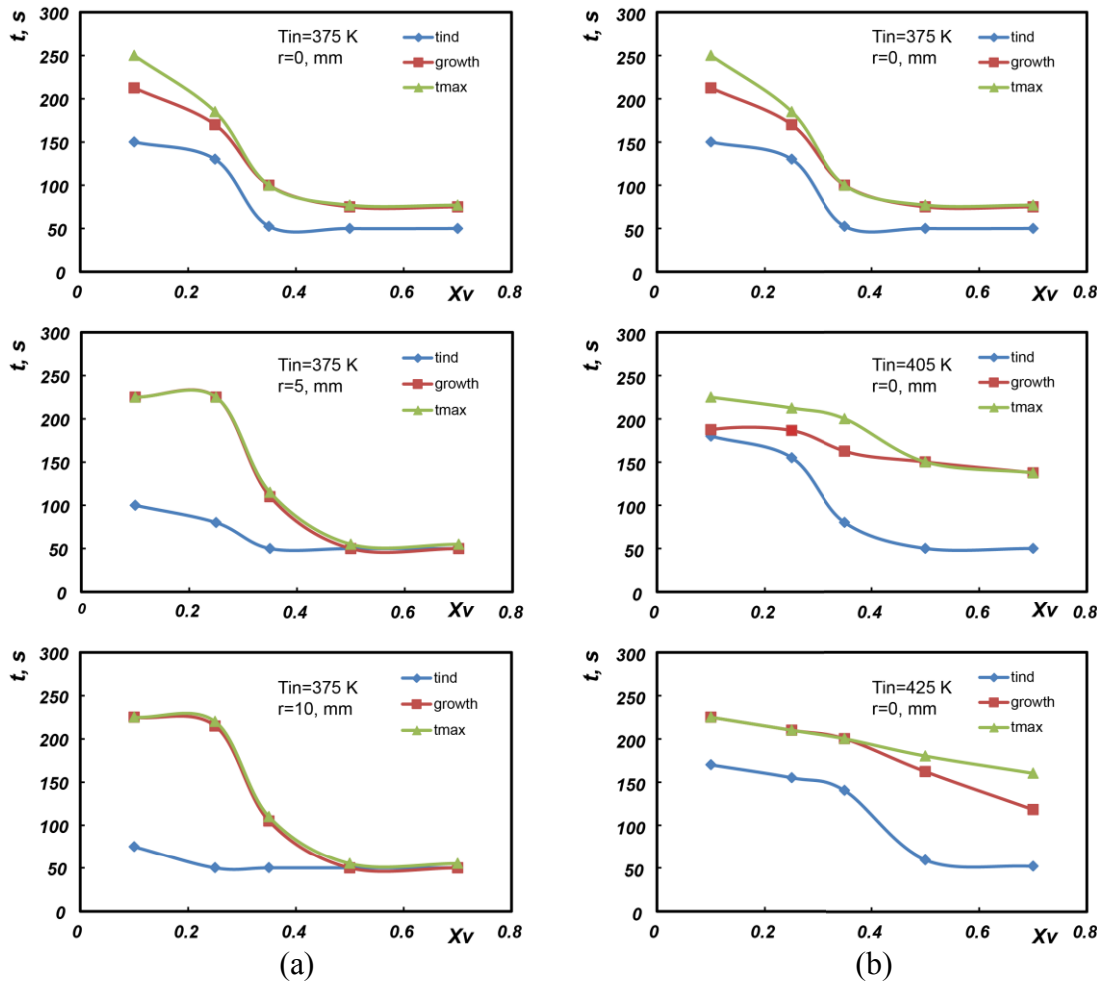


Figure 5.25: Characteristic times in presence of graphite particles

The results shows that characteristic time of process, for  $T_{in}=375$ K, gradually decreases passing from  $r=0$  up to  $r=10$  mm. It is worth nothing that in the case of higher vapor concentration condition the growth time  $t_{growth}$  and stabilization time  $t_{max}$  are the same, this condition is reached when the polarization ratio profiles shows an oscillating behavior (or when the polarization ratio profiles presents a plateau after reaching its maximum value, or when the growth time is relatively high and reach its maximum value at  $t=t_{res}$ ). Figure 5.25(b) shows the characteristic time of process by increasing inlet temperature again as asserted

before, an increase of inlet temperature results in a delay of the induction time. It is interesting to note that for  $T_{in}=375\text{K}$  and  $405\text{K}$  the induction time is almost constant starting from  $X_v=0.35$ . The behavior pointed out from Figure 5.25a with respect to radial position of signal detection is due to local variation of temperature value as shown from temperature axial profile showed in Figure 5.26. the characteristic time evaluated at  $r=0\text{ mm}$  for  $T_{in}=375\text{ K}$  are quite similar to showed for graphite particles showed in Figure 5.9. Furthermore In that case results were carried out by an integral measurement among chamber axis.

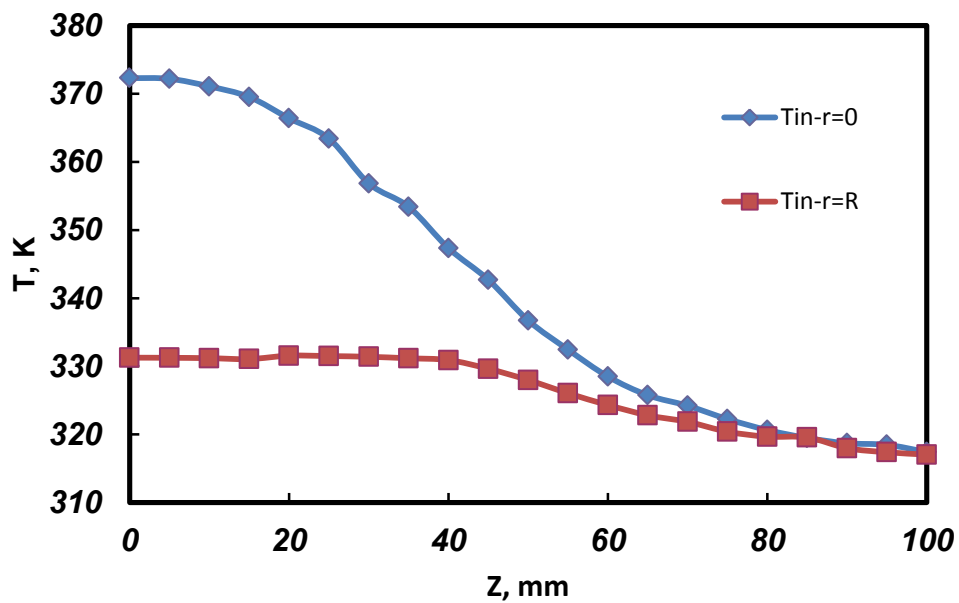


Figure 5.26: Temperature profile as function of axial coordinate for  $T_{in}=375\text{ K}$  measured at  $r=0$ , and  $r=10\text{ mm}$

### 5.7 Evaluation of particles dimension and growth factor

An evaluation of the final dimensions reached by the drops, was performed by means of a numerical procedure that associates the value of droplet diameter related to a specific value of polarization ratio.

Experimental values of polarization ratio, evaluated in all working condition analyzed, were compared with polarization ratio profiles numerically evaluated by means of extended effective medium approximation and reported in Figure 5.27.

Figure 5.27 shows the polarization ratio profiles of a composite droplet hosting a graphite ( $D_p=10$  or  $150$  nm), iron ( $D_p=150$  nm) and nickel ( $D_p=150$  nm) particle respectively as function of droplet diameter fixing the size of included particle and increasing the size of water shell. It is worth to note that in the size range considered, the polarization ratio value reported are independent from the optical properties and size of the particle included in the water shell, as suggested from polarization ratio profiles related to the various particles specie that overlap each others.

Thus, from the experimental value of polarization ratio is possible to evaluate the corresponding droplet diameter.

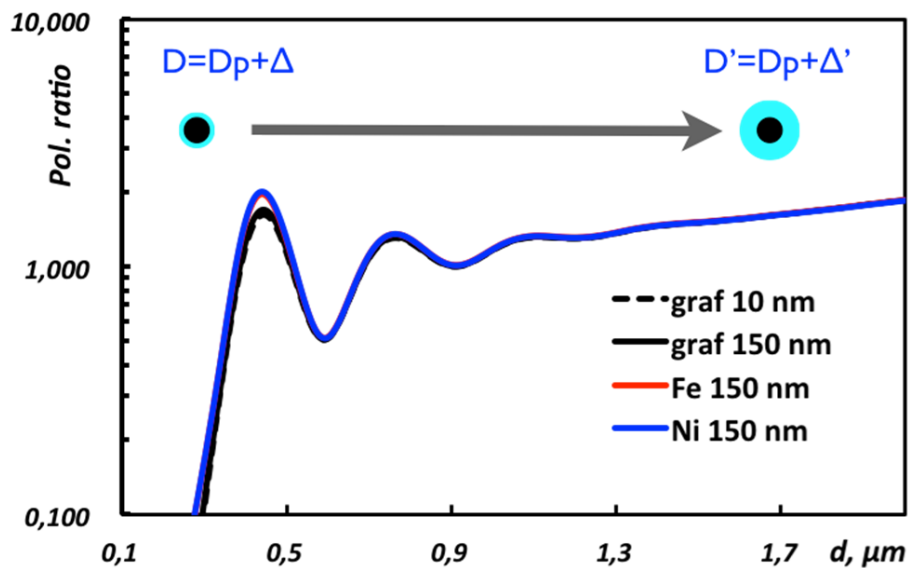


Figure 5.27: Trends of polarization ratio for composite droplet hosting a particle evaluated increasing water shall radius

Figure 5.28 shows the experimental polarization ratio values evaluated for  $T_{in}=375$  K and  $X_v=0.35$  ( $X_v=0.25$ ) as function of axial coordinate (i.e. time) and the corresponding droplet size obtained for graphite inlet particles with a mean diameter  $D_p=150$  nm. The droplet size

was evaluated by means the numerical procedure described above. For  $X_v=0.35$  the final droplet size is approximately of 367 nm while for  $X_v=0.25$  droplet reach a final dimension of about 330 nm .

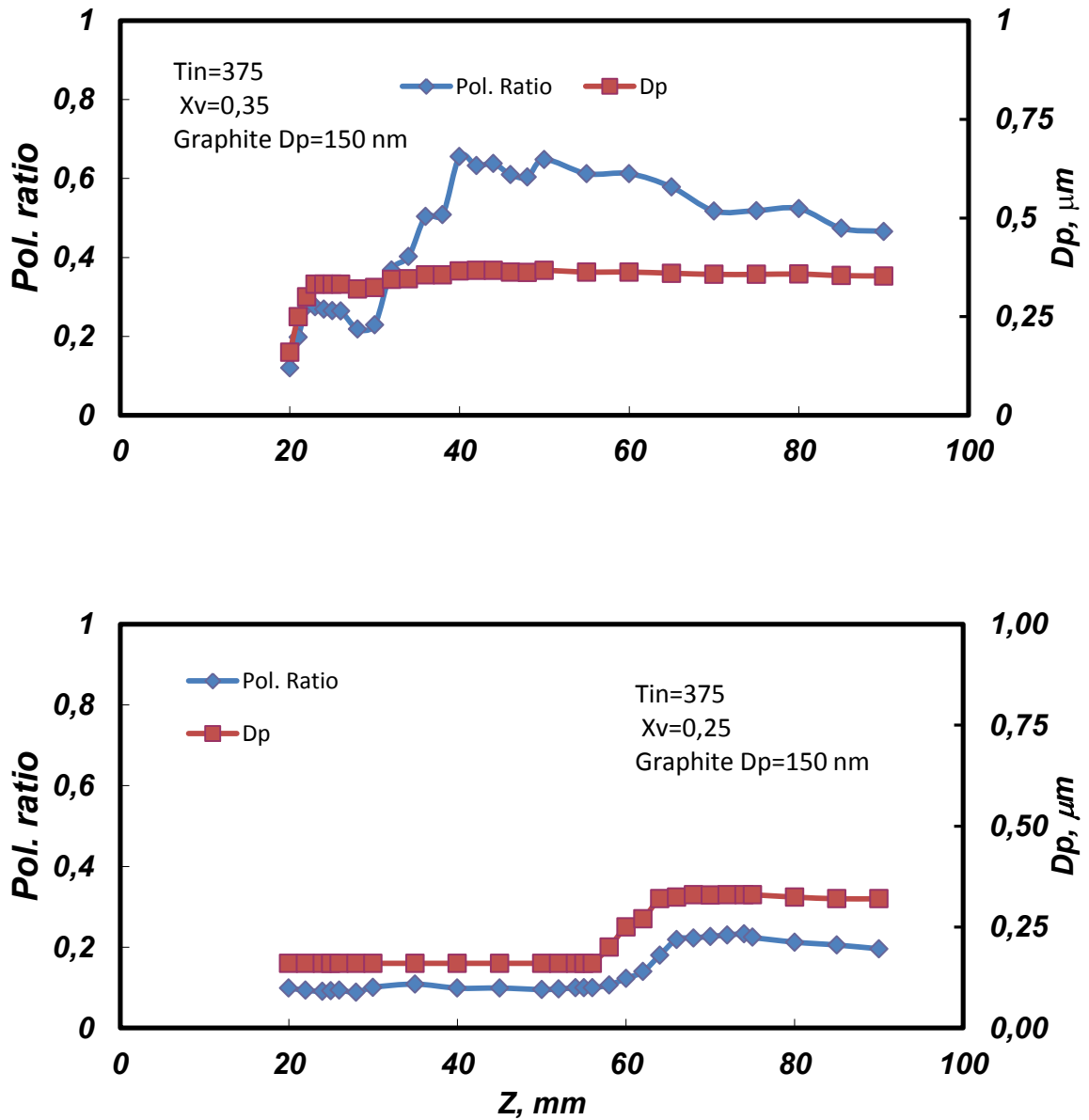


Figure 5.28: Experimental polarization ratio profiles and calculated droplet diameter

Different consideration can be carried out for higher vapor concentration cases. Figure 5.29 show the experimental polarization ratio profiles, as function of axial coordinate for  $T_{in}=375$  K and  $X_v=0.7$  for a values of axial coordinate  $r=10$  mm in presence of graphite particles with

$D_p=150$  nm. The trends of polarization ratio clearly shows an oscillating behavior after reaching a value of approximately 1. The polarization ratio profiles reported present three peaks of gradually smaller amplitude ( $X_v=0.7$ ), suggesting that water droplets reach a dimension of at least 1 micrometer as shown in figure 5.27. Same considerations are valid for  $X_v=0.5$ . In this case even if disappearing of oscillation behavior does not evident, such polarization ratio profiles suggest that droplet size is about of 1 micron.

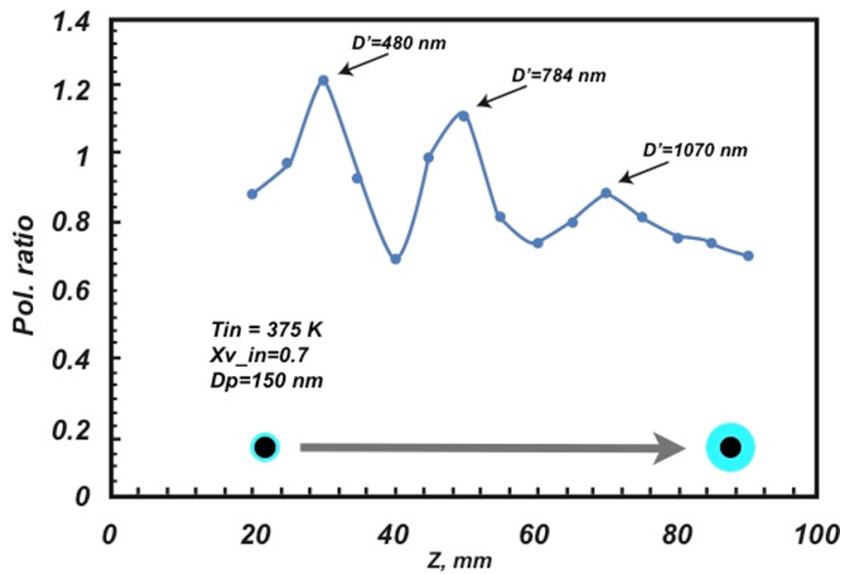


Figure 5.29: Polarization ratio profiles evaluated at  $X_v=0.7$  and  $T_{in}=373$  K for graphite particles with mean diameter  $D_p=150$  nm ( $r=10$  mm)

With this procedure, in all the conditions considered in the experimental campaign, the final size of water droplet including solid particles formed due to heterogeneous condensation process, has been evaluated and summarized in Table 3 Appendix A. Summarizing, two particle growth mechanism, involving different physical processes have been identified. The first already active at undersaturation conditions ( $S < 1$ ) which involves phenomena related to the morphological and physicochemical properties of the particle such as adsorption, absorption, followed by capillary condensation (in pores network) and by the swelling of the particles (structural changes). In addition, these processes improve the cohesion/sticking between the particles, because they are covered by a liquid layer. In these conditions the

variation in size of the particles is relatively low. Furthermore the polarization ratio shows an increasing trend with time, reaching a steady state condition. The second mechanism is active at supersaturation conditions ( $S > 1$ ). In this condition the particle is activated by heterogeneous nucleation mechanism. In such a case the particle covering is enhanced by the mass transport of water vapor toward particle surface. The final size of the composite droplet in this case is of the order of micron. The related polarization ratio profile shows an oscillating behavior, after that it reaches a value of about 1, much higher than that measured at  $X_v = 0$ . (i.e. absence of vapor). Figure 5.30 shows the qualitative temporal profile of polarization ratio in this condition. It provides a scheme of interpretation of the mechanisms involved in the growth process of the droplets in dependence on saturation conditions ( $S < 1$  or  $S > 1$ ).

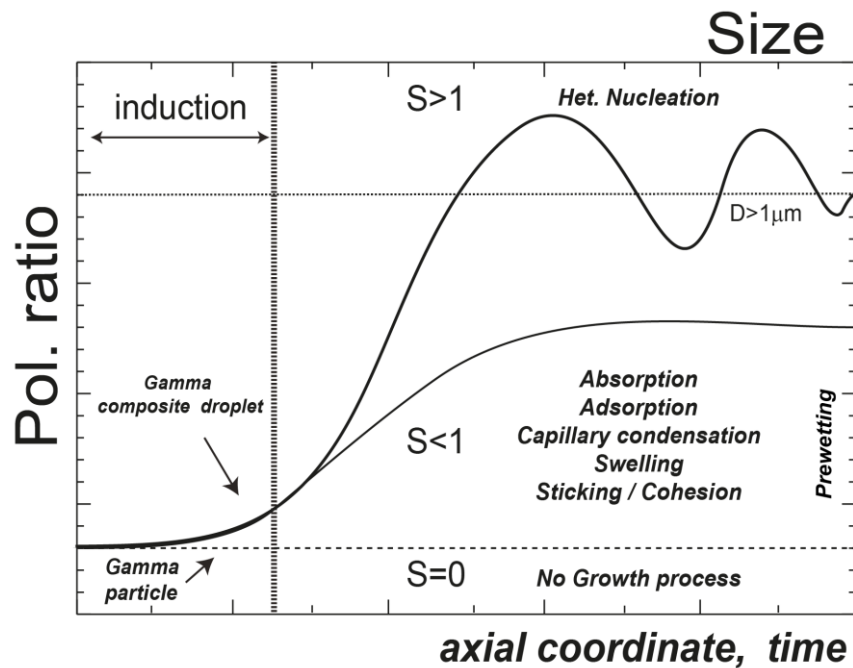


Figure 5.30: Scheme of interpretation of qualitative polarization ratio trend

Once that final size of water droplet is known it is possible to define a growth factor comparing the final size of droplet with the respect initial particles size. An indication of the

efficiency and the characteristic time of particles growth process can be obtained by evaluating a growth factor,  $gf$ , defined as:

$$gf = \frac{D_{fin}}{D_0}$$

The growth factor is an increasing function of scatterer diameters and is equal to unity when no particles size variation occurs.

Figure 5.31 shows the maximum values of  $gf$  evaluated for graphite particles ( $D_p=150\text{nm}$ ) at different  $X_v$  from 0.1 up to 0.7 as a function of  $T_{in}/T_{sat}$ , where  $T_{sat}$  is the saturation temperature corresponding to the inlet  $X_v$  considered. The growth factor increased for all values of the vapor concentration, as the system moved towards saturation conditions ( $T_{in}/T_{sat} \rightarrow 1$ ). At the lowest  $X_v$  of 0.1, the growth factor did not strongly depend on inlet temperature. This factor increased from 2.06 to 2.16, passing from  $T_{in}/T_{sat} = 1.33$  to 1.27 and remaining nearly constant up to  $T_{in}/T_{sat} = 1.18$ . This trend shows that for this vapor concentration, a further increase in droplet size ceased and an equilibrium condition between the droplet and the environment was reached. Same considerations are valid for  $X_{v\_in}=0.25$  and 0.35, where the growth factor varies from 2.1 to 2.2 passing from  $T_{in}/T_{sat} = 1.25$  to 1.1 and from 2.29 to 2.4 passing from  $T_{in}/T_{sat} = 1.22$  to 1.08 respectively. The equilibrium conditions were not reached for high vapor concentrations, where a significant increment of  $gf$  occurs. At  $X_v=0.5$ ,  $gf$  increased from 2.36 to 7.33 with a decrease of  $T_{in}/T_{sat}$  from 1.2 to 1.05. At  $X_v=0.7$ , the growth factor reached the maximum value of 8 for  $T_{in}/T_{sat} = 1.03$ .

Of note, in the range of  $T_{in}/T_{sat}$  between 1.3 and 1.14, the growth factor had a consistent value that ranged from 2 to 2.2 for all the experimental conditions. In addition, the dependence of  $T_{in}/T_{sat}$  on droplet growth appeared notably similar when the system was far from the equilibrium conditions, independent of the  $T_{in}/T_{sat}$  range. Same considerations are valid for iron and nickel particles the growth factor for such species are listed in Table 3 Appendix A

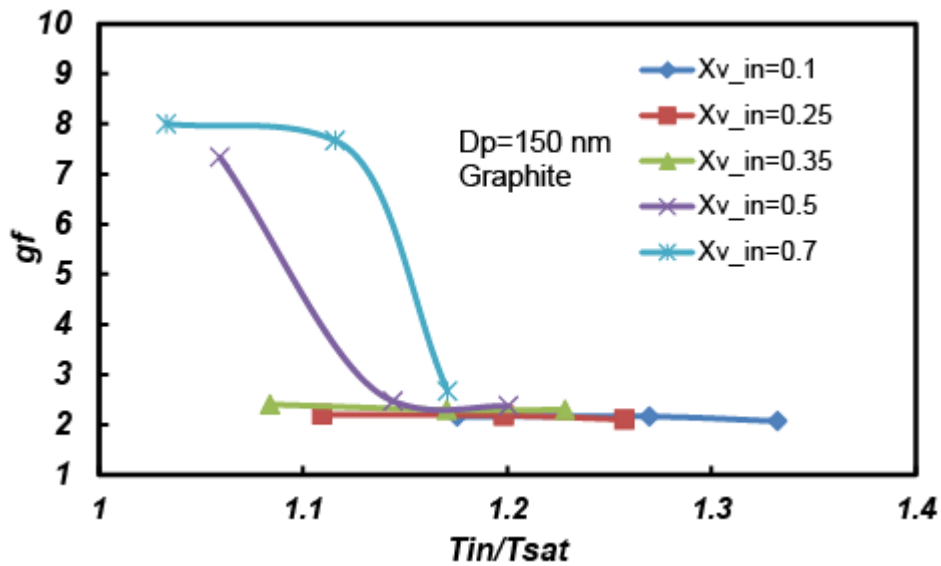


Figure 5.31: Maximum value of the growth factor as a function of  $T_{in}/T_{sat}$ .

From the results shown in Fig. 5.31, it is evident that the  $gf$ , i.e., the final size reached from a water droplet, is strongly influenced by the initial water vapor concentration.

Figure 5.32 shows the  $gf$  evaluated at  $X_{v\_in} = 0.7$  as a function of  $T_{in}/T_{sat}$  for graphite, iron, and nickel particles. It is worth noting that when transitioning from graphite particles to nickel particles, the maximum value of  $gf$  increases from 8 to 8.46 at  $T_{in}/T_{sat} = 1.03$ . For higher  $T_{in}/T_{sat}$  ranges, the  $gf$  values are very similar for the three different particle species.

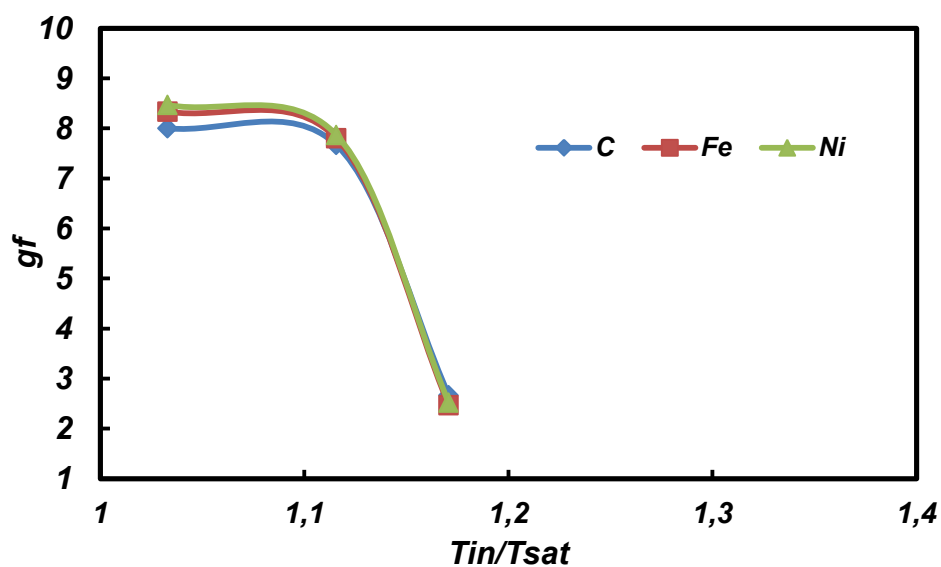


Figure 5.32: Maximum value of the growth factor as a function of  $T_{in}/T_{sat}$  for graphite, iron, and nickel particles

The particles chemical nature effect on nucleation process is mainly attributable to the occurrence of induction time. Furthermore higher particles wettability results in higher water coverage and so in higher collection efficiency as clear from result shows in Figure 5.32.

Figure 5.33 shows the final  $gf$  as function of  $T_{in}/T_{sat}$  for graphite particle with  $D_p=10$  and  $150$  nm evaluated at  $T_{in}=375$  K  $X_v=0.25$  and  $0.35$ . The results shows in figure suggest that the final  $gf$  i.e. mean final size of droplet (including particle) is almost the same for fine ( $150$  nm) and ultrafine ( $10$  nm) particles. In this case it worth to note that capture process of ultrafine particle due to higher coverage degree is higher with the respect of fine particle. In fact the  $gf$  reaches a value of approximately  $36$  for ultrafine graphite particle ( $D_p=10$  nm) while for the same coverage degree (i.e. same final droplet size) its values is about of  $2.4$  for fine particles ( $D_p=150$ nm) at  $T_{in}/T_{sat}=1.08$ .

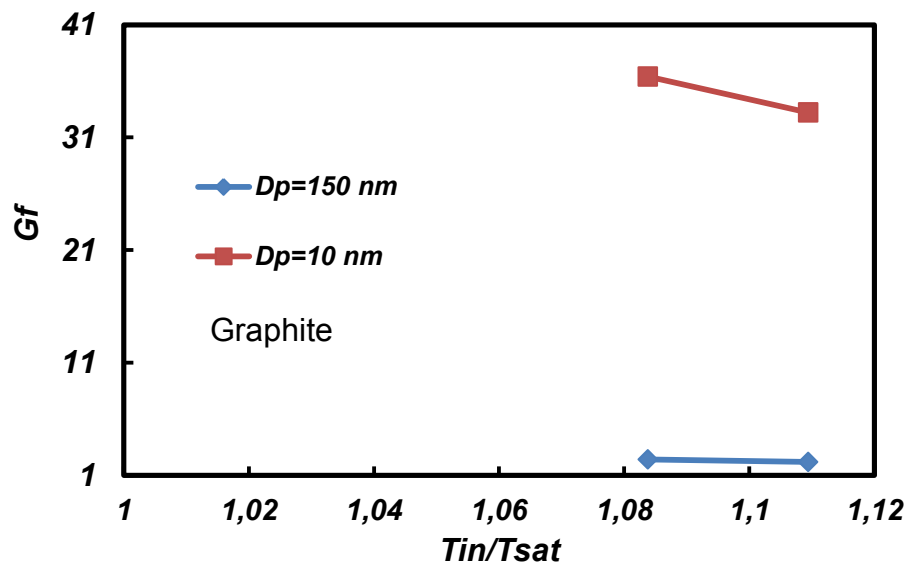


Figure 5.33: Maximum value of the growth factor as a function of  $T_{in}/T_{sat}$  for graphite particles

Figure 5.34 shows the final  $gf$  i.e. droplet size as function of  $T_{in}/T_{sat}$  for  $T_{in}=405$  K varying  $X_v$  from  $0.1$  to  $0.35$  and parametric in particles number concentration.

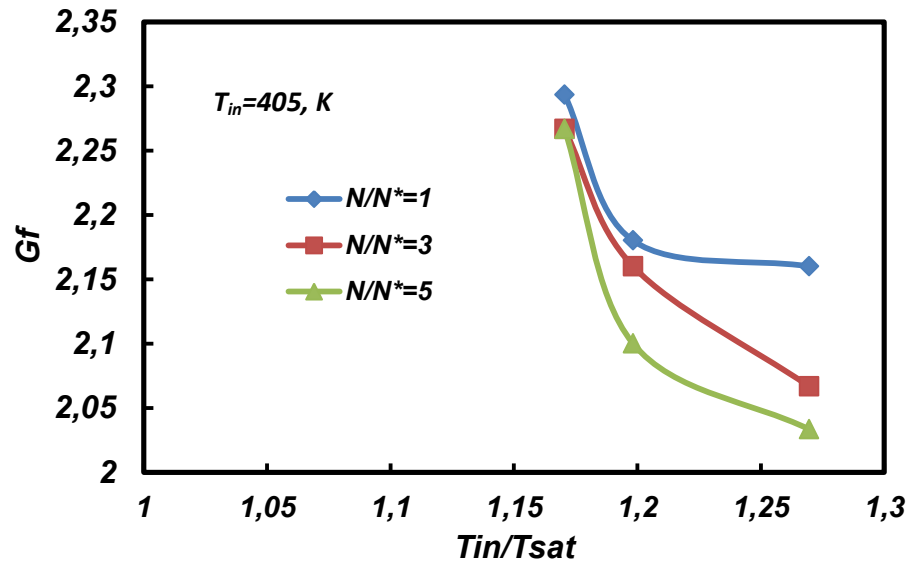


Figure 5.34 Evaluation droplet final size and collection efficiency as function of inlet temperature parametric in particles number concentration

The results show in figure 5.34 suggest that increasing particles number concentration results in a lower  $gf$  (i.e. lower final droplet size) . By varying particles number concentration from  $N/N^*=1$  up to  $N/N^*=5$  growth factor varies from 2.29 to 2.26 at  $T_{in}/T_{sat} = 1.17$  ( i. e.  $X_v=0.35$ ) and from 2.16 to 2.03 at  $T_{in}/T_{sat} = 1.26$  (i.e.  $X_v=0.1$ ) respectively. Again the vapor concentration relatively strongly affect the particles growth with respect to number particles concentration. (Table 3 in appendix A) summarize the values of  $gf$  and evaluated final droplet size for all condition analyzed during the experimental campaign.

## ***Chapter 6***

### ***Conclusion***

The capture of particulate in a certain range of dimension is a key feature of the treatments of many combustion and industrial derived flue gases.

For particle diameters ranging from 0.1  $\mu\text{m}$  to 1  $\mu\text{m}$  (Greenfield gap), the removal efficiency of traditional abatement systems based on diffusion, inertial impact, as well as sedimentation, decreases to approximately 25%, thereby making the application of these systems impractical. Improvements in the operation at optimal working conditions might be facilitated by increasing the dimension of the particles to be eliminated upstream of the standard cleaning processes.

A promising technique for both industrial and domestic applications relies on increasing the diameter of fine and ultra-fine particles by condensing water vapor onto the particles themselves thus improving the performances of traditional particle collection devices. The easy availability of vapor at relatively low temperatures makes this technique interesting for a wide range of industries, including chemical, glass, cement and metallurgy production systems and combustion facilities, all of which are interested in the removal of fine particles from waste gases. It might be even more relevant to combustion systems containing significant amounts of vapor, such as MILD or coal oxy-fuel combustion processes.

In this work an experimental and theoretical evaluation of efficiency of the flue gases cleaning process by means of activation heterogeneous water nucleation mechanism has been carried out. The process of particles activation via heterogeneous nucleation was analyzed as function of working condition, (inlet temperature and vapor concentration) with particular regard to the effect particles dimension, number concentration and chemical nature. During

this process, the particles act as condensation nuclei so that the drops are formed and grow on the particle surface until to reach micrometer sized in certain working conditions.

The study has been conducted carrying out a very deep bibliographic research, illustrated in Chapter 1, concerning the process of vapor nucleation and formation of droplets to identify the dependencies of the process from environmental parameters and the characteristics of the particle acting as condensation nucleus. Furthermore the theory of capillary condensation is considered and recognized as a useful tool for the interpretation of experimental result and for the evaluation of the induction time of the process. The experimental apparatus and diagnostic techniques used are widely described in Chapters 2 and 3. Experimental tests for the characterization of particles and for the evolution of condensation process has been carried out by means of off-line and in situ measurements.

Several off-line measurement systems were employed to analyze particles fed into the chamber; DLS was used for the evaluations of particles dimension collected on a filter trap, UV-Vis Spectroscopy for the determination of particles concentration, TEM and HRTEM images for characterization of particle surface morphology, B.ET. for evaluation of specific surface area, FTIR to verify the presence of oxygenated functional groups on particles, TG to analyze the solid sample stability. Furthermore an estimation of residual charge on particles surface is obtained by means an electrostatic low pressure impactor.

Afterwards an experimental campaign was carried out in a condensation laminar chamber, and the formation and growth of droplets were characterized by means of optical diagnostics. For this purpose instrumented lab scale equipment has been designed, constructed and tested. Experimental protocols and measurement techniques have been optimized. The core of the equipment is the laminar flow chamber optically accessible for in situ optical diagnostics applications. The sizing of the system has been based on the results of a theoretical evaluation of characteristic time of droplet formation and growth. The main characteristics of the laminar condensation chamber that make the experimental apparatus unique in the field of

condensation studies are the modulation and control of parameters independently from each other, the optical accessibility for implementation of laser diagnostic technique that allow for in situ spatially and temporally resolved measurements and flexibility with respect to plant modifications.

Thus the temporal evolution of droplet growth process has been studied by using submicronic particles with a different wettability (C, Fe and Ni). The particles have been produced by means of an aerosol spark generator. Vapor nucleation on submicronic particles has been followed along the axis of the laminar flow chamber in dependence of operative conditions and particles characteristics by measuring the intensity of vertical ( $I_{VV}$ ) and horizontal ( $I_{HH}$ ) component of elastically scattered light and then evaluating the polarization ratio  $\gamma = I_{HH}/I_{VV}$ . Induction and growth characteristic times have been evaluated by the analysis of axial profiles of polarization ratio. By means a specific numerical modeling the polarization ratio of composite sphere made by a water shell hosting a solid particles was been calculated. In such a way the final size of droplet and so the particle growth factor have been evaluated.

The results have been compared with some theoretical predictions with the purpose of verifying the effectiveness of the available models for the process characterization.

From the analysis of experimental results have been observed that particles growth process takes place in such condition far from saturation of vapor bulk phase. Several theory reported in the literature suggest that this phenomenon occurs due to adsorption of condensing species on particles surface even though no clear experimental identification of this process was available.

An evaluation of the particle condensational growth demonstrated that the dispersed particles, acting as condensation nuclei, were captured in the nucleated water droplets with high efficiency, depending on the operating conditions. The final size of the particles was increased with high inlet vapor concentrations and low working temperature, improving their removal from the gas stream. For example at  $X_v=0.5$ , the particles size increased from 355 nm up to

1100 nm for  $T_{in}$  ranging from 425 K to 375 K. This means that in this last condition the final dimension increases of more than 600% with respect of initial particles dimension. Furthermore in these condition a reduction of the induction time of process was observed.

The presence in the system of higher wettable particles anticipates the occurrence of the induction time and improve the water uptake from gas flow (higher growth factor).

It is worth to note that passing from graphite to nickel particles, i.e. increasing particle wettability the growth factor of particles evaluated at  $T_{in}=375$  K and  $X_v=0.35$  increase from 2.4 to 3.33 respectively. This means that the final dimension passes from 150 nm to 360 nm for graphite particles and from 150 nm to 526 nm for nickel particles with a percentage increase of 140% and 250% respectively

Furthermore the increasing in particles number concentration does not affect the occurrence of the induction time but reduces the final covering degree of particles. In fact the growth factor evaluated at  $T_{in}=375$  K and  $X_v=0.25$  varying the number concentration from  $N/N^*=1$  to  $N/N^*=5$  vary from 2.18 to 2.1 respectively.

Finally, it was shown that also ultrafine particles can be actived by nucleation mechanism. In addition because of the final size of particle is strongly influenced by inlet vapor concentration, the growth rate and also the coverage degree of ultrafine particles seems to be very higher with the respect of larger particles. The value of growth factor for particle distribution with a mean diameter of 10 nm is about of 33 in the tests conditions considered.

The evaluation of the particle abatement by means of condensational growth demonstrated that the dispersed particles, acting as condensation nuclei, were captured in the nucleated water droplets with high efficiency, depending on the operating conditions.

The primary aim of this PhD thesis has been achieved. The results obtained represent a first database for kinetic data of condensation process. They shows that particle growth mechanism involves different physical processes. The main result obtained is that particle covering process related to its morphology and chemical properties is active at subsaturation condition

i.e.  $S < 1$ . In these conditions absorption and adsorption processes followed by capillary condensation and swelling of particles (i.e. structural modification) leads to a size variation of particles, also improving sticking and cohesion between them, even if their size variation is relatively low. While for  $S > 1$  the particles coverage is enhanced by mass transport of vapor species toward particles surface. In such a case the final size of the composite droplet is of the order of micron. It is worthwhile to note that both mechanism are particularly effective for particles capture (high growth factor) showing an unitary activation efficiency in the operative conditions considered.

It is worth noting that extreme working conditions may be useful for the particle coverage. In addition, this work demonstrated that the theoretical prediction related to classical nucleation theory can be used to determine the process effectiveness at higher  $X_v$  and lower  $T_{in}$ , even though it fails to predict the induction time. At low values of  $X_v$ , this approach was not valid in predicting the occurrence of the vapor condensation on particles. For this purpose the theory of capillary condensation seems to be an useful tool to predict the vapor deposition on particles and the induction time of growth process in so severe condition.

In this PhD thesis, it was assessed that the characteristic induction and growth times are compatible with practical applications. The identification and estimation of this information can be useful in the design and dimensioning of a real abatement unit. The data presented in this work are broadly applicable and intrinsically relevant because the simple system used for the experimental tests, was designed to temporally resolve the single sub-processes into a wide range of parameters.

As a result, it may be beneficial to separate the abatement process into sequential steps at different vapor concentrations, depending on the context of the application. After an initial condensational growth unit, the decrease to zero of the contact angle due to the water layer deposition on the particles strongly could increase the nucleation rate in a successive condensational growth unit. In addition, the successive growth of the particles could be used

to control the final dimension of the droplet, depending on the downstream unit used for droplet removal. This twofold effect could lead to a significant increase in the overall plant efficiency. Similar considerations are applicable for the process dependence on the inlet temperature.

The rich database collected during the experimental works of this thesis represent a valid first step in the development of the required knowledge on these new particles collection mechanism. Although several data are collected, there is still the need to enlarge the range of parameters investigated. The variation of the chemical nature of particles and the carrier gas (CO<sub>2</sub>), exploitation of wider vapor concentration and particle dimension, are just some of the potential future challenges which scientific research has to face.

### ***Summary of the main findings***

- The growth process was observed also for saturation condition  $S < 1$
- It was pointed out that particles activation process is based on absorption of water vapor on particles surface
- All particles are simultaneously activated: the activation efficiency is 100% even for relatively low vapor concentration
- The droplet final diameter, in all condition considered for the experimental tests, were evaluated
- In general the particle coverage is high: even in the case lower vapor concentration the final size of droplet is twice that initial particles dimension
- Vapor inlet concentration strongly affects the final droplet size (Higher vapor concentration results in larger droplet size and particle coverage)
- Inlet temperature weakly affects the final size (Lower inlet temperature positively affect the final size and efficiency particle coverage)

- Higher particles wettability results in higher water coverage and lower induction time
- Ultrafine particles (10 nm) can be captured by condensation technique
- Higher particles concentration results in a lower final droplet size and coverage degree

**Appendix A**

*Table 1. Characteristic elements produced by different industrial processes*

Oil Power heat station	V, Ni
Incineration of waste	Zn, Sb, Cu, Cd, Hg
Coal combustion	Se, As, Cr, Co, Cu, Al
Refineries	V
Foundries of non-ferrous metal	As, In (fusione del nichel), Cu
Metallurgy of iron and steel	Mn
Copper refinery	Cu

Table 2: Ratio between the concentrations of aerosol in the plume  
and in the base of the flue gases

<i>Città</i>	Khabarovsk		Ermak	Pavlodar		Nizhnii Tagil			Norilsk
<i>Impianto</i>	<i>Power</i>	<i>Power</i>	<i>Power</i>	<i>Alu-</i>	<i>Carriage</i>	<i>Ural</i>	<i>Metall</i>	<i>Coke</i>	<i>Non-</i>
<i>Comp.</i>	<i>heat(1)</i>	<i>heat(3)</i>	<i>heat</i>	<i>minium</i>	<i>building</i>	<i>chemical</i>	<i>urgical</i>	<i>battery</i>	<i>ferrous</i>
	<i>station</i>	<i>station</i>	<i>station</i>	<i>plant</i>	<i>plant</i>	<i>plastpolymer</i>	<i>works</i>	<i>plant</i>	<i>mining</i>
F <sup>-</sup>	-	-	-	-	344	<b>1136</b>	<	21	2
Na <sup>+</sup>	133	30	8	<	75	<	<	<b>260</b>	5
K <sup>+</sup>	<b>256</b>	99	8	55	132	<	<	<	21
Cl	138	92	10	73	<b>2642</b>	262	109	72	1
Br <sup>-</sup>	<	<	114	33	<b>288</b>	136	8	12	-
NH <sub>4</sub> <sup>+</sup>	<	1733	49	28	<b>2272</b>	<	<	442	1
NO <sub>3</sub> <sup>-</sup>	<	<	75	<	<b>353</b>	<	55	8	1
SO <sub>4</sub> <sup>2-</sup>	<	<	42	2	<b>66</b>	<	<	23	17
Hg <sup>2+</sup>	8	<	32	1	4	18	124	15	-
As <sup>5+</sup>	<	<b>187</b>	59	2	<	10	<	<	-
Zn <sup>2+</sup>	<b>67</b>	45	5	4	<	<	27	<	-
Cd <sup>2+</sup>	<	<	1	<	<	<	50	<	-
Al	<b>248</b>	133	177	147	200	<	211	122	58
Ca	187	112	319	156	264	87	1	135	16
Fe	<b>170</b>	59	167	155	39	20	77	51	7
Mn	37	28	33	97	3	<	<	68	81
Mg	208	98	4	1	<b>655</b>	95	25	188	256
Si	634	113	155	198	<	<	<	83	<b>3700</b>
Pb	<	<	27	180	<	<	<b>500</b>	<	234
Cr	<	13	125	46	<b>186</b>	66	103	103	1
Ni	<b>160</b>	27	-	-	1	7	78	10	148
Cd	<	167	<b>189</b>	172	-	-	-	-	-
Cu	<b>280</b>	10	22	1	9	12	167	17	39
V	50	8	67	<b>80</b>	65	43	<	30	3
Zn	<b>1800</b>	640	390	-	-	-	-	-	28

Table 3: Summary of analyzed experimental tests condition

$T_{in}$ , K	$xv_{in}$	theta °	$Dp_0$ (nm)	$N/N^*$	gamma_ max	$D_{fm}$ (nm)	gf	$t_{ind}$ (ms)	$t_{growth}$ (ms)
375	0.1	85	150	1	0.2	324	2.16	125	225
	0.25				0.22	327	2.18	120	185
	0.35				0.58	360	2.4	60	75
	0.5				>1	1100	7.33	<50	
	0.7				>1	1200	8	<50	
405	0.1				0.2	324	2.16	150	225
	0.25				0.22	327	2.18	140	200
	0.35				0.38	344	2.29	100	150
	0.5				>1	370	2.46	60	137
	0.7				>1	1150	7.6	<50	
425	0.1				0.15	310	2.06	170	225
	0.25				0.17	315	2.1	155	210
	0.35				0.37	344	2.29	140	200
	0.5				0.55	355	2.36	60	162
	0.7				0.6	360	2.4	52.6	118
375	0.25		10		0.3	332	33.2	120	185
	0.35				0.62	364	2.42	60	75
	0.25		150		0.22	327	2.18	120	185
	0.35				0.58	360	2.4	60	75
405	0.1		150		0.2	324	2.16	150	225
	0.25				0.22	327	2.18	140	200
	0.35				0.38	344	2.29	100	150
	0.1			3	0.14	310	2.06	150	225
	0.25				0.22	324	2.16	140	200
	0.35				0.32	340	2.26	100	150
	0.1			5	0.13	305	2.03	150	225
	0.25				0.16	315	2.1	140	200
	0.35				0.32	340	2.26	100	150
375	0.1	50	150	1	0.25	317	2.13	100	225
	0.25				0.42	340	2.26	90	160
	0.35				1	372	2.48	<50	100
	0.5				>1	1200	8	<50	
	0.7				>1	1250	8.3	<50	
405	0.1			1	0.3	324	2.16	125	225
	0.25				0.4	335	2.23	110	190
	0.35				0.55	350	2.33	100	160
	0.5				0.958	380	2.53	50	145
	0.7				>1	1170	7.8	<50	
425	0.1				0.26	320	2.13	130	225
	0.25				0.32	330	2.2	125	225
	0.35				0.48	344	2.29	105	175

	0.5				0.7	360	2.4	56	160
	0.7				0.76	370	2.46	<50	137
375	0.1	20	150	1	0.25	317	2.11	80	190
	0.25				0.35	332	2.21	72	125
	0.35				>1	526	3.33	<50	80
	0.5				>1	1200	8	<50	
	0.7				>1	1270	8.46	<50	
405	0.1		150	1	0.25	317	2.11	110	200
	0.25				0.3	330	2.2	90	145
	0.35				0.62	356	2.37	80	140
	0.5				1	390	2.5	56	111
	0.7				>1	1180	7.3	<50	
425	0.1		150	1	0.22	310	2.06	125	225
	0.25				0.3	330	2.2	120	200
	0.35				0.52	348	2.32	115	172
	0.5				0.7	360	2.4	62.5	125
	0.7				0.88	377	2.51	<50	110

Table 4: Surface area from B.E.T.

Species	Specific surface area m <sup>2</sup> /g (no wet)	Specific surface area m <sup>2</sup> /g (wet)
Graphite	310 (Kunznetsov et al. 2003)	644
Iron	143	173
Nickel	266	

**Appendix B**

Property			Unit
Molar mass	$M_v$	18.015	kg kmol <sup>-1</sup>
		0.018	kg mol <sup>-1</sup>
Surface tension	$\sigma_{lv}$	$(93.6635 \times 10^{-3} + 9.133 \times 10^{-6} T - 2.75 \times 10^{-7} T^2) \times 1000$	mNm <sup>-1</sup>
Vapor pressure	$p_s$	$\exp\left[73.649 - \frac{7258.2}{T} - 7.3037 \times \ln(T) + 4.1653 \times 10^{-6} \times T^2\right]$	Pa
Density	$\rho_l$	$\frac{5.459}{0.30542 \left[1 + (1 - T/647.13)^{0.081}\right]}$	Kmol m <sup>-3</sup>
Boltzmann constant	$k_B$	$1.380 \times 10^{-23}$	J k <sup>-1</sup>
		$1.380 \times 10^{-16}$	erg k <sup>-1</sup>
Pressure	$p$		Pa
Super saturation	$S = p_s/p$		a.u.
Temperature	$T$		K
Avogadro's number	$N_a$	$6.02283 \times 10^{23}$	mol <sup>-1</sup>
Specific volume	$v_l$	$1/\rho$	cm <sup>3</sup> g <sup>-1</sup>
Gas universal Constant	$R$	8,31400	J/mol K
		83140000	erg/mol K
	$n_L$	$N_a/M_v = 3.33 \times 10^{22}$	#/cm <sup>3</sup>
Molar volume	$v_L$	$M_v/N_a \rho_l$	cm <sup>3</sup> /#
Vapor molecular mass	$m_l$	$M_v/N_a = 2.992 \times 10^{-23}$	g

Table 4: Van der Waals interaction coefficient and parameters related to wettability between water and solid surface

parametri	C	BN	Al	Au	LiF
$\epsilon$	0,619	0,38	0,98	0,84	0,31
$E_s$ (a.u.)	0,667	0,71	0,473	0,888	0,74
$C_{perm}$	104	64	166	142	51
$C_{vdw}$	971	614	1278	1502	511
$C$ (meV Å <sup>3</sup> )	1074	678	1444	1644	562

Table 5: Interaction potential parameters and contact angle value for other surfaces

parameters	Surface						
	C	Al	Au	Ni	Cu	Pd	Si
$\epsilon$	0,619	0,98	0,84	0,74	0,857	0,785	0,84
$E_s$ (a.u.)	0,667	0,473	0,888	0,7	0,652	0,629	0,43
$C_{perm}$	104	166	142	131,46	152,2444	139,4537	149,2244
$C_{vdw}$	971	1278	1502	1213,27	1356,945	1220,636	1057,238
$C$ (meV Å <sup>3</sup> )	1074	1444	1644	1344,73	1509,189	1360,09	1206,463
$D$ (meV)	100	250,3545	168,5822	258,5647	242,9069	131,7198	232,0825
$\theta$	85°	4,6°	53°	7,1°	9,6°	74°	38°

Tabella 6: Parameter for the evaluation of vapor specie diffusivity

Atomic and Structural Diffusion Volume increments			
<i>C</i>	15,9	<i>F</i>	14,7
<i>H</i>	2,31	<i>Cl</i>	21,0
<i>O</i>	6,11	<i>Br</i>	21,9
<i>N</i>	4,54	<i>I</i>	29,8
<i>Aromatic Ring</i>	-18,3	<i>S</i>	22,9
<i>Heterocyclic ring</i>	-18,3		
Diffusion Volumes of simple Molecules			
<i>He</i>	2,67	<i>CO</i>	18,0
<i>Ne</i>	5,98	<i>C<sub>2</sub>O</i>	26,9
<i>Ar</i>	16,2	<i>N<sub>2</sub>O</i>	35,9
<i>Kr</i>	24,5	<i>NH<sub>3</sub></i>	20,7
<i>Xe</i>	32,7	<i>H<sub>2</sub>O</i>	13,1
<i>H<sub>2</sub></i>	6,12	<i>SF<sub>6</sub></i>	71,3
<i>D<sub>2</sub></i>	6,84	<i>Cl<sub>2</sub></i>	38,4
<i>N<sub>2</sub></i>	18,5	<i>Br<sub>2</sub></i>	69,0
<i>O<sub>2</sub></i>	16,3	<i>SO<sub>2</sub></i>	41,8
<i>Air</i>	19,7		

*Appendix*

A molecule placed in an electric field  $E$ , acquires an induced dipole moment proportional to  $E$ ,

$$p_{\text{induced}} = \alpha E$$

where  $\alpha$  is the polarizability (tendency of a charge to orientate according to an external electric field). The polarizability is a molecular property which increases with the number of electrons constituting the molecule and is inversely proportional to the ease of ionizing the molecule:

$$\alpha \propto \frac{Z(\text{atomic number})}{I(\text{ionization potential})}$$

The molecular polarizability has the dimensions of a volume, and is equal to:

$$\alpha = 4\pi\epsilon_0 R^3$$

$$(4\pi\epsilon_0)\text{\AA}^3 = (4\pi\epsilon_0) 10^{-30} \text{ m}^3 = 1.11 \times 10^{-40} \text{ C}^2\text{m}^2\text{J}^{-1}.$$

$$K_B = 1.380 \times 10^{-23} \text{ J/K}$$

$$\epsilon_0 = 8.85 \times 10^{-12} \text{ C}^2/\text{J m}$$

Considering:

$$1 \frac{mN}{m} = 1 \frac{dyne}{cm} = 1 \frac{erg}{cm^2}$$

$$1 dyne = 1 \frac{g cm}{s^2} = 10^{-5} \frac{kg m}{s^2} = 10^{-5} N$$

$$1 \frac{dyne}{cm^2} = 1 \frac{g}{cm s^2} = 10^{-1} Pa$$

$$1 erg = 1 \frac{g cm^2}{s^2} = 10^{-7} J$$

$$1 au(\alpha) = 0.1482 \text{ \AA}^3$$

$$1 au (Ea) = 27.21 \text{ eV}$$

$$1 \text{ meV} = 11.6 \text{ K} \rightarrow 1 \text{ K} = (1/11.6) \text{ meV}$$

$$1 \text{ Debye} = 3.33 \times 10^{-30} \text{ C m}$$

Obtain:

$$\begin{aligned} (\text{Debye})^2 &= (3.33 \times 10^{-30})^2 C^2 m^2 = \frac{(3.33 \times 10^{-30})^2 C^2 m^2}{K_B \frac{J}{K} (4\pi\epsilon_0) \frac{C^2}{J m}} = \frac{(3.33 \times 10^{-30})^2 m^3 K}{K_B (4\pi\epsilon_0)} \\ &= \frac{(3.33 \times 10^{-30})^2 \left(\frac{1}{11.6}\right) (10^{10})^3 \text{ meV } \text{ \AA}^3}{K_B (4\pi\epsilon_0)} \end{aligned}$$

## References

Adams AV .*Physical chemistry of surfaces*. Wiley, NY, 1990.

Andreae, M. O. and Rosenfeld, D.: *Aerosol-cloudprecipitation interactions. Part 1: The nature and sources of cloud-active aerosols*, *Earth Sci. Rev.*, 89, 13–41, 2008.

Bahcall, J. N., *Solar Neutrinos, I. Theoretical*, *Phys. Rev. Letters* 12, 300, 1964

Bailey, A., Cadenhead, D. A., Davies, D. H., Everett, D. H., & Miles, A. J., *Low-pressure hysteresis in the adsorption of organics vapours by porous carbons*. *Journal of the Transactions of the Faraday Society*, 67, 231–243.,1971

Barbieri L., *Wetting properties of flat-top periodically structured superhydrophobic surfaces*, *THÈSE N 3692*, 2006

Beretta F., A. Cavaliere, A. Alessio, *Combustion Science and Technology* 36, (1) 19-37, 1984

Bohren C.F., Huffman D.R., *Absorption and Scattering of Light by Small Particles*, Wiley-VCH Verlag GmbH, 2007

Borghese F., Denti P., Saija R, *J. Opt. Soc. Am. A* 9 ,1327, 1992

Brown R. C., Miake-Lye R. C, Anderson M. K. and Kolb C. E., *J. Geophys. Res., Atmos.*, 101, 22939, 1996

Bruch L. W., Cole M. W., Zaremba E., *Physical Adsorption Forces and Phenomena*, Clarendon Press: Oxford., 1997

Bruggeman D.A.G, *Berechnung verschiedener physikalischer Konstanten von heterogenen Substanzen* , *Ann. Phys.* 24, 636.,1935

Cassie A, Baxter S., *Wettability of porous surfaces*, *Trans Faraday Soc* 40:546–551, 1944

## References

- Charlson R.J., Schwartz S.E., Hales J.M. Cess R.D., Coakley J.A., Hansen J.E., Hofmann D.J.,  
*Science* 255,254, 1992
- Chen C.C., Hung L.C. and. Hsu H. K, *J. Colloid Interface Sci.* 157, 465, 1993
- Cheng, E., Cole M. W., Saam W. F., Treiner J., *Wetting transitions of classical liquid films: a nearly universal trend, Phys. Rev., vol. B48, pp. 18214-18221, 1993*
- Cheng E., Cole M.W., Dupont-Roc J., Saam W.F., Treiner J., *Novel wetting behavior in quantum films, Rev. Mod. Phys., vol. 65, pp. 557-567.,1993*
- Chizmeshya A., Cole M.W., Zaremba, E., *Weak binding potentials and wetting transitions, J. Low Temp. Phys., vol. 110, pp. 677-684, 1998*
- Chukanov V. N. and Korobitsyn B. A., *Specifics of Nucleation in superheated Water and Supersaturated Vapor, Journal of Engineering Thermophysics, Vol. 16, No. 3, pp. 192–199, 2007*
- Chy'lek P., Srivastava V., Pinnick R.G., Wang R.T., *Scattering of electromagnetic waves by composite spherical particles: experiment and effective medium approximations, Appl. Optics* 27,2396, 1988
- Chy'lek P., Lesins G.B., Videen G, Wong J.G.D., Pinnick R.G., Ngo D., Klett J. D, *Black carbon and absorption of solar radiation by clouds, J. Geophys. Res.* 101,365, 1996
- Chy'lek P., Ramaswamy V., Cheng., *Effect of graphitic carbon on the albedo of clouds, J. Atmos. Sci.* 41,3076., 1984
- Chy'lek P., Srivastava V., *Dielectric constant of a composite inhomogeneous medium, Phys. Rev. B* 27,5098.,1983
- Chy'lek P., Videen G., Ngo.D, Pinnick R.G., Klett. J. D. J, *Effect of black carbon on the optical properties and climate forcing of sulfate aerosols, J. Geophys. Res.* 100 ,325., 1995

## References

- Chy'lek P., Videen G., *Scattering by a composite sphere and effective medium approximations, Optics Comm. 146, 15., 1998*
- Curtarolo, S.; Stan, G.; Bojan, M. J.; Cole, M. W.; Steele, W.A. *Phys. ReV. E, 61, 1670, 2000*
- Drossinos Y. and Kevrekidis P.G., *Classical nucleation theory revisited. Physical Review E, p. 026127, 2003.*
- Dubin M. M., *Carbon, 1980, 18, 355.*
- Ebner, C.; Saam, W. F. *Phys. ReV. B, 35, 1822, 1987*
- Erbil HY, Demirel AL, Avci Y. *Transformation of a simple latic into a superhydrophobic surface. Science 299:1377–1380, 2003*
- Fikioris J.G., Uzunoglu N.K., *J. Opt. Soc. Am. 69,1359, 1979*
- Fladerer, A. and Strey R., *Growth of homogeneously nucleated water droplets: a quantitative comparison of experiment and theory, Atmospheric Research, , 65(3-4): p.161-187., 2003*
- Fletcher N. H., *Size effect in Heterogeneous Nucleation, The Journal of chemical physics. 29: p. 572. 1958*
- Frenkel, J., *Kinetic Theory of Liquids. Dover, New York, 1955*
- Friedlander, S. K.. *Smoke Dust and Haze. Oxford Univ. Press, Oxford. p.210, 2000*
- Friedlander, S. K.. *Smoke, Dust and Hue. Wiley, New York., 1977*
- Fuchs N. A. and Sutugin A. G., *High dispersed aerosols, in: Topics in Current Aerosol Research (Part 2), edited by: Hidy, G. M. and Brock, J. R., Pergamon, New York., 1971*
- Fuller K.A., *Scattering and absorption by inhomogeneous spheres and calculations for external aggregation, J. Opt. Soc. Am. A 12 ,893,1995*
- Gatica S.M.; Johnson, J.K.; Zhao X.C., Cole M.W., *Wetting transition of water on graphite and other surfaces. Journal of Physical Chemistry B., vol. 108, pp. 11704-11708, 2004*

## References

Gelbard F., Seinfeld J. H., *The general dynamics equation for aerosols*, *J. Colloid Interface Sci.* 68(2):363-382., 1979

Giechaskiel B., Wang X., Gilliland D., Drossinos Y., *The effect of particle chemical composition on the activation probability in n-butanol condensation particle counters*. *Journal of Aerosol Science* 42 20–37, 2011

Gregg S. J. and Sing K. S. W., *Adsorption, Surface Area and Porosity*, Academic Press, New York, 2nd edn., 1982.

Hagen D. E., Trueblood, M. B., and Whitefield P. D., *A field sampling of the jet exhaust aerosols*. *Particle Science and Technology*, 10, 53–63, 1992

Hamill P., Turco R.P., Kiang C.S., Toon O.B., Whitten R.C., *An analysis of various nucleation mechanisms for sulfate particles in the stratosphere*. *Journal of Aerosol Science*, 13 pp. 561–585., 1992

Hayoz J., Pillo Th., Fasel R., Schlapbach L., Aebi P.. *Physical Review B* 59, issue 24, 15975-15989, 1999

Heist R. H., Honghai H., *Review of vapor to liquid nucleation experiments from 1968 to 1992*. *Department of Chemical Engineering, University of Rochester*, 1994

Helsper C., Mölter W., Löffler F., Wadenpohl C., Kaufmann S.. *Atmospheric Environment*, vol. 27°, No.8., 1993

Helsper C., Mholter W., LHoVer F., Wadenpohl C., Kaufmann S., Wenninger G., *Investigation of a new aerosol generator for the production of carbon aggregate particles*. *Atmospheric Environment*, 27A, 1271–1275, 1993

Hering S., Stolzenburg M., *A Method for Particle Size Amplification by Water Condensation in a Laminar, Thermally Diffusive Flow*. *Aerosol Science and Technology* 39, 5 2005

## References

Hirsikko A., Laakso L., Hörrak U., Aalto, P. P., Kerminen V.M., Kulmala, M., Annual and size dependent variation of growth rates and ion concentrations in boreal forest, *Boreal Environ. Res.*, 10, 357–369, 2005.

Iland K., Wedekind J., Wölk J., Homogeneous nucleation rates of 1-pentanol. *Journal of chemical Physics* Volume 121, number 24., 2004

Israelachvili J.N., *Intermolecular and surface forces*, 2nd edn. Academic Press, London., 1992.

Schulte J. and Schweiger G., Inelastic scattering on spherical microparticles with inclusions, *JOSA A*, Vol. 22, Issue 6, pp. 1048-1052, 2005

Jacobson M.Z., Development and application of a new air pollution modeling system-II, Aerosol module structure and design. *Atmospheric Environment*, Vol. 31, N. 2, 131-144., 1997a

Kalberer M., Ammann M., Arens F., Gaggeler H. W., Baltensperger U., Heterogeneous formation of nitrous acid(HONO) on soot aerosol particles. *Journal of Geophysical Research*, 104, 13825–13840, 1999a

Kalberer M., Ammann M., Gaggeler H. W., Baltensperger U., Adsorption of NO<sub>2</sub> on carbon aerosol particles in the low ppb range. *Atmospheric Environment*, 33, 2815–2822, 1999b

Kampia R.D., Lakhtakia A., Bruggeman model for chiral particulate composites, *J. Phys. D* 25,1390., 1992

Kara E., Huff Hartz, Joshua E., Tischuk, Man Nin Chan, Chak K. Chan, Neil M. Donahue, Spyros N., Pandis, Cloud Condensation nuclei activation of limited solubility organic aerosol, *Atmospheric environment*, 40, 605-617, 2006.

Karcher B., Peter Th., Biermann U. M. and Schumann U., *J. Atmos. Sci.*, 53, 3066, 1996

## References

Kashchiev D., *Analysis of experimental data for the nucleation rate of water droplets. The Journal of chemical physics*,. 125: p. 044505., 2006

Kiehl J.T, Briegleb B.P., *The relative roles of sulfate aerosols and greenhouse gases in climate forcing, Science* 260, 311, 1993

Kirchner U., Scheer V., and Vogt R., *FTIR spectroscopic investigation of the mechanism and kinetics of the heterogeneous reactions of NO<sub>2</sub> and HNO<sub>3</sub> with soot. Journal of Physical Chemistry*, 104, 8908–8915, 2000

Köhler H., *The nucleus in and the growth of hygroscopic droplets, Transactions of the Faraday Society*, 43, 1152., 1936.

Kotzick R., Panne U. and Niessner R., *Changes in condensation properties of ultrafine carbon particles subjected to oxidation by ozone. Journal of Aerosol Science* 28, 5, 725-735, 1996

Kulmala M. and Wagner P. E., *Mass accommodation and uptake coefficients – a quantitative comparison, J. Aerosol Sci.*, 32, 833–841, 2001.

Kulmala M., Laaksonen A. and Girshick S.L., *The self-consistency correction to homogeneous nucleation: extension to binary systems. J. Colloid Interface Sci.* 23:209-212., 1992

Kulmala M., Toivonen A., Mäkelä J. M., and Laaksonen A., *Analysis of the growth of nucleation mode particles observed in Boreal forest, Tellus B*, 50, 449–462, 1998.

Kuznetsov B.V., Rakhmanova T.A, Popovicheva O.B., Shonija N.K., *Water adsorption and energetic properties of spark discharge: Specific features of hydrophilicity. Aerosol Science* 30, 1465-1479, 2003

Lakhtakia A., *General theory of Maxwell-Garret model for particulate composite with bi-isotropic host materials”, Int. J. Electron.* 6 73,1355-1362, 1992

## References

- Lakhtakia A., *Microsc. Opt. Tech. Lett.* 11,290.,1996
- Lazaridis M., Kulmala M. and Laaksonen A., *Binary heterogeneous nucleation of a water-sulphuric acid system: The effect of hydrate interaction. Journal of Aerosol Science*, 22 , pp. 823–830., 1991
- Lehtinen K. E. J., and Kulmala M., *A model for particle formation and growth in the atmosphere with molecular resolution in size, Atmos. Chem. Phys.*, 3, 251–257, 2003
- M. Schrader, *J. Phys. Chem.*, 1975, 79, 2508.
- Mall-Gleible S., Schaaber K., *Generation of Supersaturated Gas-Vapour Mixtures and Nucleation of Water in ICPWS XV, Berlin, September 8-11, 2008*
- Matijević E., Kerker M. and Schulz K. F., *Discuss. Faraday Soc.*30, 178-184.,1960
- Maxwell Garnett J.C., *Colours in Metal Glasses and in Metallic Films, Trans. Roy Soc. A* .203- 385. 1904
- Mikhailov E., Vlasenko S., Martin S. T., Koop T. and Pöschl, U., *Amorphous and crystalline aerosol particles interacting with water vapor – Part I: Microstructure, phase transitions, hygroscopic growth and kinetic limitations, Atmos. Chem. Phys. Discuss.*, 9, 7333–7412, 2009
- Nieminen T., Lehtinen K. E. J. and Kulmala M., *On condensational growth of clusters and nanoparticles in sub-10 nm size range, Atmos. Chem. Phys Discuss.*, 10, 1963-1717, 2010
- Niklasson G.A., Granquist C.G., Hunderi O., *Effective medium models for the optical properties of inhomogeneous materials, Appl. Optics* 20,26, 1986
- Nink A., Saatho H., Schnaiter M. and Mhohler O., *Laboratory investigation of the impact of aircraft particulate emissions on cirrus cloud formation. Air pollution research report 74 Aviation, aerosols, contrails and cirrus clouds, EC*, pp. 149–153, 2001

## References

Oberdöster G., *Pulmonary effects of inhaled ultrafine particles. Int Arch Occup Environ Health*, 74: 1-8.,2001

Popovicheva O., Persiantseva N. M., Shonija N. K., DeMott P., Koehler K., Petters M., Kreidenweis S., Tishkova V., Demirdjian B. and. Suzanne J., *Water interaction with hydrophobic and hydrophilic soot particles, Phys Chem Chem Phys.* 7;10(17):2332-44, 2008

Ossenkopf V., *Effective-Medium Theories for Cosmic Dust Grains, Astron. Astrophys.* 251,210., 1991

Oxtoby D.W., *Journal of Physics: Condensed Matter* 4, 7627, 1992

Patanka S. V., *Numerical Heat Transfer and Fluid Flow. McGraw-Hill, New York, 1980*

Penner J.E., Dickinson R.E., O'Neill C.A, *Science* 256,1432, 1992

Perrin J.M., Lamy .P.L., *On the validity of effective-medium theories in the case of light extinction by inhomogeneous dust particles,Astrophys. J.* 364 ,146.1990

Persiantseva N. M., Popovicheva O. B. and Shonija N. K., *Wetting and hydration of insoluble soot particles in the upper troposphere, J. Environ. Monit.,* 6, 939 – 945, 2004

Petters M. D. and Kreidenweis S. M., *A single parameter representation of hygroscopic growth and cloud condensation nucleus activity, Atmos. Chem. Phys.,* 7, 1961–1971, 2007

Poling B. E., Prausnitz, J. M., and O'Connell, J. P., *The properties of gases and liquids, 5th edn., McGraw-Hill, New York, 2001.*

Popovicheva O., E. Kireeva, N. Persiantseva, T. Khokhlova, N. Shonija, V. Tishkova, B. Demirdjian, *Atmospheric Research* 90, (2-4) 326-337, 2008

Pöschl U., Rose D., and Andreae M. O., *Climatologies of cloudrelated aerosols – Part 2: Particle hygroscopicity and cloud condensation nucleus activity, in: Clouds in the perturbed climate system – Their relationship to energy balance, atmospheric dynamics, and*

## References

- precipitation, edited by: Heintzenberg, J. and Charlson, R. J., MIT Press, Cambridge, 58–72, 2009.
- Pratsinis, S. E.. *Simultaneous nucleation, condensation, and coagulation in aerosol reactors. J. Colloid Interface Sci.* 124(2):416-427., 1988
- Prodi F., *Organinc effect on the precipitation SMM-2004.* 2004
- Pruppacher H. K. and Klett J. D., *Microphysics of Clouds and Precipitation*, D. Reidel, Dodrecht, pp. 714. 1978
- Quere D., *Physica A (Amsterdam)*, 313, 32., 2002
- Ragil, K.;Meunier, J; Broseta, D.; Indekeu, J.;Bonn, D. *Phys. ReV. Lett.*, 77, 1532., 1996
- Reutterl P., Sul H., Trentmann J., Simmel M., Rose D., Gunthe S. S., Wernli H., Andreae M. O., and Pöschl U., *Aerosol- and updraft-limited regimes of cloud droplet formation: influence of particle number, size and hygroscopicity on the activation of cloud condensation nuclei (CCN) Atmos. Chem. Phys.*, 9, 7067–7080, 2009
- Rose D., Gunthe S. S., Mikhailov E., Frank G. P., Dusek U., Andreae M. O., and Pöschl, U., *Calibration and measurement uncertainties of a continuous-flow cloud condensation nuclei counter (DMT-CCNC): CCN activation of ammonium sulfate and sodium chloride aerosol particles in theory and experiment, Atmos. Chem. Phys.*, 8, 1153–1179, 2008a,
- Rose D., Nowak A., Achtert P., Wiedensohler A., Hu M., Shao M., Zhang Y., Andreae M. O., and Pöschl, U., *Cloud condensation nuclei in polluted air and biomass burning smoke near the mega-city Guangzhou, China – Part 1: Size-resolved measurements and implications for the modeling of aerosol particle hygroscopicity and CCN activity, Atmos. Chem. Phys. Discuss.*, 8, 17343–17392, 2008b,
- Roth C., Ferron G. A., Karg E., Lentner B., Schumann G., Takenaka S., Heyder J. -. *Aerosol Sckence and Technology*, 38: 228-235., 2004

## References

Russell A. and Dennis R. *NARSTO critical review of photochemical models and modeling*.  
Vol. 34, N. 12-14, 2283-2324, 2000

Seinfeld J.H. *Air Pollution: Atmospheric Chemistry and Physics of Air Pollution*, John Wiley & Sons. ,1986

Seinfeld J.H. and Pandis S.N. *Atmospheric chemistry and physics. From air pollution to climate change*, John Wiley & Sons, 1998

Seinfeld J. H. and Pandis S. N., *Atmospheric Chemistry and Physics*, John Wiley & Sons, Inc., New Jersey, 2006.

Shanker B., Lakhtakia A., *Extended Maxwell Garnett model for chiral-in-chiral-composites*,  
*J. Phys. D* 26,1740.,1993

Simonenkov Denis V., Boris D. Belan, and Gennadii N. Tolmachev - *Chemical composition of industrial aerosol in some regions*.

Skaropoulos N.C., Ioannidow. M.P., Chrissoulidis D.P, *Indirect mode-matching solution to scattering from a dielectric sphere with an sphere with an eccentric inclusion*, *J. Opt. Soc. Am. A* 11 ,1859-1886. ,1994

Sorjamaa R. and Laaksonen A., *The effect of H<sub>2</sub>O adsorption on cloud drop activation of insoluble particles: a theoretical framework*, *Atmos. Chem. Phys.*, 7, 6175-6180, 2007.

Spence, John C. H., *Experimental high-resolution electron microscopy*, New York Oxford U. Press.,1988

Stephens G.L., Tsay S.C, Q.J.R., *Meteorol. Soc.* 116,671. ,1991

Stroud D., Pan. F.P, *Self-consistent approach to electromagnetic wave propagation in composite media: Application to model granular metals*, *Phys. Rev. B* 17 ,1602. 1978,

Stuebaker M. L. and Snow C. W., *J. Phys. Chem.* 59, 973, 1955

## References

Talbot L., Cheng R. K., Schefer R. W. and Willis. D., *Thermophoresis in a heated boundary layer. J. Fluid Mech.* 101, 737-75, 1980

Vartapetian R. Sh. and Voloshchuk A. M., *Russ. Chem. Rev.*, 64, 985, 1995

Videen G., Ngo D., Chy'lek P, *Optics Lett.* 21 ,1675. ,1995

Videen G., Ngo D., Chy'lek P., Pinnick R.G., *Light scattering from a sphere with an irregular inclusion , J. Opt. Soc.Am. A* 12 ,922. ,1995

Videen G., Pinnick R.G., Ngo D., Fu Q. , Chy'lek P., *Asymmetry Parameter and Aggregate Particles, Appl.Optics* 37 ,1104, 1998

Wagner P.E., Kaller D., Vrtala A., Lauri A., Kulmala M. and Laaksonen A., *Nucleation probability in binary heterogeneous nucleation of water-n-propanol vapor mixtures on insoluble and soluble particles. Physical Review E*, 67 , p. 021605., 2003

Weiglhofer W.S., Lakhtakia A., Michel B., *Microsc. Opt.Tech. Lett.* 15, 263.,1997

Weingartner E., Burtscher, H., and Baltensperger U., *Hygroscopic properties of carbon and diesel soot particles. Atmospheric Environment*, 31, 2311–2327, 1997

Wentzel M., Gorzawski H., Naumann K.H., Saatho H., Weinbruch S., *Transmission electron microscopical and aerosol dynamical characterization of soot aerosols, Aerosol Science* 34 1347–1370, 2003

Wenzel R.N., *Resistance of solid surfaces to wetting by water, Ind Eng Chem* 28:988–994, 1936.

Werder T., Walther J., Jaffe R., Koumoutsakos P., *Water-carbon interactions: Potential energy calibration using experimental data, Citeseer*, 2003

Wexler A.S., Lurmann F.W. and Seinfeld J.H., *Modelling urban and regional aerosols - I. Model development. Atmos Env. V.* 28, N. 3, pp.531-546, 1994

## References

- Whitby E. R., *Modal aerosol dynamics modeling. Ph.D. thesis, University of Minnesota, Minneapolis., 1989*
- Whitby K.T., *The physical characterization of sulfur aerosols, Atmospheric Environment 12, 135-159., 1978*
- Wilck M., Stratmann F., *A 2-D Multicomponent Modal Aerosol Model, 1997*
- Wilson C. T., *R. Proc Royal Soc. 265-307. 1897*
- Wilson C. T., *R. Pyhl Trans Royal Soc. 265-307. 1899.*
- Winkler P.M., Steiner G., Vrtala A., Vehkamäki H., Noppel M. and Lehtinen K.E.J, Reischl G. P., Wagner P. E., Kulmala M., *Heterogeneous nucleation experiments bridging the scale from molecular ion clusters to nanoparticles. Science, 319 pp. 1374–1377., 2008*
- Yost F.G., Michael J.R., Eisenmann E.T., *Extensive wetting due to roughness. Acta Metall Mater 45:299–305.,1995*